

LEVEL II

(2)

AD A078865

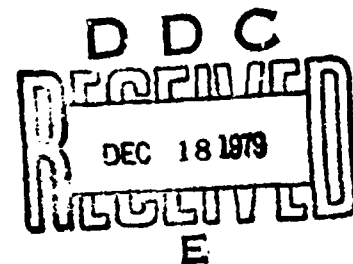
AFAPL-TR-79-2045

MAGNETOHYDRODYNAMIC (MHD) MAGNET MODELING

Z. J. J. Stekly, R. D. Pillsbury, Jr.  
A. R. Beckwith, R. D. Holmes

MAGNETIC CORPORATION OF AMERICA  
Waltham, Massachusetts 02154

GENERAL DYNAMICS CORPORATION, CONVAIR DIVISION  
San Diego, California 92138



JUNE 1979

DDC FILE COPY

Interim Report

~~17~~ March 1978 - September 1978

Approved for public release; distribution unlimited.

AIR FORCE AERO PROPULSION LABORATORY  
AIR FORCE WRIGHT AERONAUTICAL LABORATORIES  
AIR FORCE SYSTEMS COMMAND  
WRIGHT-PATTERSON AIR FORCE BASE, OHIO 45433

79 12 18 14

NOTICE

When Government drawings, specifications, or other data are used for any purpose other than in connection with a definitely related Government procurement operation, the United States Government thereby incurs no responsibility nor any obligation whatsoever; and the fact that the government may have formulated, furnished, or in any way supplied the said drawings, specifications, or other data, is not to be regarded by implication or otherwise as in any manner licensing the holder or any other person or corporation, or conveying any rights or permission to manufacture, use, or sell any patented invention that may in any way be related thereto.

This report has been reviewed by the Information Office (OI) and is releasable to the National Technical Information Service (NTIS). At NTIS, it will be available to the general public, including foreign nations.

This technical report has been reviewed and is approved for publication.



FREDERICK C. BROCKHURST, CAPT, USAF  
Project Engineer  
Power Systems Branch



PAUL R. BERTHEAUD  
Technical Area Manager  
Power Systems Branch

FOR THE COMMANDER



JAMES D. REAMS  
Chief, Aerospace Power Division

"If your address has changed, if you wish to be removed from our mailing list, or if the addressee is no longer employed by your organization please notify AFAPL/POP-2, W-PAFB, OH 45433 to help us maintain a current mailing list".

Copies of this report should not be returned unless return is required by security considerations, contractual obligations, or notice on a specific document.

Unclassified

SECURITY CLASSIFICATION OF THIS PAGE (When Data Entered)

REPORT DOCUMENTATION PAGE		READ INSTRUCTIONS BEFORE COMPLETING FORM
1. REPORT NUMBER (18) AFAPL-TR-79-2045	2. GOVT ACCESSION NO.	3. RECIPIENT'S CATALOG NUMBER
4. TITLE (and Subtitle) (6) MAGNETOHYDRODYNAMIC (MHD) MAGNET MODELING.	5. TYPE OF REPORT & PERIOD COVERED Technical-Interim March-September 1978	
6. AUTHOR(s) (14) Z. J. J. Stekly, R. D. Pillsbury, Jr., A. R. Beckwith, and R. D. Holmes	7. PERFORMING ORG. REPORT NUMBER MCAWP13-01	
8. PERFORMING ORGANIZATION NAME AND ADDRESS Magnetic Corporation of America 179 Bear Hill Road Waltham, Massachusetts 02154	9. CONTRACT OR GRANT NUMBER(s) (15) F33615-77-C-3117	
11. CONTROLLING OFFICE NAME AND ADDRESS Air Force Arm Propulsion Laboratory Air Force Systems Command - US Air Force Wright-Patterson Air Force Base, Ohio	10. PROGRAM ELEMENT, PROJECT, TASK AREA & WORK UNIT NUMBERS (16) 3145-26-39	
12. MONITORING AGENCY NAME & ADDRESS (if different from Controlling Office) (9) Int. ...	12. REPORT DATE June 1979	
	13. NUMBER OF PAGES 210	
	15. SECURITY CLASS. (of this report) Unclassified	
	15a. DECLASSIFICATION/DOWNGRADING SCHEDULE	
16. DISTRIBUTION STATEMENT (of this Report) Approved for public release; distribution unlimited. (14) AIC-1-WP13-14		
17. DISTRIBUTION STATEMENT (of the Abstract entered in Block 20, if different from Report)		
18. SUPPLEMENTARY NOTES		
19. KEY WORDS (Continue on reverse side if necessary and identify by block number) Magnetohydrodynamics (MHD) Power Generation Superconducting Magnet		
20. ABSTRACT (Continue on reverse side if necessary and identify by block number) This report presents the results of a study to establish scaling criteria for a lightweight, superconducting magnet system for use in magnetohydrodynamic power generation. The scaling criteria are used to determine the appropriate size for a model magnet to be built to demonstrate the major system parameters of a full scale, 30 MWe, magnet system.		

DD FORM 1 JAN 73 1473

EDITION OF 1 NOV 68 IS OBSOLETE

Unclassified

SECURITY CLASSIFICATION OF THIS PAGE (When Data Entered)

4-1-11

## FOREWORD

This interim report was prepared by Magnetic Corporation of America, 179 Bear Hill Road, Waltham, Massachusetts under United States Air Force Contract No. F33615-77-C-3117 and covers work performed from March, 1978, through September, 1978.

The Principal Investigator for the program is Dr. Z. J. J. Stekly. The Program Manager is Dr. Robert D. Pillsbury, Jr. Other key contributors to this program are:

Mr. Alan R. Beckwith  
Mr. Bjorn O. Pedersen  
Mr. Samuel Mushnick  
Mr. Michael G. Rose

Included in the report, is an interim report covering the work performed by General Dynamics Convair Division, San Diego, California in support of Magnetic Corporation of America for the period April, 1978, through September, 1978.

The Program Manager at Convair is Mr. R. Doug Holmes. Other key contributors are:

Mr. Des. Vaughan, Design  
Mr. Bruce Boston, Stress Analysis  
Mr. Rod Hidde, Manufacturing

Accession For	
NTIS Grant	<input checked="checked" type="checkbox"/>
DDC ID	<input type="checkbox"/>
Unpublished	<input type="checkbox"/>
Journal Article	<input type="checkbox"/>
Book	<input type="checkbox"/>
Report	<input type="checkbox"/>
Other	<input type="checkbox"/>
Availability	
Dist	Available or Special
A	

## TABLE OF CONTENTS

<u>Section</u>		<u>Page</u>
I	Introduction and Summary	1
II	Magnet Size	15
III	Winding Design	26
IV	Conductor Design	72
V	Structural Design	83
VI	Conductor Stability	102
VII	System Charge, Discharge and Quench	135
VIII	Conclusions and Recommendations	171
Appendix	- Advanced Composite Material (ACM) Magnet Structure Scaling Criteria	175

## LIST OF FIGURES

<u>FIGURE</u>	<u>TITLE</u>	<u>PAGE</u>
1	Magnetic Field on Axis of MHD Magnet as Specified in Contract	3
2	Cutaway View of MHD Magnet	4
3	Quarter Section of Magnet Design at Midplane	5
4	Total Weight vs. Warm Bore Size	9
5	Peak Temperature in MHD Magnet Undergoing a Quench from Operating Current ( $I_{op} = 2000A$ ) vs. Bore Size	12
6	Maximum Potential in Normal Region in MHD Magnet Undergoing a Quench from Operating Current vs. Bore Size	13
7	Stored Energy vs. Warm Bore Size	18
8	Conductor Weight vs. Warm Bore Size	19
9	Structure Weight vs. Warm Bore Size	20
10	Total Weight vs. Warm Bore Size	21
11	Force Components on Saddle Winding	23
12	Total Axial Force vs. Warm Bore Size	24
13	Peak Forces in a Transverse Plane vs. Warm Bore Size	25
14	Contours of Constant Winding Effectiveness	27
15	Magnetic Field on Axis of MHD Magnet as Specified in Contract	28
16	Typical Filament Model of an MHD Annular Saddle Magnet	30
17	Magnetic Field on Axis vs. Axial Position for 20cm Design ( $j_c = 15kA/cm^2$ )	32
18	Magnetic Field on Axis vs. Axial Position for 29cm Design ( $j_c = 15kA/cm^2$ )	33

# LIST OF FIGURES

<u>FIGURE</u>	<u>TITLE</u>	<u>PAGE</u>
19	Magnetic Field on Axis vs. Axial Position for 40cm Design ( $j_c = 15\text{kA/cm}^2$ )	34
20	Magnetic Field on Axis vs. Axial Position for 50cm Design ( $j_c = 15\text{kA/cm}^2$ )	35
21	Magnetic Field on Axis vs. Axial Position for 20cm Design ( $j_c = 30\text{kA/cm}^2$ )	36
22	Magnetic Field on Axis vs. Axial Position for 29cm Design ( $j_c = 30\text{kA/cm}^2$ )	37
23	Magnetic Field on Axis vs. Axial Position for 40cm Design ( $j_c = 30\text{kA/cm}^2$ )	38
24	Magnetic Field on Axis vs. Axial Position for 50cm Design ( $j_c = 30\text{kA/cm}^2$ )	39
25	Magnetic Field on Axis vs. Axial Position for Several Values of Taper Angle, $\theta$	40
26	Field Homogeneity for 20cm Design ( $j_c = 15\text{kA/cm}^2$ ) at Inlet ( $x = .525\text{m}$ )	42
27	Field Homogeneity for 20cm Design ( $j_c = 15\text{kA/cm}^2$ ) at Midplane ( $x = 0.0\text{m}$ )	43
28	Field Homogeneity for 20cm Design ( $j_c = 15\text{kA/cm}^2$ ) at Outlet ( $x = -.525\text{m}$ )	44
29	Field Homogeneity for 29cm Design ( $j_c = 15\text{kA/cm}^2$ ) at Inlet ( $x = .525\text{m}$ )	45
30	Field Homogeneity for 29cm Design ( $j_c = 15\text{kA/cm}^2$ ) at Midplane ( $x = 0.0\text{m}$ )	46
31	Field Homogeneity for 29cm Design ( $j_c = 15\text{kA/cm}^2$ ) at Outlet ( $x = -.525\text{m}$ )	47
32	Field Homogeneity for 40cm Design ( $j_c = 15\text{kA/cm}^2$ ) at Inlet ( $x = .525\text{m}$ )	48
33	Field Homogeneity for 40cm Design ( $j_c = 15\text{kA/cm}^2$ ) at Midplane ( $x = 0.0\text{m}$ )	49
34	Field Homogeneity for 40cm Design ( $j_c = 15\text{kA/cm}^2$ ) at Outlet ( $x = -.525\text{m}$ )	50
35	Field Homogeneity for 50cm Design ( $j_c = 15\text{kA/cm}^2$ ) at Inlet ( $x = .525\text{m}$ )	51

# LIST OF FIGURES

<u>FIGURE</u>	<u>TITLE</u>	<u>PAGE</u>
36	Field Homogeneity for 50cm Design ( $j_c = 15\text{kA/cm}^2$ ) at Midplane ( $x = 0.0\text{m}$ )	52
37	Field Homogeneity for 50cm Design ( $j_c = 15\text{kA/cm}^2$ ) at Outlet ( $x = -.525\text{m}$ )	53
38	Field Homogeneity for 20cm Design ( $j_c = 30\text{kA/cm}^2$ ) at Inlet ( $x = .525\text{m}$ )	54
39	Field Homogeneity for 20cm Design ( $j_c = 30\text{kA/cm}^2$ ) at Midplane ( $x = 0.0\text{m}$ )	55
40	Field Homogeneity for 20cm Design ( $j_c = 30\text{kA/cm}^2$ ) at Outlet ( $x = -.525\text{m}$ )	56
41	Field Homogeneity for 29cm Design ( $j_c = 30\text{kA/cm}^2$ ) at Inlet ( $x = .525\text{m}$ )	57
42	Field Homogeneity for 29cm Design ( $j_c = 30\text{kA/cm}^2$ ) at Midplane ( $x = 0.0\text{m}$ )	58
43	Field Homogeneity for 29cm Design ( $j_c = 30\text{kA/cm}^2$ ) at Outlet ( $x = -.525\text{m}$ )	59
44	Field Homogeneity for 40cm Design ( $j_c = 30\text{kA/cm}^2$ ) at Inlet ( $x = .525\text{m}$ )	60
45	Field Homogeneity for 40cm Design ( $j_c = 30\text{kA/cm}^2$ ) at Midplane ( $x = 0.0\text{m}$ )	61
46	Field Homogeneity for 40cm Design ( $j_c = 30\text{kA/cm}^2$ ) at Outlet ( $x = -.525\text{m}$ )	62
47	Field Homogeneity for 50 cm Design ( $j_c = 30\text{kA/cm}^2$ ) at Inlet ( $x = -.525\text{m}$ )	63
48	Field Homogeneity for 50cm Design ( $j_c = 30\text{kA/cm}^2$ ) at Midplane ( $x = 0.0\text{m}$ )	64
49	Field Homogeneity for 50cm Design ( $j_c = 30\text{kA/cm}^2$ ) at Outlet ( $x = -.525\text{m}$ )	65
50	Contours of Constant Field in the Winding at the Inlet for the 20cm Design ( $j_c = 15\text{kA/cm}^2$ )	66
51	Contours of Constant Field in the Winding at the Inlet for the 29cm Design ( $j_c = 15\text{kA/cm}^2$ )	67



# LIST OF FIGURES

<u>FIGURE</u>	<u>TITLE</u>	<u>PAGE</u>
52	Contours of Constant Field for the 40cm Design at Inlet ( $j_c = 15\text{kA/cm}^2$ )	68
53	Contours of Constant Field in the Winding at the Inlet for the 50cm Design ( $j_c = 15\text{kA/cm}^2$ )	69
54	Contours of Constant Field for the 29cm Design at Inlet ( $j_c = 30\text{kA/cm}^2$ )	70
55	Typical Conductor Bundle Showing Relationship to Structural Teeth and Cold Bore Tube	74
56	Force Components on Saddle Winding	84
57	Quarter Section of Magnet Design at Midplane	85
58	Weight of an Aluminum Axial Structure vs. Allowable Deflection for Various Warm Bore Sizes	89
59	End Outer Shell Weight vs. Radial Deflection Membrane	90
60	Weight vs. Deflection for a Structure Limited Design	91
61	Maximum Radial Deflection vs. Warm Bore Diameter for an Aluminum Structure	92
62	Maximum Radial Deflection vs. Warm Bore Diameter for a Stainless Steel Structure	93
63	Transverse Structural Weight vs. Warm Bore Diameter for an Aluminum Structure	95
64	Transverse Structural Weight vs. Warm Bore Diameter for a Stainless Steel Structure	96
65	Transverse Structural Weight vs. Warm Bore Diameter for an Aluminum Structure	97
66	Structural Weight vs. Warm Bore Diameter for a Stainless Steel Structure	98
67	Relative Heat Input vs. Helium Volume for Different Slip Conditions	105
68	Relative Maximum Temperature vs. Helium Volume for Different Slip Conditions	106
69	Non-Dimensional Maximum Temperature Rise vs. Non-Dimensional Distance for Bundle Slip	108

# LIST OF FIGURES

<u>FIGURE</u>	<u>TITLE</u>	<u>PAGE</u>
70	Bundle Compressive Slip Model	109
71	Peak Temperature Rise Due to Conductor Slip vs. Warm Bore Size for Two Current Densities	111
72	Penetration Depth vs. Warm Bore Size for Two Current Densities	112
73	Bundle Axial Slip Model	114
74	Maximum Temperature Rise vs. Axial Slip for Various Warm Bore Sizes ( $j_c = 15\text{kA/cm}^2$ )	115
75	Bundle Radial Slip Model	116
76	Relative Motion vs. Warm Bore Size for Various Values of Deflection	117
77	Slip Energy per Unit Surface Area vs. Warm Bore Size for Various Values of Deflection	119
78	Diffusion of Magnetic Flux from Normal Superconducting Strand to Adjoining Stabilizer	123
79	Diffusion of Magnetic Flux Through Stabilizer to Central Superconducting Strand	124
80	Average Power Density vs. Time Dissipated in Stabilizer During Current Diffusion with Process Reversal	125
81	Half Length of Normal Region vs. Heat Input	127
82	Half Length of Normal Region vs. Effective Heat Flux	129
83	Maximum Net Heating vs. Effective Heat Flux	130
84	Temperature Profile Along Conductor for Times Due to a Heat Pulse of .14 J	133
85	Conductor Half Normal Length vs. Time for various Heat Pulse Inputs	134
86	Circuit Models for Magnet Protection	136
87	Equations for Magnet Charge and Discharge	137

# LIST OF FIGURES

<u>FIGURE</u>	<u>TITLE</u>	<u>PAGE</u>
88	Secondary (Normalized) Current vs. (Normalized) Time	140
89	Power and Energy Dissipated in Structure for Several Charge Rates vs. Time	141
90	Magnet Current, Dumped Power and Dumped Energy vs. Time for System Discharge	142
91	Structure Current, Dissipated Power and Dissipated Energy vs. Time for System Discharge	143
92	Energy Dissipated in Structure vs. Charge Time of Magnet System	144
93	Energy Dissipated in Structure vs. Discharge Time Constant of Magnet System	145
94	Normalized Magnet Current, Normalized Internally Absorbed Power and Normalized Internally Absorbed Energy in Quenching System vs. Normalized Time	147
95	Normalized Structure Current, Normalized Structure Dissipated Power and Normalized Structure in Quenching System vs. Normalized Time	148
96	Peak Temperature vs. Time for an MHD Magnet Undergoing Quench	152
97	Potential Difference Across Normal Region vs. Time for an MHD Magnet Undergoing Quench	153
98	Peak Temperature vs. Time for an MHD Magnet Undergoing Quench	154
99	Potential Difference Across Normal Region vs. Time for an MHD Magnet Undergoing Quench	155
100	Peak Temperature vs. Time for an MHD Magnet Undergoing Quench	156
101	Potential Difference Across Normal Region vs. Time for an MHD Magnet Undergoing Quench	157
102	Peak Temperature vs. Time for an MHD Magnet Undergoing Quench	158
103	Potential Difference Across Normal Region vs. Time for an MHD Magnet Undergoing Quench	159

## LIST OF FIGURES

<u>FIGURE</u>	<u>TITLE</u>	<u>PAGE</u>
104	Peak Temperature vs. Time for an MHD Magnet Undergoing Quench	160
105	Potential Difference Across Normal Region vs. Time for an MHD Magnet Undergoing Quench	161
106	Peak Temperature vs. Time for an MHD Magnet Undergoing Quench	162
107	Potential Difference Across Normal Region vs. Time for an MHD Magnet Undergoing Quench	163
108	Peak Temperature vs. Time for an MHD Magnet Undergoing Quench	164
109	Potential Difference Across Normal Region vs. Time for an MHD Magnet Undergoing Quench	165
110	Peak Temperature vs. Time for an MHD Magnet Undergoing a Quench	166
111	Potential Difference Across Normal Region vs. Time for an MHD Magnet Undergoing Quench	167
112	Peak Temperature in MHD Magnet Undergoing Quench	168
113	Maximum Potential in Normal Region in MHD Magnet Undergoing Quench	169
114	Total Relative System Cost Versus Warm Bore Diameter	173
A-1	Concept A - Graphite/Epoxy Filament Wound	184
A-2	Concept B - Boron/Aluminum Structure	186
A-3	Concept C - Graphite/Epoxy Structure	187
A-4	Initial Stress Analysis Procedure	189
A-5	GD/C Finite Element Model YZ Midplane of MHD	190
A-6	Influence of Design Variables on Stress in Structural Components of MHD Concept "A" - 29cm Model	192

## LIST OF FIGURES

<u>FIGURE</u>	<u>TITLE</u>	<u>PAGE</u>
A-7	Computer Graphics Plot of GDC Finite Element Model at MHD Transverse Midplane	195
A-8	Stress Contour Plot of Maximum Principal Stress due to Magnetic Loads	196
A-9	Stress Contour Plot of Minimum Principal Stress due to Magnetic Loads	197
A-10	Stress Contour Plot of Maximum Principal Stress due to Thermal Loads	198
A-11	Stress Contour Plot of Minimum Principal Stress due to Thermal Loads	199
A-12	Stress Contour Plot of Maximum Principal Stress for Combined Magnetic and Thermal Loading	200
A-13	Stress Contour Plot of Minimum Principal Stress for Combined Magnetic and Thermal Loading	201
A-14	MHD Magnet Modeling Manufacturing Sequence Concept A - Graphite/Epoxy, Filament Wound	204
A-15	MHD Magnet Modeling Manufacturing Sequence Concept B - Boron/Aluminum Structure	205
A-16	MHD Magnet Modeling Manufacturing Sequence Concept C - Graphite Epoxy Structure	206

# LIST OF TABLES

<u>TABLE</u>	<u>TITLE</u>	<u>PAGE</u>
1	MHD Tapered Saddle Magnet Design Typical of a 30 Mwe Generator	2
2	System Characteristics for Four Bore Sizes (15,000 A/cm <sup>2</sup> Conductor)	7
3	System Characteristics for Four Bore Sizes (30,000 A/cm <sup>2</sup> Conductor)	8
4	Conductor Specifications	10
5	Magnet Characteristics for Four Bore Sizes (15,000 A/cm <sup>2</sup> Conductor)	16
6	Magnet Characteristics for Four Bore Sizes (30,000 A/cm <sup>2</sup> Conductor)	17
7	Magnetic Field Data	31
8	Conductor Specifications	74
9	Conductor Design Limits	76
10	Advantages and Disadvantages of Various Stabilizer and Superconducting Materials	78
11	Material Properties for Candidate Materials	86
12	Structural Scaling Relationships	99
13	Summary of Slip Calculations 15,000 A/cm <sup>2</sup> Conductor	119
14	Summary of Slip Calculations 30,000 A/cm <sup>2</sup> Conductor	120
15	Conductor Specifications for Quench Analysis	148
16	Winding Specifications for Quench Analysis	149
A-1	Characteristics	179
A-2	Design Variable Inputs for Concept A, 29 cm Model	191
A-3	MHD Concept A Summary for 29 cm, 40 cm and 50 cm Models	193
A-4	Stress Comparison Between Concepts A, B and C for 29 cm Models	194
A-5	MHD Magnet Modeling Concept Comparison	209
A-6	Structural Weights (lbs)	210
A-7	Weight Breakdown of Concepts A, B and C ~ 29 cm Size	210

## SECTION I

### INTRODUCTION AND SUMMARY

Magnetic Corporation of America (MCA) is under contract to the United States Air Force Systems Command, Wright-Patterson Air Force Base, Ohio, to develop a lightweight, superconducting, magnetohydrodynamic (MHD) magnet system. The total program is a forty-eight (48) month, six (6) phase effort. The phases are:

- Phase I - Model Magnet Criteria Selection
- Phase II - Model Magnet Design
- Phase III - Model Magnet Fabrication and Test
- Phase IV - Cryogenic Containment Fabrication
- Phase V - Lightweight Model Magnet Design
- Phase VI - Lightweight Model Magnet Fabrication and Test

This interim report presents the results of the Phase I efforts to establish the criteria for modeling a superconducting MHD magnet system capable of generating 30 MWe. The system characteristics for such a system are illustrated in Table 1. The axial magnetic field profile requirements for this system and for the model magnet are illustrated in Figure 1.

The criteria established during Phase I are used to select the scale for a model MHD magnet system. The scale is chosen such that an experimental demonstration of the model will represent a complete test of all critical design features of the full scale (30 MWe) system.

Figure 2 and 3 illustrate the basic magnet system configuration. Figure 2 shows a cutaway view with the major components indicated. Figure 3 shows a quarter section of the system at the magnet midplane. The winding is in the form of a segmented annular saddle with round end turn crossovers.

The winding segments or bundles are separated by structural teeth. These teeth are used to pick up the circumferential Lorentz body forces from the

TABLE 1  
MHD TAPERED SADDLE MAGNET DESIGN  
TYPICAL OF A 30 Mwe GENERATOR

Dimensions

Dewar

Inlet Warm Bore Dia. (m)	0.29
Flange Dia. at Inlet (m)	0.305
Outlet Warm Bore Dia. (m)	0.53
Inlet Outside Dia. (m)	0.74
Outlet Outside Dia. (m)	1.10
Length Overall (m)	2.20

Magnet

Inner Dia. at Inlet (m)	0.35
Inner Dia. at Outlet (m)	0.59
Winding Build (m)	0.034
Length Between End Turns (m)	1.20
Length Overall (m)	1.57

Magnetic Characteristics (Unshielded)

Field at Inlet (t)	4.0
Field at Outlet (T)	2.75
Length of Field (m)	1.05
Peak Field (T)	5.6
Transverse Variation (%) Across MHD Channel	5.0
Stored Energy ( $10^6$ J)	2.50
Inductance (H)	1.24
Current (A)	2,000
Overall Current Density ( $10^8$ A/m <sup>2</sup> )	1.5
Ampere-Meters ( $10^6$ A-m)	9.86
Number of Turns	1,164
Ampere-Turns ( $10^6$ A-T)	2.33
Length of Conductor (m)	4,930
<u>Total Heat Load</u>	
Boiloff of Liquid Helium (1/hr)	6.5



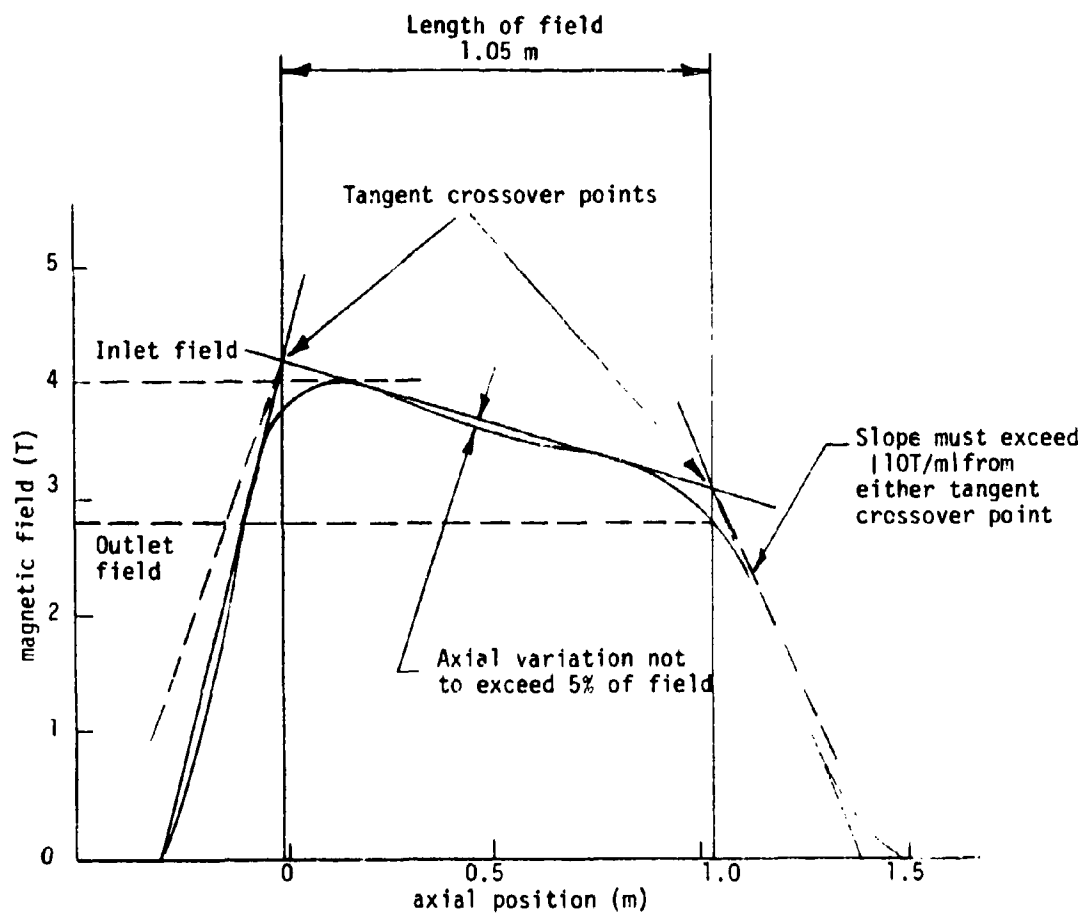


Figure 1. Magnetic Field on Axis of MHD Magnet as Specified in Contract

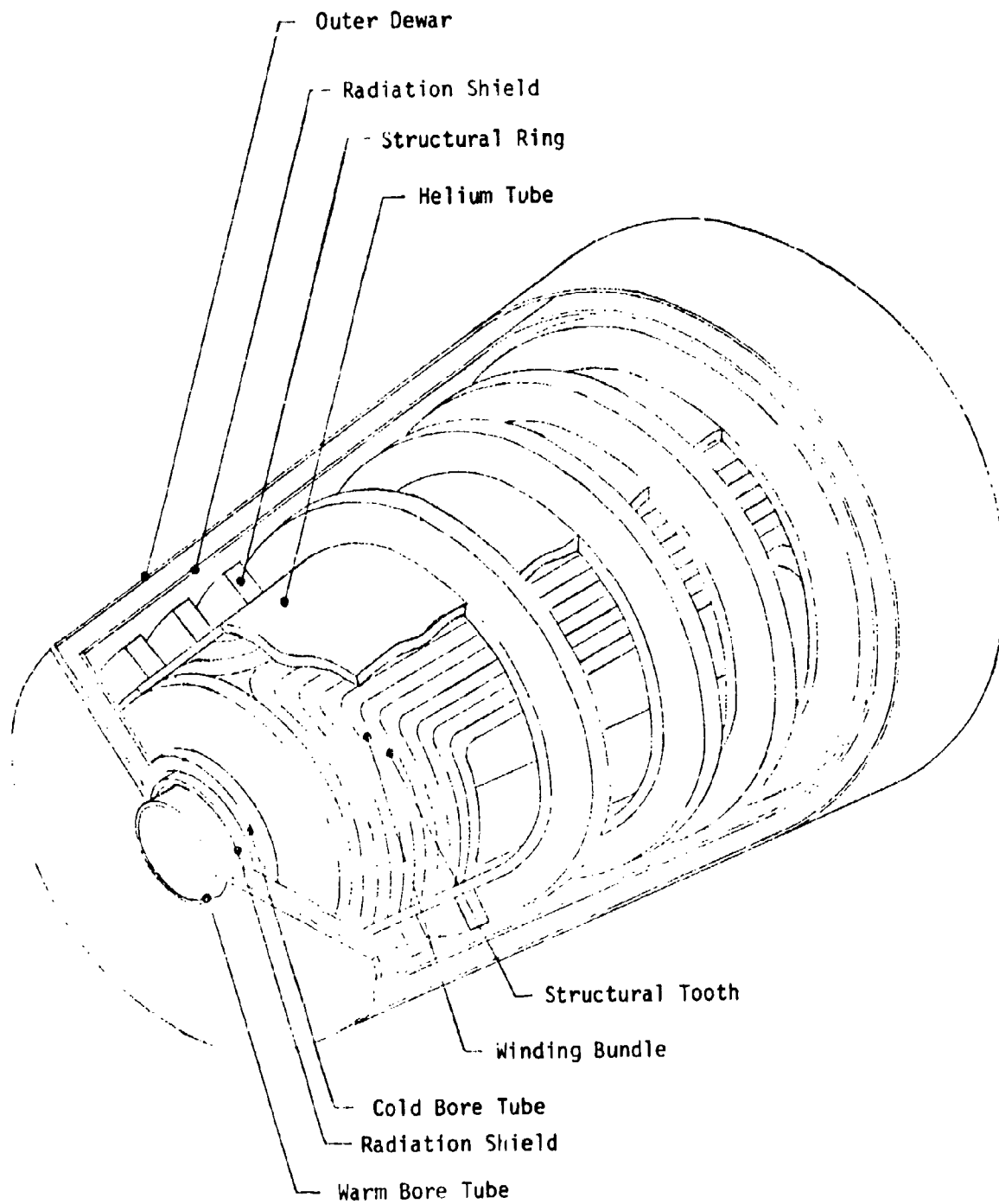


Figure 2 Cutaway View of MHD Magnet

FA-4719

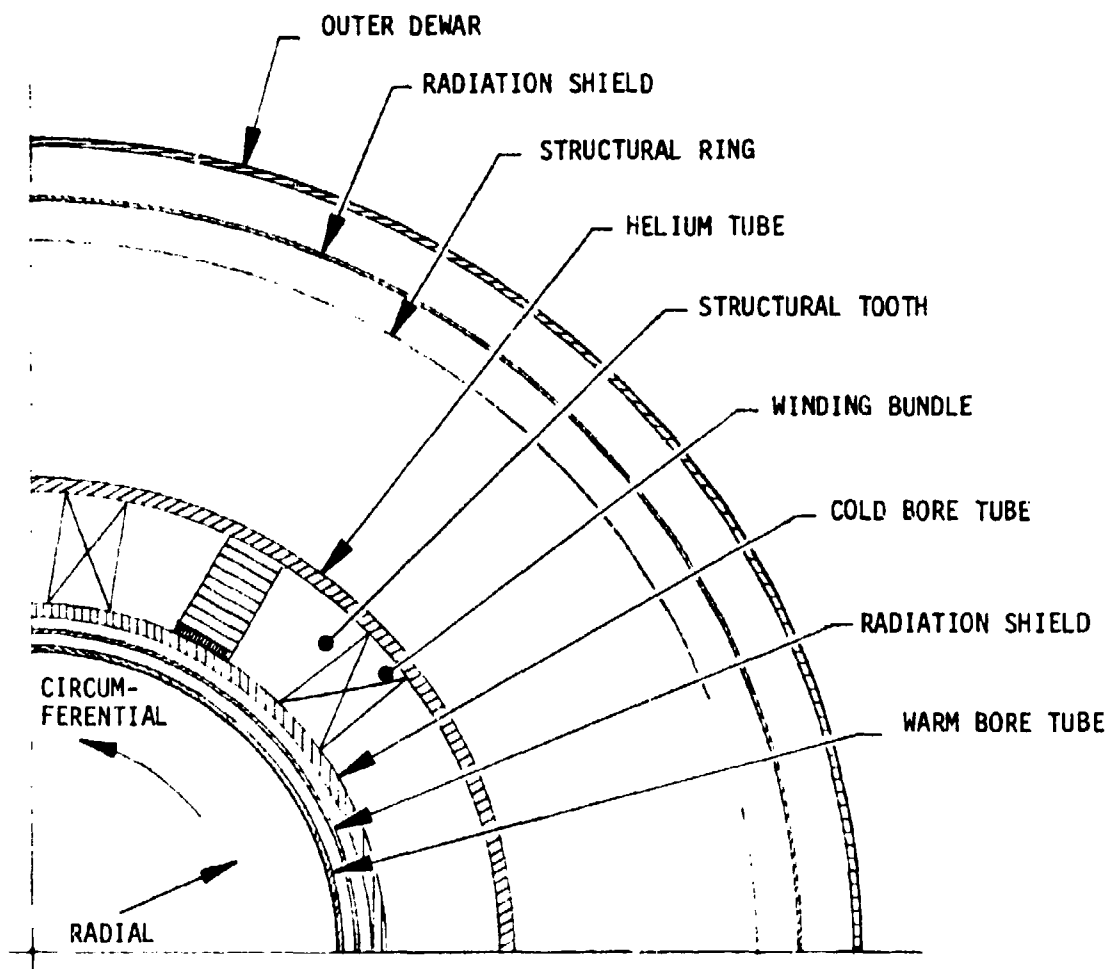


Figure 3. Quarter Section of Magnet Design at Midplane

bundles and transmit them to the cold bore tube and the outer helium vessel. These tubes carry the loads to the plane of symmetry between magnet halves where they are equilibrated by the loads from the quadrant's mirror image. The circumferential load is large compared to the total loads on a cross-section and, hence, the structural teeth are necessary to prevent the conductor from being crushed. The radial loads are contained by a series of external rings as shown. Axial loads are carried by the cold bore and helium tubes. The primary structural material was chosen to be aluminum.

In order to establish the effects of scale on the critical system parameters, four magnet sizes were carried through a preliminary design during Phase I. The four sizes chosen for this study are based on inlet warm bore diameters of 20, 29, 40, and 50 cm. The 29 cm design corresponds to the one characterized in Table 1.

Two conductor current densities were used for each magnet size. An increase in current density will have the effect of decreasing the overall system weight. However, there is a concomitant increase in the risk of and permanent damage due to a magnet quench. The nominal conductor current densities used for Phase I were 15,000 and 30,000 A/cm<sup>2</sup>.

Preliminary system characteristics were determined for each of the four magnet sizes for each conductor current density. These characteristics are listed in Tables 2 and 3. Table 2 corresponds to a 15,000 A/cm<sup>2</sup> conductor; Table 3 to a 30,000 A/cm<sup>2</sup> conductor. The total system weight for each current density is plotted versus magnet size in Figure 4. It can be seen that by doubling the current density a weight reduction of one-third is possible.

The basic conductor configuration chosen for the magnet is a 97 strand, partially solder-filled braid. The strand is copper stabilized multifilamentary niobium titanium. Table 4 lists the primary characteristics of the

TABLE 2  
SYSTEM CHARACTERISTICS FOR FOUR BORE SIZES  
(15,000 A/cm<sup>2</sup> Conductor)

<u>Dewar Dimensions</u>	<u>20 cm</u>	<u>29 cm</u>	<u>40 cm</u>	<u>50 cm</u>
Inlet warm bore dia. (m)	0.20	0.29	0.40	0.50
Outlet warm bore dia. (m)	0.36	0.53	0.64	0.74
Inlet outside dia. (m)	0.72	0.88	1.08	1.26
Outlet outside dia. (m)	0.88	1.12	1.32	1.50
Length overall (m)	1.58	1.80	1.97	2.13
<u>Magnet Dimensions</u>				
Inner dia. at inlet (m)	0.28	0.40	0.52	0.64
Inner dia. at outlet (m)	0.58	0.70	0.82	0.96
Winding build (m)	0.129	0.160	0.171	0.182
<u>Characteristics</u>				
Ampere turns (10 <sup>6</sup> A-T)	2.49	3.32	4.16	4.92
Number of turns	1276	1740	2088	2406
Length of conductor (m)	3959	6235	8367	10680
Total Weight (kg)	1150	1811	2506	3457

TABLE 3  
SYSTEM CHARACTERISTICS FOR FOUR BORE SIZES  
(30,000 A/cm<sup>2</sup> Conductor)

<u>Dewar Dimension</u>	<u>Design</u>			
	<u>20 cm</u>	<u>29 cm</u>	<u>40 cm</u>	<u>50 cm</u>
Inlet warm bore dia. (in)	0.20	0.29	0.40	0.50
Outlet warm bore dia. (m)	0.36	0.53	0.64	0.74
Inlet outside dia. (m)	0.67	0.84	1.02	1.16
Outlet outside dia. (m)	0.83	1.08	1.26	1.40
Length overall (m)	1.57	1.77	1.94	2.09
<u>Magnet Dimensions</u>				
Inner dia. at inlet (m)	0.28	0.40	0.52	0.64
Inner dia. at outlet (m)	0.58	0.70	0.82	0.96
Winding build (m)	0.101	0.141	0.143	0.134
<u>Characteristics</u>				
Ampere turns (10 <sup>6</sup> A-T)	2.28	3.19	3.96	4.58
Number of turns	1187	1680	2000	2259
Length of conductor (m)	3607	5898	7846	9721
Total Weight (kg)	747	1270	1777	2388

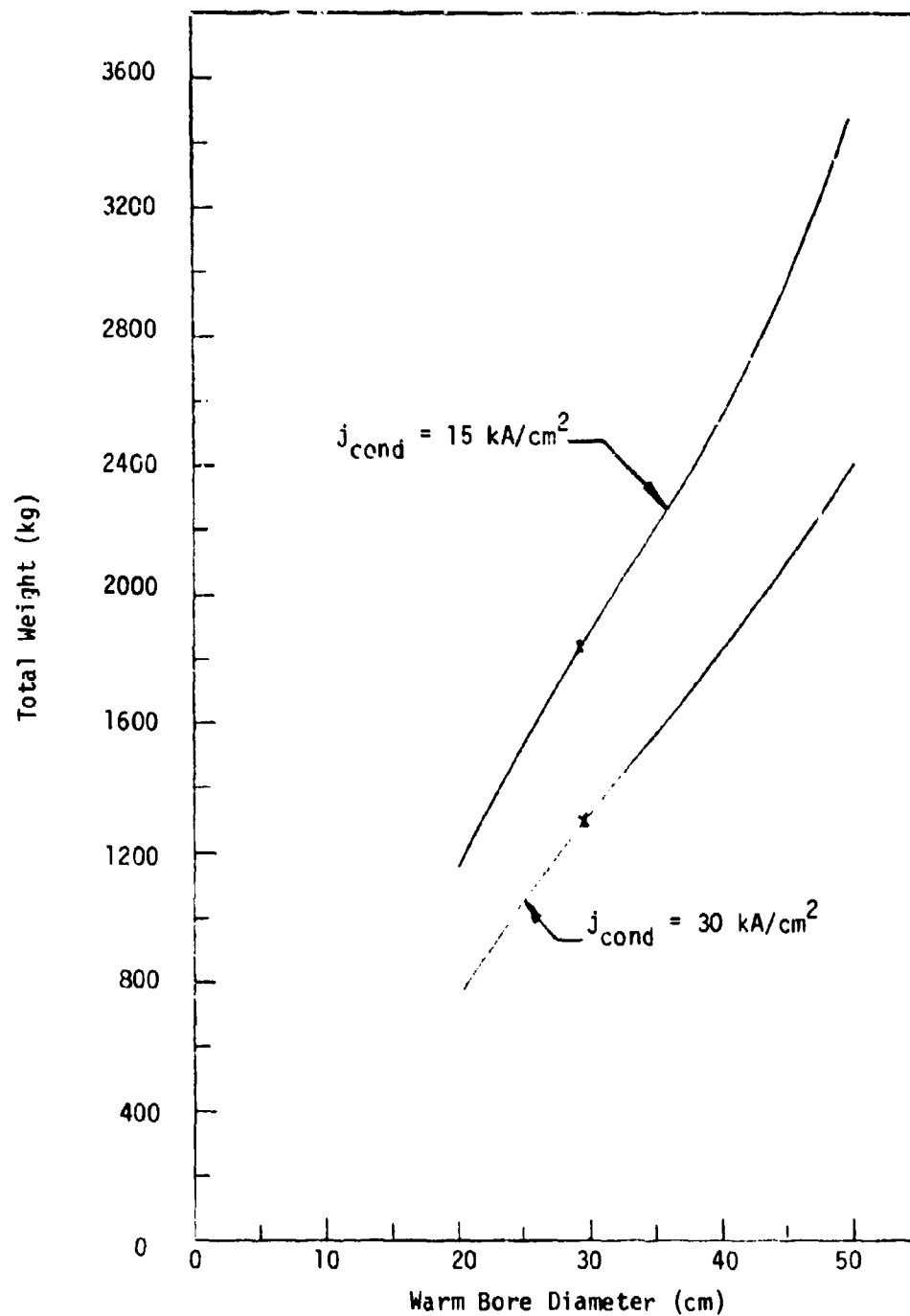


Figure 4 Total Weight vs. Warm Bore Size

TABLE 4  
CONDUCTOR SPECIFICATIONS

	<u><math>j_{\text{cond}} = 15 \text{ kA/cm}^2</math></u>	<u><math>j_{\text{cond}} = 30 \text{ kA/cm}^2</math></u>
<u>Strand Configuration</u>		
Diameter, mm	0.4064	0.3048
CuSC ratio	5.0:1	3.0:1
Number of filaments	138	207
Filament diameter ( $\mu\text{m}$ )	14.1	10.6
<u>Guaranteed Performance</u>		
Critical Current at 3T, A	60	51
Critical Current at 4T, A	48	41
Critical Current at 5T, A	40	34
Critical Current at 6T, A	32	27
<u>Braid Configuration</u>		
Number of strands	97	97
Width, mm	0.847	0.635
Thickness, mm	21.84	16.38
Insulation thickness, mm	0.127	0.127
Operating current, $I_{\text{op}}$ , A	2000	2000
Critical Current, $I_{\text{c}}$ , A	3420	2900
$I_{\text{op}}/I_{\text{c}}$	0.58	0.69



two braids. Since they have the same number of strands the desired current densities are obtained by varying the strand diameters. The braid configuration is one that has been used successfully by Brookhaven National Laboratories for the Isabelle magnets and, hence, represent a conductor with established performance and manufacturability.

Each braid will be spiral-wrapped with .127 mm 8-stage epoxy-glass insulation. The combination of the spiral wrap insulation (with 50% surface area coverage) and the braid interstitial passages yield a 25% local helium volume which greatly enhances the conductor thermal stability. After the magnet is wound, it is cured so that the insulation will act to rigidize the winding bundles. The overall effect from the stability standpoint is that of a partially impregnated or potted winding with advantages of both open-cooled and fully potted designs.

The stability of the conductor can be defined as its ability to retain or to recover to its superconducting state if perturbed by a local heat input. Conductor stability is the most critical item to be addressed in the design of a lightweight, superconducting magnet. If a lightweight system was not required, sufficient copper stabilizer could be added to the conductor to minimize the possibility of an induced quench. Similarly, a winding protection scheme could be included to reduce the possibility of permanent damage if a quench did occur. Damage could occur during a quench due to either a high peak temperature in the winding caused by the resistive heating in the copper or a high resistive potential from one conductor to the next.

Figures 5 and 6 show the effect of magnet size and conductor current density on the maximum temperature rise and peak voltage that occur during a quench assuming no external protection system. As can be seen in Figure 5, peak temperatures less than 450 K occur for bore sizes less than 35 cm and a current density of  $15,000 \text{ A/cm}^2$ . Most solders will melt at temperatures on

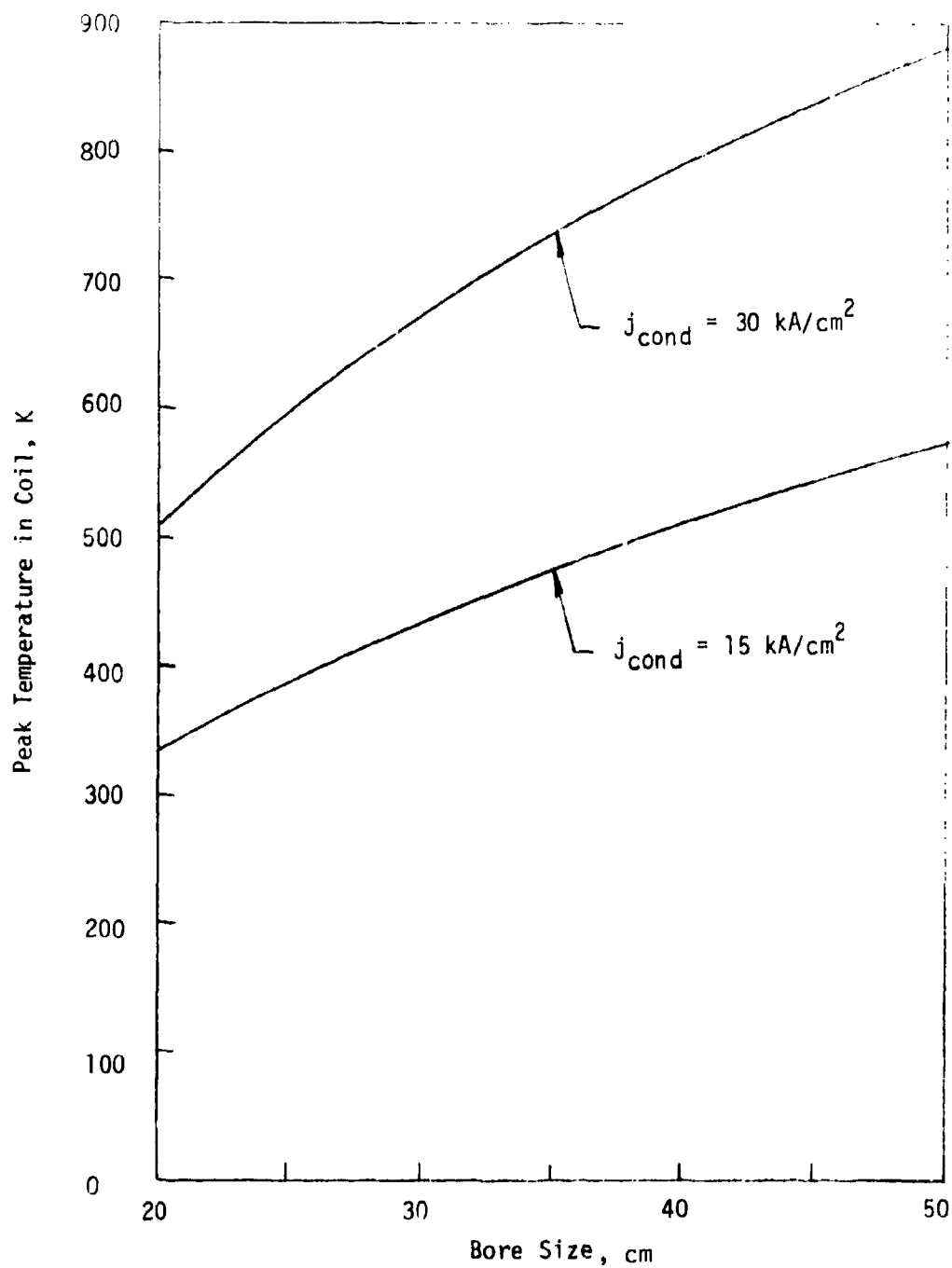


Figure 5 Peak Temperature in MHD Magnet Undergoing a Quench from Operating Current ( $I_{\text{op}} = 2000\text{A}$ ) vs. Bore Size

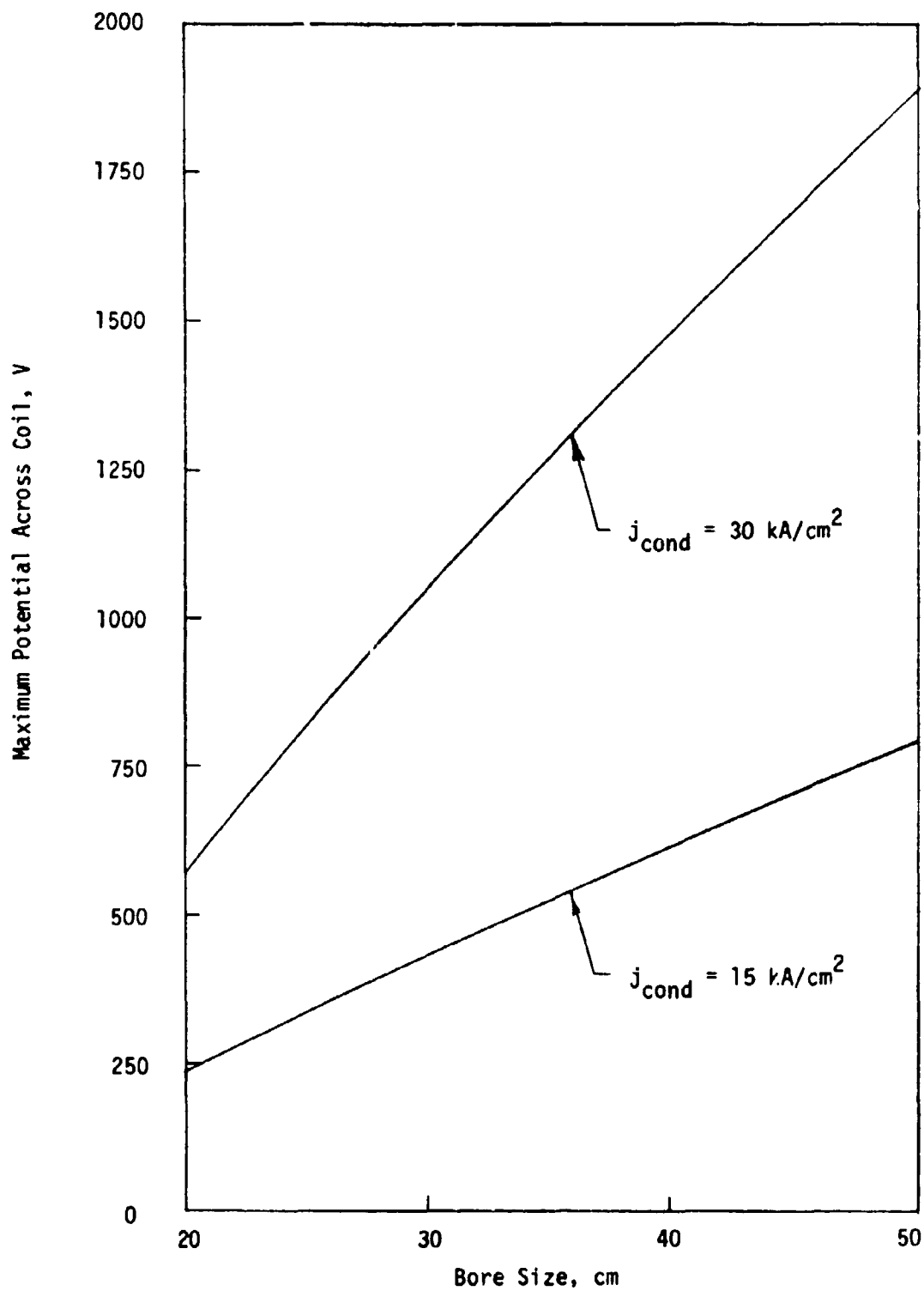


Figure 6 Maximum Potential in Normal Region in MHD Magnet Undergoing a Quench from Operating Current ( $I_{\text{op}} = 2000\text{A}$ ) vs. Bore Size

FA 4723

the order of 450 - 500 K. Therefore, quench temperature rises must be held below this range. It should be noted that the  $30,000 \text{ A/cm}^2$  current density yields peak temperatures well above this limit for all magnet sizes. If a higher current density is sought then some quench protection scheme is necessary. The peak voltages in the coil are well within reasonable limits for the insulation. The maximum turn-to-turn voltage is on the order of 10-15 V.

The most probable cause of a quench is associated with a conductor motion or slip relative to the structure, insulation, or another conductor. The frictional energy released during the slip can be large enough to raise the temperature of the conductor in the neighborhood of the slip above the critical value and, thereby, drive the conductor normal. If there is sufficient heating - both frictional and resistive - and insufficient cooling, the normal region will propagate and the magnet will quench.

A major portion of the Phase I effort was concerned with determining an allowable conductor slip. The allowable slip was used to determine allowable external structural deflections. Preliminary analysis indicate that if structural deflections are limited to .5 mm, the conductor and local helium will be able to absorb the slip energy input without inducing a quench.

The remainder of this report will deal in detail with the major items summarized above. That is, it will deal with magnet size, winding design, conductor design, structural design, conductor stability, and with system charge, discharge, quench and quench protection. Finally, a concluding summary and list of recommendations is included.

A report of the results of the work performed by General Dynamics, Convair Division, in support of MCA is presented in the Appendix. The effort includes the study of the effect on scale, risk, and cost of employing advanced composite materials (ACM) for the structure.

## SECTION II

### MAGNET SIZE

In order to ascertain the effect of scale on the critical system parameters, and thereby establish the criteria to be used to select the model magnet size, four magnet sizes were carried through a preliminary design during Phase I. The four sizes chosen are based on inlet warm bore tube diameters of 20, 29, 40 and 50 cm. The 29 cm size corresponds to the full scale (30 MWe) system. It was felt that the 20 cm size would represent a minimum with respect to demonstrating the critical system behavior. The 40 and 50 cm sizes were considered in order to establish trends in the neighborhood of the 29 cm size. Two conductor current densities - 15,000 and 30,000 A/cm<sup>2</sup> - were considered for each size.

Tables 5 and 6 list the major system characteristics for each magnet size. Table 5 corresponds to the 15,000 A/cm<sup>2</sup> conductor and Table 6 to the 30,000 A/cm<sup>2</sup> conductor. The system stored energy is also plotted versus magnet size in Figure 7. The stored energy is an important system parameter because during a quench the winding (plus external resistors, if present) must be able to withstand the dissipation (through resistive heating) of this amount of energy. It can be seen that by doubling the bore diameter the system energy goes up by nearly a factor of four. Therefore, the risk of damage to the winding during a quench is higher.

Figures 8, 9, and 10 are plots of conductor, structure, and system weight versus bore size. The 29 cm design point is indicated on each figure by an x. It can be seen that a majority of the weight savings that accrue from an increased current density comes from the decreased conductor weight (Figure 8). For example, doubling the current density for the 20 cm size halves the conductor weight and reduces the total weight by one-third.

TABLE 5  
MAGNET CHARACTERISTICS FOR FOUR BORE SIZES  
(15,000 A/cm<sup>2</sup> Conductor)

<u>Dimensions</u>	<u>Design</u>			
	<u>20 cm</u>	<u>29 cm</u>	<u>40 cm</u>	<u>50 cm</u>
Dewar				
Inlet warm bore dia. (m)	0.20	0.29	0.40	0.50
Outlet warm bore dia. (m)	0.36	0.53	0.64	0.74
Inlet outside dia. (m)	0.72	0.88	1.08	1.26
Outlet outside dia. (m)	0.88	1.12	1.32	1.50
Length overall (m)	1.58	1.80	1.97	2.13
Magnet				
Inner dia. at inlet (m)	0.28	0.40	0.52	0.64
Inner dia. at outlet (m)	0.58	0.70	0.82	0.96
Winding build (m)	0.129	0.160	0.171	0.182
<u>Electrical Characteristics</u>				
Design field at inlet (T)	4.0	4.0	4.0	4.0
Design field at outlet (T)	2.75	2.75	2.75	2.75
Design length of field (m)	1.05	1.05	1.05	1.05
Total stored energy (10 <sup>6</sup> J)	1.46	2.96	4.62	6.62
Current (10 <sup>3</sup> A)	2.0	2.0	2.0	2.0
Ampere turns (10 <sup>6</sup> A-T)	2.49	3.32	4.16	4.92
Number of turns	1276	1740	2088	2406
Length of conductor (m)	3959	6235	8367	10680
Inductance (H)	0.728	1.483	2.309	3.308
<u>Weights</u>				
Conductor (kg)	607	854	1101	1429
Structure (kg)	229	419	624	915
Dewar (kg)	312	536	780	1113
Total (kg)	1150	1811	2506	3457
Helium boiloff (l/hr)	6.8	7.1	7.4	7.7

TABLE 6  
MAGNET CHARACTERISTICS FOR FOUR BORE SIZES  
(30,000 A/cm<sup>2</sup> Conductor)

<u>Dimensions</u>	<u>20 cm</u>	<u>29 cm</u>	<u>40 cm</u>	<u>50 cm</u>
<b>Dewar</b>				
Inlet warm bore dia. (m)	0.20	0.29	0.40	0.50
Outlet warm bore dia. (m)	0.36	0.53	0.64	0.74
Inlet outside dia. (m)	0.67	0.84	1.02	1.16
Outlet outside dia. (m)	0.83	1.08	1.26	1.40
Length overall (m)	1.57	1.77	1.94	2.09
<b>Magnet</b>				
Inner dia. at inlet (m)	0.28	0.40	0.52	0.64
Inner dia. at outlet (m)	0.58	0.70	0.82	0.96
Winding build (m)	0.101	0.141	0.143	0.134
<b><u>Electrical Characteristics</u></b>				
Design field at inlet (T)	4.0	4.0	4.0	4.0
Design field at outlet (T)	2.75	2.75	2.75	2.75
Design length of field (m)	1.05	1.05	1.05	1.05
Total stored energy (10 <sup>6</sup> J)	1.30	2.76	4.29	5.96
Current (10 <sup>3</sup> A)	2.0	2.0	2.0	2.0
Ampere turns (10 <sup>6</sup> A-T)	2.28	3.19	3.96	4.58
Number of turns	1187	1680	2000	2259
Length of conductor (m)	3607	5898	7846	9721
Inductance (H)	0.649	1.377	2.145	2.979
<b><u>Weights</u></b>				
Conductor (kg)	285	408	525	662
Structure (kg)	200	379	557	792
Dewar (kg)	261	481	694	933
Total (kg)	747	1270	1777	2388
Helium boiloff (l/hr)	6.6	7.0	7.2	7.9

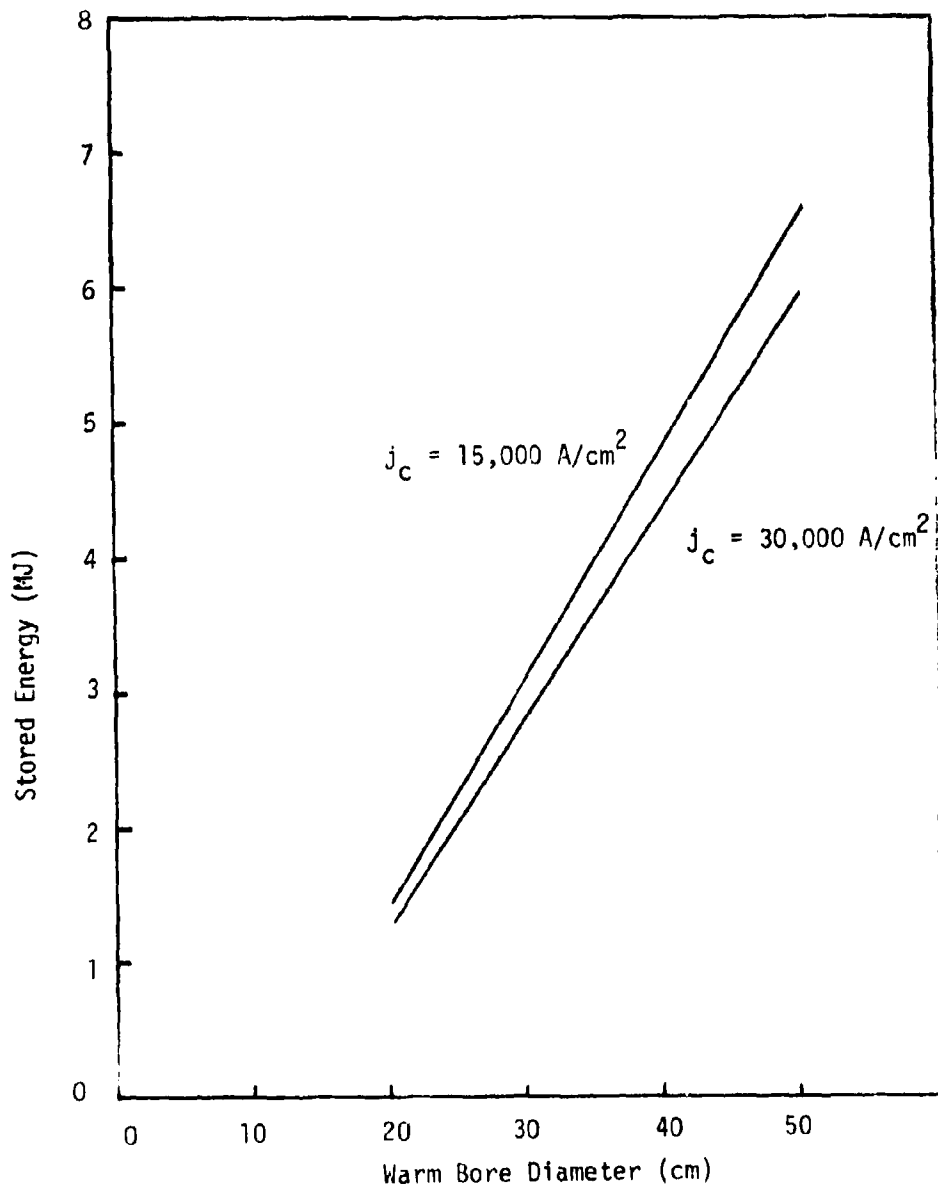


Figure 7 Stored Energy versus Warm Bore Size



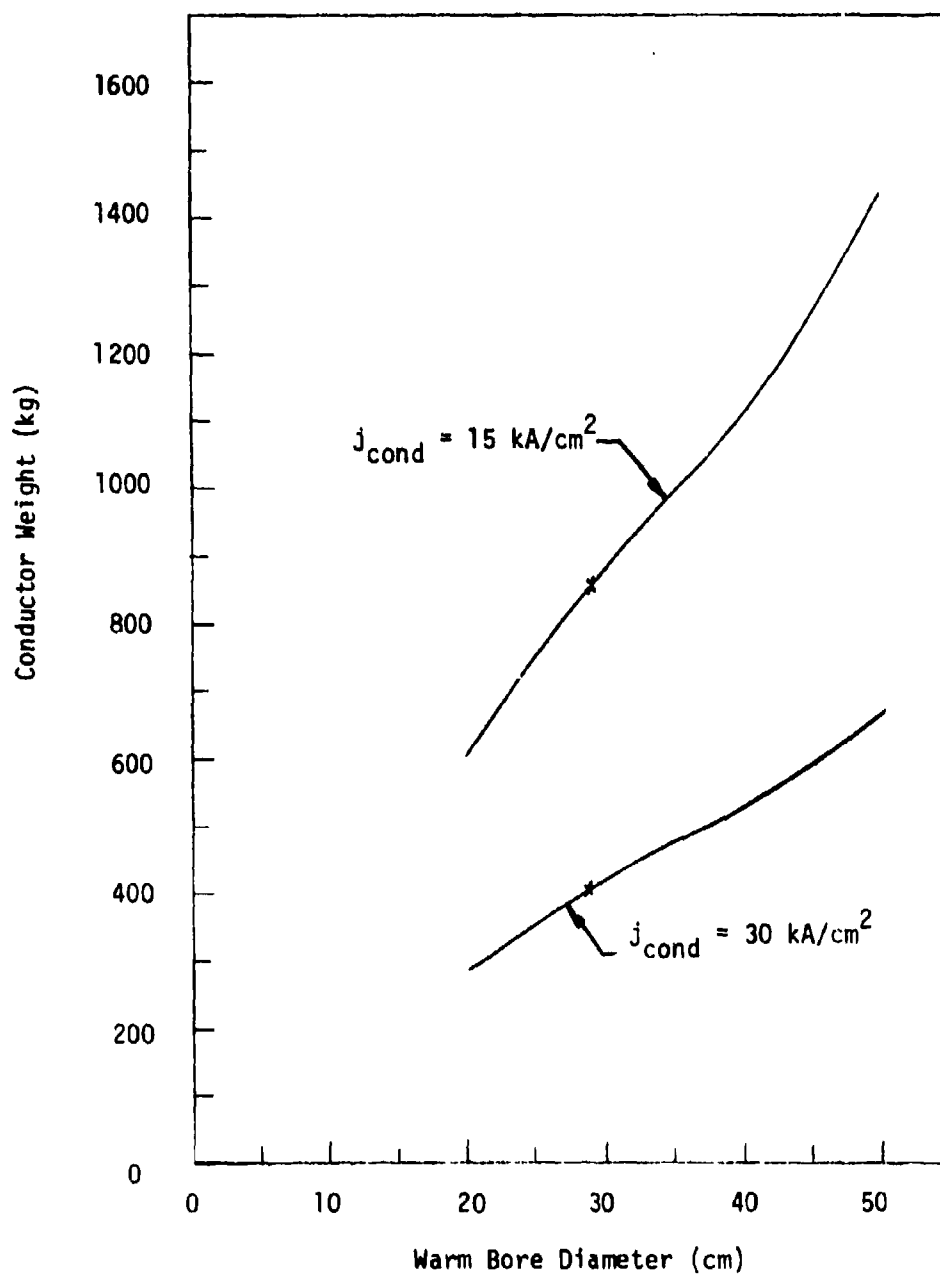


Figure 8 Conductor Weight vs. Warm Bore Size

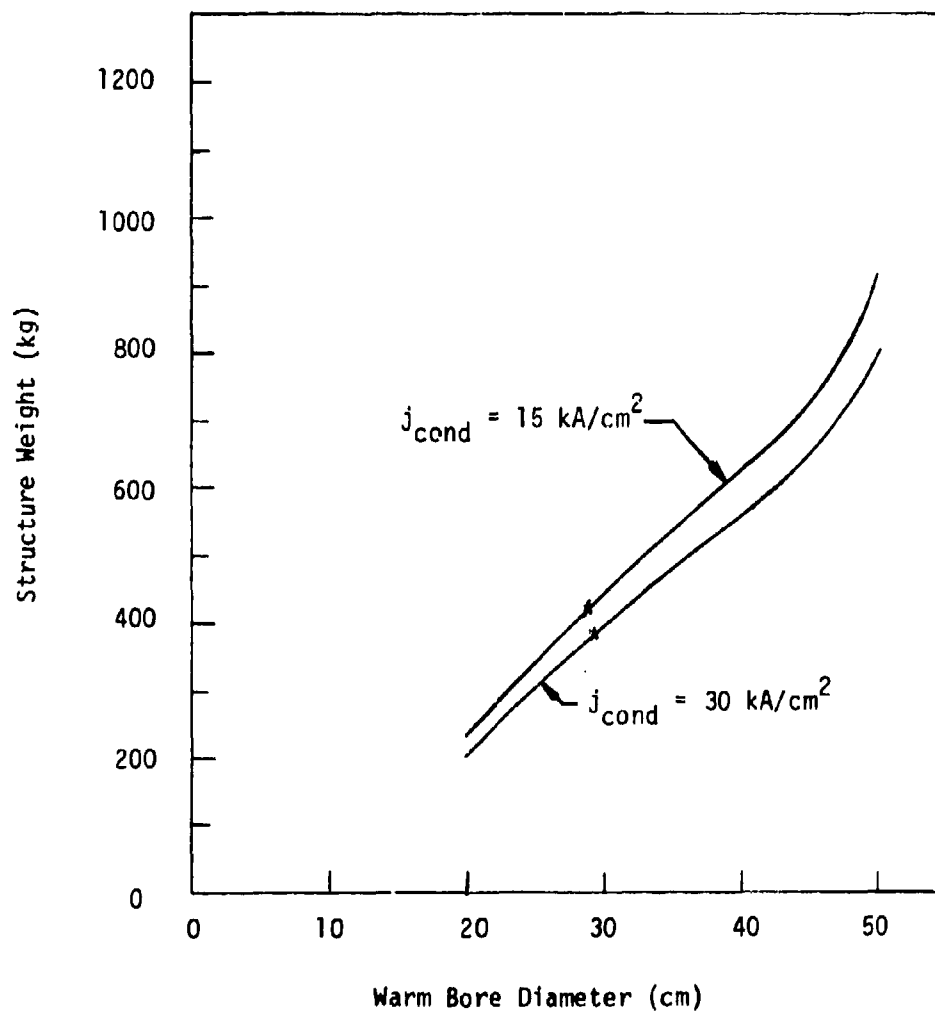


Figure 9 Structure Weight vs. Warm Bore Size

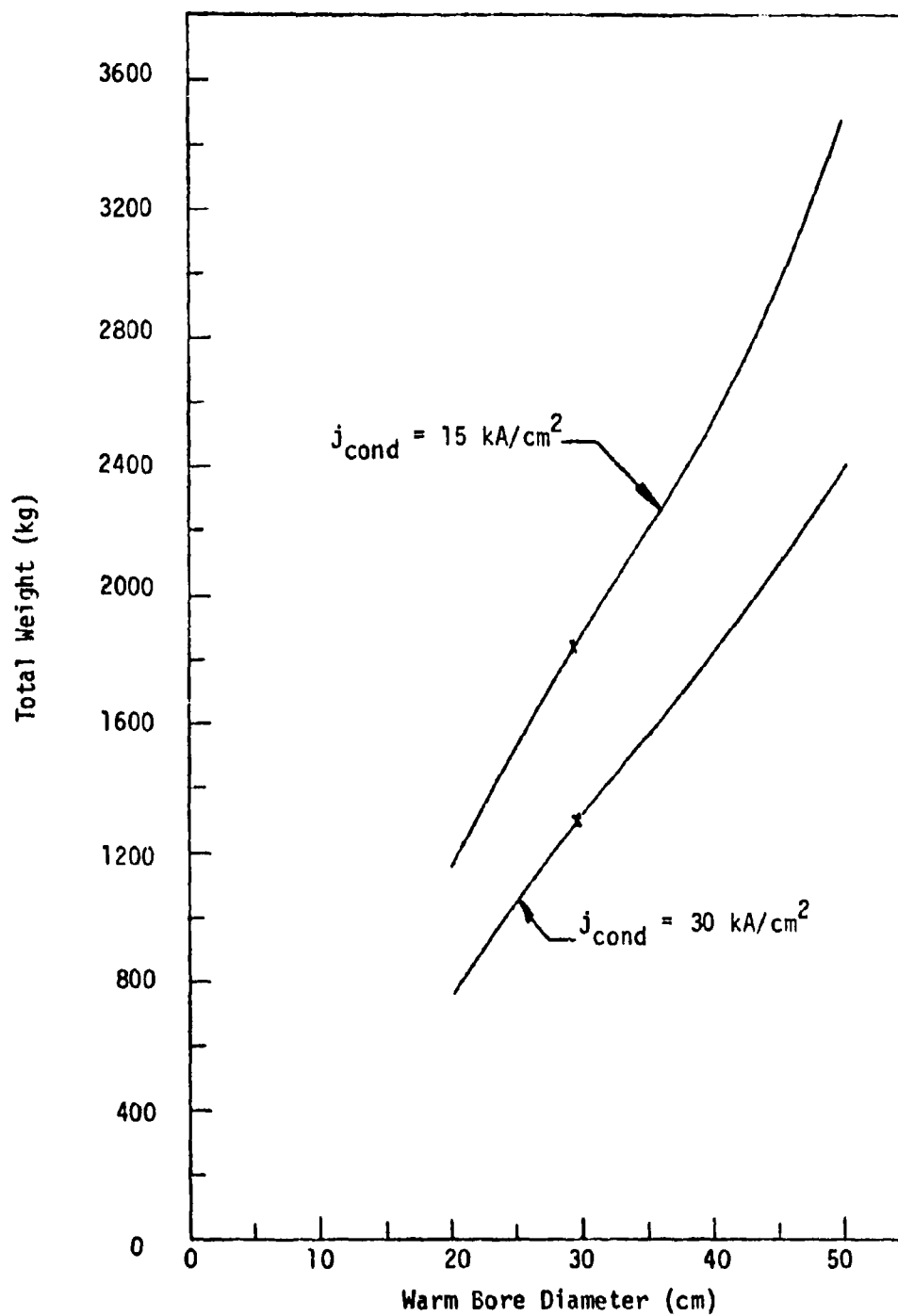


Figure 10 Total Weight vs. Warm Bore Size

The structural weights change with current density primarily because of the change in the winding build and, hence, in the inner structural diameter. The local magnetic body forces are proportional to the stored energy density which is in turn proportional to the magnetic field squared. Since the field requirements in terms of magnitude, length, etc., are held constant, the local forces are relatively constant.

The forces produced by and acting on the windings were also calculated for each size and for each current density. Figure 11 illustrates the types of loading seen by the magnet and the directions. Figures 12 and 13 show the variation of the force magnitudes as a function of bore size. Figure 12 shows the total axial (x-directed) load on the inlet end turn crossover. The large increase in total force with increase in size is partly due to the constant field length and constant current requirements. Thus, the warm bore diameter increases, the required number of ampere-turns and, hence, the winding build increases. This increase in build implies an increase in size of the end turn crossovers. Since the distance between crossovers is relatively constant due to the field length requirement and the ampere-turns increase, the repulsion between the two increases.

Figure 13 illustrates the peak circumferential and radial forces per unit length (measured along the straight sections) acting in a plane transverse to the axis at the midplane. The peak loads do not occur at the same circumferential position. The maximum radial force occurs near the centerline between magnet halves. The maximum circumferential force on the other hand occurs at the farthest circumferential position from this centerline. Perhaps the most significant fact shown by the figure is the order of magnitude difference between the two components. Since the circumferential loads are roughly 90% of the total, some circumferential structure is needed to prevent the conductors from being crushed.

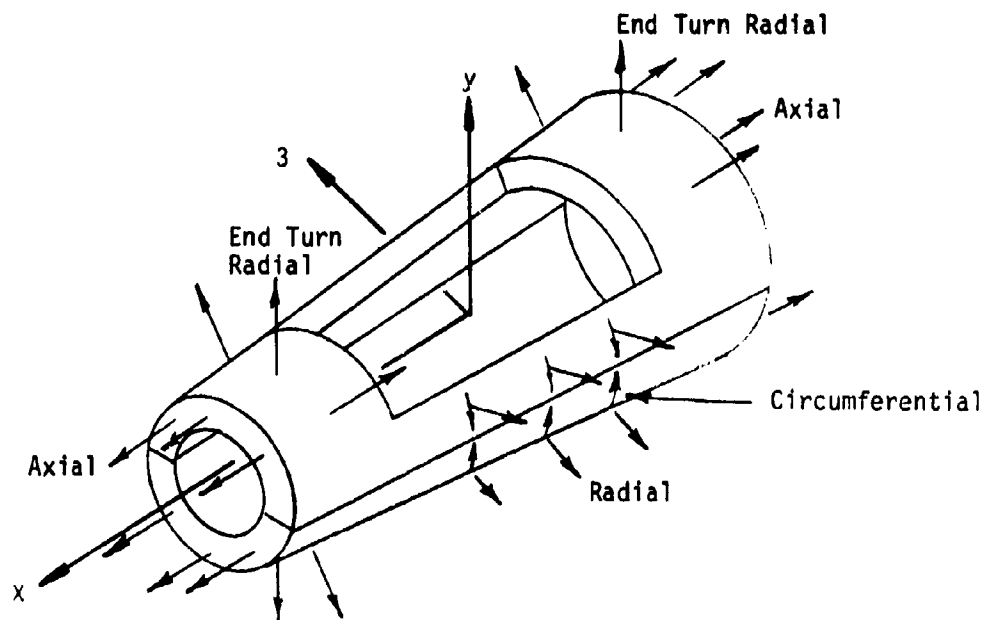


Figure 11 Force Components on Saddle Winding

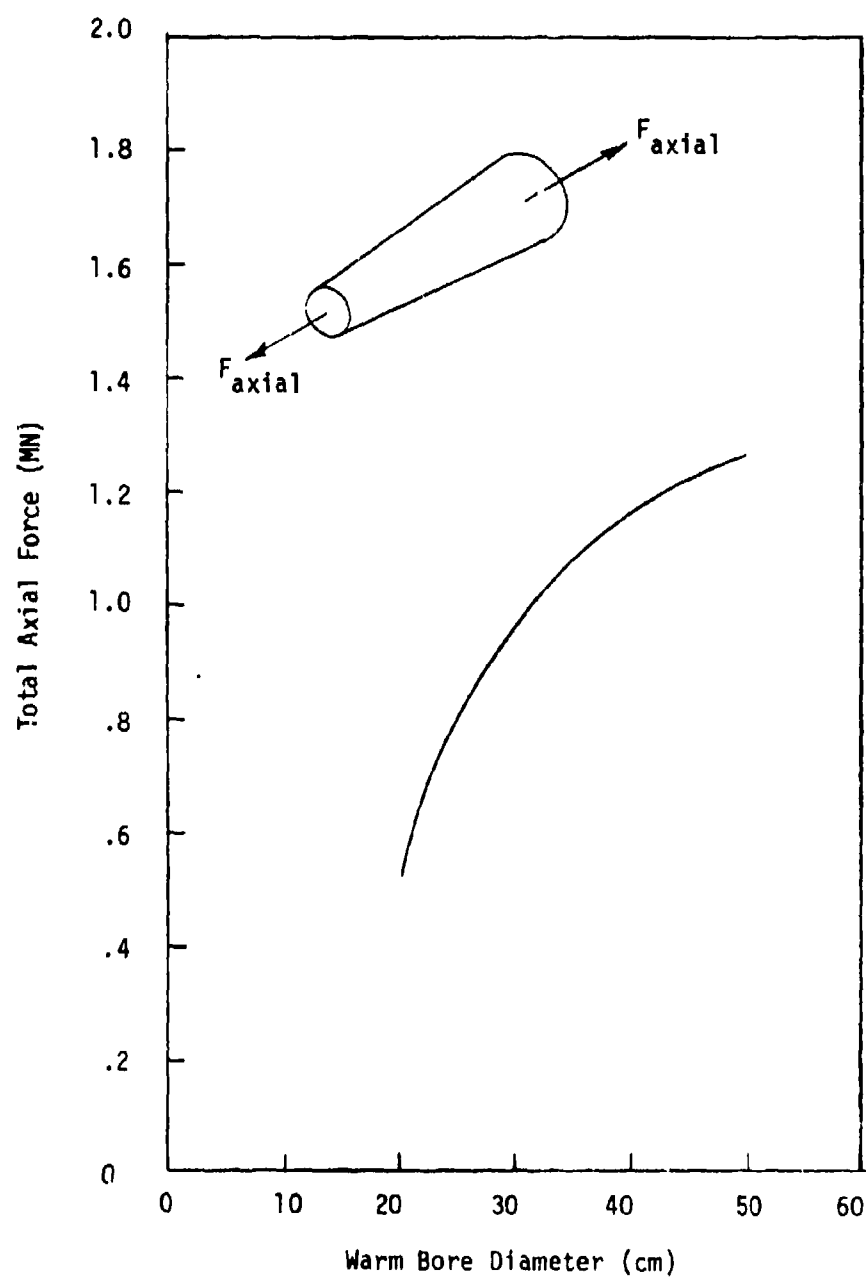


Figure 12 Total Axial Force vs. Warm Bore Size

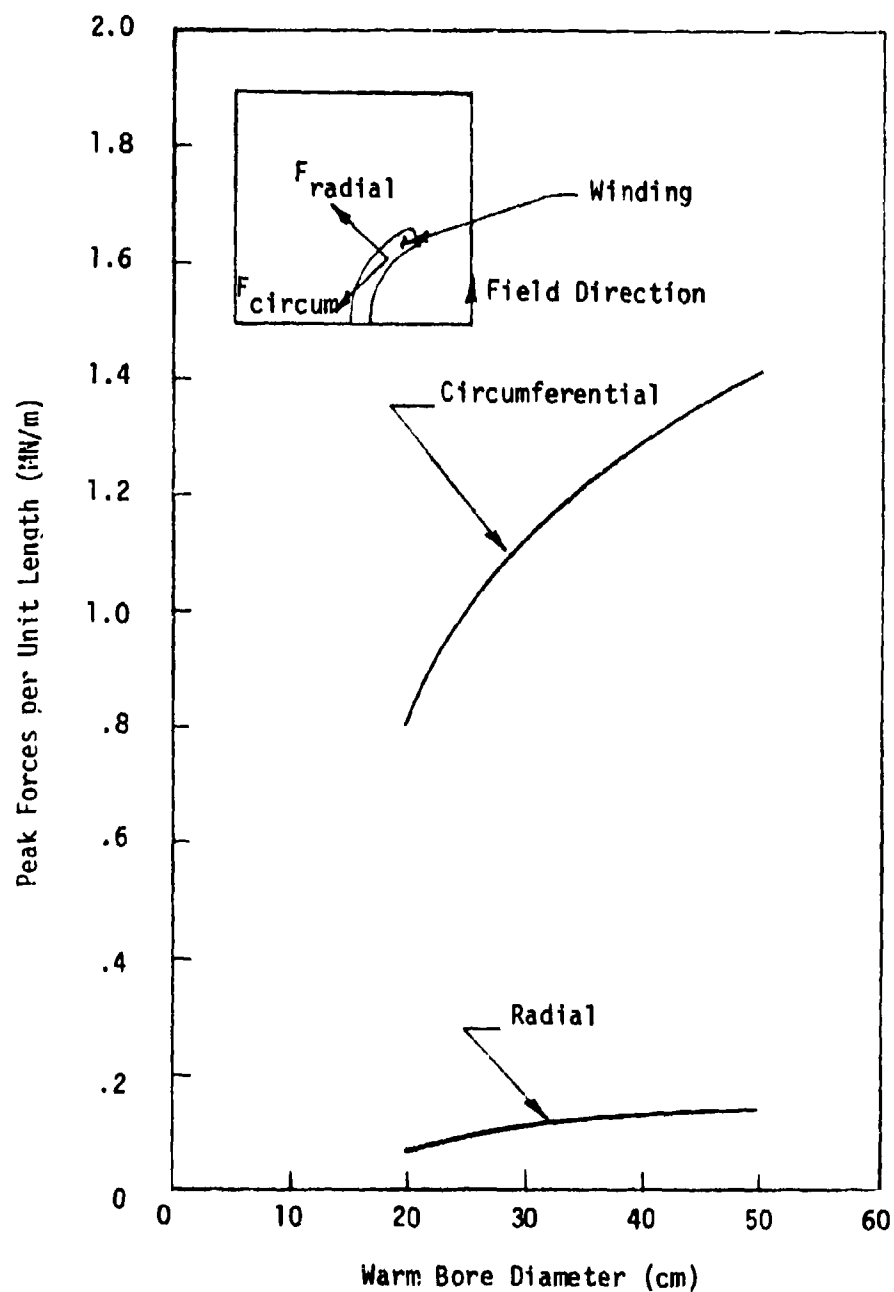


Figure 13 Peak Forces (per Unit Length) in a Transverse Plane vs. Warm Bore Size

### SECTION III

#### WINDING DESIGN

The basic winding geometry adopted for the MHD magnet is that of an annular saddle with round end turns. An annular shape was chosen over a rectangular one on the basis of the information presented in Figure 14. This figure shows the contours of constant relative winding effectiveness superposed on an annular winding envelope for a transverse section. The contours are numbered and indicate the relative effectiveness of a conductor with respect to creating the central field. For example, a conductor located on the .5-contour would only have 50% of the effect of a conductor located on the 1.0-contour. It can be seen that the proposed envelope is effective.

The round end turn configuration is adopted in order to reduce the overall system envelope. Other configurations, such as arched end turns, are possible and would reduce the peak field magnitude at the winding, but the conductor weight and system envelope would increase.

As was mentioned previously, four magnet sizes, each with two current densities, were carried through a preliminary design. The first step in the design sequence was to locate and size the winding in order to meet the system field requirements. The axial field profile, magnitude, length, and inlet and outlet gradient requirements are shown in Figure 15.

Initially a uniform distribution of current in winding envelope was assumed. However, preliminary conductor stress analyses indicated the need to provide internal structure to prevent the crushing of the conductor by the accumulated circumferential body forces. The basic annular saddle geometry was modified to include structure within the winding. The result was a segmented saddle with structural teeth between winding segments or bundles. For the preliminary design, it was assumed that the bundles were evenly spaced circumferentially and each contained the same number of conductors.



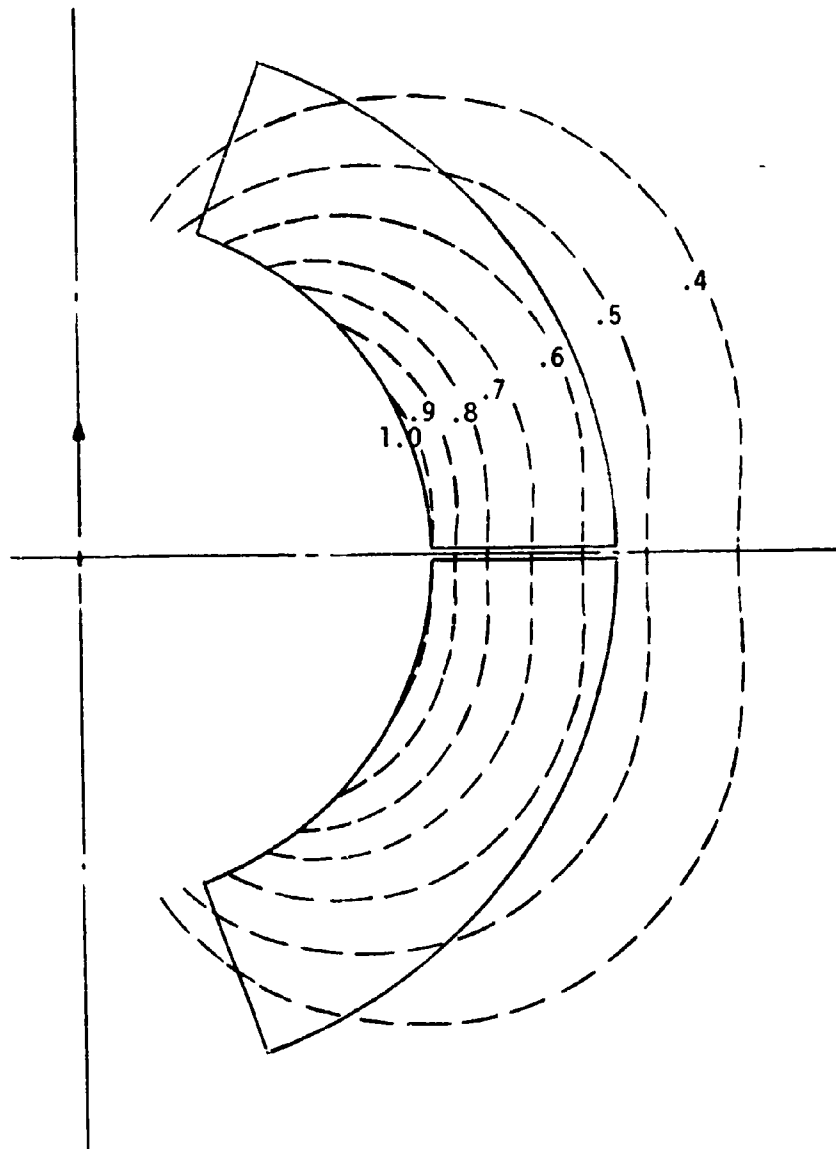


Figure 14 Contours of Constant  
Winding Effectiveness

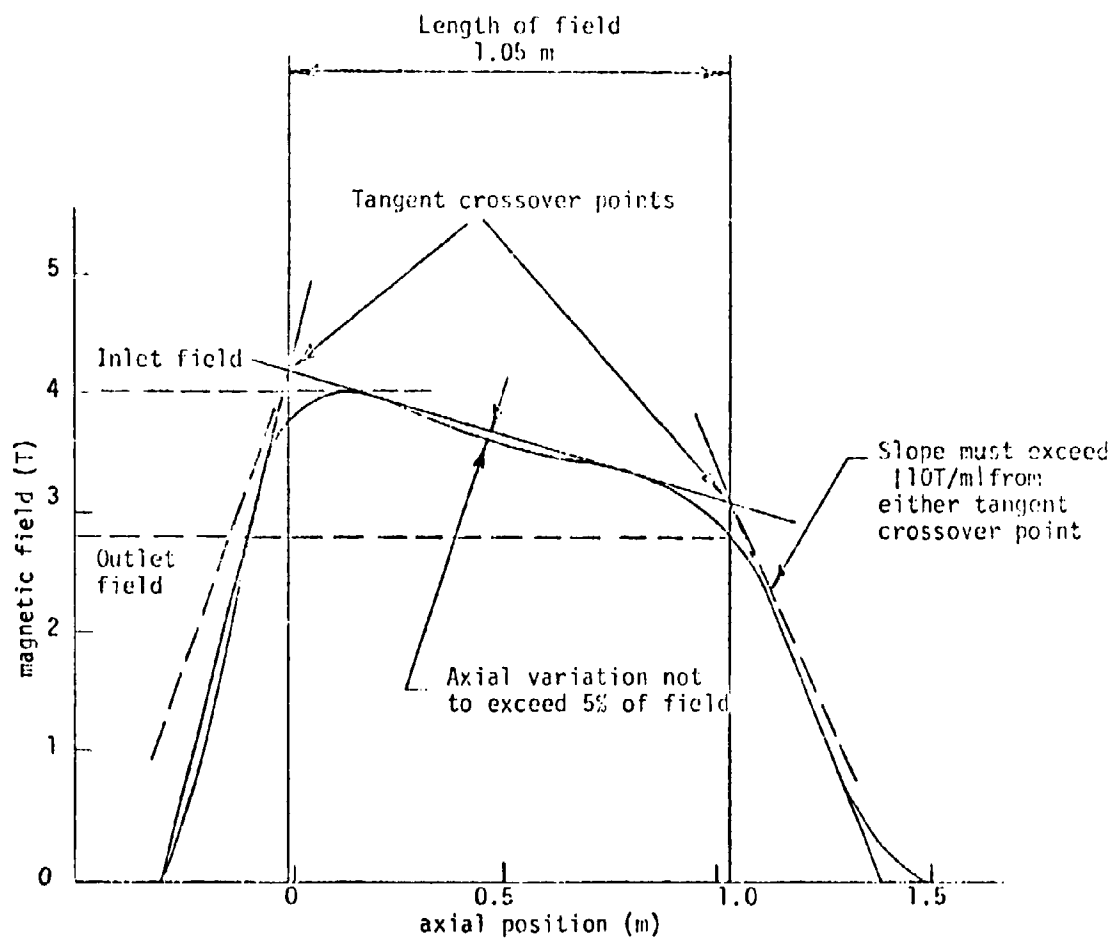


Figure 15 Magnetic Field on Axis of MHD Magnet as Specified in Contract

Each bundle was then modeled by a lumped current filament placed at the bundle center and composed of a number of straight sticks. Figure 16 shows a typical filament model of the magnet. The winding inner and outer radii at the inlet and outlet, the length between end turn crossovers, the number of bundles, and the total ampere-turns were then varied until the design gave a satisfactory field profile. The thickness of the structural tooth between bundles was checked to see if it was sufficient to carry the bundle circumferential loads. If it wasn't, the process was repeated.

Table 7 summarizes the magnetic field data generated. The field profiles for the 20, 29, 40, and 50 cm designs at  $15,000 \text{ A/cm}^2$  are shown in Figures 17 through 20. The profiles for the four designs at  $30,000 \text{ A/cm}^2$  are presented in Figures 21 through 24.

As is seen in Table 7, the inlet field magnitude of  $4 \text{ T} (\pm 5\%)$  and the active field length of 1.05 m requirements are met by all four designs. The outlet field magnitude of  $2.75 \text{ T} (\pm 5\%)$  and inlet field gradient of  $10 \text{ T/m} (-2.5\%)$  can be met by the 20 and 29 cm designs. The larger sizes do not meet the gradient conditions at either end or the outlet field magnitude. Even the 20 and 29 cm sizes cannot meet the  $10 \text{ T/m}$  gradient condition at the outlet.

The outlet field magnitude and gradient conditions are difficult to meet simultaneously. This is especially true for the large sizes since the end turn crossovers are very wide in the axial direction and the field length is constant with size. Figure 25 illustrates the effect of varying the magnet taper on the axial field profile. The inlet inner radius, the winding build, the number of bundles, and the length between end turn crossovers were held constant. The outlet inner radius (and, hence, the taper angle) was then varied. The total ampere-turns was also changed in order to meet the  $4 \text{ T}$  inlet field level. The required ampere-turns increased approximately 7% per  $5^\circ$  increment in taper angle.

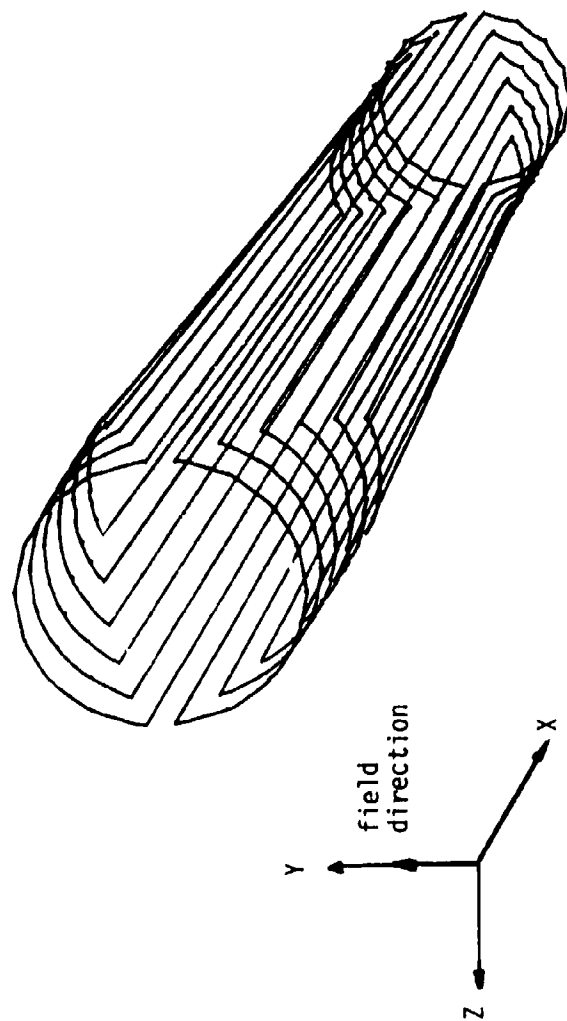


Figure 16 Typical Filament Model of an MHD Annual Saddle Magnet

TABLE 7

MAGNETIC FIELD DATA  
 15,000 A/cm<sup>2</sup> Conductor

	<u>20 cm</u>	<u>29 cm</u>	<u>40 cm</u>	<u>50 cm</u>
B Inlet (T)	4.0	4.0	4.0	4.0
B Outlet (T)	2.60	2.95	3.10	3.22
Field Length (m)	1.05	1.05	1.05	1.05
Gradient, Inlet (T/m)	14.25	9.75	9.25	7.75
Gradient, Outlet (T/m)	5.75	5.00	4.75	4.00

30,000 A/cm<sup>2</sup> Conductor

	<u>20 cm</u>	<u>29 cm</u>	<u>40 cm</u>	<u>50 cm</u>
B Inlet (T)	4.0	3.975	3.95	4.0
B Outlet (T)	2.60	2.80	3.00	3.125
Field Length (m)	1.05	1.05	1.05	1.05
Gradient, Inlet (T/m)	17.	11.25	9.25	7.75
Gradient, Outlet (T/m)	5.75	5.10	5.00	4.25

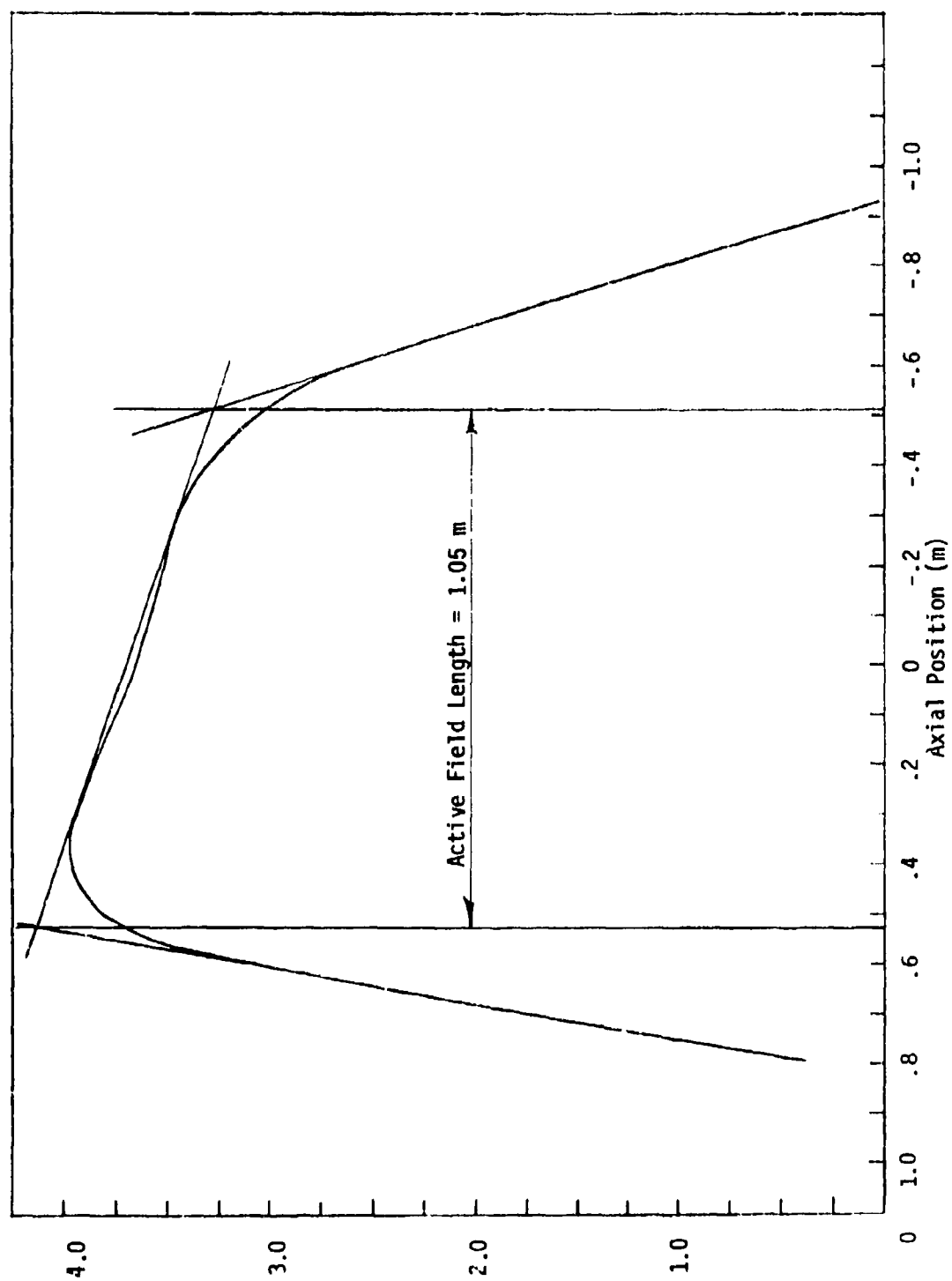


Figure 17 Magnetic Field on Axis vs. Axial Position for 20 cm Design ( $j_c = 15 \text{ kA/cm}^2$ )

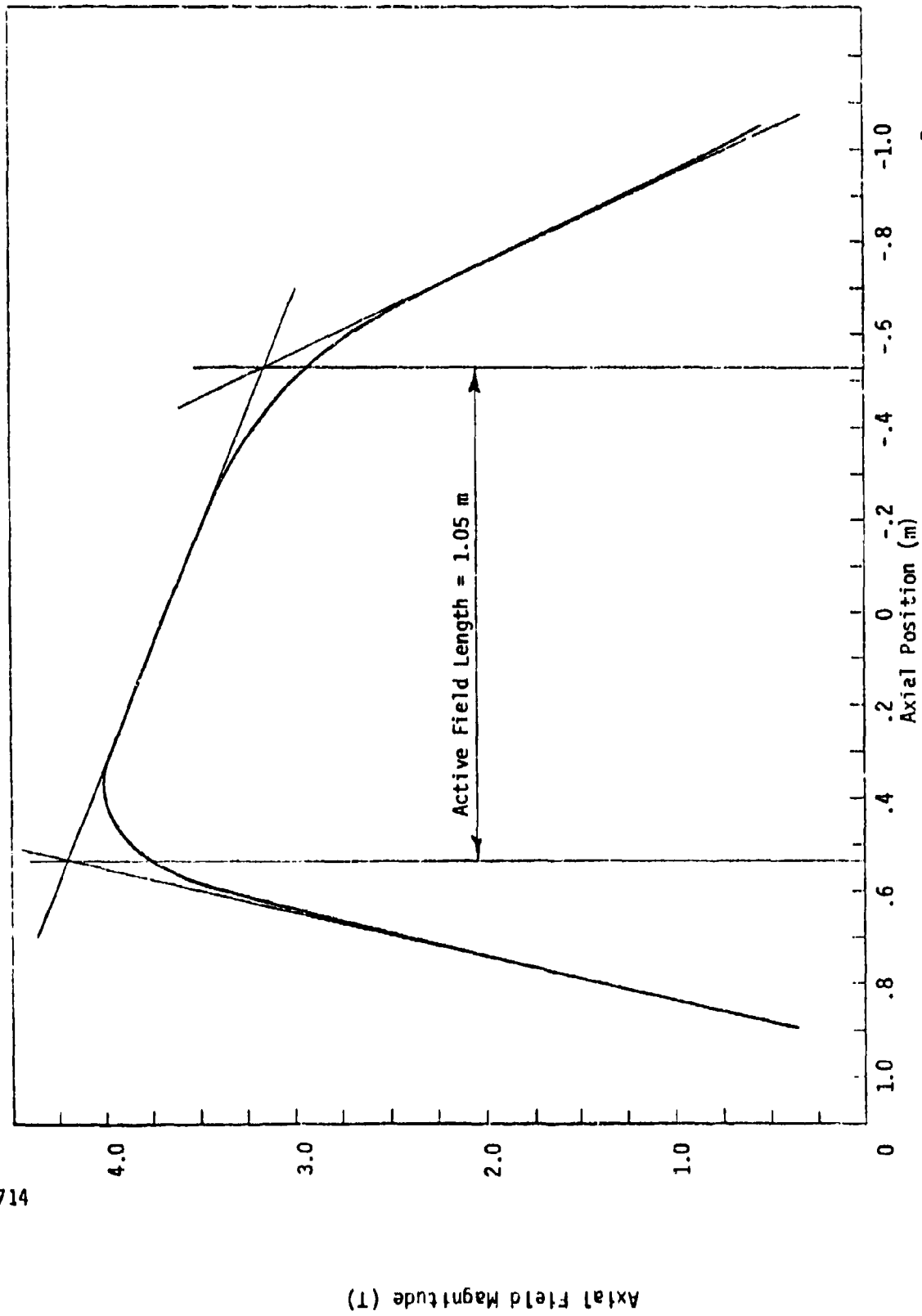


Figure 18 Magnetic Field on Axis vs. Axial Position for 29cm Design ( $j_c = 15 \text{ kA/cm}^2$ )

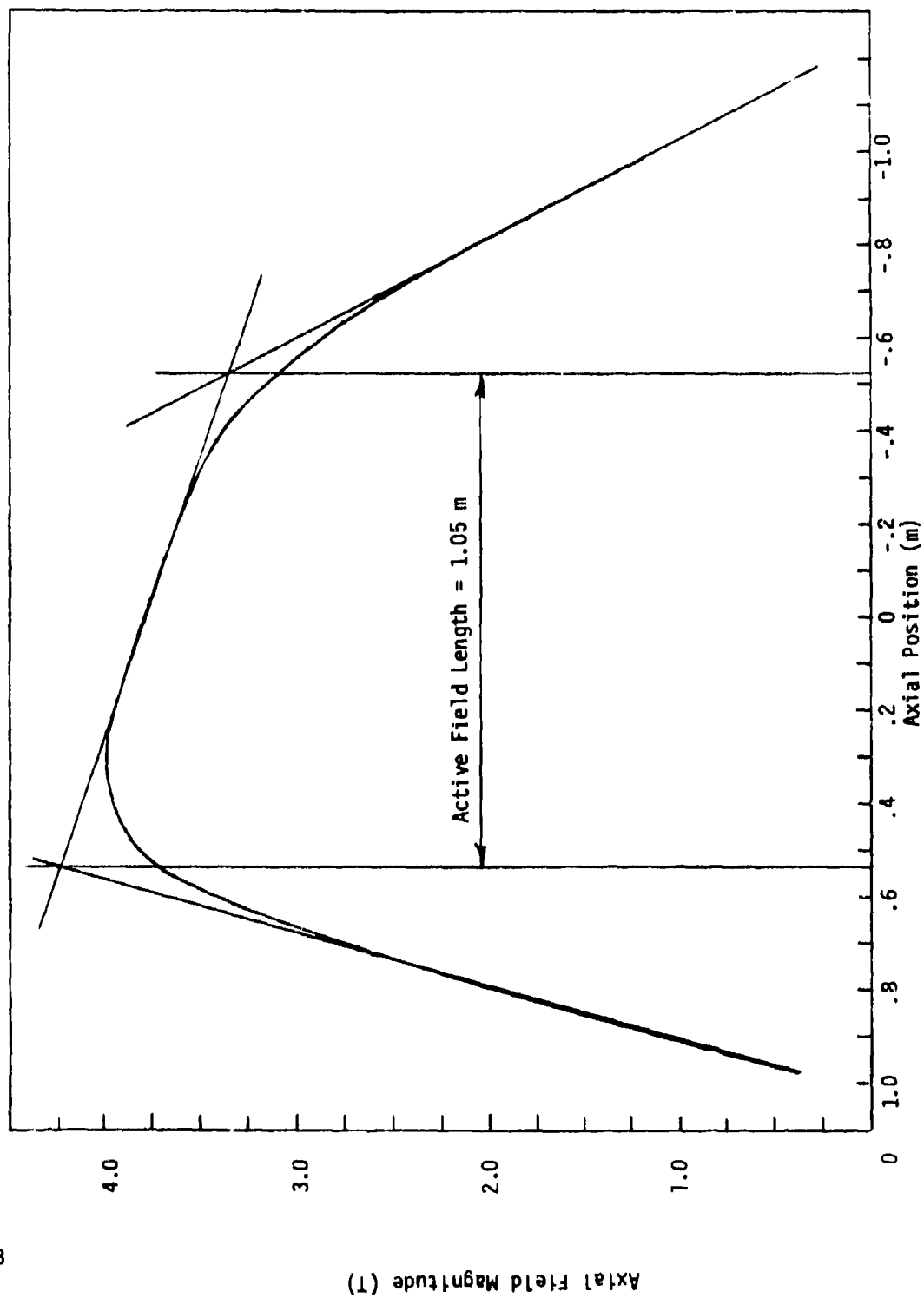


Figure 19 Magnetic Field on Axis vs. Axial Position for 40 cm Design ( $j_c = 15 \text{ kA/cm}^2$ )



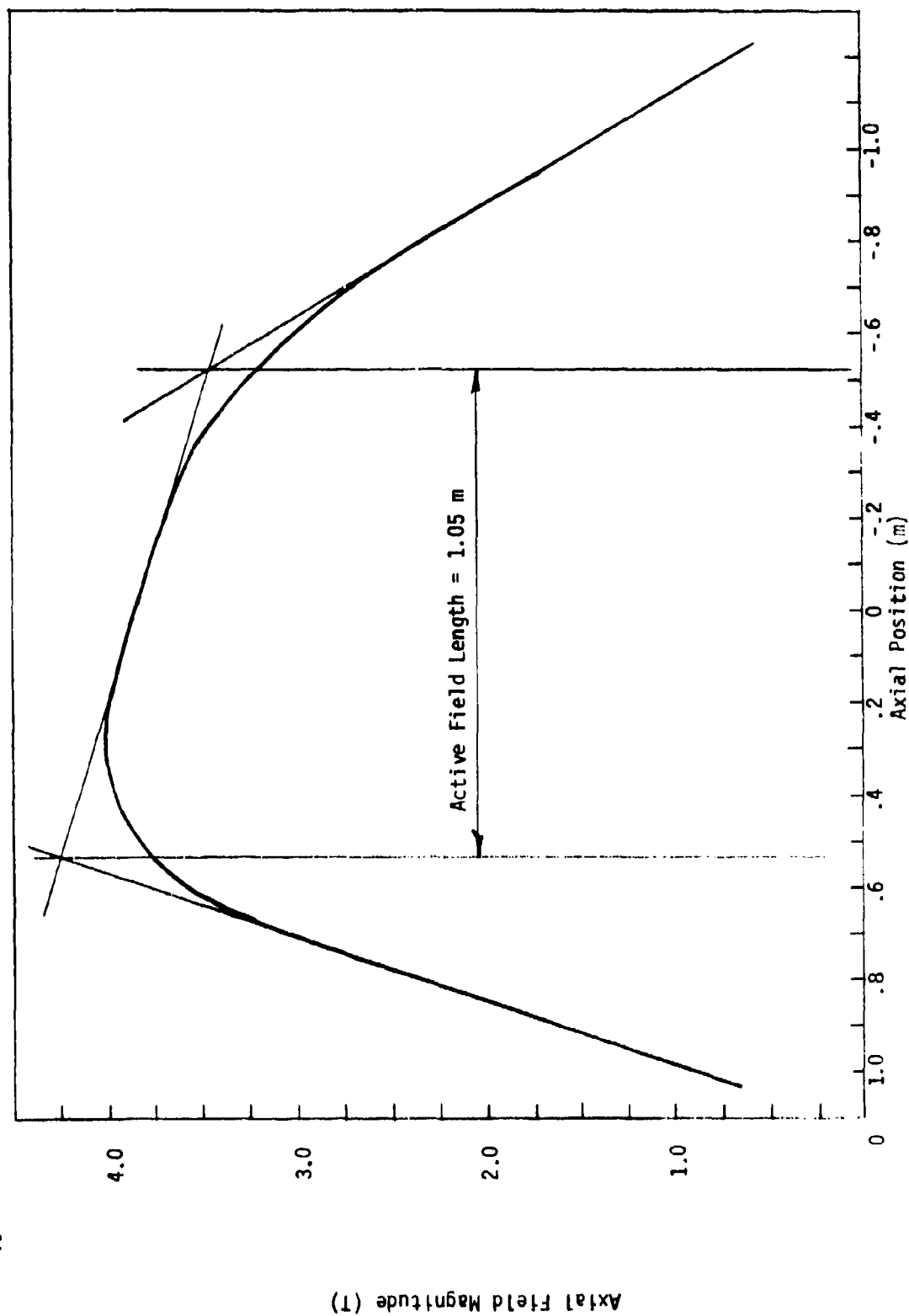


Figure 20 Magnetic Field on Axis vs. Axial Position for 50 cm Design ( $j_c = 15\text{kA/cm}^2$ )

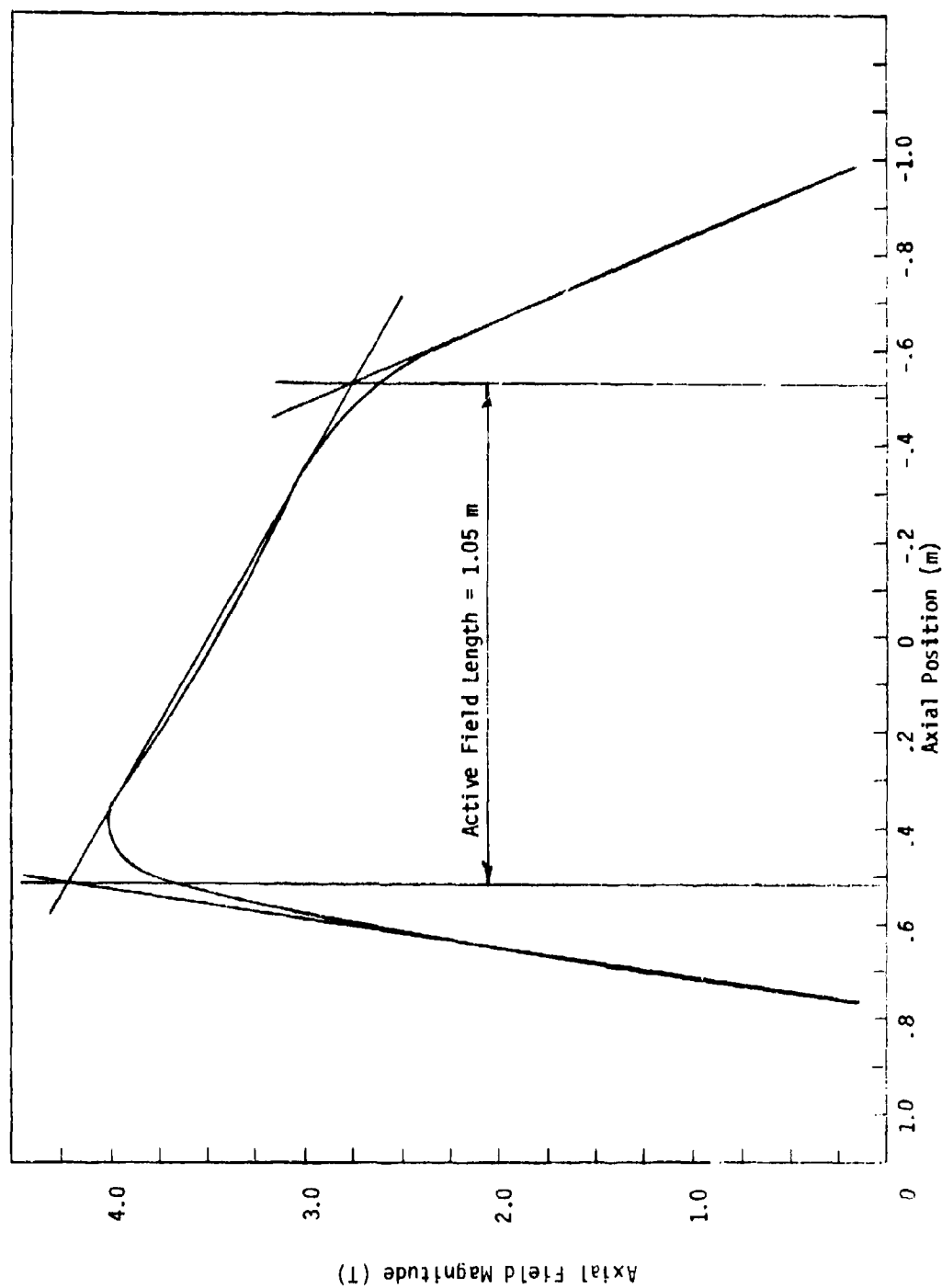


Figure 21 Magnetic Field on Axis vs. Axial Position for 20 cm Design ( $j_c = 30 \text{ kA/cm}^2$ )

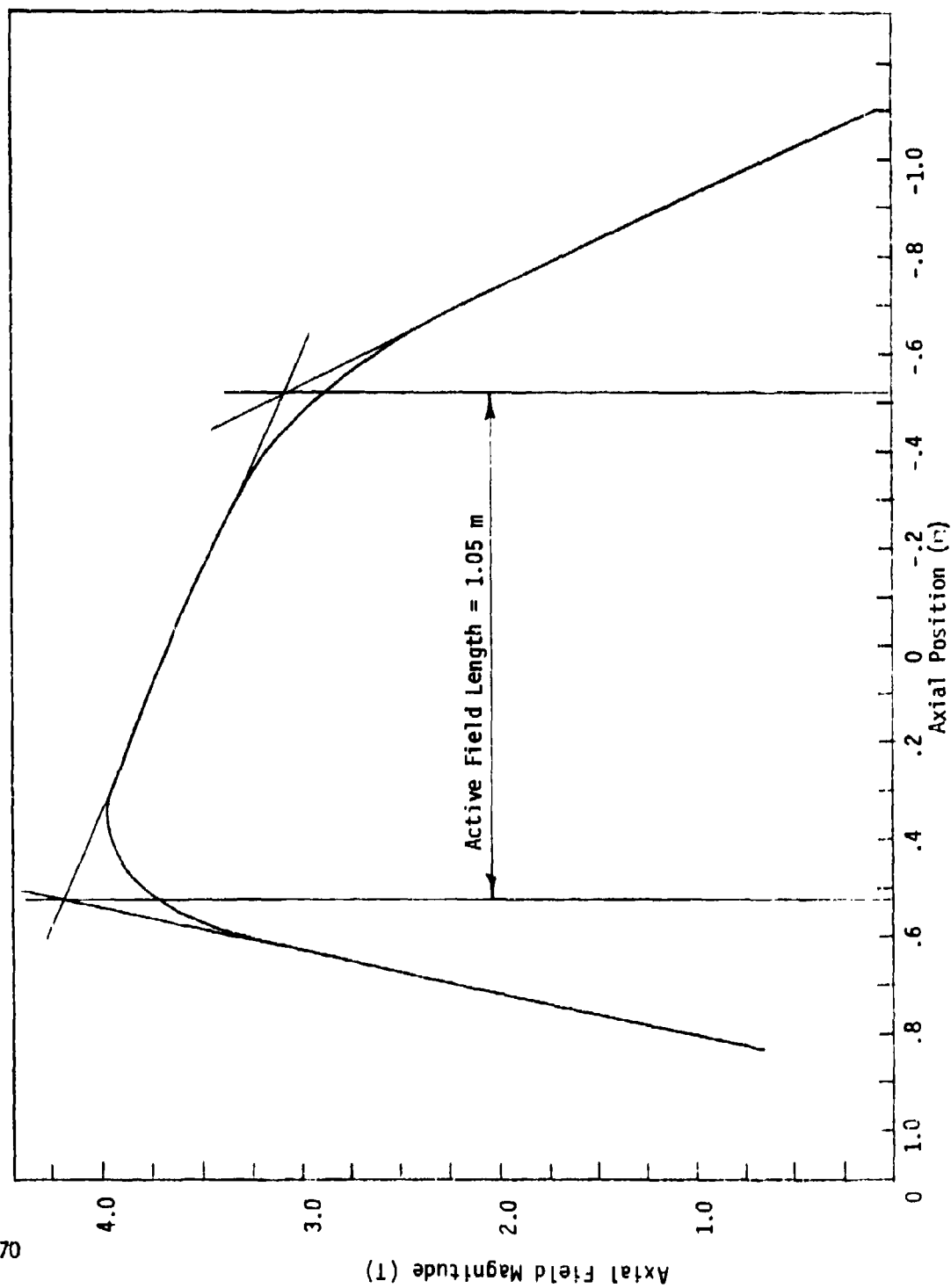


Figure 22 Magnetic Field on Axis vs. Axial Position for 29 cm Design ( $j_c = 30 \text{ kA/cm}^2$ )

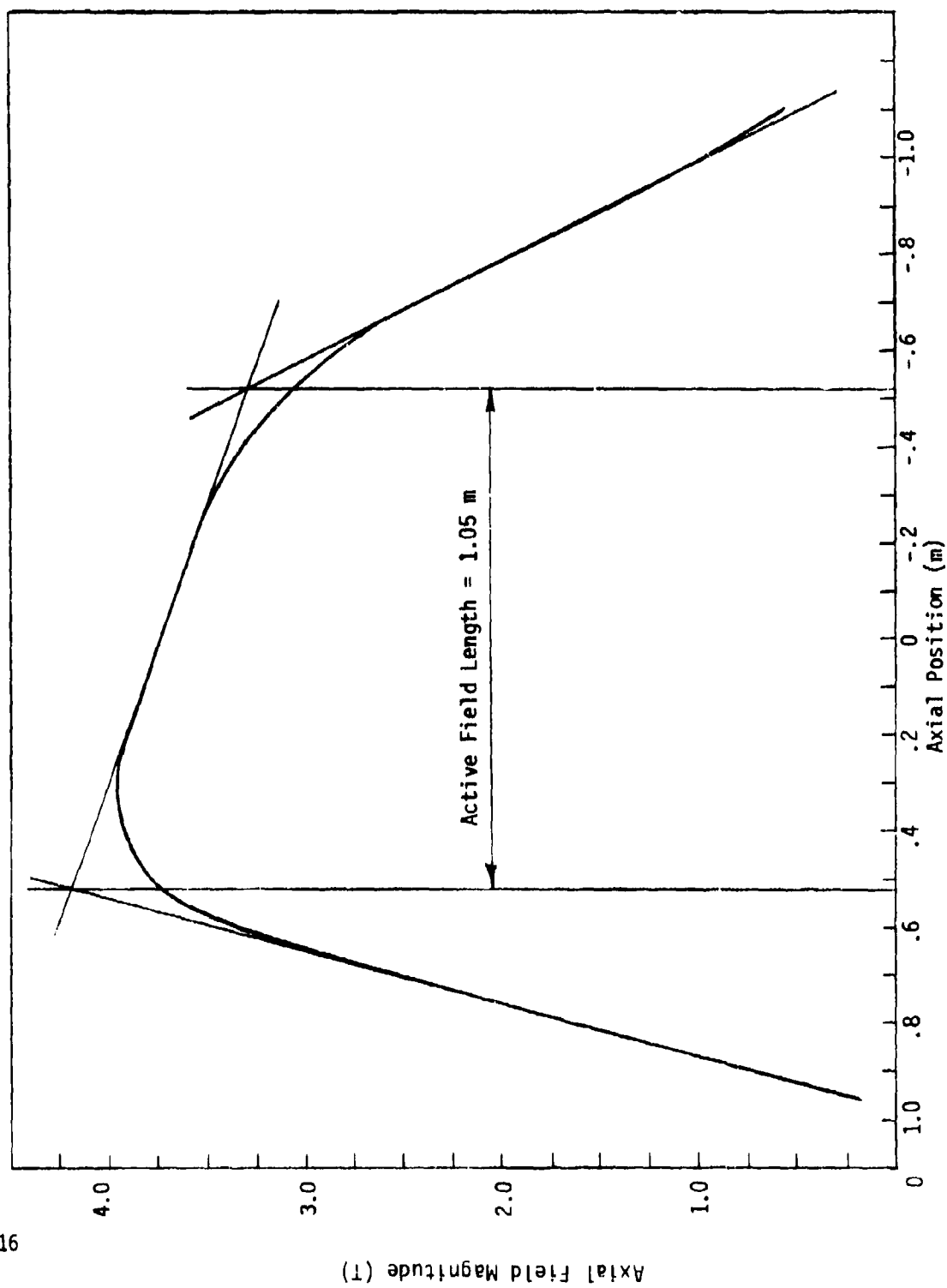


Figure 23 Magnetic Field on Axis vs. Axial Position for 40 cm Design ( $j_c = 30 \text{ kA/cm}^2$ )

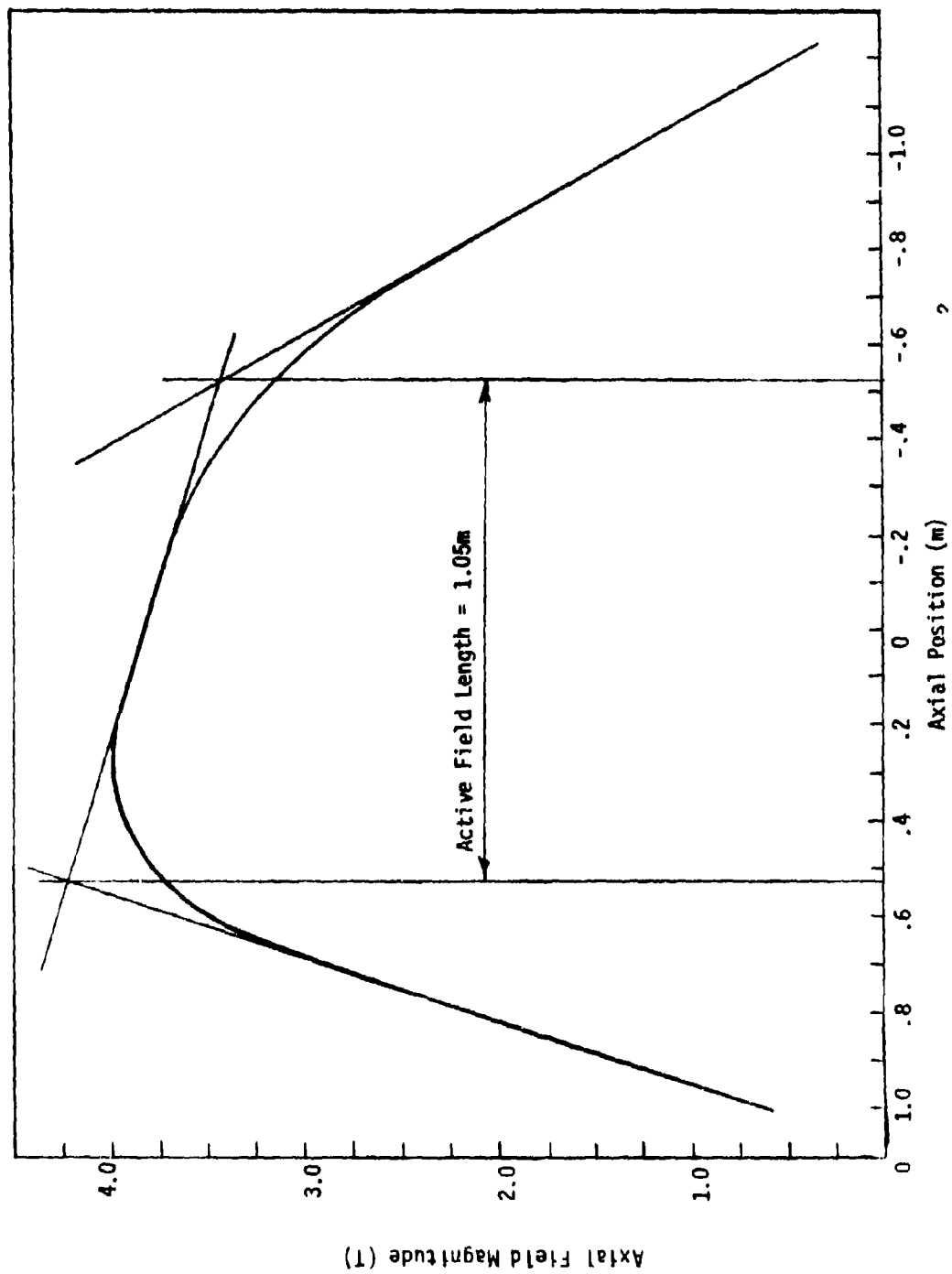


Figure 24 Magnetic Field on Axis vs. Axial Position for 50 cm Design ( $j_c = 30 \text{ kA/cm}^2$ )

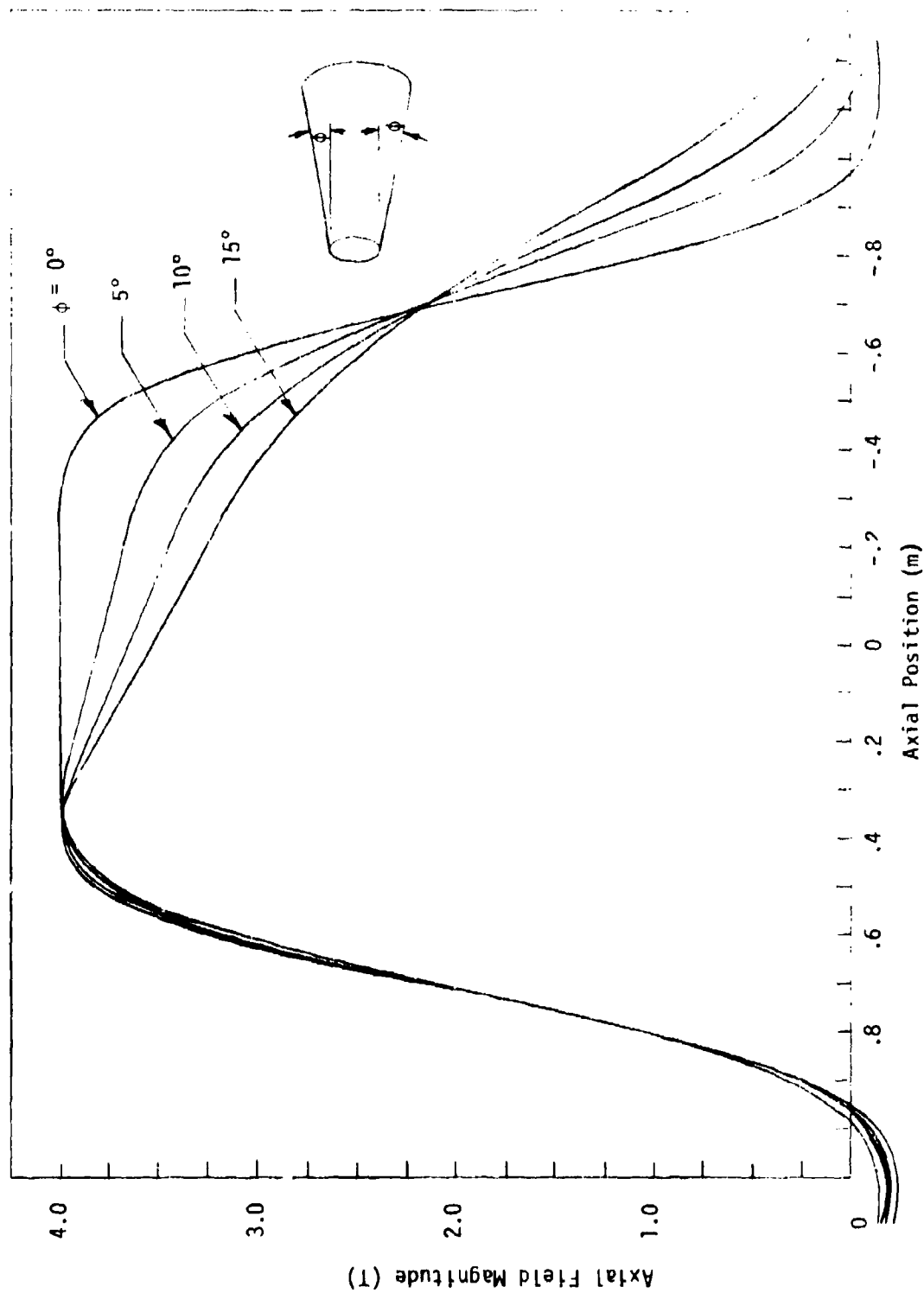


Figure 25 Magnetic Field on Axis vs. Axial Position for Several Values of Taper Angle,  $\phi$ , for the 29 cm Magnet Design (15kA/cm<sup>2</sup>)

It can be seen that as the taper increases, the outlet field level decreases. Therefore, the field requirement can be met by a judicious choice of taper angle. However, the outlet field gradient also decreases with increasing taper, and therefore, the requirements are difficult to meet simultaneously with the geometry chosen. The requirements probably can be met by employing one or more of the following more sophisticated winding techniques:

- 1) Having early crossovers
- 2) Employing small racetrack "trim" coils
- 3) Compressing the winding envelope at the outlet back to the inlet size\*

The use of these techniques, however, requires a significant design and fabrication effort.

The filament model discussed above was refined so that each winding bundle was modeled by 4 filaments. This model was then used to calculate the magnetic field homogeneity in the MHD channel region. Three axial positions were chosen for the calculations. These were the inlet, mid-plane and outlet. Figures 26 through 49 illustrate the calculated field homogeneity at the three locations for the four magnet sizes, each with two current densities. These figures present the ratio of the y-component of field at the point to the central field magnitude. The results are out of the range defined by the requirements - i.e.,  $\pm 5\%$  of the central field magnitude for the outlet of all designs. The 20, 29, and 40 cm sizes have a maximum variation of 7% for the outlet at the largest radii checked. The inlet and midplane results for these three sizes are within the specified range. It was assumed that the useful MHD channel bore would have 80% of the warm bore radius. The 50 cm size did not make the 5% homogeneity at both the inlet and the outlet.

\*Since the winding tapers the distance between bundles grows from inlet to outlet. The outlet crossover therefore takes more space than does the inlet crossover.

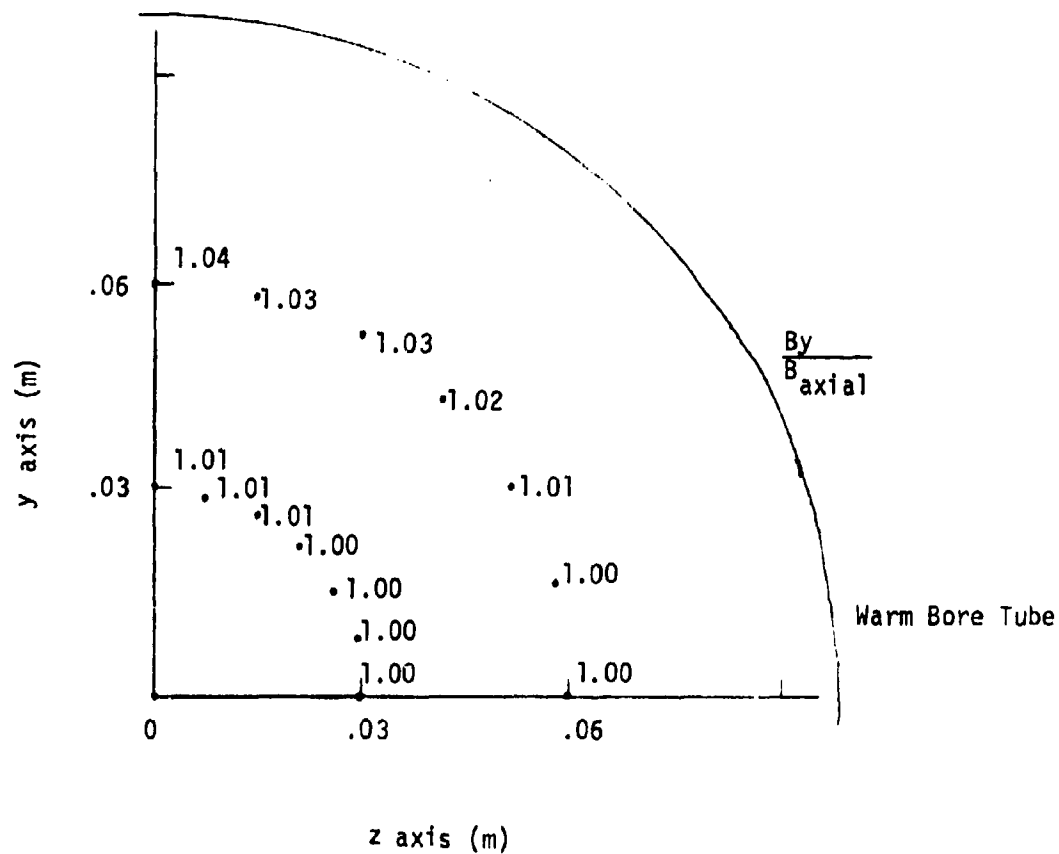


Figure 26 Field Homogeneity for 20 cm Design  
( $j_c = 15 \text{ kA/cm}^2$ ) at Inlet ( $x = .525 \text{ m}$ )



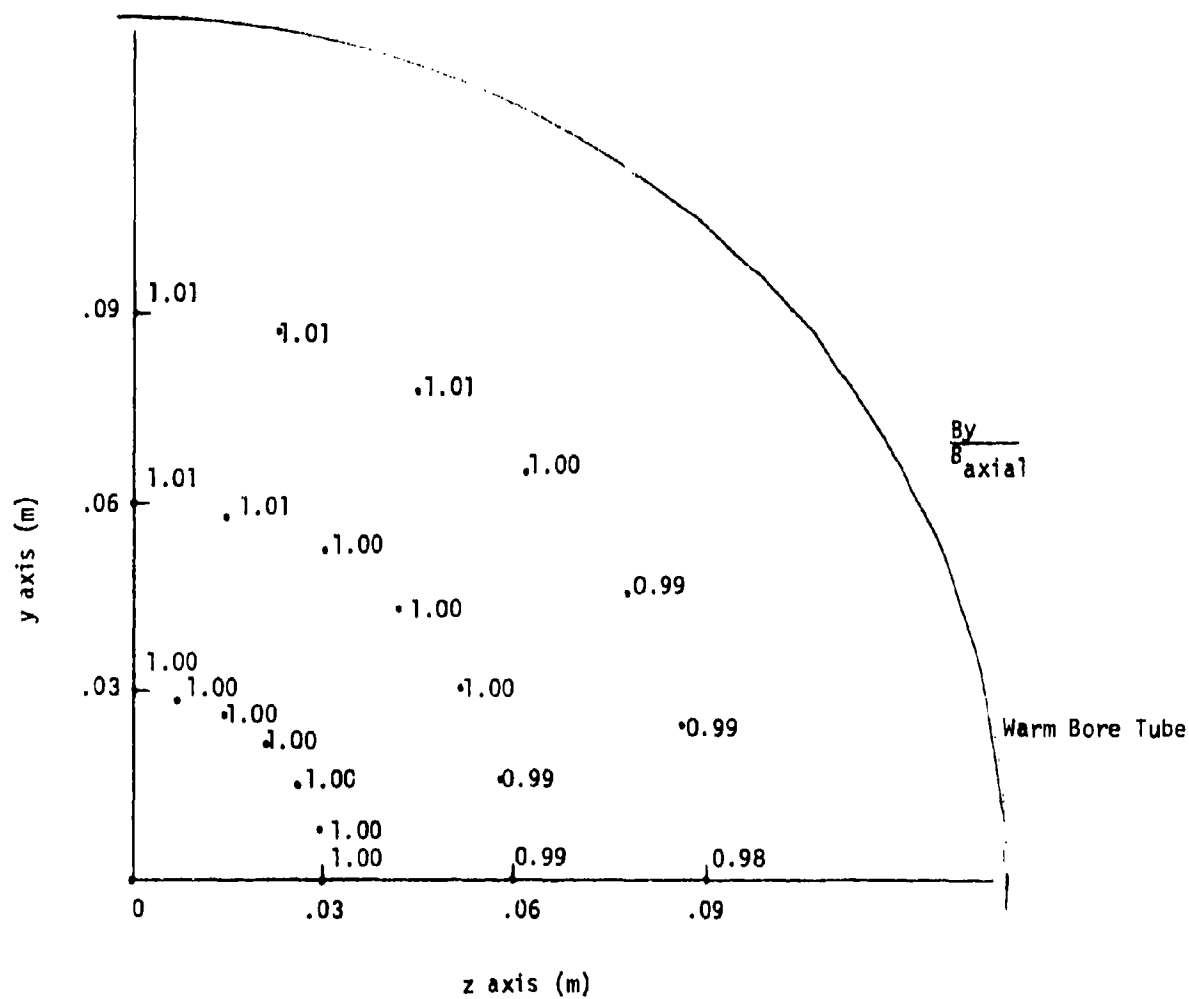


Figure 27 Field Homogeneity for 20 cm Design  
( $j_c = 15 \text{ kA/cm}^2$ ) at Midplane ( $x = 0.0$ )

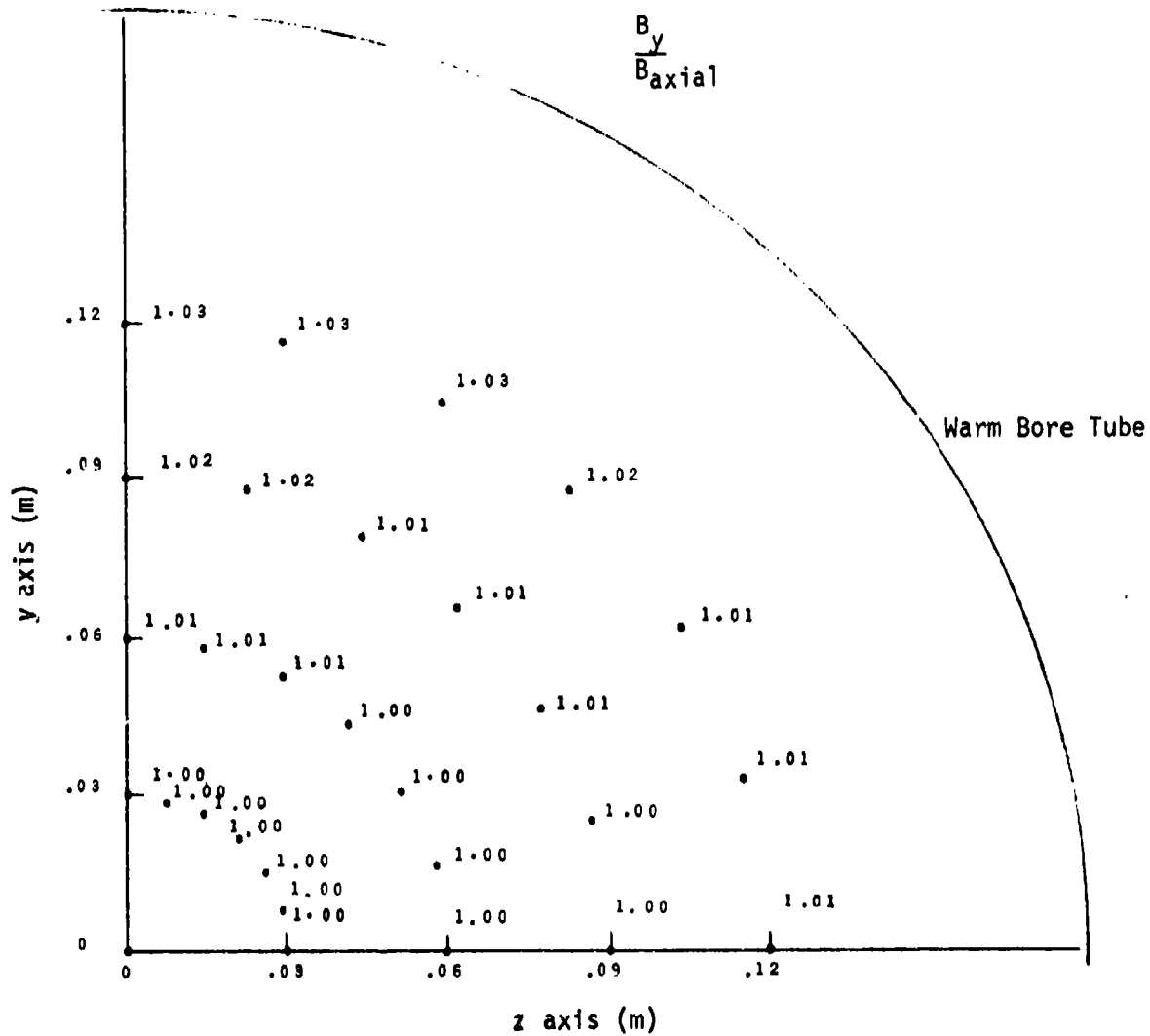


Figure 28 Field Homogeneity for 20 cm Design  
( $j_c = 15\text{kA/cm}^2$ ) at Outlet ( $x = -.525\text{m}$ )

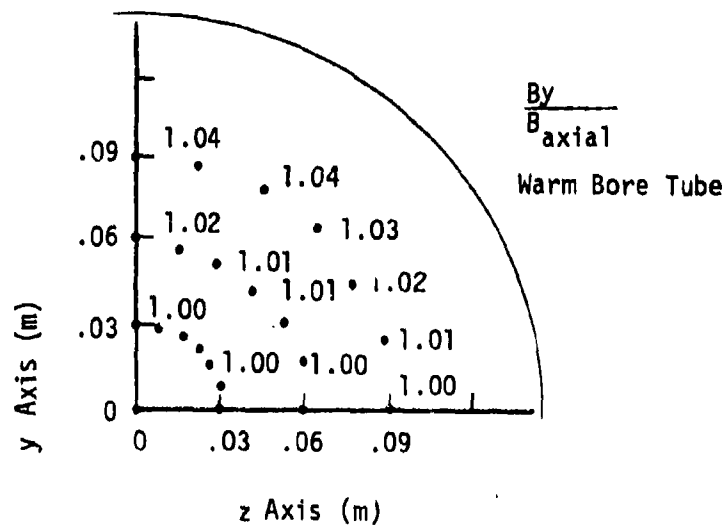


Figure 29 Field Homogeneity for 29 cm Design ( $j_c = 15 \text{ kA/cm}^2$ )  
at Inlet ( $X = .525 \text{ m}$ )

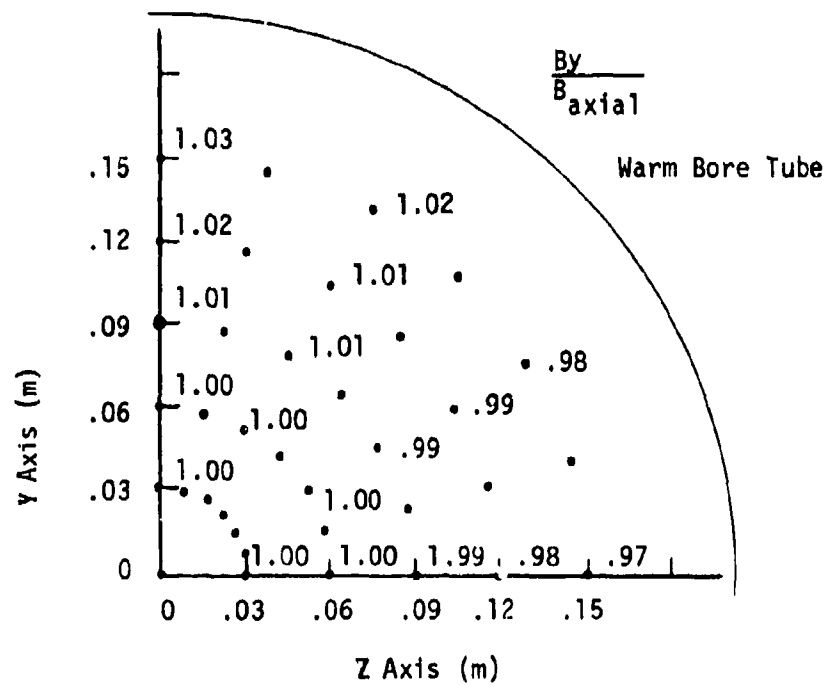


Figure 30 Field Homogeneity for 29 cm Design ( $j_c = 15 \text{ kA/cm}^2$ ) at Midplane ( $X = 0.0\text{m}$ )

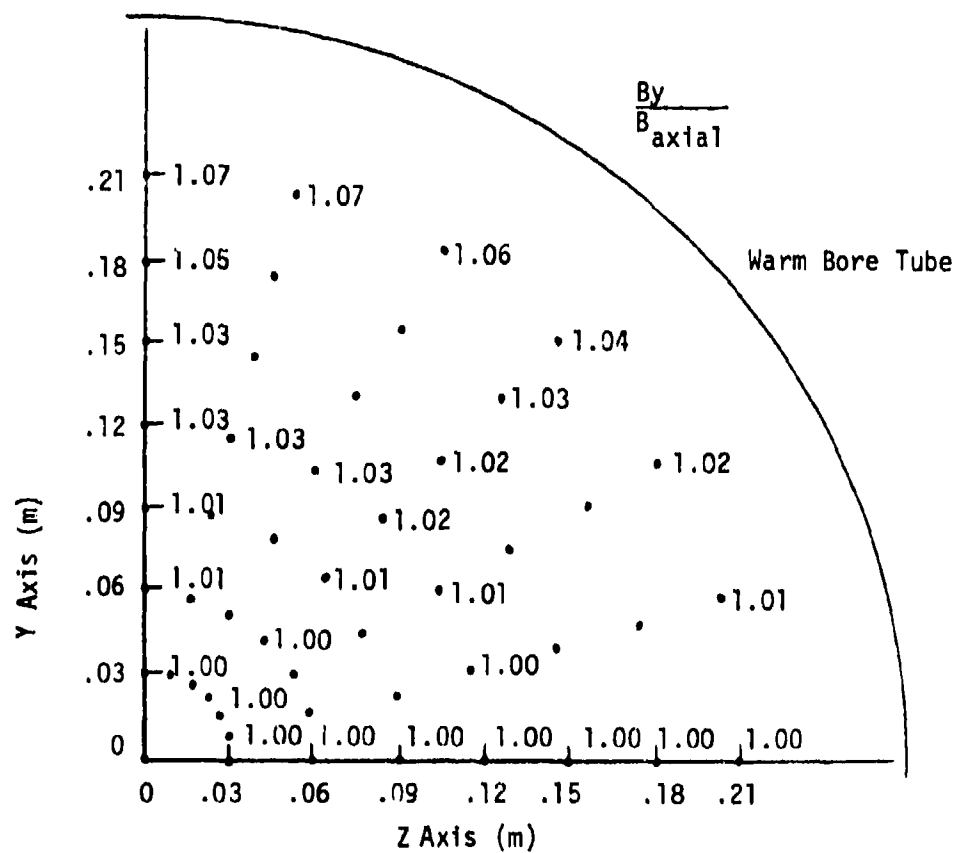


Figure 31 Field Homogeneity for 29 cm Design ( $j_c = 15 \text{ kA/cm}^2$ ) at Outlet ( $X = .525\text{m}$ )

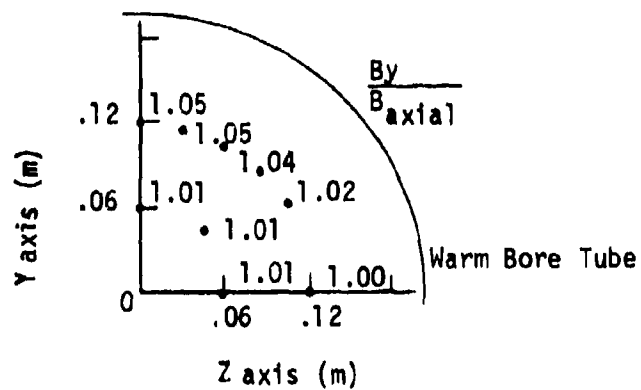


Figure 32 Field Homogeneity for 40 cm Design  
 ( $j_c = 15 \text{ kA/cm}^2$ ) at Inlet ( $x = .525 \text{ m}$ )

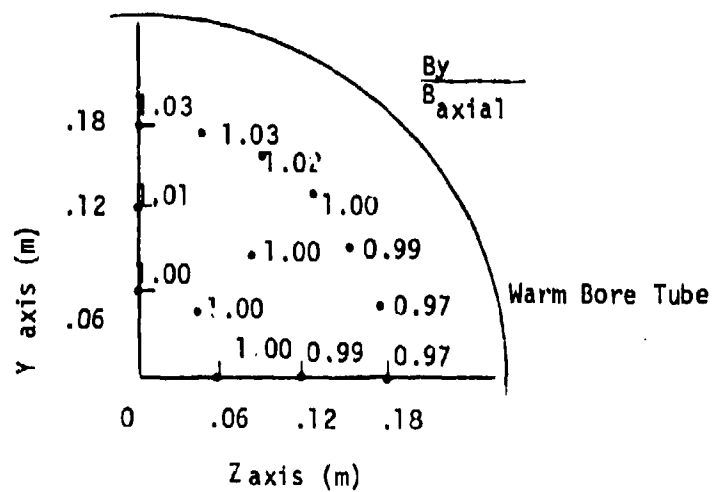


Figure 33 Field Homogeneity for 40 cm Design  
( $j_c = 15 \text{ kA/cm}^2$ ) at Midplane ( $x = 0.0 \text{ m}$ )

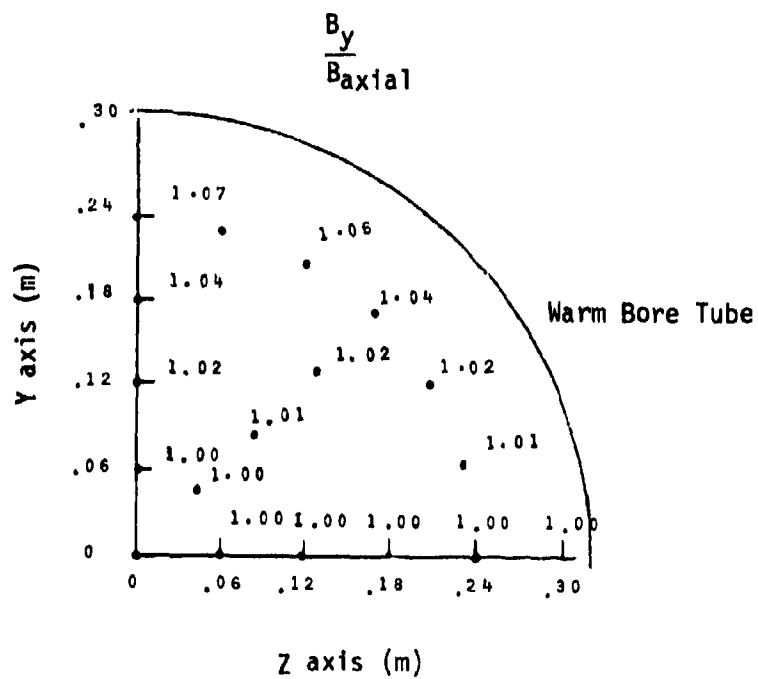


Figure 34 Field Homogeneity for 40 cm Design  
( $j_c = 15 \text{ kA/cm}^2$ ) at Outlet ( $x = -.525 \text{ m}$ )



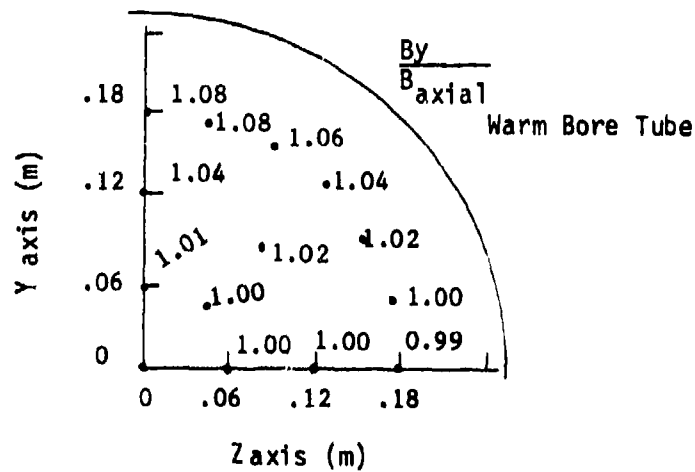


Figure 35 Field Homogeneity for 50 cm Design  
( $j_c = 15 \text{ kA/cm}^2$ ) at Inlet ( $x = .525 \text{ m}$ )

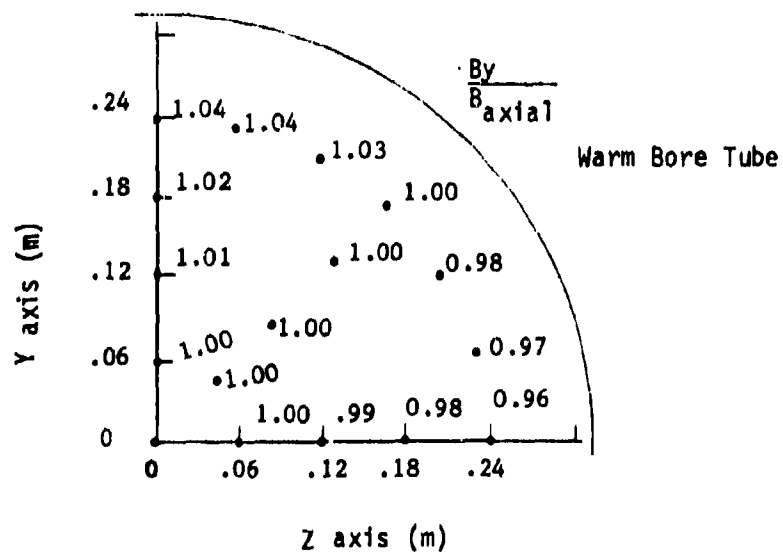


Figure 36 Field Homogeneity for 50 cm Design  
( $j_c = 15 \text{ kA/cm}^2$ ) at Midplane ( $x = 0.0 \text{ m}$ )

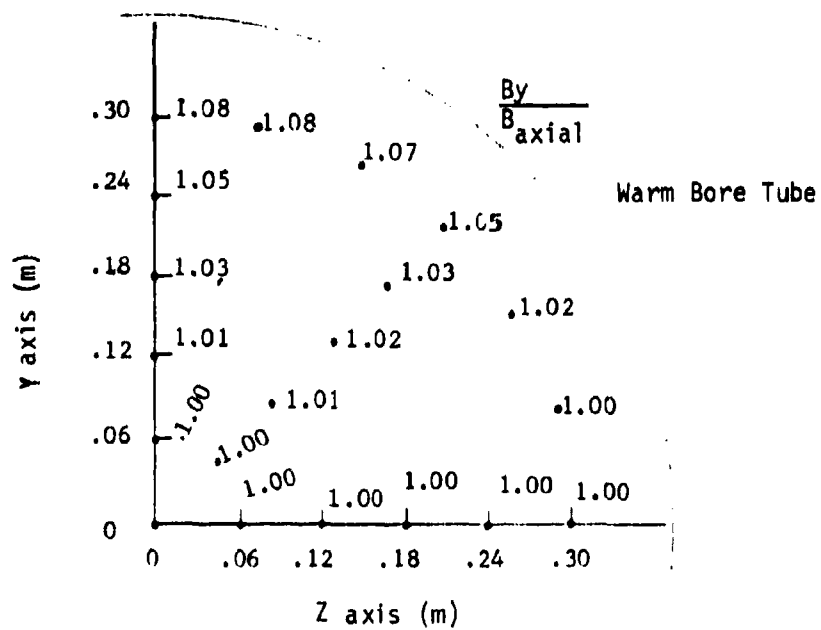


Figure 37 Field Homogeneity for 50 cm Design  
( $j_c = 15 \text{ kA/cm}^2$ ) at Outlet ( $x = -.525 \text{ m}$ )

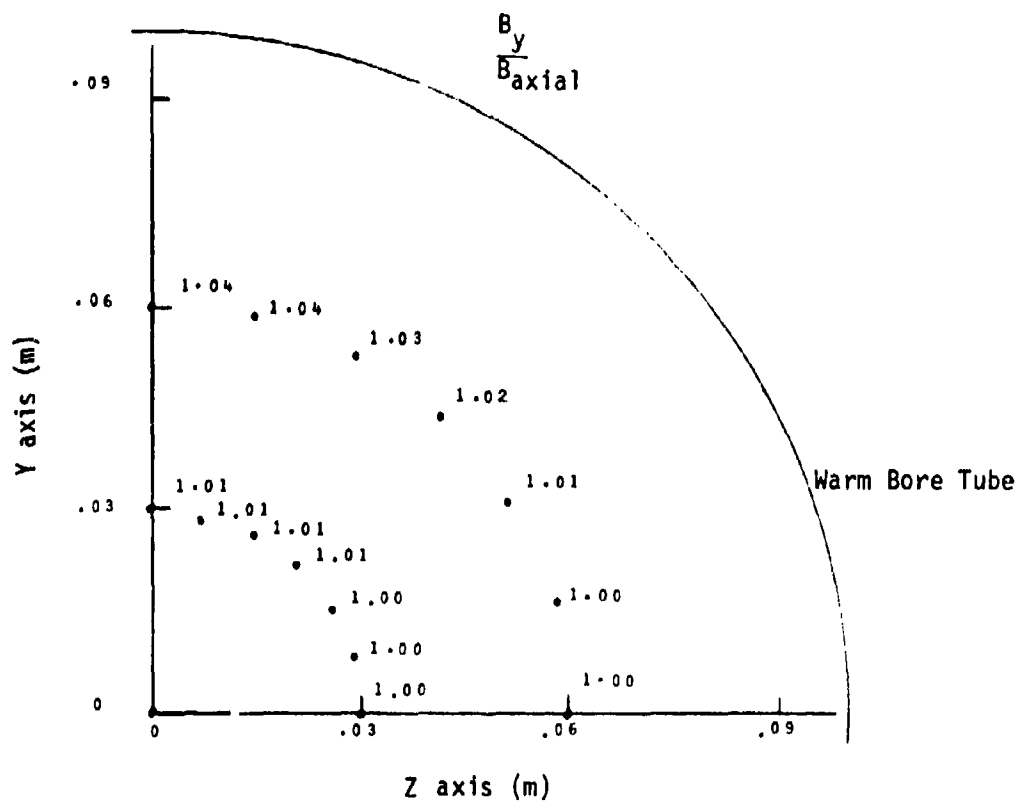


Figure 38 Field Homogeneity for 20 cm Design  
( $j_c = 30 \text{ kA/cm}^2$ ) at Inlet ( $X = .525\text{m}$ )

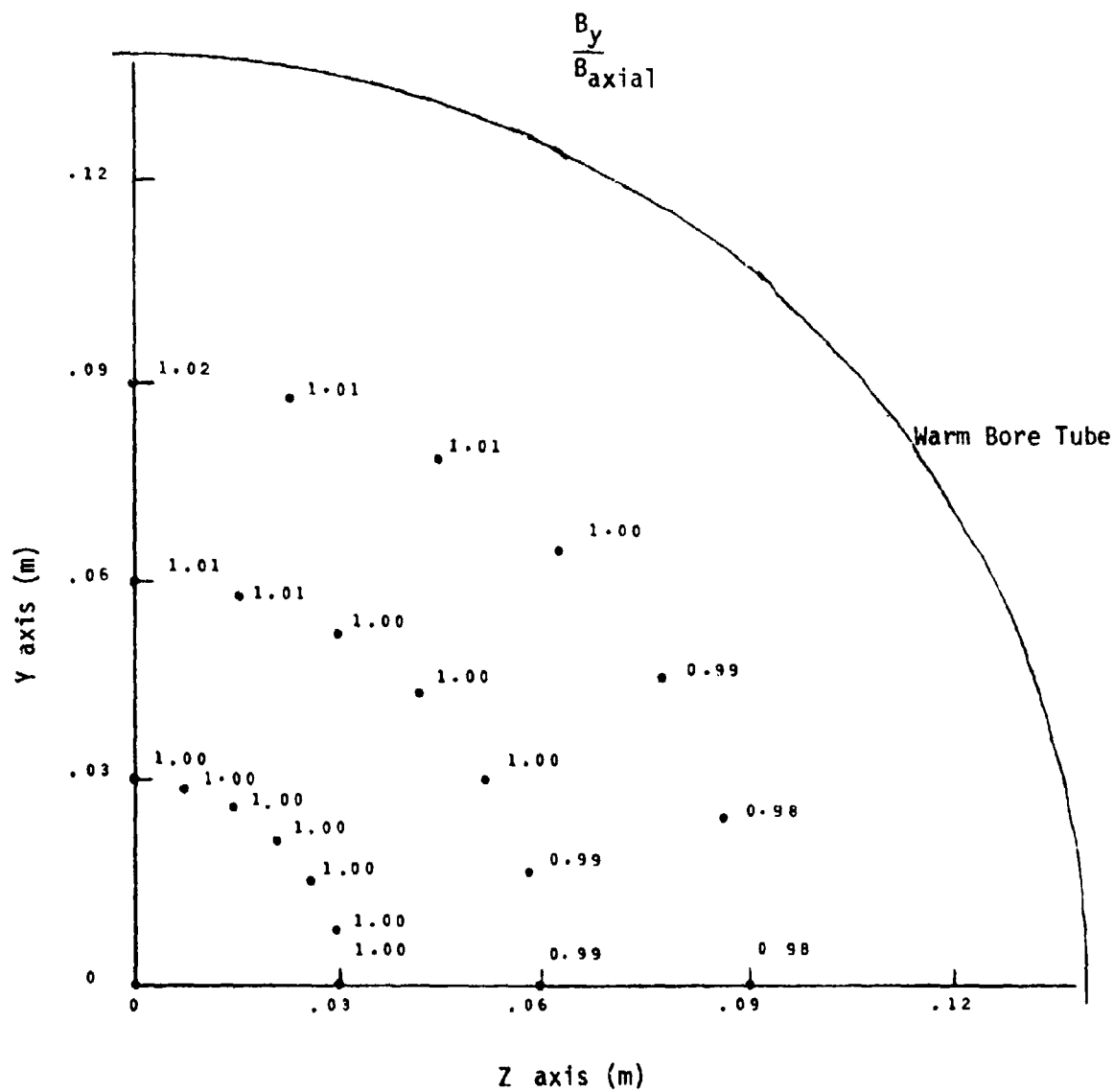


Figure 39 Field Homogeneity for 20 cm Design  
 $(j_c = 30 \text{ kA/cm}^2)$  at Midplane ( $X = 0.0$ )

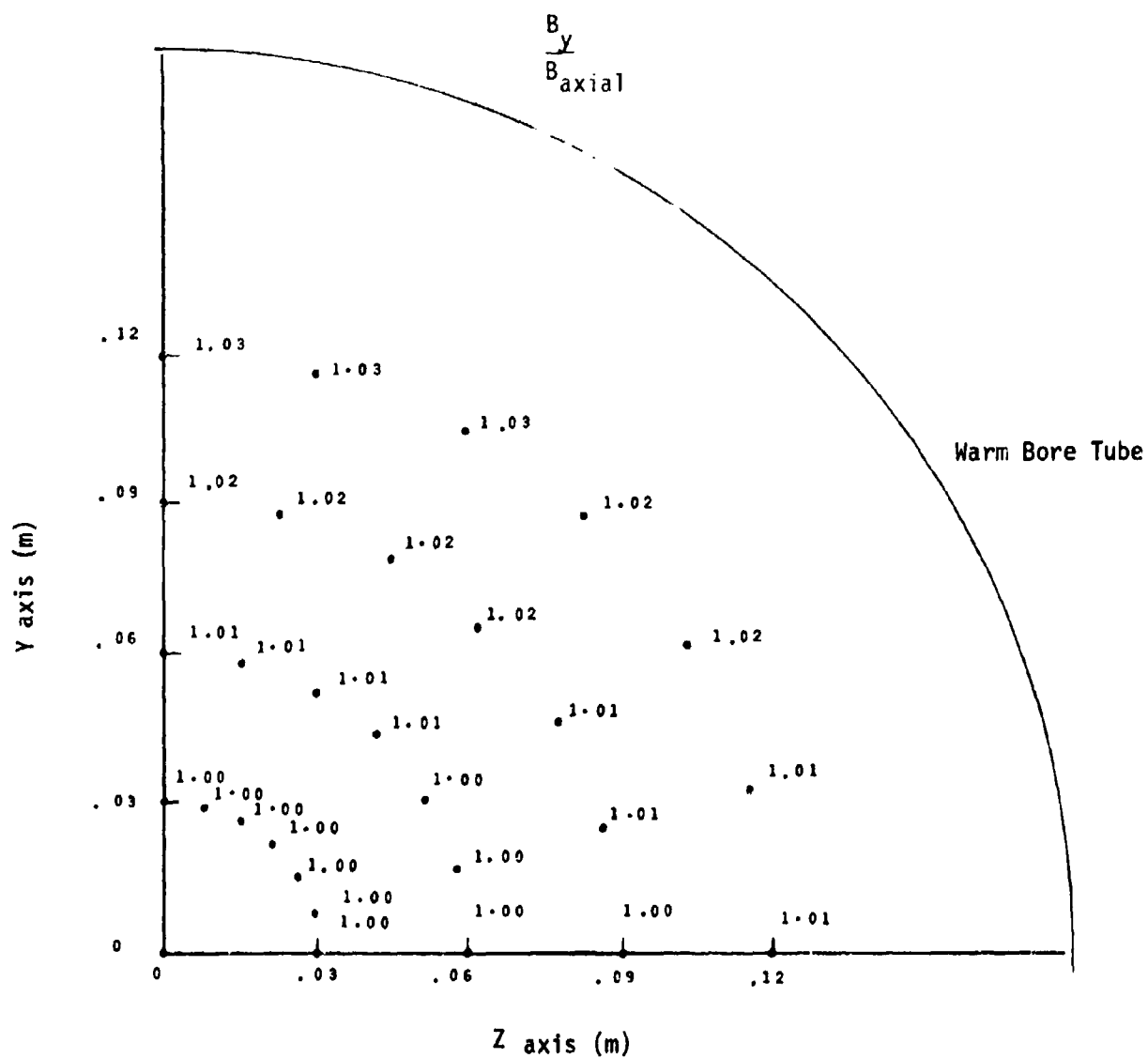


Figure 40 Field Homogeneity for 20 cm Design  
 $(j_c = 30 \text{ kA/cm}^2)$  at Outlet ( $x = -.525 \text{ m}$ )

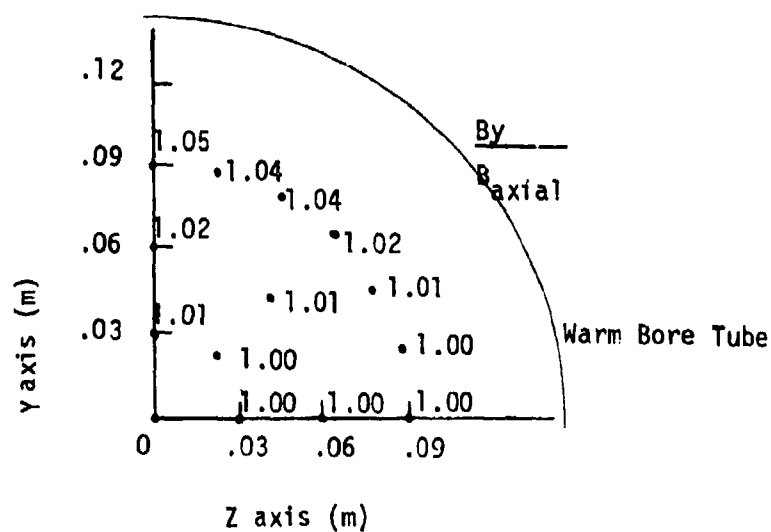


Figure 41 Field Homogeneity for 29 cm Design  
 $(j_c = 30 \text{ kA/cm}^2)$  at Inlet ( $x = .525 \text{ m}$ )

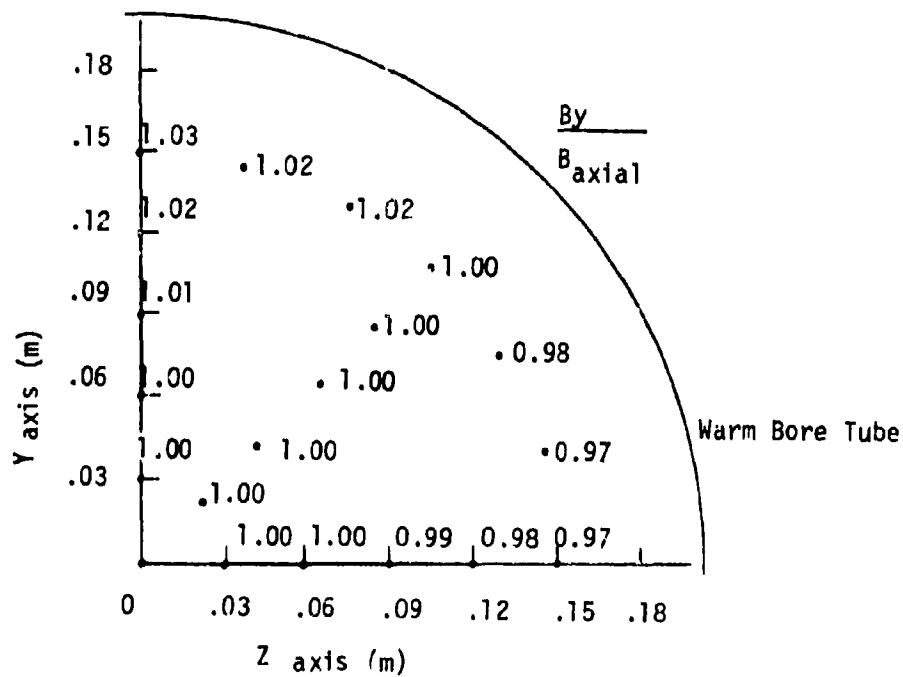


Figure 42 Field Homogeneity for 29 cm Design  
 $(j_c = 30 \text{ kA/cm}^2)$  at Midplane ( $x = 0.0 \text{ m}$ )



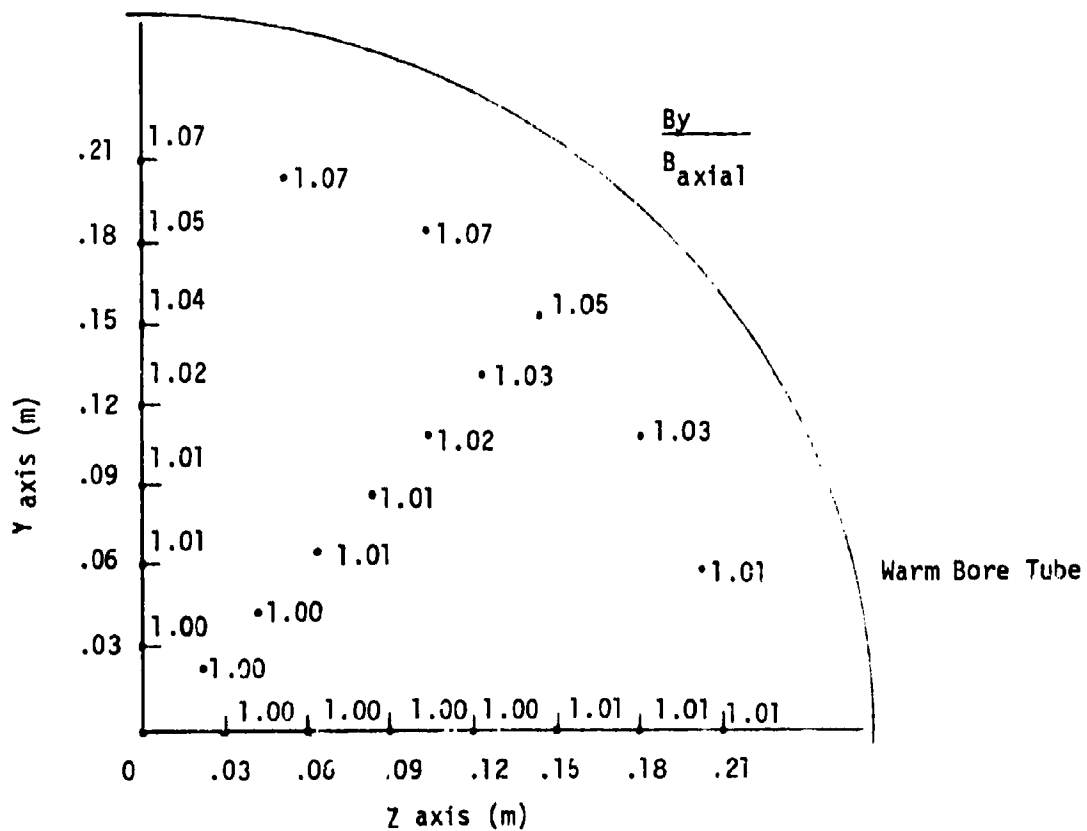


Figure 43 Field Homogeneity for 29 cm Design  
 $(j_c = 30 \text{ kA/cm}^2)$  at Outlet ( $x = -.525 \text{ m}$ )

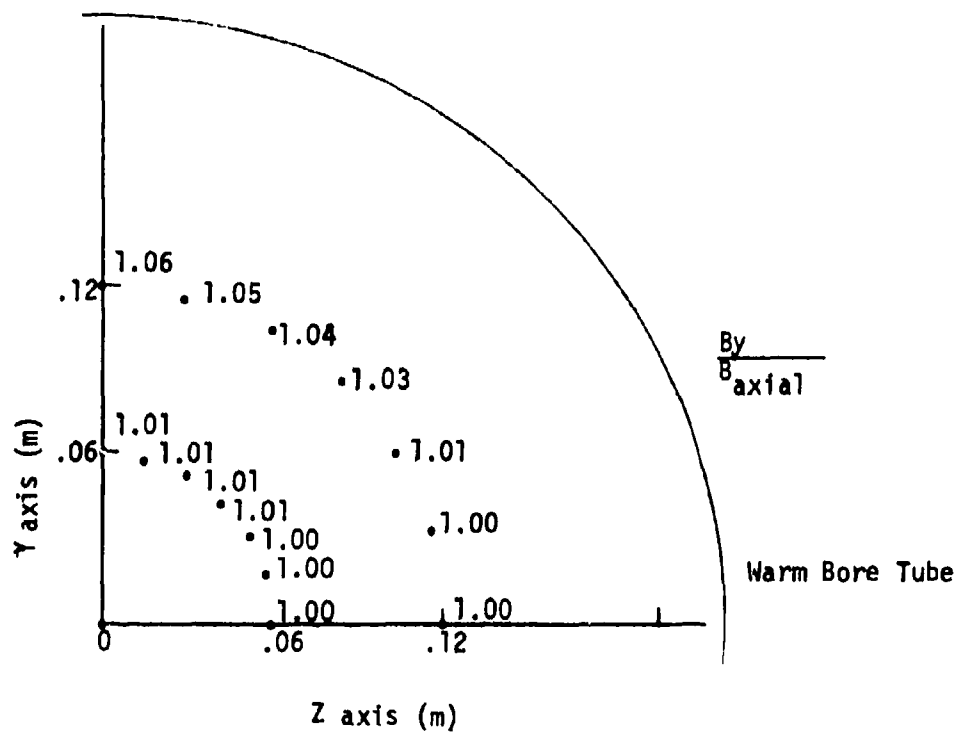


Figure 44 Field Homogeneity for 40 cm Design  
 $(j_c = 30 \text{ kA/cm}^2)$  at Inlet ( $x = .525 \text{ m}$ )

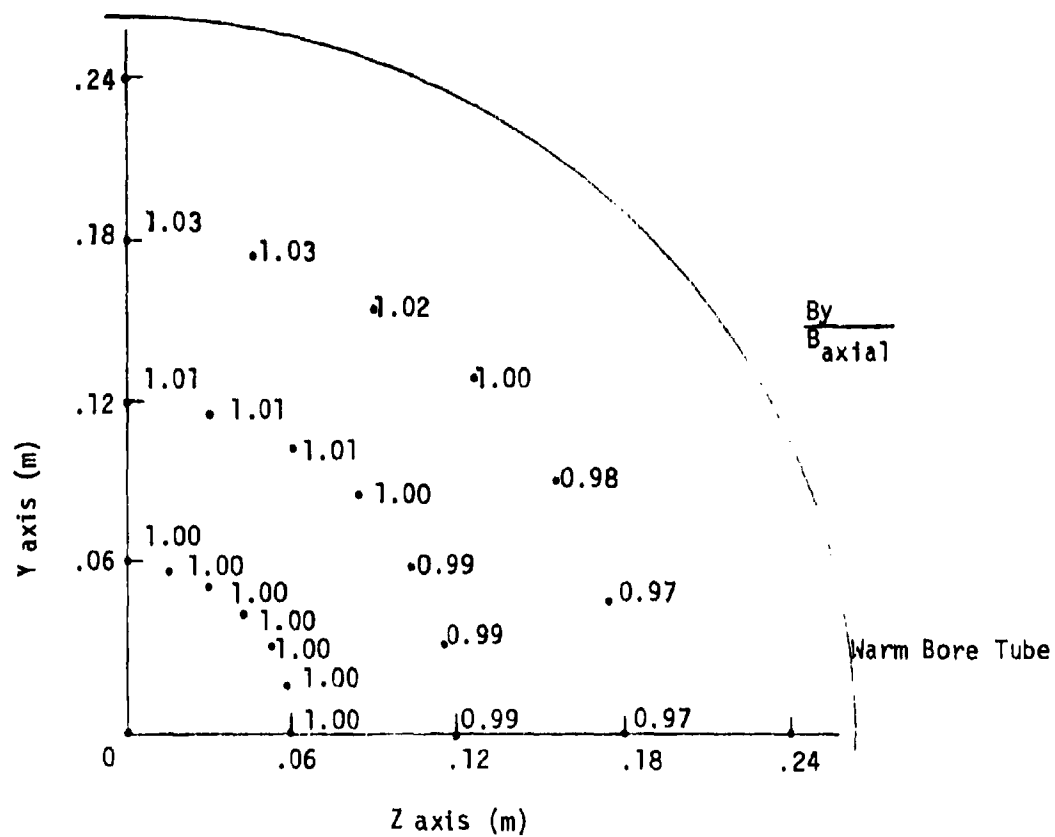


Figure 45 Field Homogeneity for 40 cm Design  
 $(j_c = 30 \text{ kA/cm}^2)$  at Midplane ( $x = 0.0 \text{ m}$ )

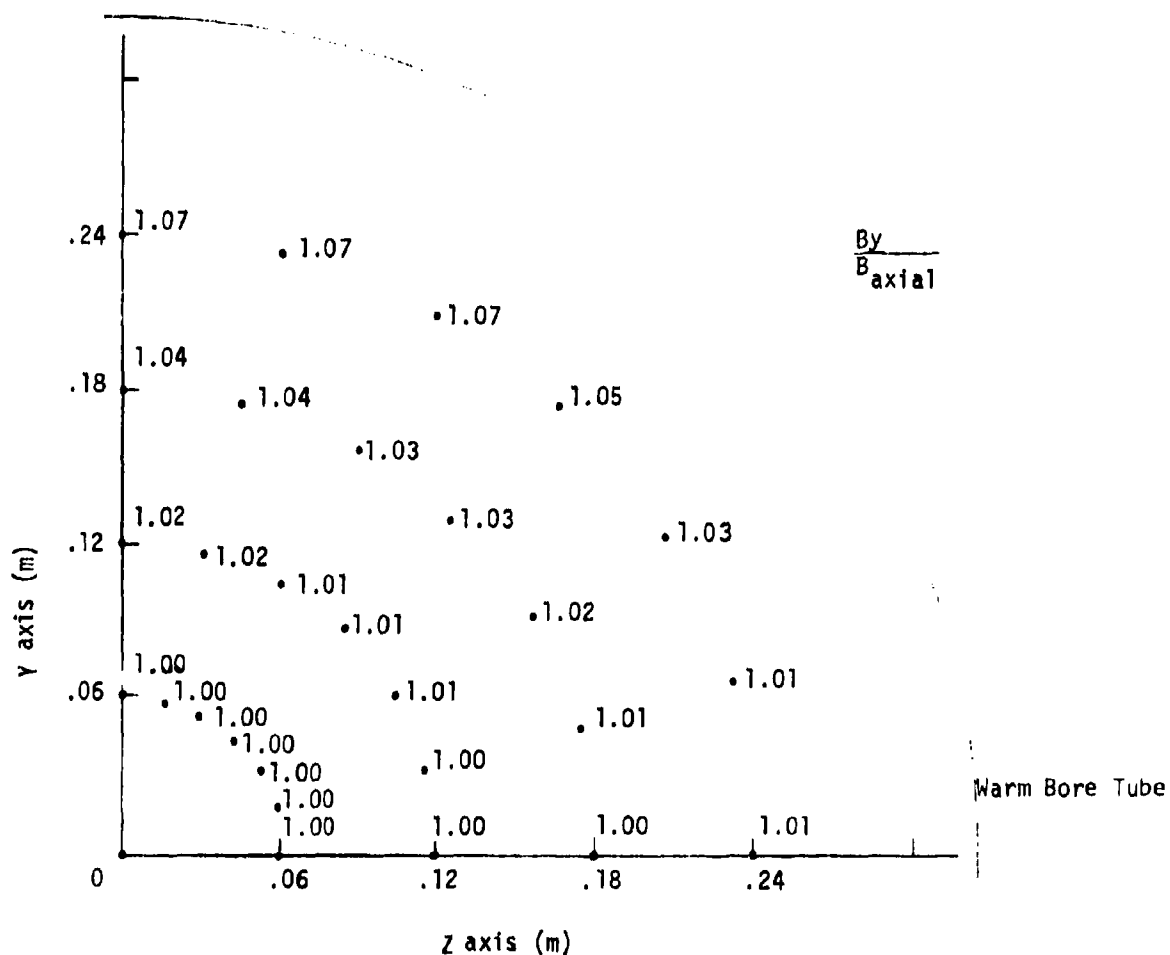


Figure 46 Field Homogeneity for 40 cm Design  
 $(j_c = 30 \text{ kA/cm}^2)$  at Midplane ( $x = -.525 \text{ m}$ )

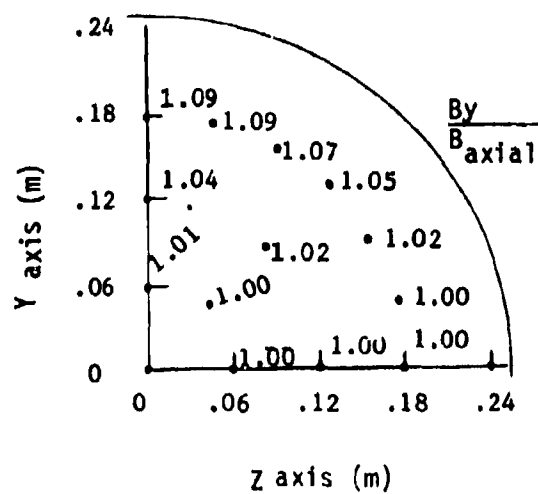


Figure 47 Field Homogeneity for 50 cm Design  
 $(j_c = 30\text{kA/cm}^2)$  at Inlet ( $x = .525\text{m}$ )

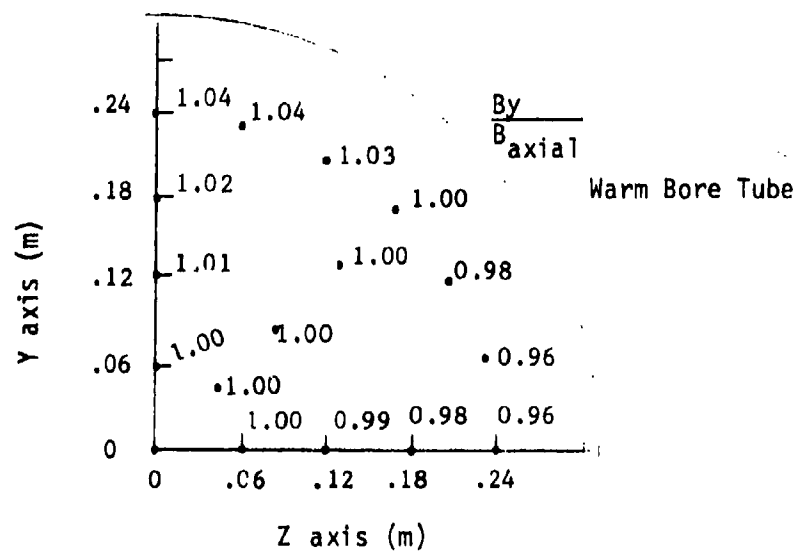


Figure 48 Field Homogeneity for 50 cm Design  
( $j_c = 30\text{kA/cm}^2$ ) at Midplane ( $x = 0.0\text{m}$ )

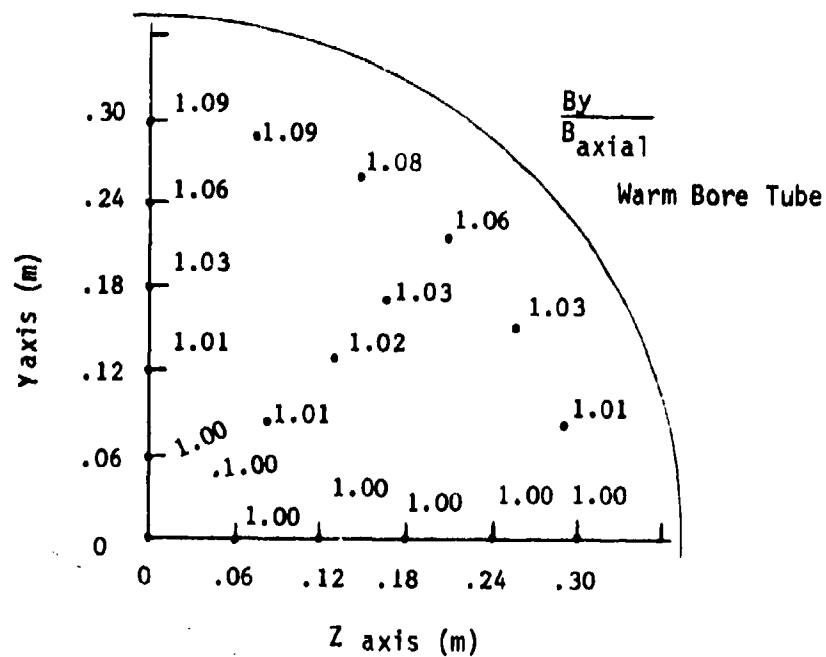


Figure 49 Field Homogeneity for 50 cm Design  
 $(j_c = 30 \text{ kA/cm}^2)$  at Outlet ( $x = -.525 \text{ m}$ )

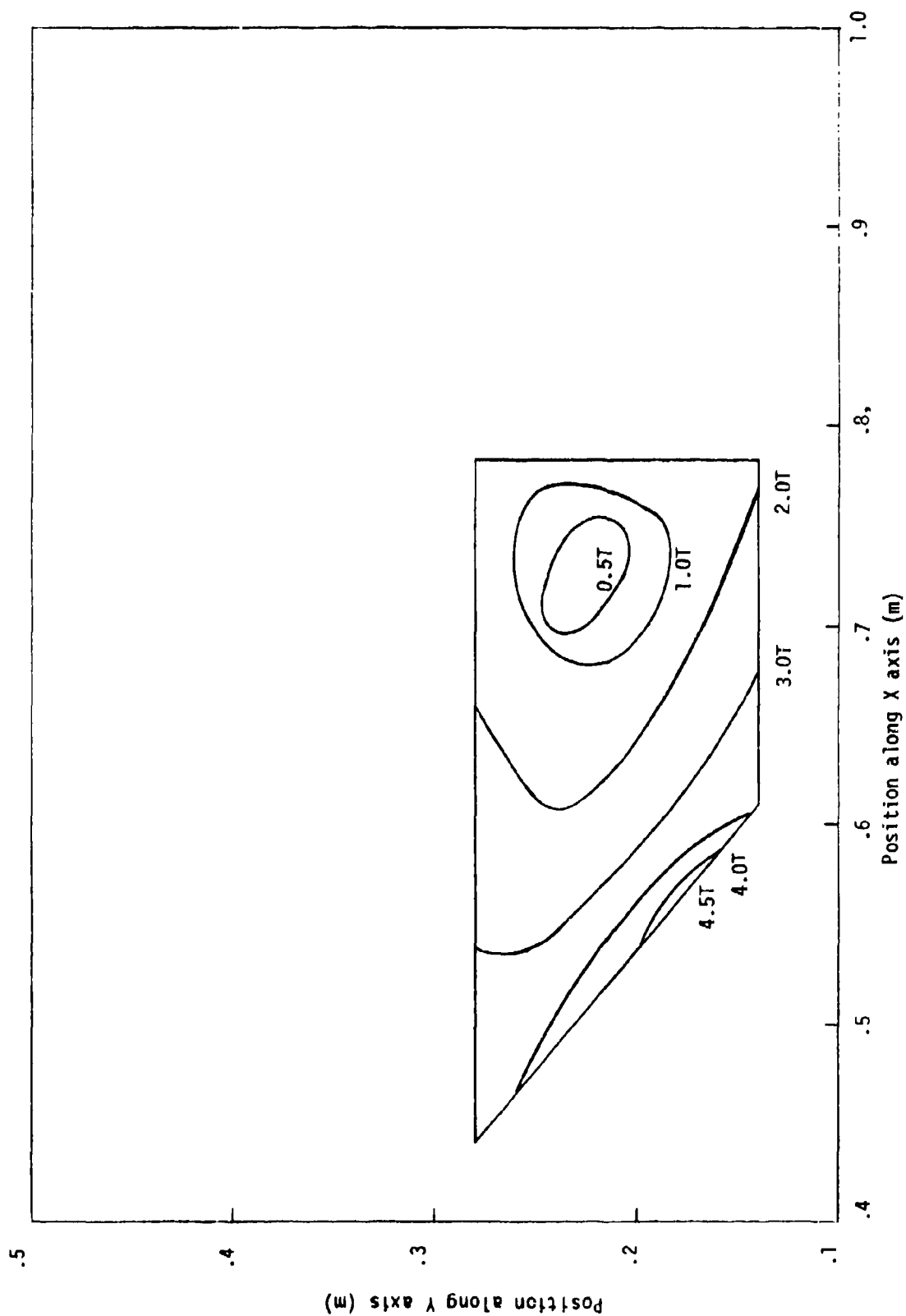


Figure 50 Contours of Constant Field in the Winding at the Inlet ( $Z = 0$ )  
for the 20 cm Design ( $j_c = 15 \text{ kA/cm}^2$ )



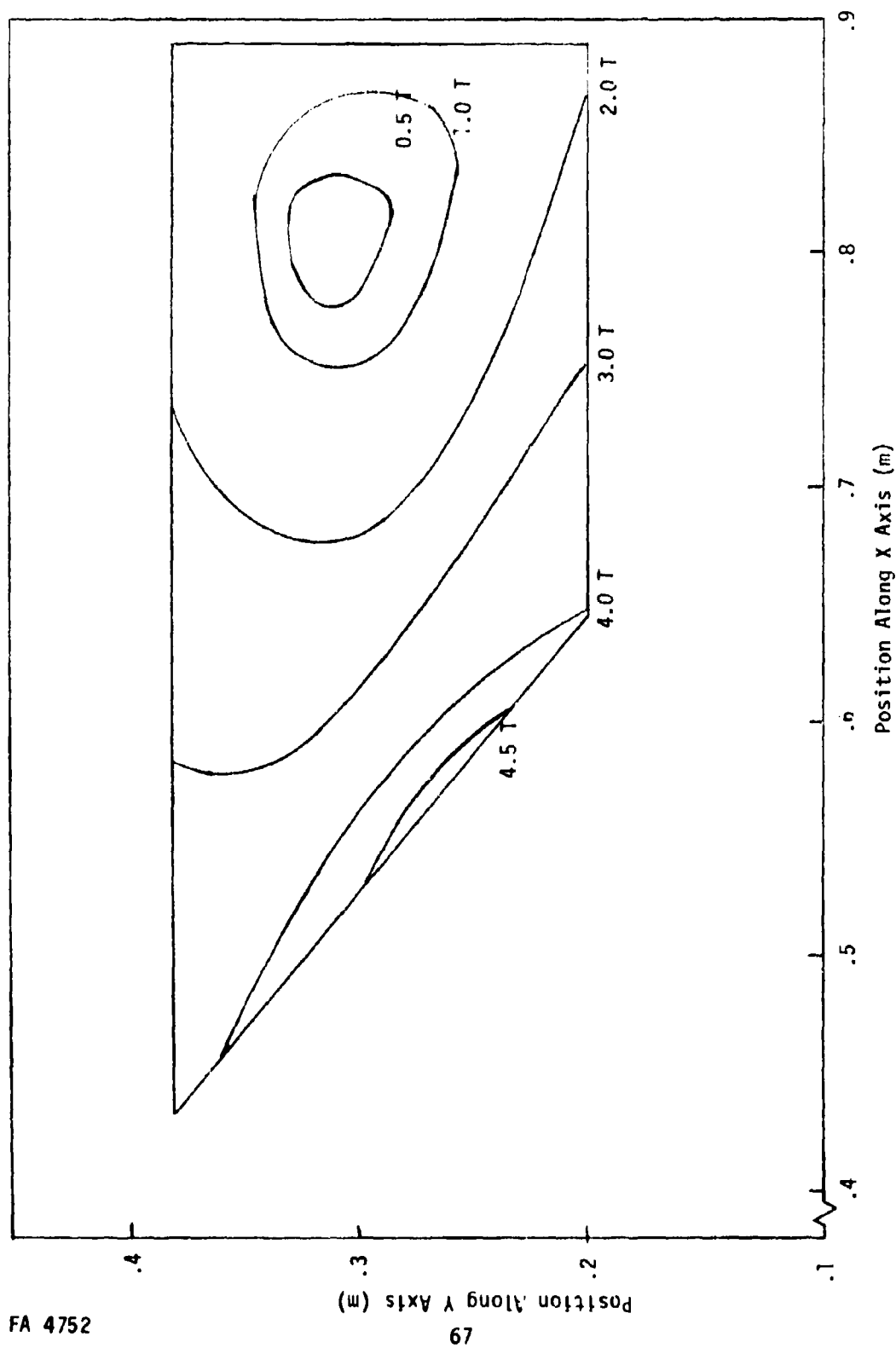


Figure 51 Contours of Constant Field in the Winding at the Inlet ( $Z = 0$ )  
for the 29 cm Design ( $j_c = 15 \text{ kA/cm}^2$ )

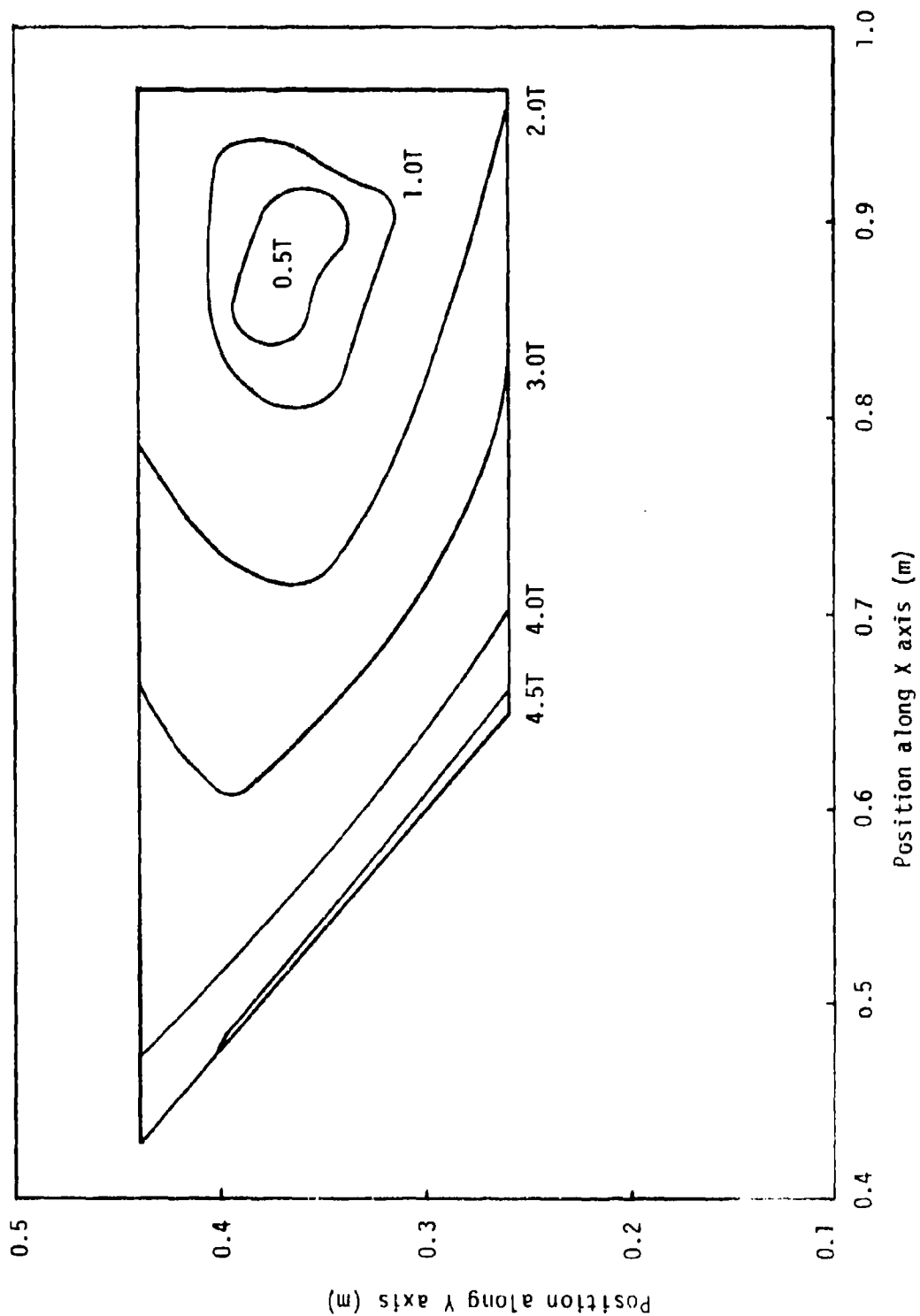


Figure 52 Contours of Constant Field for 40 cm Design ( $j_c = 15 \text{ kA/cm}^2$ )  
at Inlet ( $Z = 0$ )

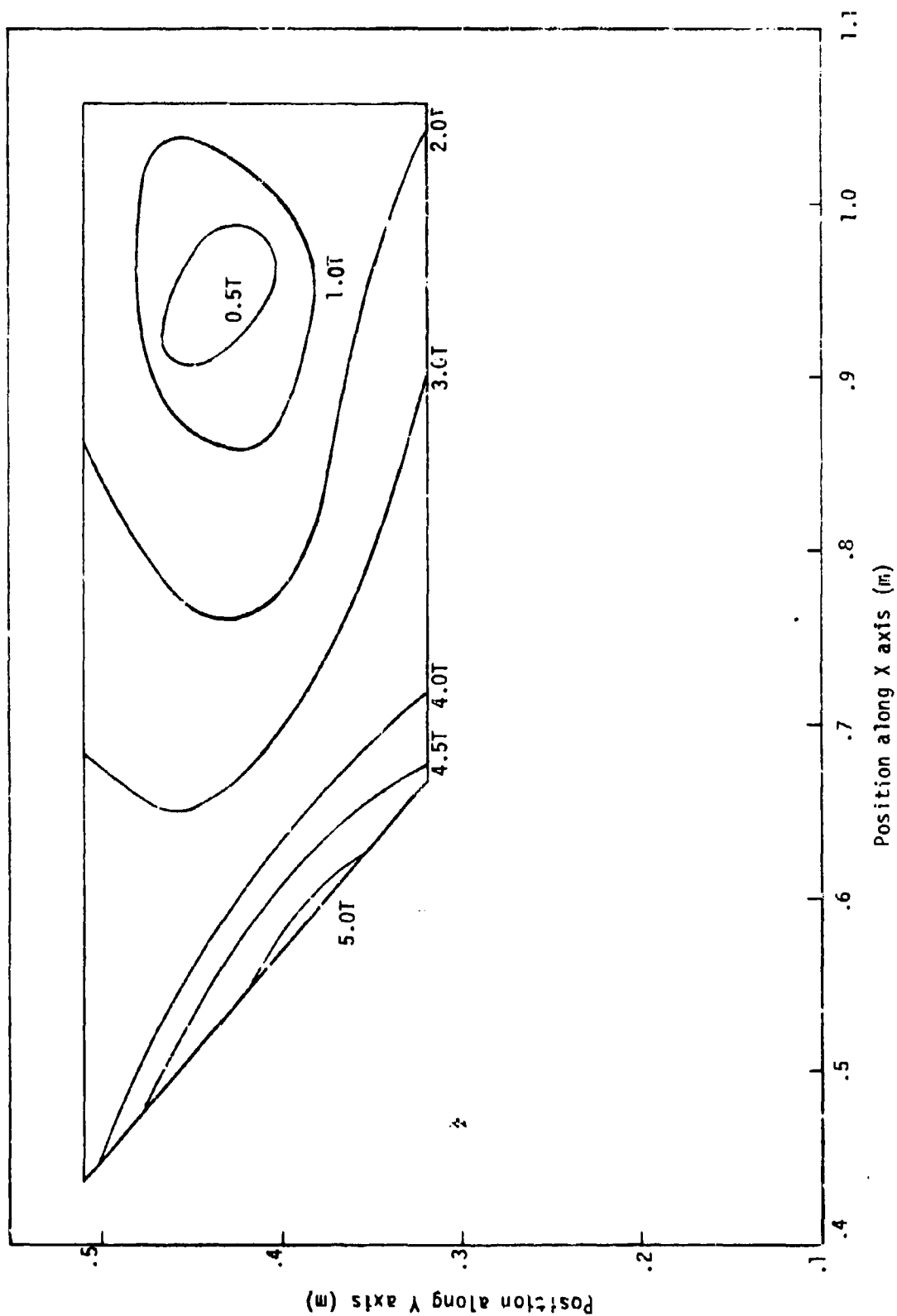


Figure 53 Contours of Constant Field in the Winding at the Inlet ( $Z = 0$ )  
for the 50 cm Design ( $j_c = 15 \text{ kA/cm}^2$ )

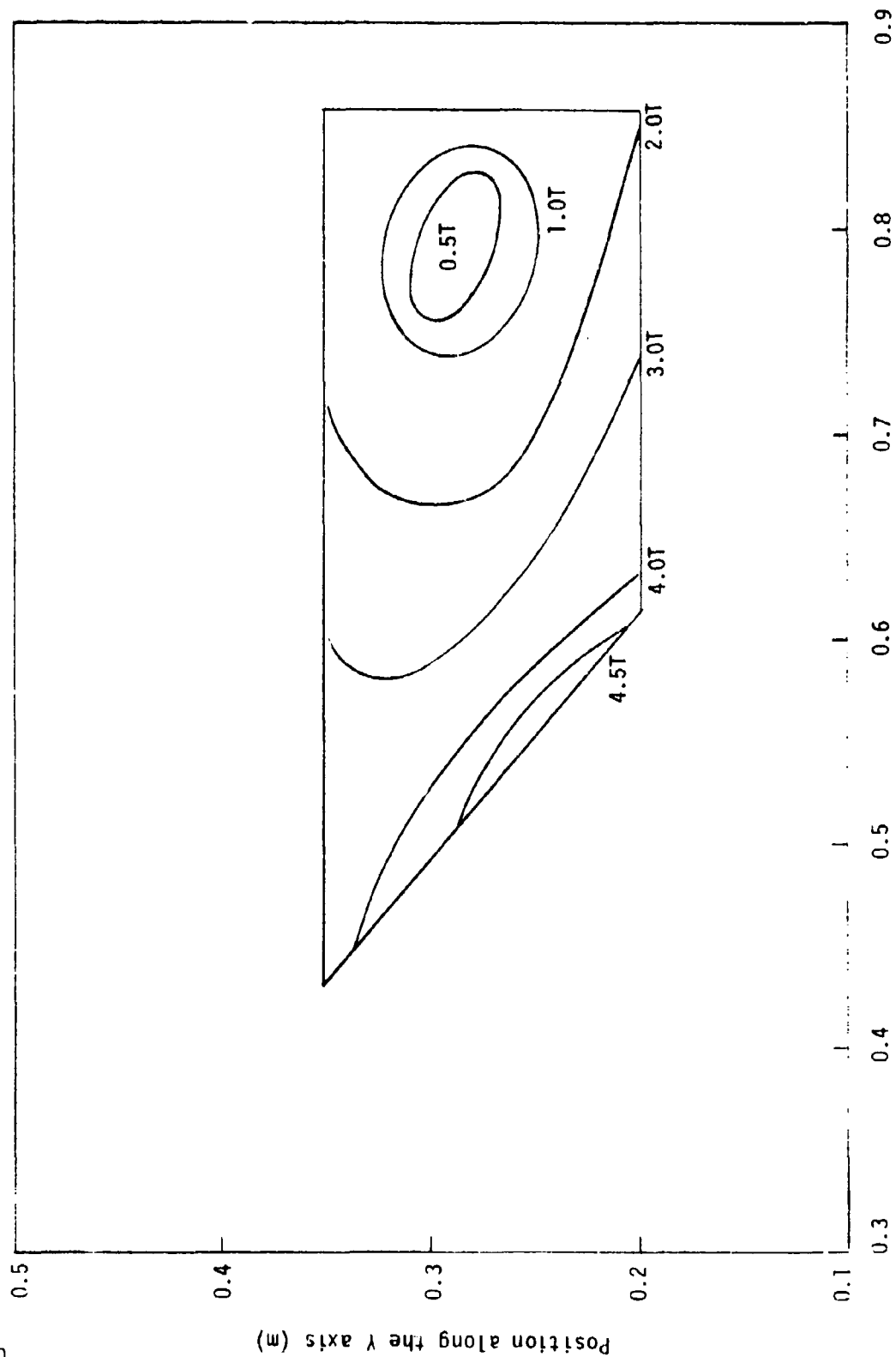


Figure 54 Contours of Constant Field for 29 cm Design ( $j_c = 30 \text{ kA/cm}^2$ ) at Inlet ( $Z = 0$ )

The filament model was refined further in order to calculate the maximum field in the windings. This value is important in the conductor design and enters into the stability considerations. The midpoint of the inlet end turn crossover was chosen as the primary search plane. The contours of constant field magnitude for the four sizes at a current density of  $15,000 \text{ A/cm}^2$  are shown in Figures 50 through 53. The peak field for these sizes is approximately 4.8 T. During Phase II a more detailed search will be performed. It is felt that the peak field will be found in the transition region between the straight sections and the crossover at the magnet inlet. Figure 54 shows the field contours for the 29 cm size at a  $30,000 \text{ A/cm}^2$  current density. The size of the winding envelope is different; however, the behavior is similar to the  $15,000 \text{ A/cm}^2$  case.

#### 4.0 CONDUCTOR DESIGN

A fully-transposed flat braided configuration was chosen as the basic conductor design. An integrally-braided conductor has much more dimensional stability than a flattened braid or cabled conductor. A fully-transposed design will equalize the strain on each strand of the conductor as it is wound as well as to allow for minimum induced losses due to alternating or changing fields. By tinning the strands before the braiding operation, then heating, a partially solder-filled conductor is effected. This results in an even more stable conductor shape.

This configuration is identical to a conductor MCA has been fabricating for use by Brookhaven National Laboratory. A choice of 97 strands was dictated by the capability of braiding machinery available. This conductor configuration represents the state-of-the-art and there are no new procedures which must be developed in order to manufacture it.

The braided unit is spiral-wrapped with a B-stage fiberglass-epoxy tape 5 mils thick. The conductor will be wound onto the magnet before this wet lay-up is cured. After curing, the winding will be permeable due to the many spaces in the 50 percent covered wrap allowing the helium into intimate contact with each strand of the braid. If the braid is half solder-filled, calculations show that the helium volume fraction is 25 percent. Approximately half of the helium volume is within the braid interstices. From a thermal standpoint, the interstitial helium makes the conductor appear as a composite with a greatly enhanced heat capacity. Local heating will vaporize this internal helium very quickly. Since the internal passages are very small, the gaseous helium cannot escape quickly to allow more liquid helium in. The net result is that internal helium will extract from the local energy perturbation its heat of vaporization, but once vaporize will not be effective in slowing the velocity of propagation of the normal front, if it exists. As will be discussed in

in Section 7.0, a higher velocity of propagation reduces the peak temperature and peak voltage that occur during a quench.

The braid dimensional stability and strength can be improved by full solder filling. Similarly, the chances of strand-to-strand motion would be reduced. However, the transient response to a temperature perturbation would be worsened by one hundred percent solder fill. In addition, replacing solder with helium will lower the system weight.

Wet winding the magnet and curing afterwards assures an excellent bond between the layers of conductor which provides for a very stable (physical) system. The advantages of a fully-potted winding are achieved, while also allowing for helium circulation in the conductor.

Ten mils of insulation, turn-to-turn, is electrically substantial. Calculations have shown the worst failure case to apply less than 2 volts/mil and this insulation can withstand far greater potentials than this. In order to maintain the local helium content in the windings no insulation should be removed despite the overprotection against electrical loads.

Figure 55 shows how each of the components of the conductor are integrated into the final configuration.

To investigate the effect of conductor current density the magnet designs were carried out with two conductors, nominally 15,000 A/cm<sup>2</sup> and 30,000 A/cm<sup>2</sup> current densities. As each braid had 97 strands, the strand sizes were chosen to achieve the desired current density. Referring to Table 8, the strand sizes selected were 16 mil diameter and 12 mil diameter round wire.

The copper-to-superconductor ratio is determined by the desired current versus field and temperature characteristic for the conductor. At a flux density of 5.6 Tesla and a temperature of 4.2 K, the 15 kA/cm<sup>2</sup> braid with a copper-to-superconductor ratio of 5.0:1 has a critical current of 3420 A; at the operating current of 2000 A, this is a 0.58 fraction of critical. The 30 kA/cm<sup>2</sup> braid

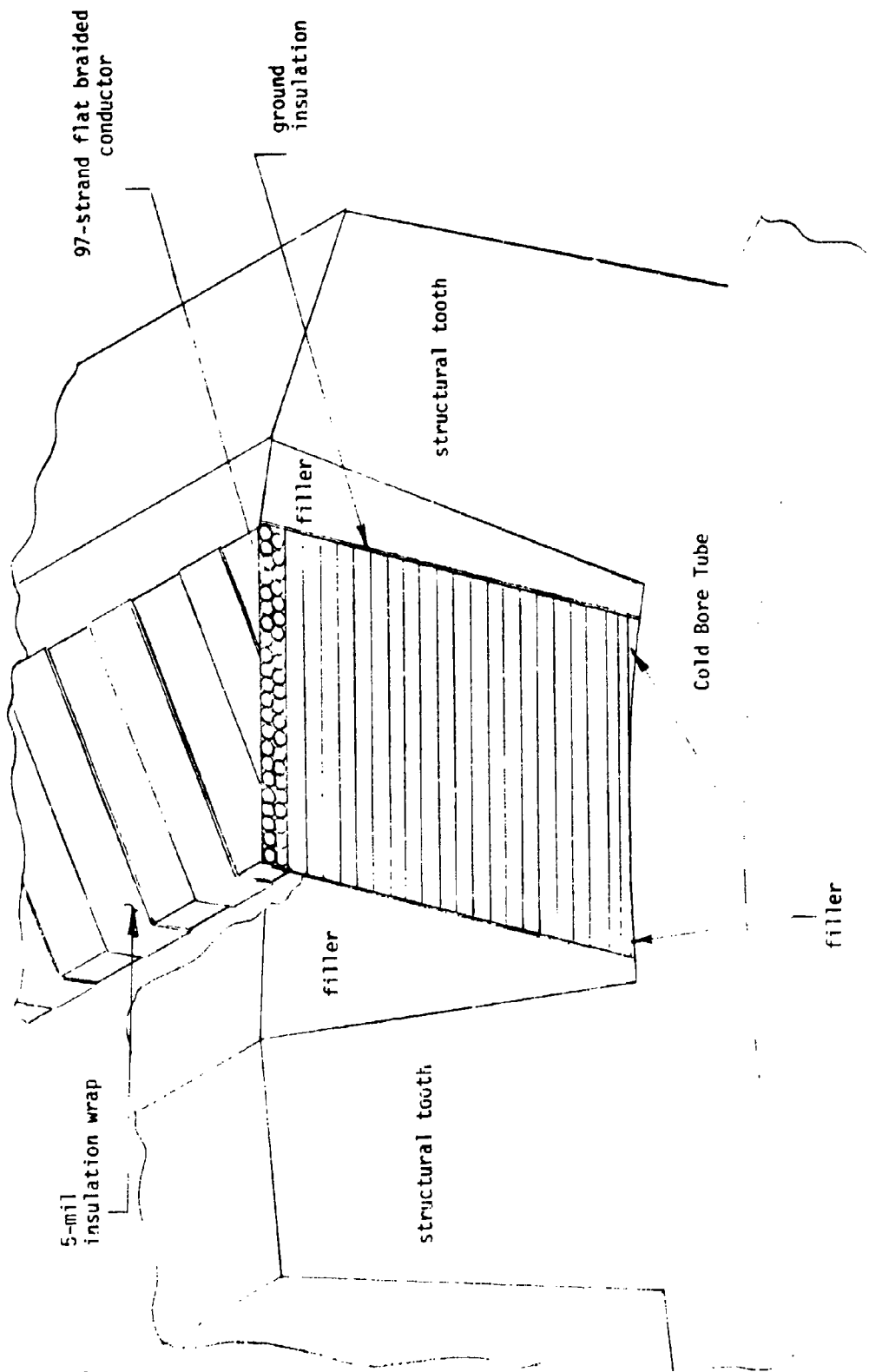


Figure 55 Typical Conductor Bundle Showing Relationship to Structural Teeth and Cold Bore Tube



TABLE 8  
CONDUCTOR SPECIFICATIONS

	<u><math>j_{\text{cond}} = 15 \text{ kA/cm}^2</math></u>	<u><math>j_{\text{cond}} = 30 \text{ kA/cm}^2</math></u>
<u>Strand Configuration</u>		
Diameter, mm	0.4064	0.3048
CuSC ratio	5.0:1	3.0:1
Number of filaments	138	207
Filament diameter ( $\mu\text{m}$ )	14.1	10.6
<u>Guaranteed Performance</u>		
Critical Current at 3T, A	60	51
Critical Current at 4T, A	48	41
Critical Current at 5T, A	40	34
Critical Current at 6T, A	32	27
<u>Braid Configuration</u>		
Number of strands	97	97
Width, mm	0.847	0.635
Thickness, mm	21.84	16.38
Insulation thickness, mm	0.127	0.127
Operating current, $I_{\text{op}}$ , A	2000	2000
Critical Current, $I_{\text{c}}$ , A	3420	2900
$I_{\text{op}}/I_{\text{c}}$	0.58	0.69

operates at 0.69 fraction of its 2900 A critical current exposed to the same 5.6 T, 4.2 K environment.

The number of filaments is chosen by consideration of manufacturing requirements and the filament diameter is determined by the reduction of area from the initial billet to the final strand size. The adiabatic stability criterion for filament diameter is then applied to assure conductor performance in the anticipation of flux jumps.

The physical dimensions of the braid are determined by the geometry and size of constituent parts after the braiding and compacting operations are completed. To further assure the dimensional stability of the conductor, it is compacted to 68%. A 100% compaction corresponds to a cross section with no interstitial space. This is within the range of compaction achieved on similar braided conductors and has not produced any indications of strand damage. The braid is then heated, allowing the solder coating to bond the strands together. The insulation is applied just before the conductor is wound into the saddle shape.

Table 9 gives a more complete description of the conductor operation over a range of field and currents experienced in the magnet. These design limits were derived from data supplied by the Hiconductor Division of MCA and represent achievable operating conditions on wire supplied by them.

The two conductors are very similar. In order to make a choice between them, it is necessary to weigh the additional risk of operating at a higher current density against the advantage of a lighter, smaller magnet system.

The higher current density operation results in a smaller magnet, with less structure and a smaller dewar. It is possible to reduce the total system weight by 40 percent over the weight of a system utilizing a physically larger conductor. That larger conductor, however, is also a much more stable design. In the event of a local normal region, a conductor can return to the superconducting state if the available cooling is greater than the heat generation.

TABLE 9  
CONDUCTOR DESIGN LIMITS

Operating Current = 2000 A

Critical Current at Maximum Field (5.6 T)

30 kA/cm<sup>2</sup> Conductor = 2900 A

15 kA/cm<sup>2</sup> Conductor = 3450 A

$I_{\text{operating}}/I_{\text{critical}}$

30 kA/cm<sup>2</sup> Conductor = 0.69

15 kA/cm<sup>2</sup> Conductor = 0.58

CRITICAL TEMPERATURE DEPENDENCE

<u>B</u>	<u>I<sub>op</sub></u>	Critical Temperature	
		15 kA/cm <sup>2</sup> Conductor	30 kA/cm <sup>2</sup> Conductor
5.6 T	2.0 kA	5.34 K	5.04 K
	1.5	5.73	5.50
	1.0	6.12	5.97
5.0	2.0	5.52	5.25
	1.5	5.86	5.67
	1.0	6.21	6.08
4.0	2.0	5.76	5.54
	1.5	6.05	5.88
	1.0	6.33	6.22
3.0	2.0	5.99	5.82
	1.5	6.22	6.09
	1.0	6.45	6.36

Surface heat fluxes of 0.5 to 1.0 W/cm<sup>2</sup> have been reported for windings with small integral channels for the helium; calculations indicate the proposed 15 kA/cm<sup>2</sup> conductor will generate 0.50 W/cm<sup>2</sup> heat in a normal region. This is small enough that local cooling should be sufficient to allow the conductor to return to the superconducting state. In the 30 kA/cm<sup>2</sup> conductor, however, the calculated heat generation is over 1.3 W/cm<sup>2</sup>, indicating that a normal region will heat up and propagate due to the insufficient cooling available.

The higher current density conductor is less well-protected from transient heating with a lower critical temperature versus operating condition than the larger conductor. It is also not well-protected in the event of a local hot spot forming. The necessity of protecting the conductor from small thermal pulses (as from friction during slip) has been established and in that light the high current density conductor is not acceptable.

The choice of constituent materials was made only after careful consideration of many choices. A copper-stabilized, multifilamentary, Niobium Titanium conductor was selected due to its ability to meet all system requirements at low cost with proven manufacturing and design techniques. Table 10 denotes some of the considerations made in determining which conductor system best met system requirements.

The candidate materials for use as a stabilizer were copper and aluminum. Copper is a strong, readily-available metal which has become the industry standard for superconductor applications. Aluminum offers the advantages over copper of being lightweight and, at high magnetic fields, having lower resistivity.

Extensive experience with copper allows the confident analysis of its application as a substrate. The mechanical, thermal, and electrical performance of the conductor can all be accurately evaluated so as to minimize the required safety factors. The structure required to support the conductor need

TABLE 10  
ADVANTAGES AND DISADVANTAGES OF VARIOUS STABILIZER  
AND SUPERCONDUCTOR MATERIALS

<u>Stabilizer</u>	<u>Advantages</u>	<u>Disadvantages</u>
Copper	<ul style="list-style-type: none"> <li>- Readily Available</li> <li>- Greater Mechanical Strength</li> <li>- Extensive Manufacturing Experience</li> </ul>	<ul style="list-style-type: none"> <li>- High Density</li> </ul>
Aluminum	<ul style="list-style-type: none"> <li>- Low Density</li> <li>- Lower Magnetoresistance</li> </ul>	<ul style="list-style-type: none"> <li>- Very High Purity Required</li> <li>- Not Readily Available</li> <li>- Low Mechanical Strength</li> <li>- High Cost</li> <li>- Difficult to Bond to Superconductor</li> </ul>
<u>Superconductor</u>		
NbTi	<ul style="list-style-type: none"> <li>- Readily Available</li> <li>- Extensive Manufacturing Experience</li> <li>- Ductile</li> </ul>	<ul style="list-style-type: none"> <li>- Lower Critical Temperature</li> <li>- Lower Critical Field</li> </ul>
Nb <sub>3</sub> Sn	<ul style="list-style-type: none"> <li>- High Critical Temperature</li> <li>- High Critical Field</li> </ul>	<ul style="list-style-type: none"> <li>- Developmental</li> <li>- Manufacturing Technique Still Experimental</li> <li>- Brittle</li> </ul>

not be overdesigned in order to guard against design errors due to inexperience with the material. An aluminum for stabilizer use must be of a high purity. As such, it is a difficult material to characterize. Due to the lack of experience with this stabilizer, a conservative design philosophy must be followed. Thus, the disadvantages of using copper can be minimized.

The high purity of aluminum necessitates expensive production methods. A manufacturer is at the mercy of the suppliers, with little confidence in delivery dates or quality of materials but sure of its great cost.

Once obtained, the aluminum is difficult to handle. It is very soft, and any impurities can greatly deteriorate its properties. Bonding the aluminum to the superconductor is a process which is difficult at best. The best stabilizer is of little value should there be no bond between it and the superconductors. Even joining the aluminum to itself presents difficulties; although it is done regularly, copper is much easier to work with.

Admittedly, the weight savings possible by utilizing the aluminum is attractive. The contribution of the conductor to the total system weight is appreciable and using aluminum stabilizer will reduce that contribution by a factor of 2.5. This only reduces the system weight by 30 percent which does not justify the much greater risk, manufacturing problems or supply problems inherent in the selection of aluminum as the stabilizer.

The choice of a superconductor is not so limited. The original search for candidate materials included thirteen possibilities. Availability of quantities of the material then reduced the choice to either Niobium Titanium (NbTi) or Niobium Tin (Nb<sub>3</sub>Sn) which are produced by industry. The advantage of a potential weight savings can only be accomplished by using a higher current density in one conductor than the other as the densities are almost identical.

$\text{Nb}_3\text{Sn}$  has a higher critical temperature and critical field than  $\text{NbTi}$ . System operation at 4.2 K provides a large margin for the  $\text{NbTi}$ , which has a  $T_c = 9.5$  K. The advantage of  $\text{Nb}_3\text{Sn}$  having a  $T_c$  of 18 K cannot be considered very great in light of the margin available with  $\text{NbTi}$ . Comparing critical current density at temperature and field, the  $\text{Nb}_3\text{Sn}$  can carry about 5 times as much current in a similar cross-section of conductor. To operate at the same fraction of critical current only 20% of the superconductor is required. This results in a 10-14 percent reduction in conductor weight, and only a marginal reduction in total system weight.

The developmental nature of  $\text{Nb}_3\text{Sn}$  requires conservative design philosophy similar to that required in the analysis of a high purity aluminum stabilizer. This would negate some of the advantage gained by the weight savings of using less conductor.

The handling problems associated with the use of  $\text{Nb}_3\text{Sn}$  are legion. Manufacturing methods and handling techniques are in developmental stages at this time. The use of a prereacted conductor is not feasible due to the intricate winding procedure and concomitant strain which might fracture the filaments of superconductor. Winding the magnet with an unreacted conductor is attractive; the reaction involves heating the winding to 700 to 900 K which is far beyond any tolerable level for a fiberglass-epoxy insulation system. The possibility of fully-impregnating the magnet has been discarded due to the stability (helium inventory locally in the conductor) considerations discussed before.  $\text{NbTi}$  is ductile and readily handled by ordinary wire processing means. So much  $\text{NbTi}$  has been produced that manufacturers are very confident in their procedures and ability to supply multifilamentary forms in quantity.

The small advantage in weight savings of using  $\text{Nb}_3\text{Sn}$  cannot make up for the multitude of problems associated with manufacturing and handling the material.  $\text{NbTi}$  is readily available at reasonable cost for use in magnets wound

by familiar techniques. This is the clear choice for use in a coil which is being built to test marginal structural support techniques.



## SECTION V

### STRUCTURAL DESIGN

The structure for an MHD magnet system is required to contain the Lorentz body forces produced by and acting on the windings. Additional requirements, such as limiting the winding deflections, may also be imposed by considerations of conductor stability or conductor strain.

The Lorentz body force components acting on a typical annular saddle winding are illustrated in Figure 56. The straight sections of the winding experience loading that is primarily circumferential. There is also a small radial loading, but the ratio of the maximum circumferential to the maximum radial load at the midplane is approximately ten to one. For a tapered system the straight sections also experience a small component of load in the axial direction. The end turn crossovers experience axial and radial loading with little or no circumferential component.

The structure to contain the loads can be classified by the component that it is designed to carry. That is, the structural elements will be defined as: radial, circumferential, and axial.

Figure 57 illustrates the basic structural support concept for a quadrant of the magnet system at the midplane. The major structural components are: cold bore tube, interbundle teeth, outer helium vessel, and the external ring.

The circumferential load acting on a bundle is picked up by the structural interbundle tooth and transmitted to the cold bore and outer helium shells. The shells carry this load in compression to the centerline between magnet halves where it is equilibrated by the loads from the quadrant's mirror image. The radial loads are picked up by the outer helium vessel and external ring and carried in bending to the planes of symmetry. The external rings also serve as stiffeners to the shells and teeth and experience additional loading due to the tendency of the shells to deform to an egg-shaped position.

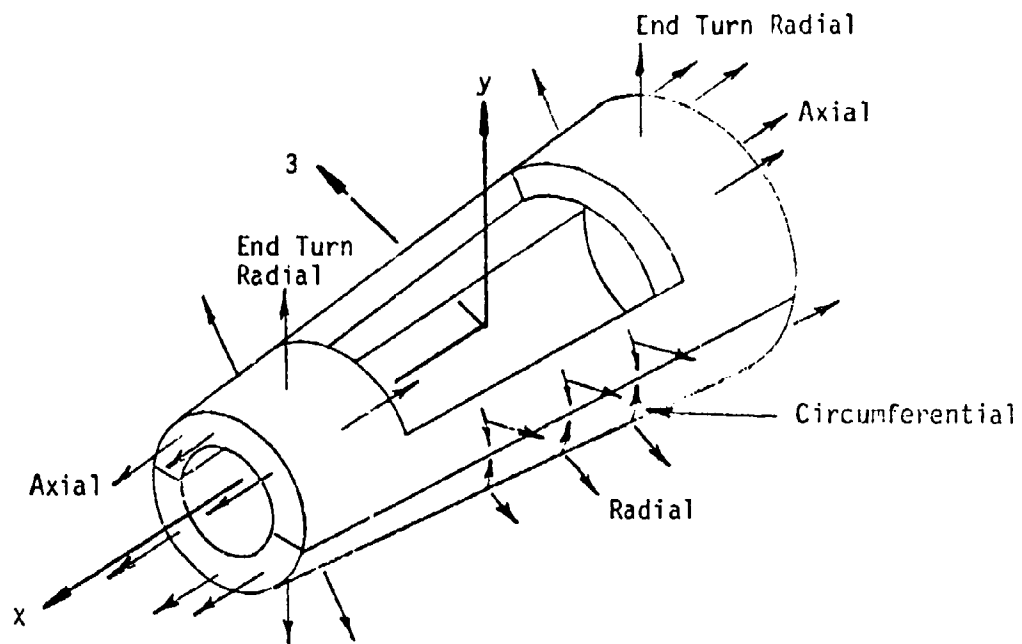


**Figure 56** Force Components on Saddle Winding

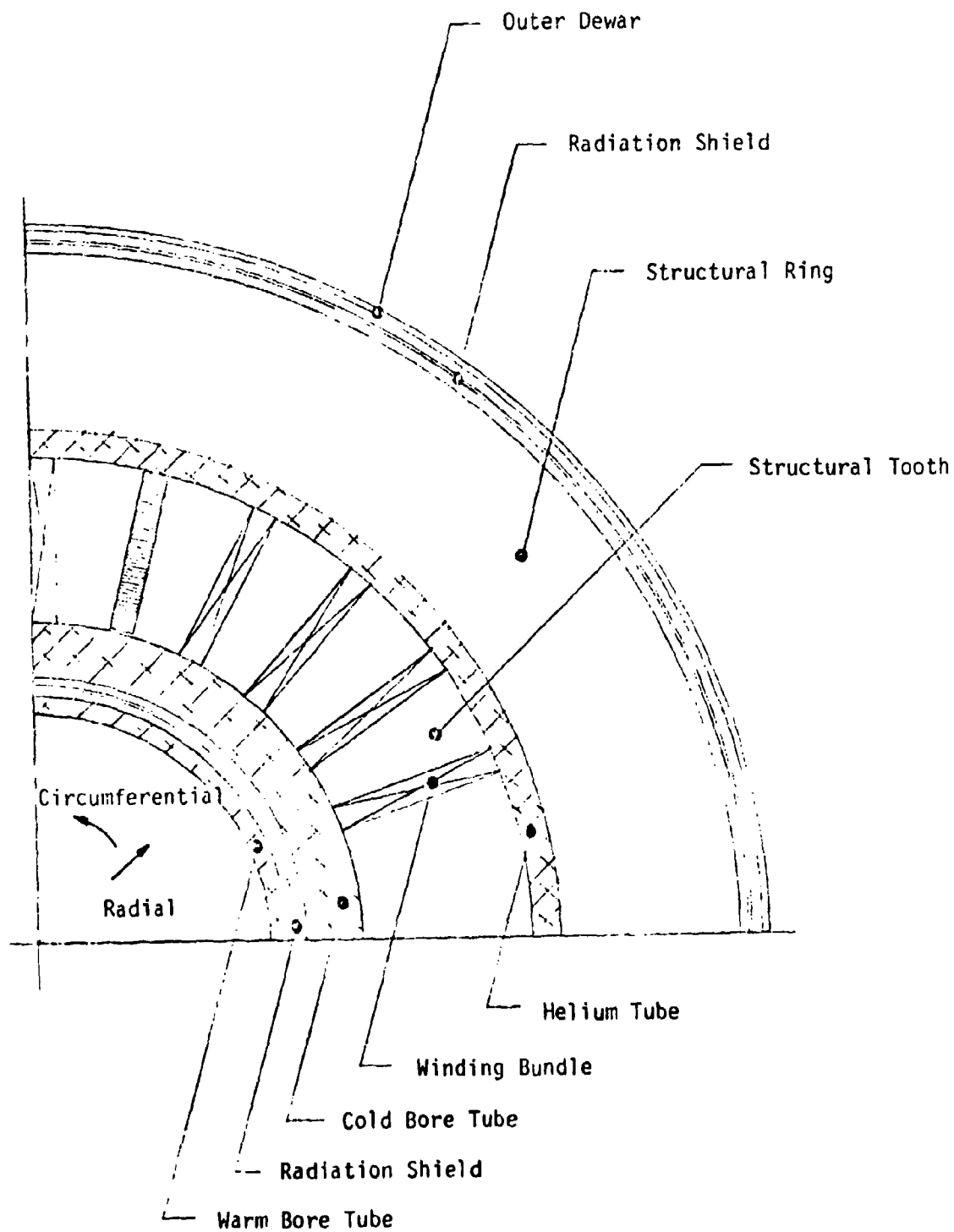


Figure 57 Quarter Section of Magnet Design at Midplane

The axial load is transmitted to the cold bore tube and outer helium vessel by the teeth in the end turn region. The end turn radial loading is carried by the ring stiffeners in the end turn region.

During Phase I several candidate structural materials were considered. Table 11 lists the materials and some of the mechanical properties at cryogenic temperatures. The candidates include two stainless steels and three aluminums. Also included are the properties of the conductor bundle constituents. The properties included are: density, modulus of elasticity, ultimate stress, working or design stress, specific modulus (density to modulus ratio), and specific stress (density to working stress ratio). The latter two entries serve as figures of merit.

The design or working stress is determined by taking the minimum of one-third of the ultimate stress or two-thirds of the yield stress at cryogenic temperatures. For 310S stainless steel, OFHC copper, glass-epoxy, 6061-T6 aluminum, and 2014-T6 aluminum the working stress is based on the ultimate. For the remainder, the yield stress criteria is used. The properties are tensile properties. An additional factor of one-half is used on the working stress for the design shear stress (i.e., the Maximum Shear Stress Theory). These factors imposed are consistent with the ASME Division 2 codes.

The two figures of merit are used since a stress limited design is governed by the specific stress and a deflection limited design by the specific modulus. That is, the structural weight can be written as a ratio of the density to limiting factor (stress or deflection) times the loading and geometry. Therefore, a low specific modulus and/or specific stress is sought. The two aluminums, 6061-T6 and 2014-T6, possess the best figures of merit. The 6061-T6 was chosen as the primary structural material on the basis of a deflection limited design.

The individual structural components were sized and component weights calculated for both stress limited and deflection limited designs. For example,

TABLE 11  
MATERIAL PROPERTIES FOR CANDIDATE MATERIALS

Material	Density kg/m <sup>3</sup> (lbs/in <sup>3</sup> )	Modulus GN/m <sup>2</sup> (10 <sup>6</sup> psi)	Ultimate* MN/m <sup>2</sup> (ksi)	Working Stress MN/m <sup>2</sup> (ksi)	Density ÷ Modulus 10 <sup>-8</sup> sec <sup>2</sup> /m <sup>2</sup> (in <sup>-1</sup> )	Density ÷ Working Stress 10 <sup>-5</sup> sec <sup>2</sup> /m <sup>2</sup> (in <sup>-1</sup> )
310S Stainless	7810 (.282)	207 (30)	1300 (188.5)	433 (60.3)	3.77 (.94)	1.80 (.45)
304L Stainless	7860 (.284)	201 (29.2)	1620 (235)	358 (51.9)	3.91 (.99)	2.20 (.55)
6061-T6 AL	2750 (.100)	86.9 (12.6)	572 (83.0)	191 (27.7)	3.16 (.79)	1.44 (.36)
2014-T6 AL	2750 (.100)	82.0 (11.8)	814 (118)	271 (39.3)	3.35 (.85)	1.01 (.25)
5083-0 AL	2750 (.100)	(82.8) (12.0)	556 (80.6)	119 (17.2)	3.37 (.86)	2.3 (.58)
NbTi	6030 (.218)	80.8 (11.6)	6900 (1000)	138 (20)	7.46 (1.88)	4.37 (.109)
OFHC Copper	8890 (.321)	149 (21.6)	500 (72.0)	167 (24.2)	5.97 (1.49)	5.32 (.133)
Glass/Epoxy	1950 (.070)	74.0 (10.73)	1744 (253)	581 (84.3)	2.64 (.65)	.34 (.083)

Figure 58 shows the weight of the axial structure versus the allowable deflection for each of the four magnet sizes. The weights for the stress limited design range from 10 to 30 kg and, hence, these points do not show on the figure. A reasonable limit of approximately 1.0 mm will yield structural weights of 40 to 110 kg.

The next analysis performed was of the structure required to carry the end turn crossover radial loading. Figure 59 shows the weight of the structure required versus allowable deflection for the four sizes assuming an equivalent radial pressure loading is carried by membrane tension. The equivalent pressure is approximately  $.8 \text{ MN/m}^2$  (120 psi) and is relatively insensitive to scale. Further analyses that take into account the nonuniformity of the loading (i.e., nonconstant pressure) and induced bending in the structure were performed and structure weights versus allowable deflection are shown in Figure 60. The model used was a box beam section with the cold bore tube and outer helium vessel as the top and bottom plates.

The major analysis effort was concerned with the transverse structure, that is, the structure that carries the circumferential and radial loads in the magnet straight sections. If the winding is assumed to be a cosine  $\theta$  distribution of current density, expressions can be derived for the maximum displacement and maximum stress in the external supporting structure.<sup>1</sup> The deflection and stress are functions of the central bore energy density, the magnet radius, and the structure moment of inertia and material.

Figures 61 and 62 present the maximum radial deflection at the design stress limit of the external ring stiffener versus magnet size for various ring height to inner radius ratios. Figure 61 presents the curves for an aluminum structure;

---

<sup>1</sup> Z. J. J. Stekly and Richard J. Thome, Electromagnetic Loading of Dewar Shell as a Result of Time Varying Magnetic Field, Fourth International Conference on Magnet Technology, Brookhaven National Laboratory, Upton, New York, Sept. 1972.

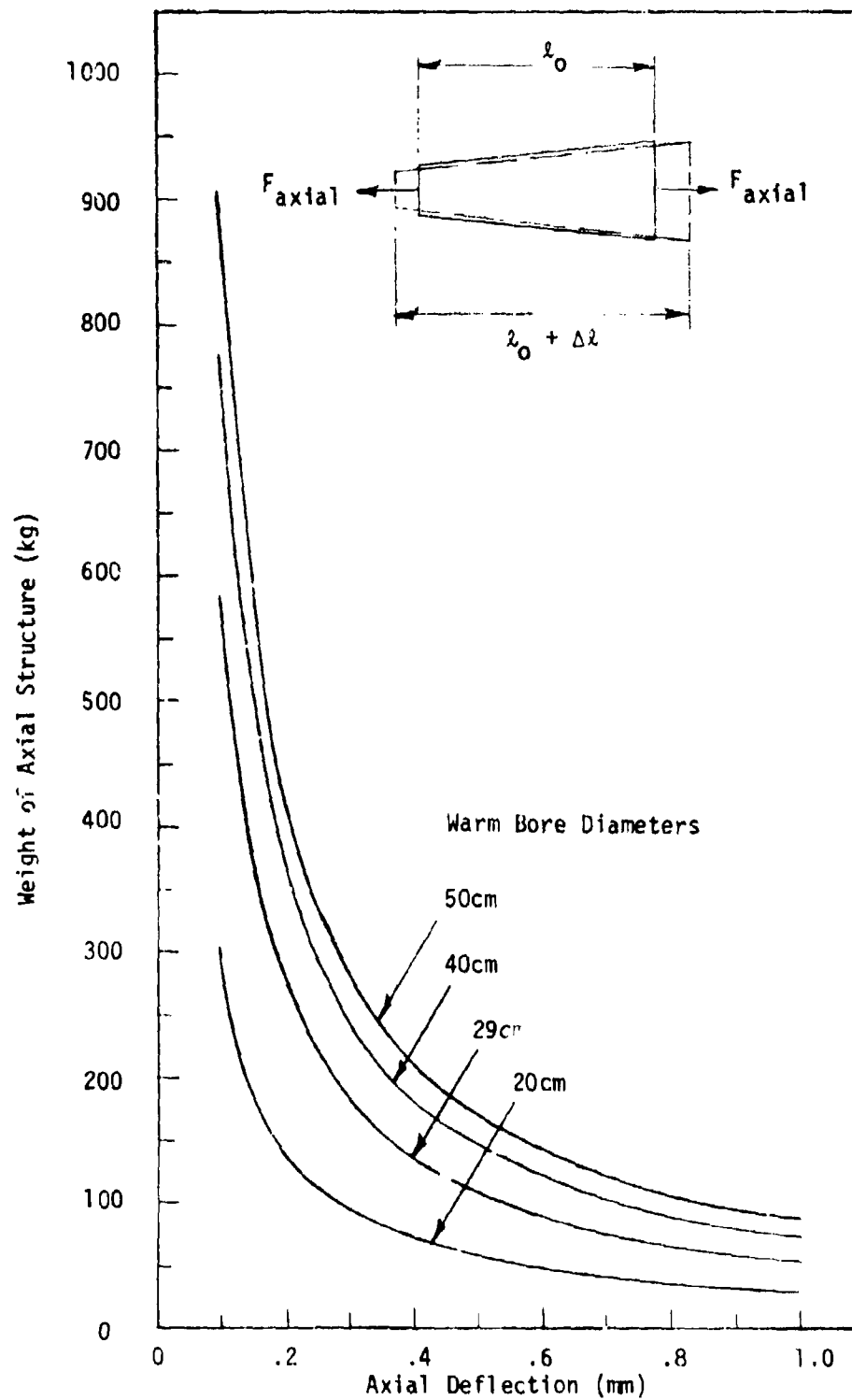


Figure 58 Weight of an Aluminum Axial Structure vs. Allowable Deflection for Various Warm Bore Sizes

FA 4728

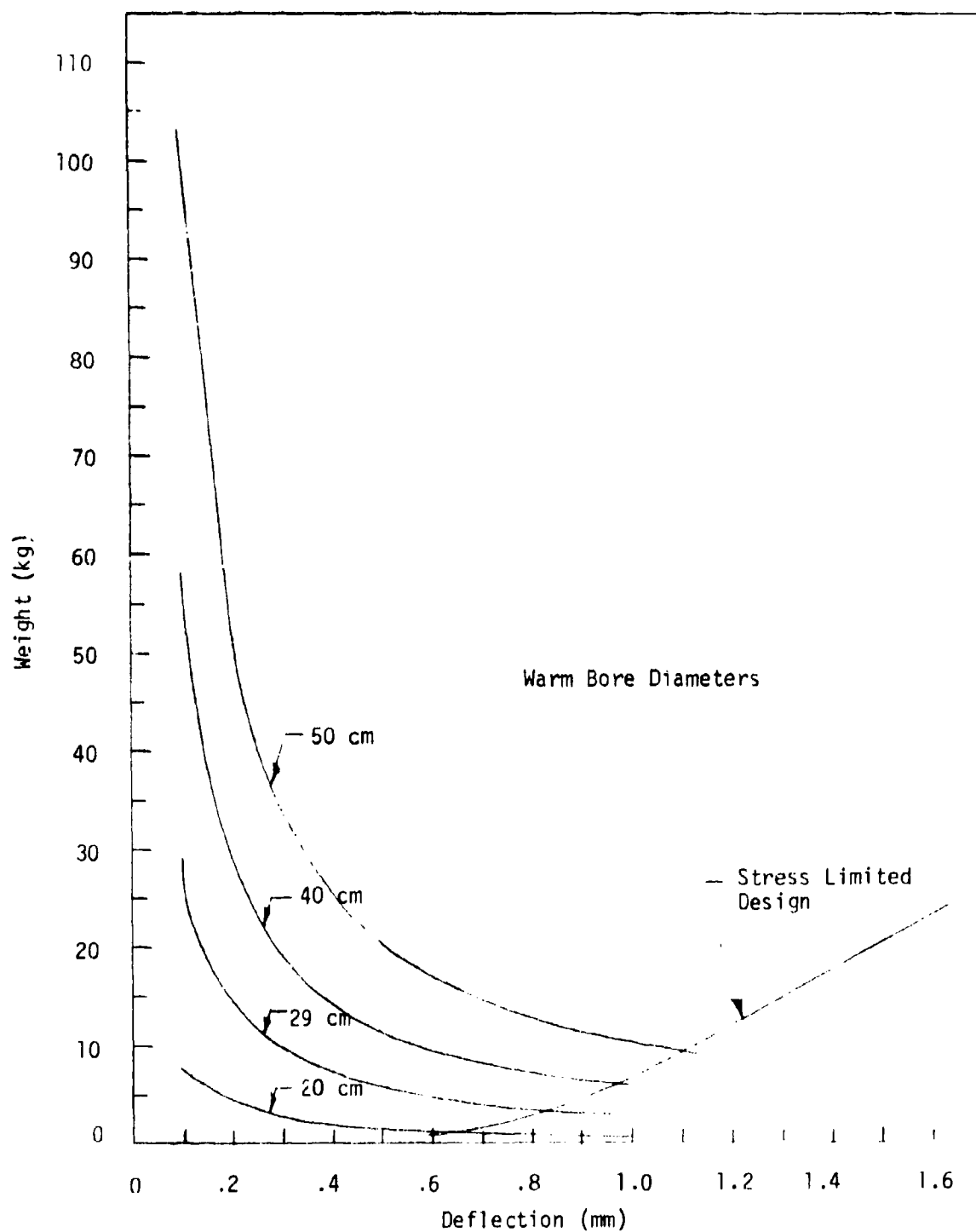


Figure 59 End Outer Shell Weight vs. Radial Deflection Membrane



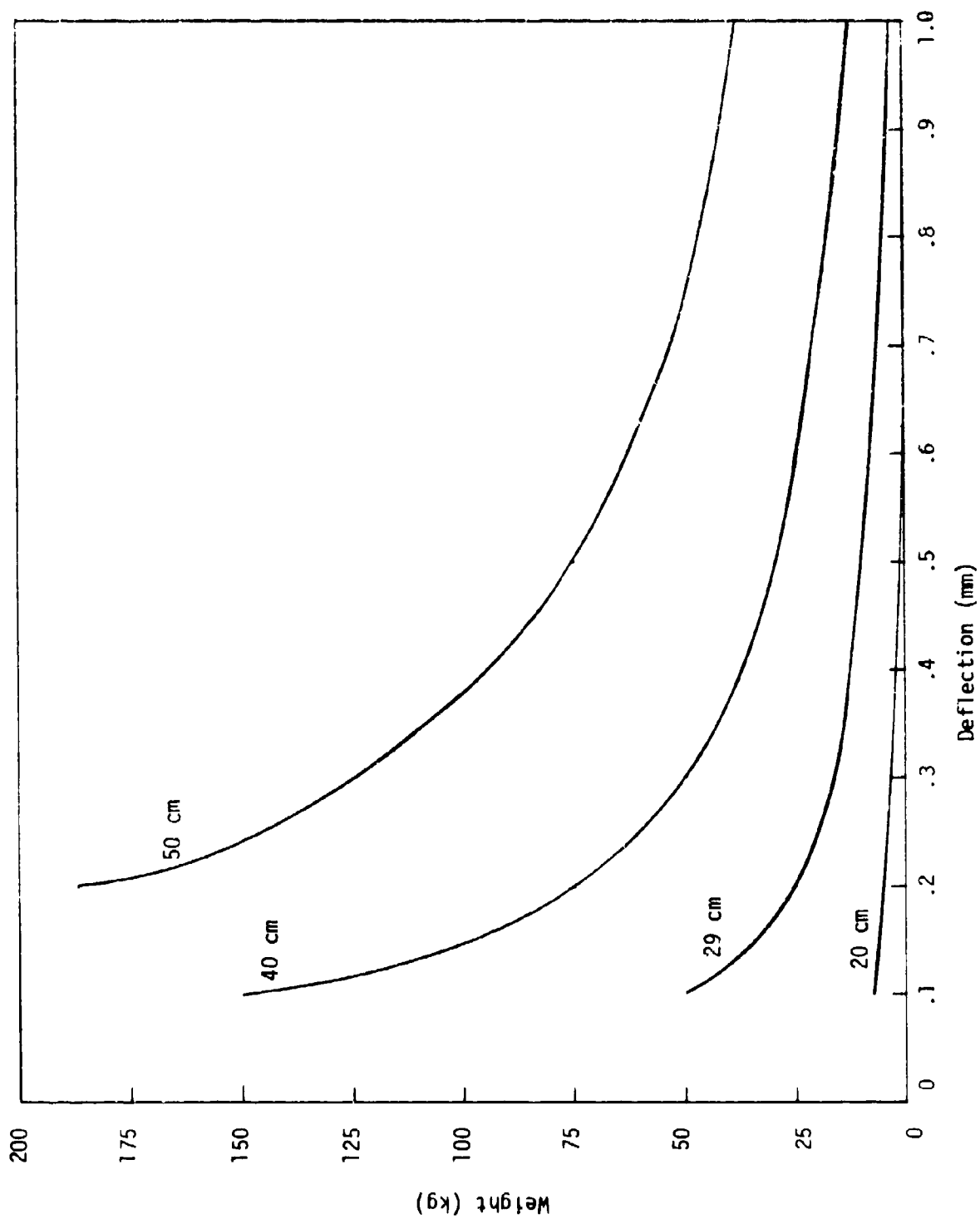


Figure 60 Weight vs. Deflection for a Stress Limited Design

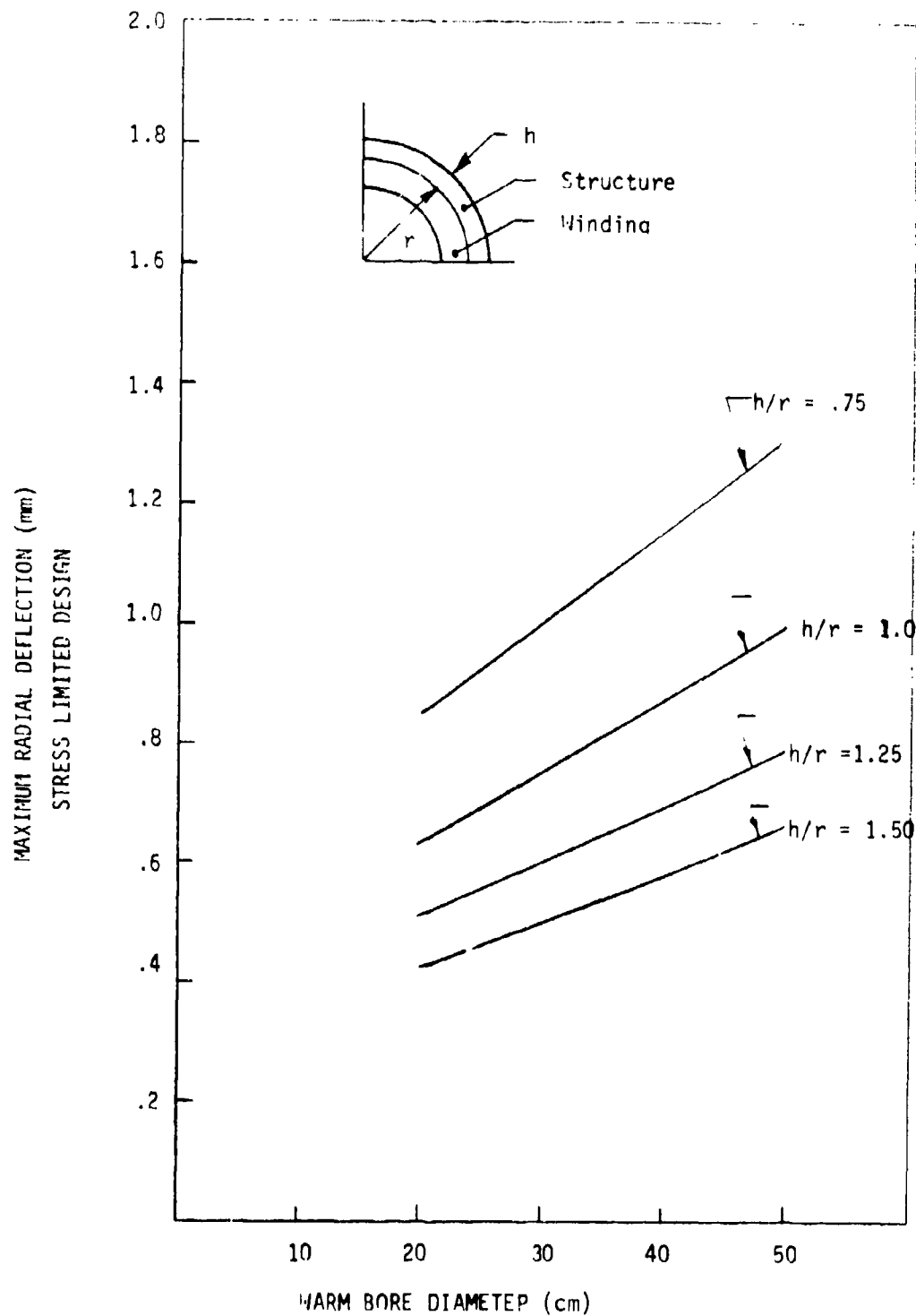


Figure 61 Maximum Radial Deflection vs. Warm Bore Diameter for an Aluminum Structure  
FA 4708

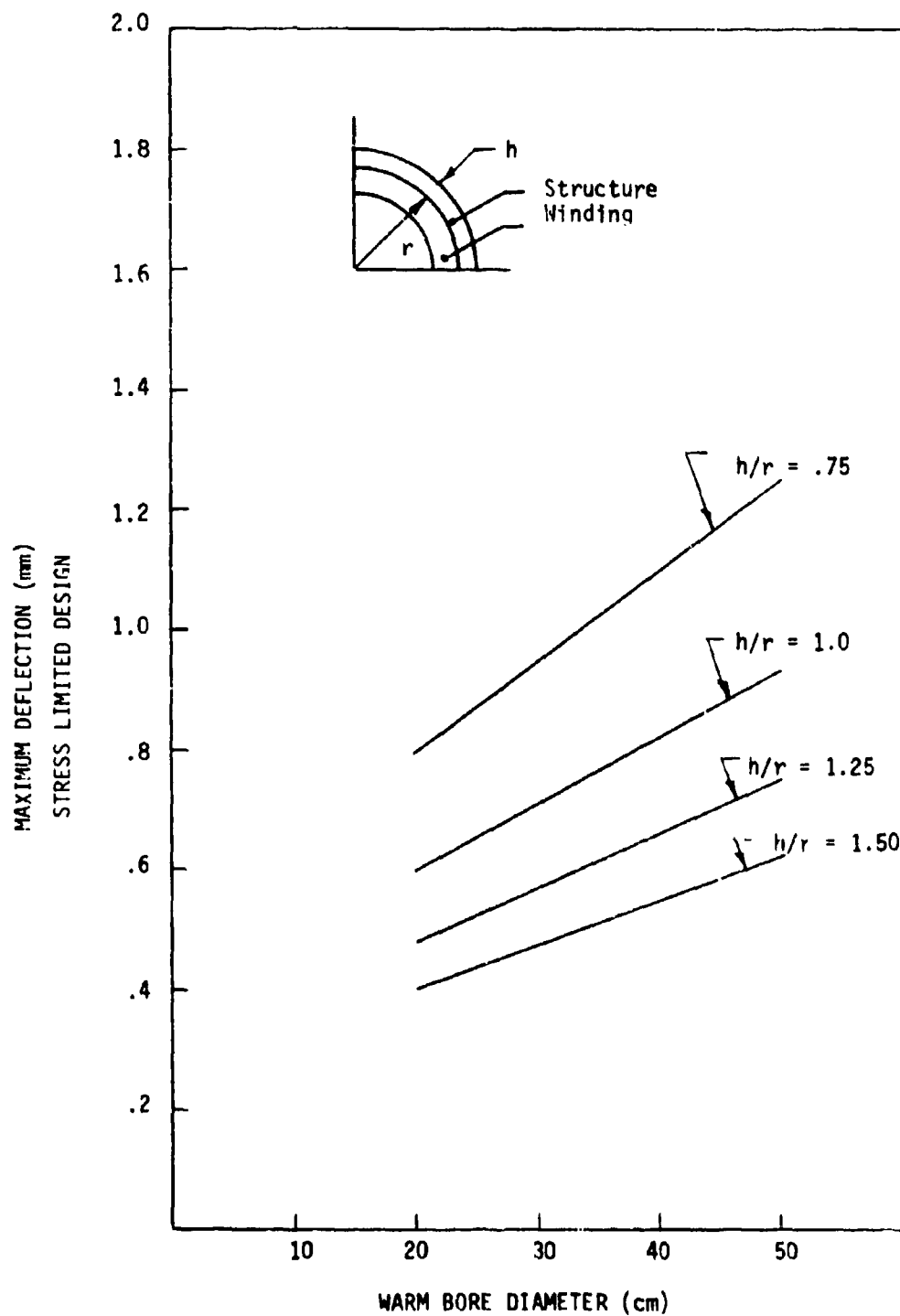


Figure 62 Maximum Deflection vs. Warm Bore Diameter for a Stainless Steel Structure

Figure 62 for stainless steel. It can be seen that the use of stainless steel results in a slightly lower deflection at the stress limit than does the aluminum. The deflection at the stress limit is proportional to the ratio of design stress to modulus. The difference in this ratio for 310S stainless steel and 6061-T6 aluminum is approximately five percent (2.09 for stainless versus 2.20 for aluminum). The bending moment of inertia of the structure is inversely proportional to the height to radius ratio and, hence, decreases with increasing  $h/r$ .

Figure 63 shows the total transverse structural weight versus magnet size for various  $h/r$  ratios for aluminum. Figure 64 shows a similar plot for stainless steel. Both figures represent weights for a stress limited design. The structural weights for the stainless are significantly higher than those for the aluminum at a fixed  $h/r$ . The stress limited design weights are proportional to the specific stress (density to design stress ratio) of the two materials. The 310S stainless steel has a specific stress twenty-five percent higher than 6061-T6 aluminum (see Table 11).

Figures 65 and 66 illustrate the effect on the transverse structural weight of imposing a deflection limit instead of a stress limit on the structure. Both figures show the variation of weight with magnet sizes for a fixed  $h/r = 1.5$  and for deflection limits of .25, .5, and 1.0 mm. Figure 65 is for an aluminum structure; Figure 66 is for stainless. Also shown on both figures is the structural weight versus magnet size for a stress limited design (the dashed line). This line divides the graph into two regions. The area above this design represents a region of feasible designs. The area below represents designs which violate the stress limits. Therefore, it is not possible to have an  $h/r = 1.5$  and a deflection of 1.0 mm without exceeding the design stress.

As will be seen in the next section, a deflection limit of .5 mm is reasonable with respect to the conductor stability under a slip condition. Such a

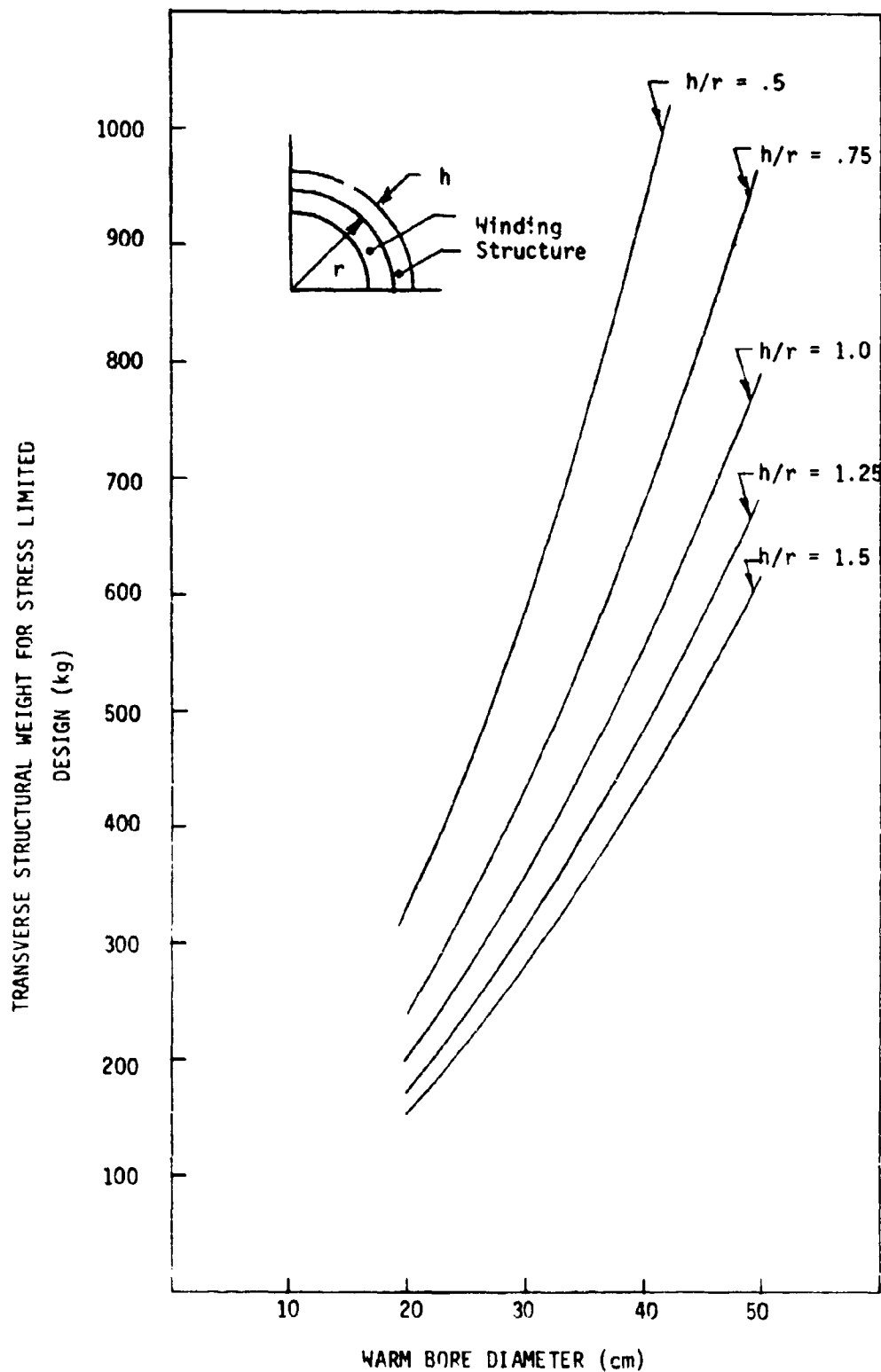


Figure 33 Transverse Structural Weight vs. Warm Bore Diameter for an Aluminum Structure

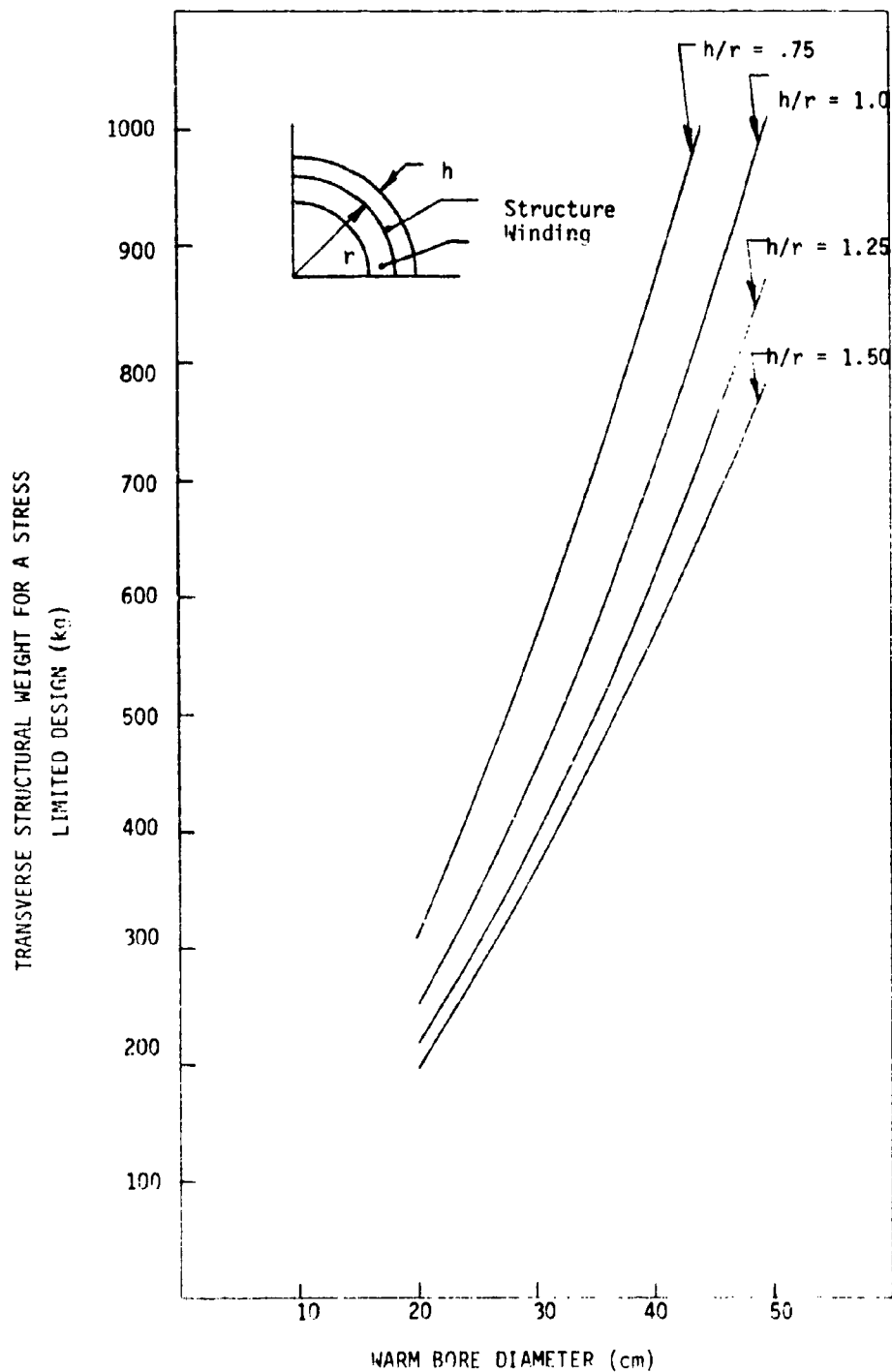


Figure 64 Transverse Structural Weight vs. Warm Bore Diameter for a Stainless Steel Structure

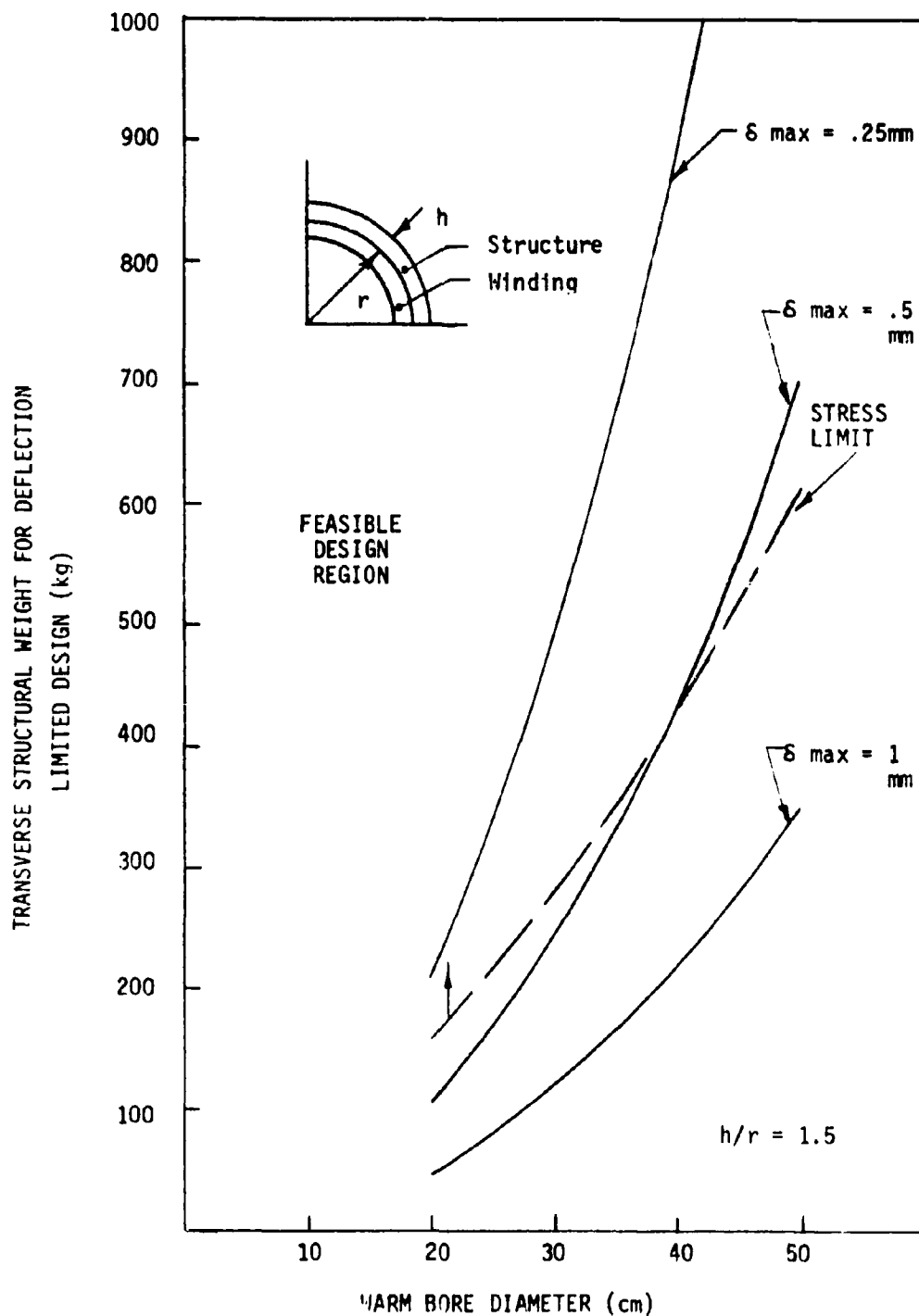


Figure 65 Transverse Structural Weight vs. Warm Bore Diameter for an Aluminum Structure

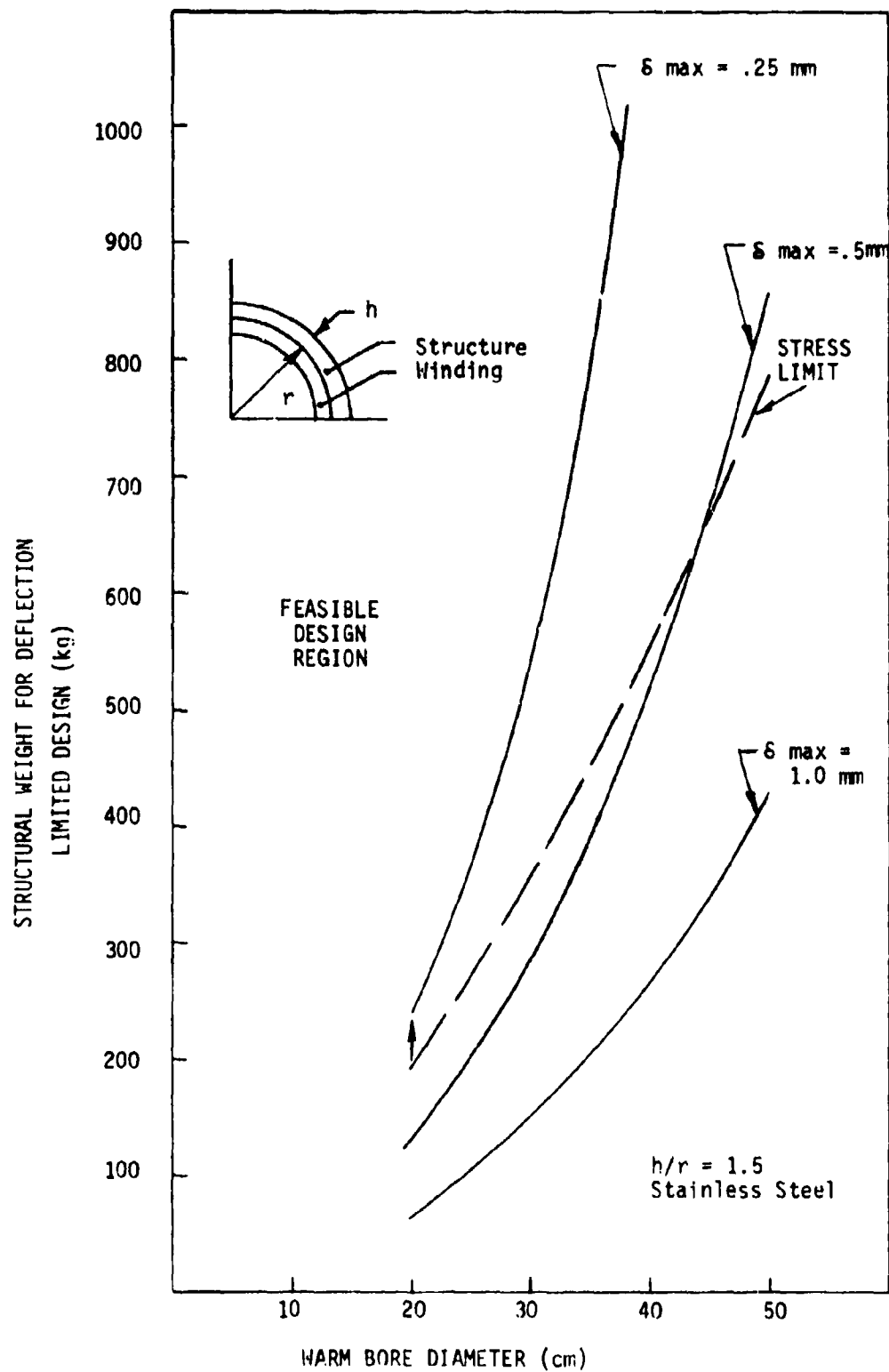


Figure 66 Structural Weight vs. Warm Bore Diameter for a Stainless Steel Structure



limit does not impose severe restrictions on the design of the transverse structure. Indeed, the optimum use of the structural weight occurs when the deflection limit and stress limit weights coincide.

Two dimensional analyses can be used to determine the structural scaling criteria. If the winding is assumed to have a cosine theta distribution, the scaling relationships listed in Table 12 hold. The primary variables are the central bore energy density which is proportional to the flux density squared, the current density, structural material and winding radius.

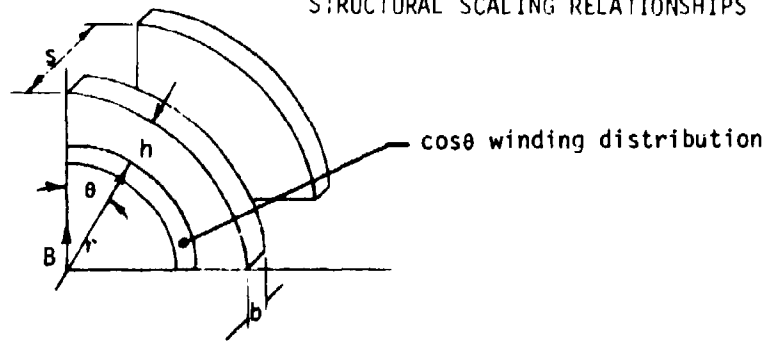
The main scaling criteria are the compressive stress in the winding, slip energy along the structure, the maximum bending moment seen by the structure, the slip energy due to a radial deflection of the structure, and structural weight. The compressive stress varies linearly with current density, central field level, and winding radius. Therefore, a 40 cm design will produce approximately twice the winding compressive stress than the 20 cm design.

The slip energy produced by the circumferential motion of the winding relative to the structure is proportional to the radius squared as is the bending moment in the structure. Doubling the radius produces four times the slip energy and, hence, four times the local temperature rise (assuming constant slip time) and four times the bending stress.

The last five entries in Table 12 are evaluated at a constant design stress limit. The maximum bending moment at the design stress yields the external ring size and/or spacing. The slip energy released by the motion of the winding relative to the structure due to a radial structural deflection is proportional to the radius, the design stress cubed, the structural spacing or packing factor and inversely proportional to the structural modulus squared.

TABLE 12

## STRUCTURAL SCALING RELATIONSHIPS



TANGENTIAL MAGNETIC LOADING	:	$\frac{B^2}{\mu_0} \sin 2\theta$
TANGENTIAL COMPRESSIVE STRESS IN THE WINDING	:	$\frac{j B r}{4} (1 + \cos 2\theta)$
TANGENTIAL SLIP ALONG THE STRUCTURE	:	$\frac{j B r^2}{4 E} (\theta + \frac{1}{2} \sin 2\theta)$
SLIP ENERGY DUE TO SLIP ALONG STRUCTURE	:	$\frac{j B^3 r^2 f}{8 E \mu_0} (1 + \cos 2\theta) (\theta + \frac{1}{2} \sin 2\theta)$
RADIAL PRESSURE ON THE STRUCTURE	:	$\frac{B^2}{2\mu_0} (1 + \cos 2\theta)$
BENDING MOMENT IN THE STRUCTURE	:	$\frac{B^2 r}{6\mu_0} \cos 2\theta$
RADIAL DEFLECTION OF THE STRUCTURE	:	$\frac{2 r}{3 E} \sqrt{\sigma^3 \left(\frac{b}{s}\right) \left(\frac{h}{B^2}\right)} \cos 2\theta$
SLIP DUE TO STRUCTURAL DEFLECTION	:	$\frac{4 \pi r \sigma^3}{9 E^2 \left(\frac{B}{\mu_0}\right)} \left(\frac{b}{s}\right) (1 + \cos 2\theta) \cos^2 2\theta$
SLIP ENERGY DUE TO STRUCTURAL DEFLECTION	:	$\frac{\pi r \sigma^3}{9 E^2} \left(\frac{b}{s}\right) (1 + \cos 2\theta) \cos^2 2\theta$
TRANSVERSE STRUCTURAL WEIGHT PER UNIT BORE ENERGY	:	$\frac{\gamma}{\sigma} \left(1 + 2 \sqrt{\frac{\sigma \mu_0}{B} \left(\frac{b}{s}\right)}\right)$

The ratio of design stress cubed to modulus squared for aluminum is approximately 900; and it is 1900 for stainless steel. Therefore, for a constant stress criterial, the aluminum leads to a design with one-half the slip energy.

The final entry is the stress limited transverse structural weight per unit bore energy. It can be seen that the specific density listed in Table 11 enters the scaling law. Once again, aluminum rather than stainless steel appears to be superior.

The external ring stiffener concept does not necessarily produce a minimum weight. For example, a ring girder (I-beam cross-section) would be lighter, but manufacturing and assembly considerations favor the simpler ring. These rings are intermittent along the length of the straight section, and local (between ring) behavior was not investigated. During Phase II, however, more detailed analyses will be carried out. Finite element analyses in both two and three dimensions will be used to investigate the local behavior, the combined thermal and magnetic loading, and the interaction of the structural components.

## SECTION VI

### CONDUCTOR STABILITY

The design of a conductor with the ability to recover from a local temperature excursion above the ambient (4.2 K) level is the most critical item to be addressed in the overall design of a lightweight, superconducting magnet system. If the conductor is unable to recover from such an excursion, a quench occurs. Even if no permanent damage to the system results, there is a loss of helium, system downtime, and an additional thermal and magnetic load cycle seen by the winding and the structure. If system weight was not a consideration, sufficient copper stabilizer could be added to the conductor to ensure its cryostability. However, the minimization of the system weight sought in this program makes this solution unacceptable. Therefore, a significant portion of the Phase I effort was invested in determining the transient and steady state thermal behavior of the chosen conductor configuration.

A frictional energy input into the conductor due to relative motion between winding bundle components is the most likely mechanism for raising the local temperature. Therefore, conductor relative motion or slip was investigated. The results of the analyses were used to place limits on the structural deflections.

Before proceeding with the slip analyses, the effect of local helium volume on the stability of the conductor was investigated. In particular, the effect of helium in the braid interstices on the temperature of the braid was determined. The analysis employs the solution of the one-dimensional, transient, temperature distribution in two adjacent materials that are at the same temperature initially. A uniform heat input is applied to the interface between the materials at time  $t = 0$ . The temperature rise in material 1 as a function of position and time is given by:

$$\Delta T_1 = q_0'' \sqrt{t} \frac{\sqrt{\alpha_1 \alpha_2}}{k_1 \sqrt{\alpha_2} + k_2 \sqrt{\alpha_1}} \left[ 2i \operatorname{erfc} \frac{y}{2\sqrt{\alpha_1 t}} \right]^* \quad (1)$$

where the subscripts refer to the two materials,  $k$  is the thermal conductivity,  $\alpha$  is the thermal diffusivity,  $y$  is the distance from the interface,  $q_0''$  is the heat input, and  $\operatorname{erfc}$  is the complementary error function. The maximum temperature rise occurs at the interface between the materials (ie at  $y = 0$ ), and is given by:

$$\Delta T_{\max_1} = q_0'' \sqrt{t} \frac{\sqrt{\alpha_1 \alpha_2}}{k_1 \sqrt{\alpha_2} + k_2 \sqrt{\alpha_1}} (1.1284). \quad (2)$$

If the maximum allowable temperature rise is set at .5 K, equation (2) can be used to determine the allowable heat input.

Equation (2) was used to determine the allowable heat input for two different slip conditions. The first slip condition corresponds to a strand of the braid moving relative to another strand. The second condition models a strand moving relative to glass-epoxy insulation. For both conditions, the strand was assumed to be a composite of copper and helium. A law of mixtures was used to determine the composite thermal properties from those of the constituents. The diffusivity of the helium was calculated from

$$\alpha = \frac{k}{\gamma C_v} \quad , \quad (3)$$

and averaged over a .5 K temperature range,  $\gamma$  is the mass density. The specific heat at constant volume was used rather than at constant pressure in order to model the effect of the helium in the braid interstitial passages. With an increase in temperature, the helium will vaporize. Since the helium is in very small passages, the bubbles will not migrate away and,

\* Carslaw and Jaeger, Conduction of Heat In Solids, Oxford University Press, 2nd Edition, p.88.

hence, the local pressure will rise. Therefore, a specific heat at constant volume is more reasonable than one at constant pressure.

Figure 67 shows the effect of local helium volume on the amount of heat input necessary to generate a maximum temperature rise at the material interface. The results are normalized to the case of strand to insulation slip with no helium present. Obviously, less heat is required if no helium is present. The strand to insulation slip produces higher temperatures than strand to strand slip since the former is basically a one sided problem ie the insulation has a much lower conductivity and, hence, the strand will see more of the heat. It can be seen that the presence of helium greatly increases the allowable heat input. For example, a 15% helium volume fraction has the effect of raising the allowable input by more than a factor of five.

The heat input necessary to raise the temperature .5 K at the interface between a strand with no helium and the insulation is used in equation (2) to generate Figure 68. The figure shows the relative maximum temperature rise versus local helium volume fraction for the two slip conditions. It can be seen that even 5% helium reduces the maximum temperature rise by 70%. Calculations discussed previously (see section 4.0) indicate that with a 50% solder filled braid, the helium volume fraction in the interstices is approximately 12%. A 12% helium volume fraction reduces the maximum temperature rise by 80%. It is for this reason that the proposed winding design is not fully potted.

Equation (1) is written for a steady heat input. In order to investigate the effect a short duration heat pulse, such as occurs due to a slip motion, equation (4) is used.

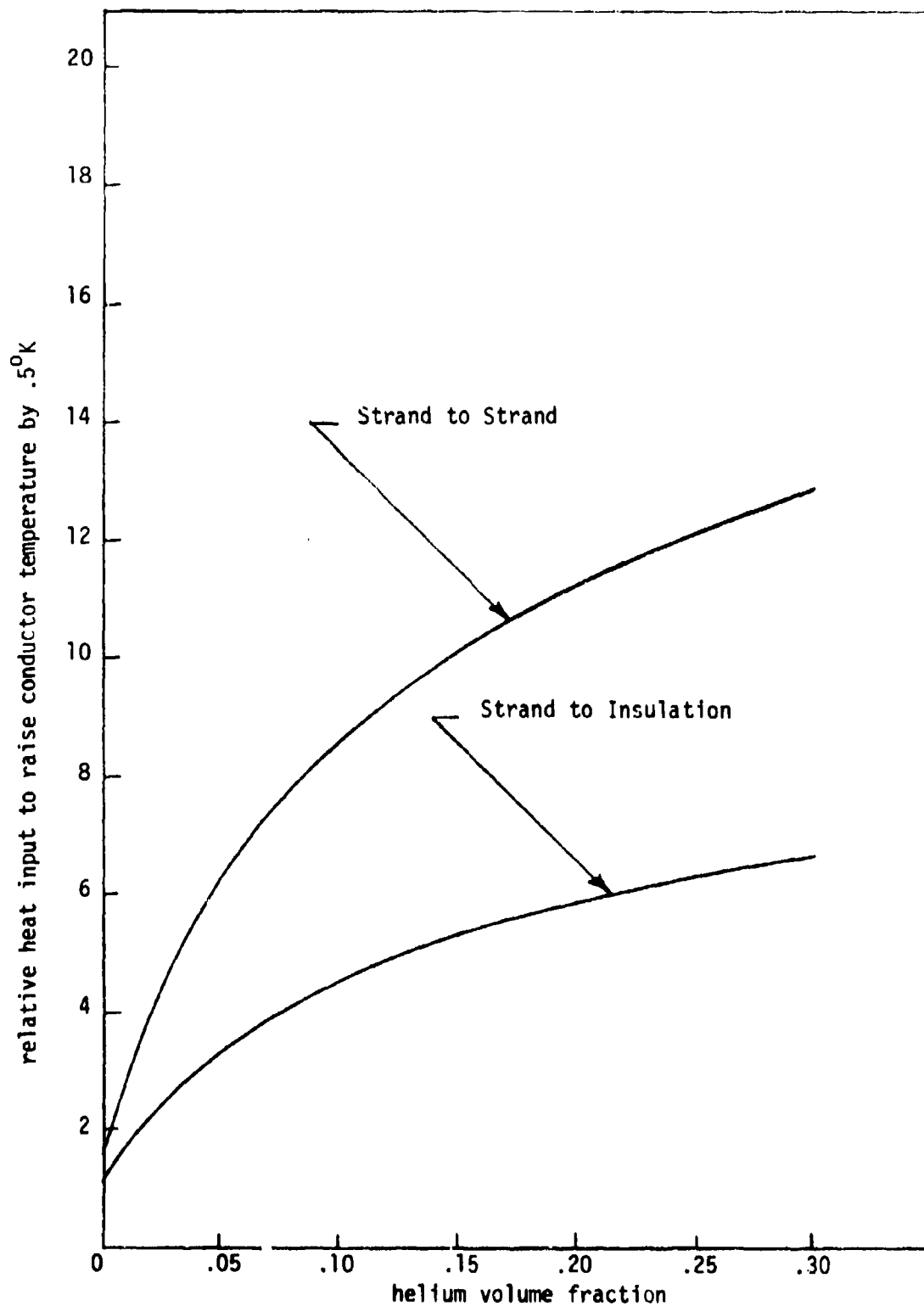


Figure 67 Relative Heat Input versus Helium Volume for Different Slip Conditions

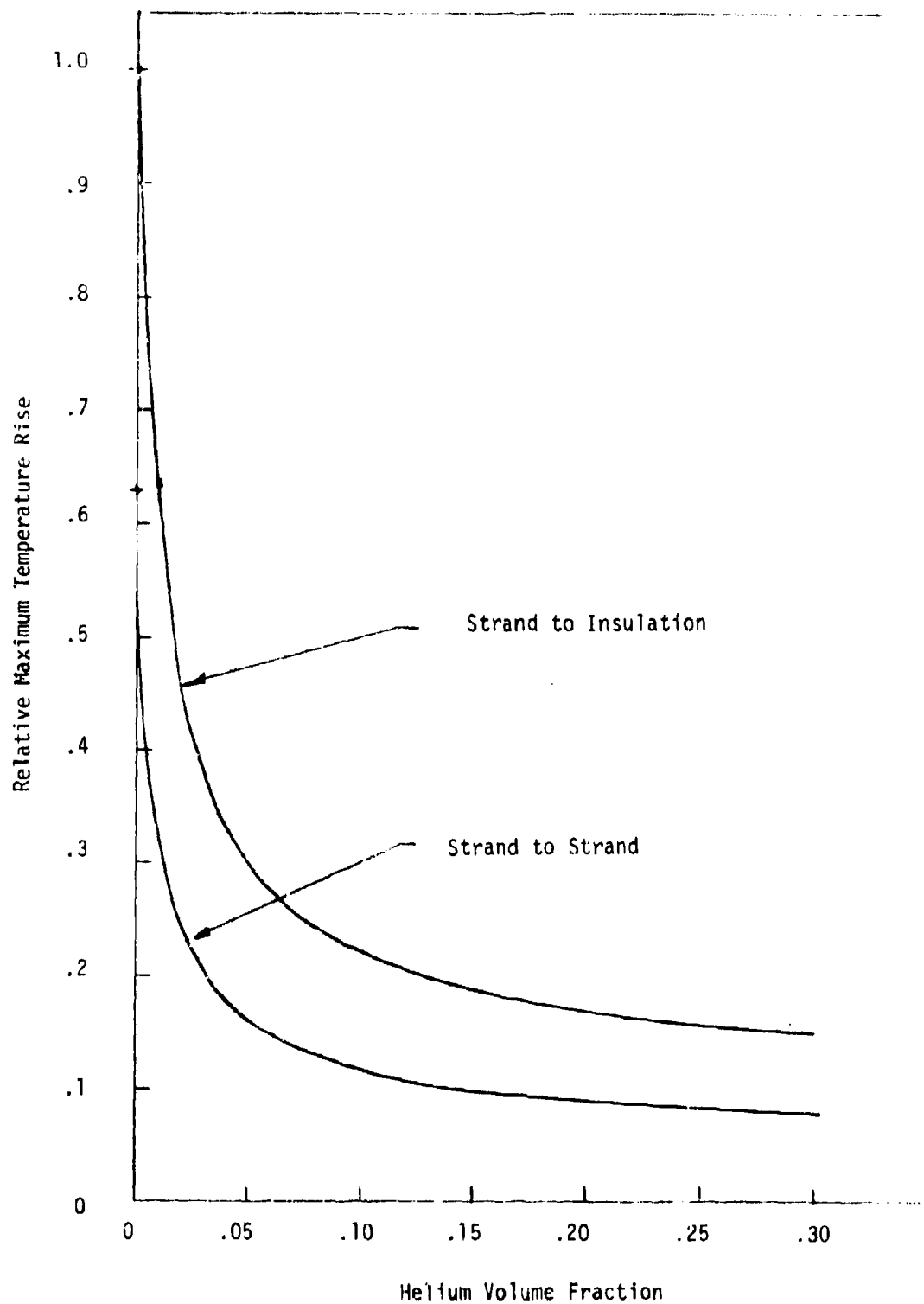


Figure 68 Relative Maximum Temperature versus Helium Volume  
for Different Conditions



$$\begin{aligned}
\Delta T_1 &= q_0'' \sqrt{t} \frac{\sqrt{\alpha_1 \alpha_2}}{k_1 \sqrt{\alpha_2} + k_2 \sqrt{\alpha_1}} \left[ 2i \operatorname{erfc} \frac{y}{2\sqrt{\alpha_1 t}} \right]_{0 \leq t \leq t_p} \\
\Delta T_1 &= q_0'' \sqrt{t} \frac{\sqrt{\alpha_1 \alpha_2}}{k_1 \sqrt{\alpha_2} + k_2 \sqrt{\alpha_1}} \left[ 2i \operatorname{erfc} \frac{y}{2\sqrt{\alpha_1 t}} \right] \\
&\quad - q_0'' \sqrt{t-t_p} \frac{\sqrt{\alpha_1 \alpha_2}}{k_1 \sqrt{\alpha_2} + k_2 \sqrt{\alpha_1}} \left[ 2i \operatorname{erfc} \frac{y}{2\sqrt{\alpha_1 (t-t_p)}} \right]_{t > t_p}
\end{aligned} \tag{4}$$

where  $t_p$  is the pulse time and  $q_0''$  is the pulse magnitude. The maximum temperature rise still occurs at the interface ( $y = 0$ ) at time  $t = t_p$ . Figure 69 shows the nondimensional peak temperature rise as a function of a nondimensional position. This curve represents the peak temperature in material 1 at any location due to the energy input. It will be used to determine the "penetration depth" in subsequent analyses. This penetration depth is defined as the distance into material 1 at which the maximum temperature rise is equal to temperature rise required to induce current sharing in the strand.

The results presented to this point are independent of the actual slip and, indeed, are valid for any heat input. The next step in the analysis was to investigate the actual slip conditions. The slip conditions investigated were: 1) the slip associated with a bundle compression due to the magnetic forces; 2) the slip associated with an axial structure deflection; and 3) the slip associated with a transverse structure deflection.

The model used for the winding bundle compressive slip analysis is shown in Figure 70. The model consists of a typical bundle that is compressed by the Lorentz body force against two surfaces that are assumed to be rigid. The other two surfaces are assumed to be free. The deformed bundle shape is shown along with the points of maximum slip. The slip

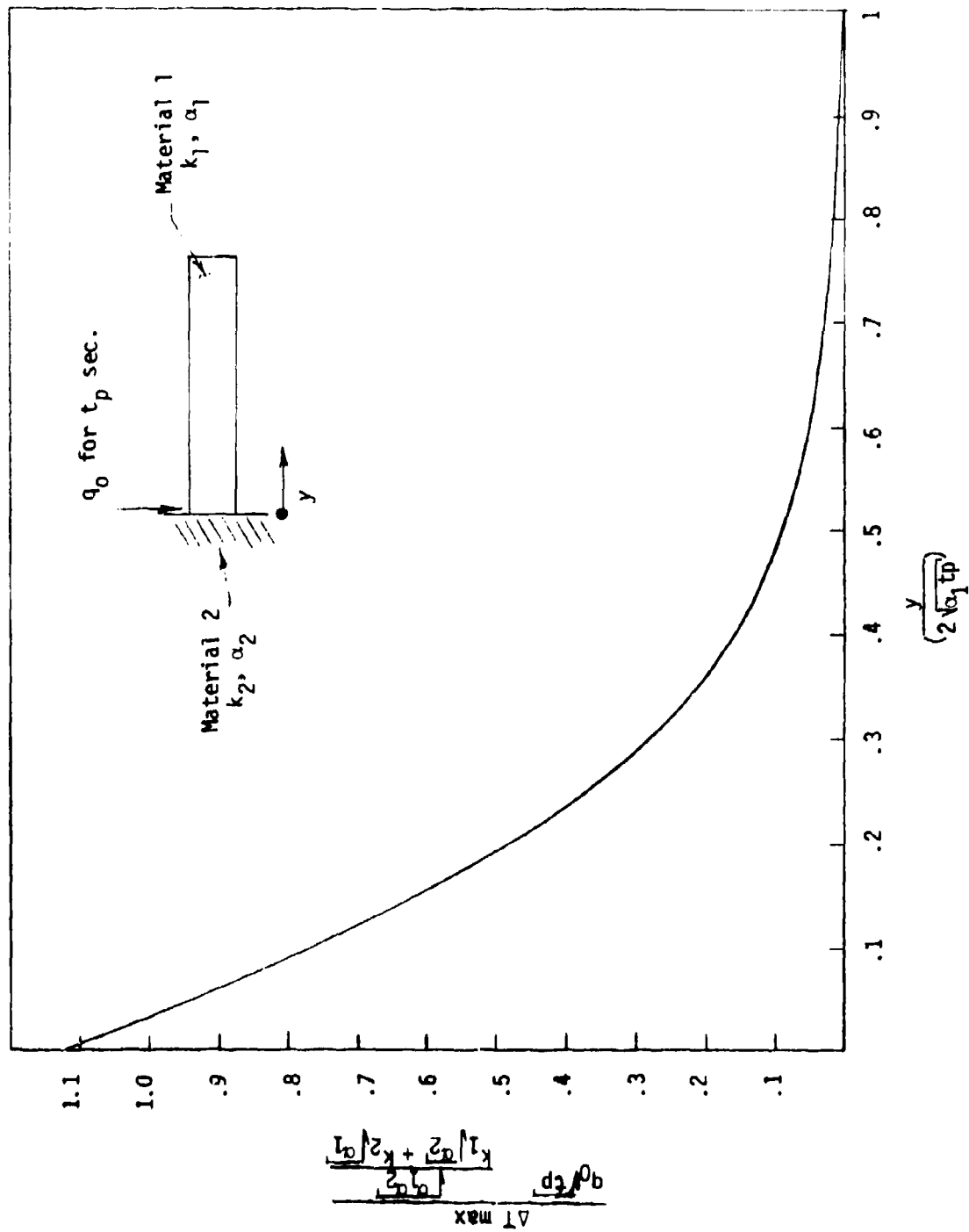


Figure 69 Non-Dimensional Maximum Temperature Rise vs. Non-Dimensional Distance for Bundle Slip

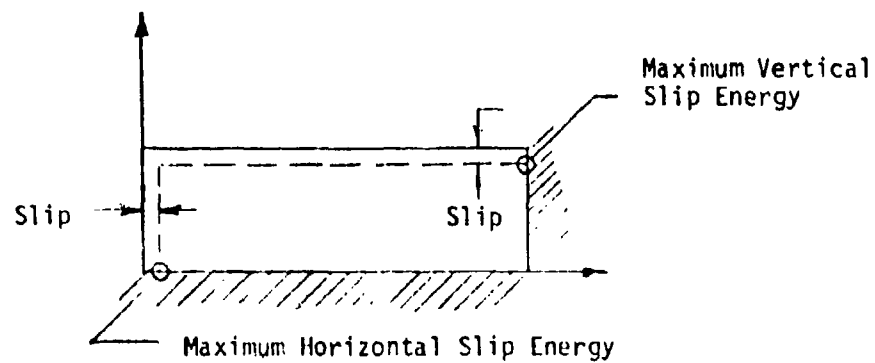
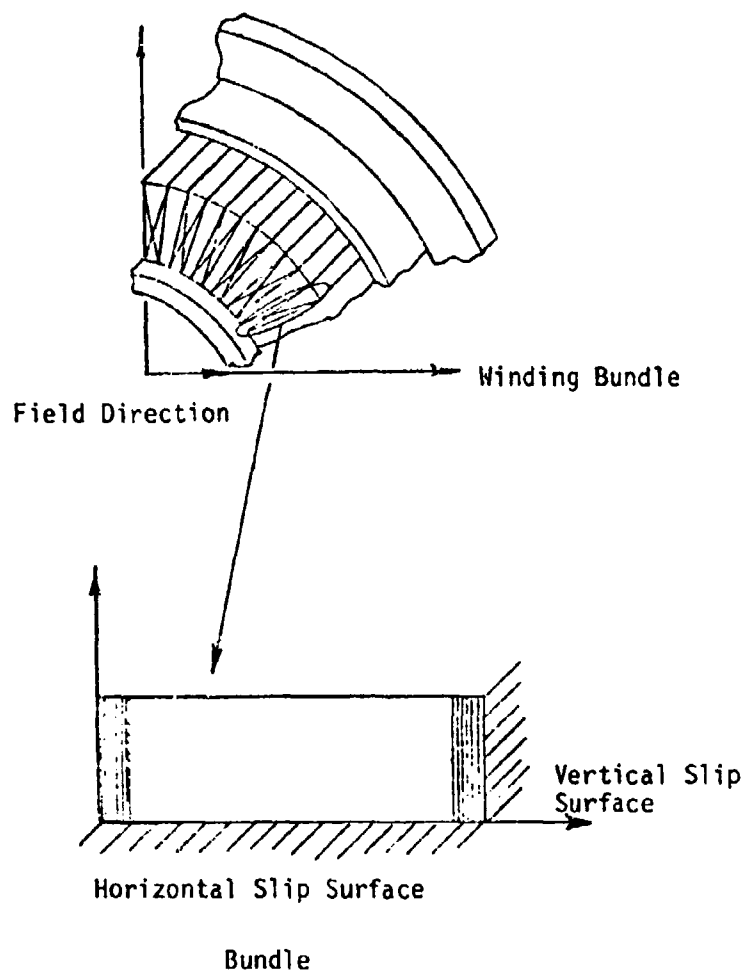


Figure 70 Bundle Compressive Slip Model

is assumed to take place at the maximum load - ie no incremental slip.

The maximum slip energies and associated slip time are then used in the following modification to equation (2) in order to find the maximum temperature rise:

$$\Delta T_{\max_1} = \frac{e}{\sqrt{t_p}} \frac{\sqrt{\alpha_1 \alpha_2}}{k_1 \sqrt{\alpha_2} + k_2 \sqrt{\alpha_1}} \quad (1.1284) \quad (5)$$

where the constant heat flux term,  $q_0'' \sqrt{t}$ , is replaced by a pulsed energy input  $e/\sqrt{t_p}$  where  $e$  is the slip energy per unit surface area and  $t_p$  is slip time. Figure 71 presents the peak temperature rise versus magnet size for two conductor current densities. The results for slip along both the horizontal and vertical surfaces are shown. The model assumes a 15% local helium volume fraction. The conductor operating regimes of superconducting, current sharing, and normal are indicated.

The slip energy is proportional to the current density squared and, hence, the higher current density yields high temperatures. It can be seen from the figure that the temperature rise due horizontal slip is most severe. Indeed, locally the conductor would be fully normal at the temperatures (and at the peak field) indicated.

Figure 72 indicates the distance into a conductor that the temperature remains above the current sharing value. The penetration depths shown are on the order of 2 mm, which is less than 20 - 25% of the conductor width. Therefore, the perturbation is truly local, and does not affect the overall behavior of the bundle.

The next slip mechanism investigated was that of a relative motion of the winding bundle to the structure due to axial loading. The model

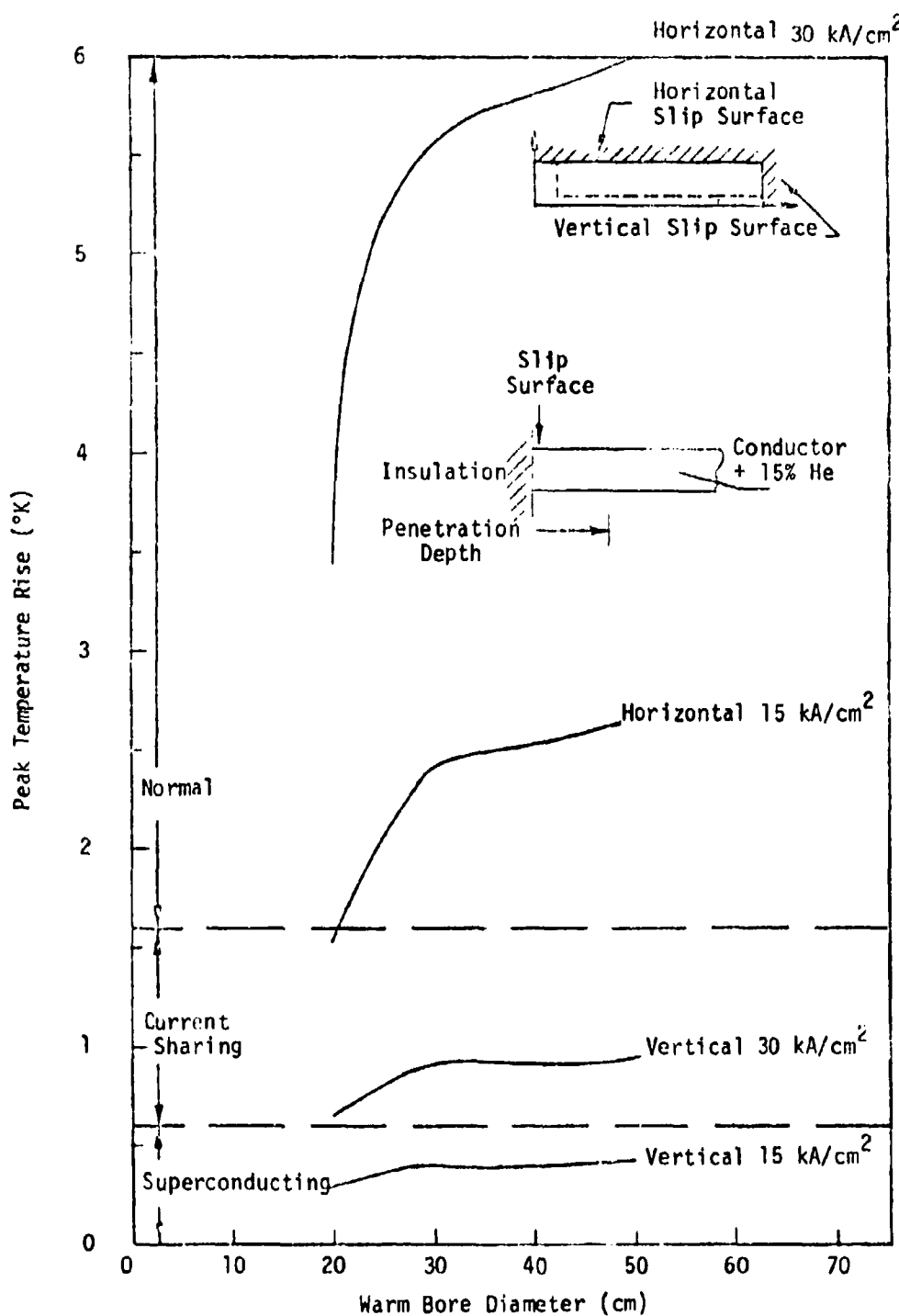
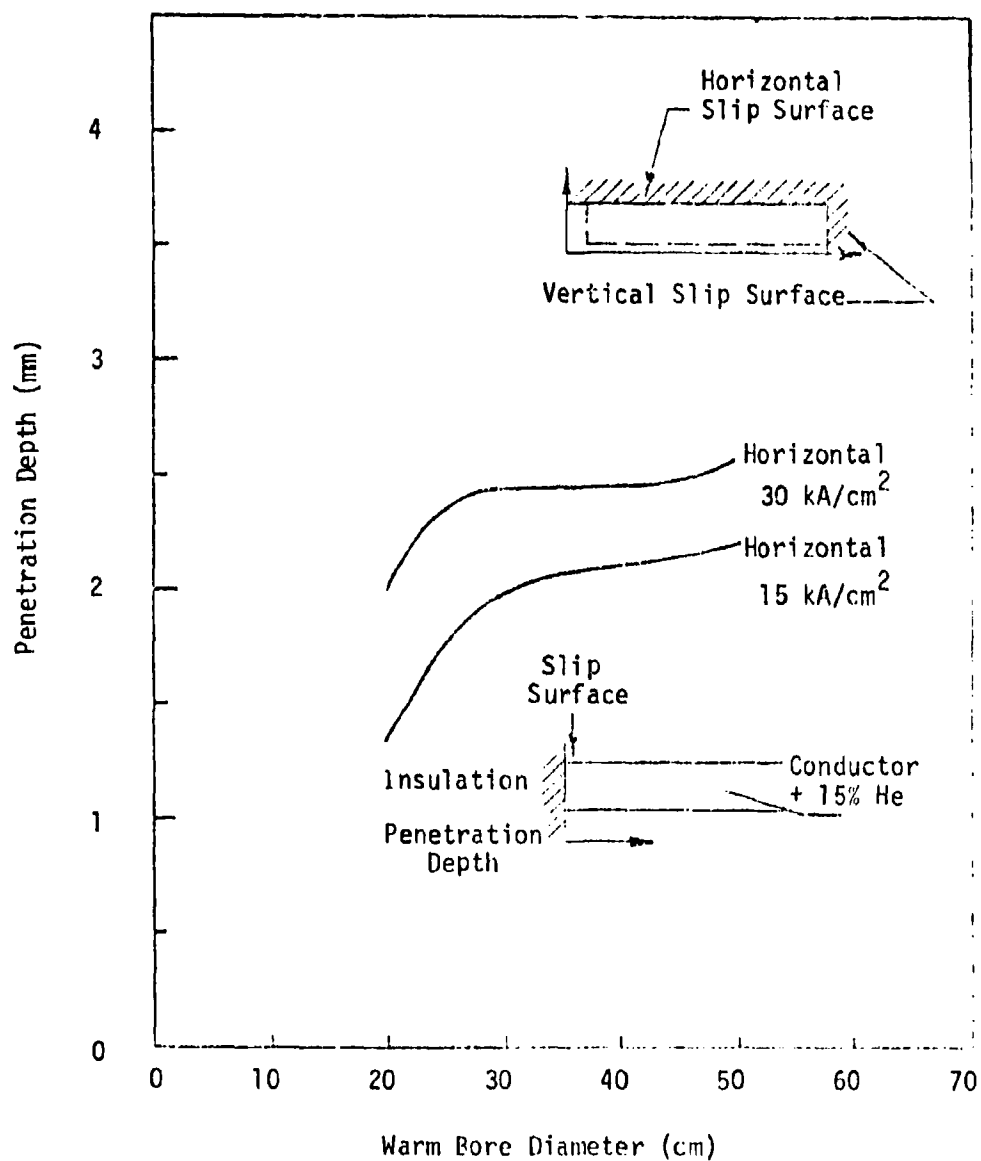


Figure 71 Peak Temperature Rise Due to Conductor Slip vs. Warm Bore Size for Two Current Densities.



**Figure 72** Penetration Depth (Depth at Which  $\Delta T = 0.6$  K) vs. Warm Bore Size for Two Current Densities.

used is illustrated in Figure 73. The peak circumferential load acting on a tranverse section of the winding is used to determine the normal stress and, hence, the frictional force.

Figure 74 shows the peak temperature rise versus axial slip for each of the magnet sizes for a conductor current density of  $15,000 \text{ A/cm}^2$ . Analyses indicate that the  $15,000 \text{ A/cm}^2$  design yields higher peak temperatures than does the  $30,000 \text{ A/cm}^2$  design.

Figure 58 (section 5.0 Structural Design) presented the weight of an axial structure versus axial deflection. A deflection held to 1 mm required 40 to 110 kg of structure depending on magnet size. If it is assumed that the conductor bundle remains stationery while the axial structure deforms, then the slip maximum seen by the bundle is one half the total deflection, and it occurs at either end of the straight lengths. This is a conservative assumption since the winding bundle will, in fact, deform somewhat along with the structure. However, with the above assumption, an axial deflection of 1 mm translates to an axial slip of .5 mm and peaks temperatures of 2.3 to 3.2 K depending on magnet size.

The final slip model used is illustrated in Figure 75. The analysis models the slip of the winding bundle along the transverse structure due to a radial structural deflection. Under the action of the loads, the winding structure will deform into an oval shape. The winding bundle motion due to the radial deflection of the structure centerline is illustrated. Figure 76 shows the amount of relative motion or slip versus magnet size for a range of structural deflections. The relative motion is inversely proportional to the initial (undeformed) winding bundle average radius. Therefore, the maximum slips, temperatures, etc. occur at the inlet end turn crossover. The normal force acting on the bundle was assumed to

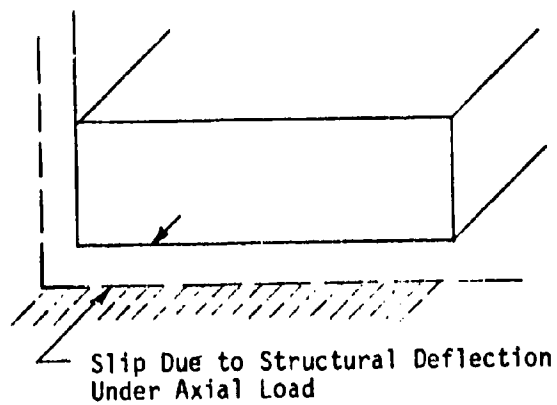
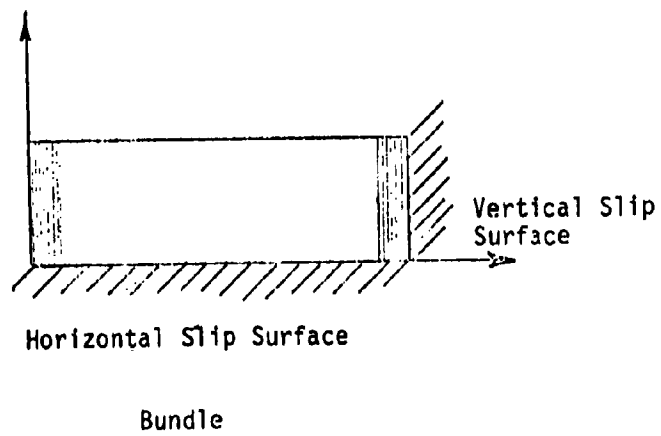
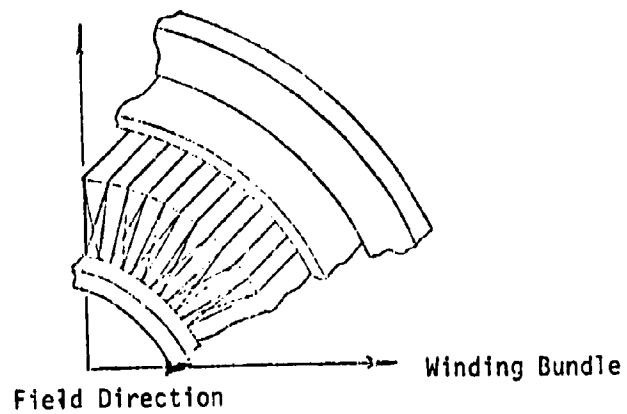
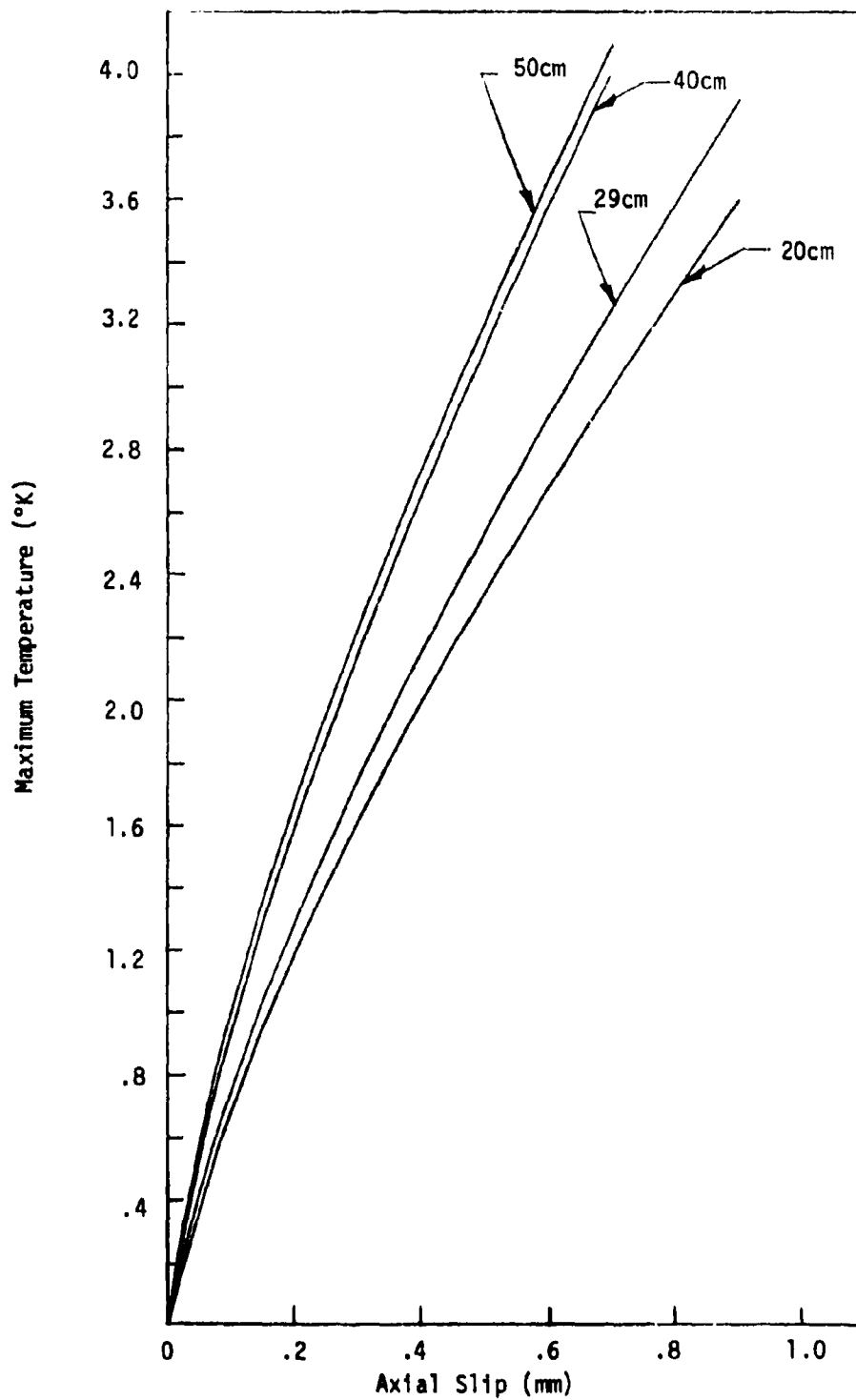


Figure 73 Bundle Axial Slip Model





FA 4727 Figure 74 Maximum Temperature Rise vs. Axial Slip for Various Warm Bore Sizes ( $j_c = 15 \text{ kA/cm}^2$ )

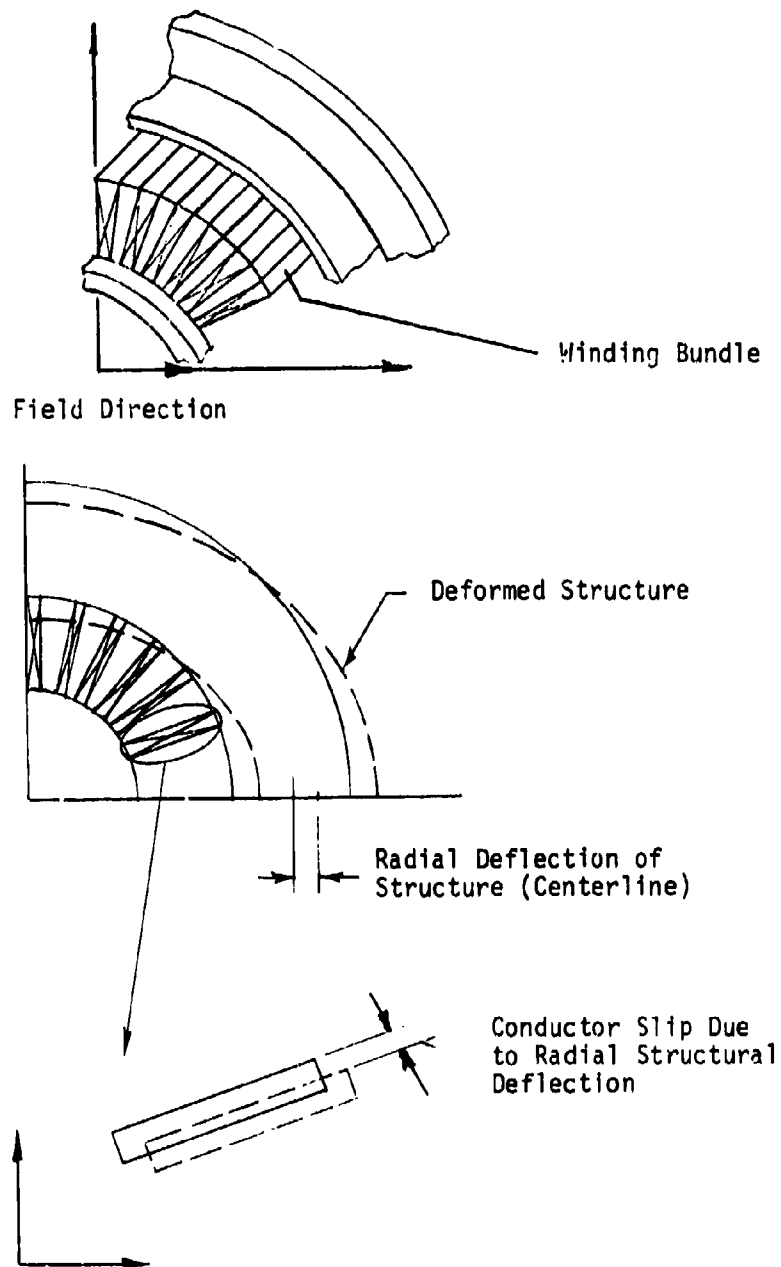


Figure 75 Bundle Radial Slip Model

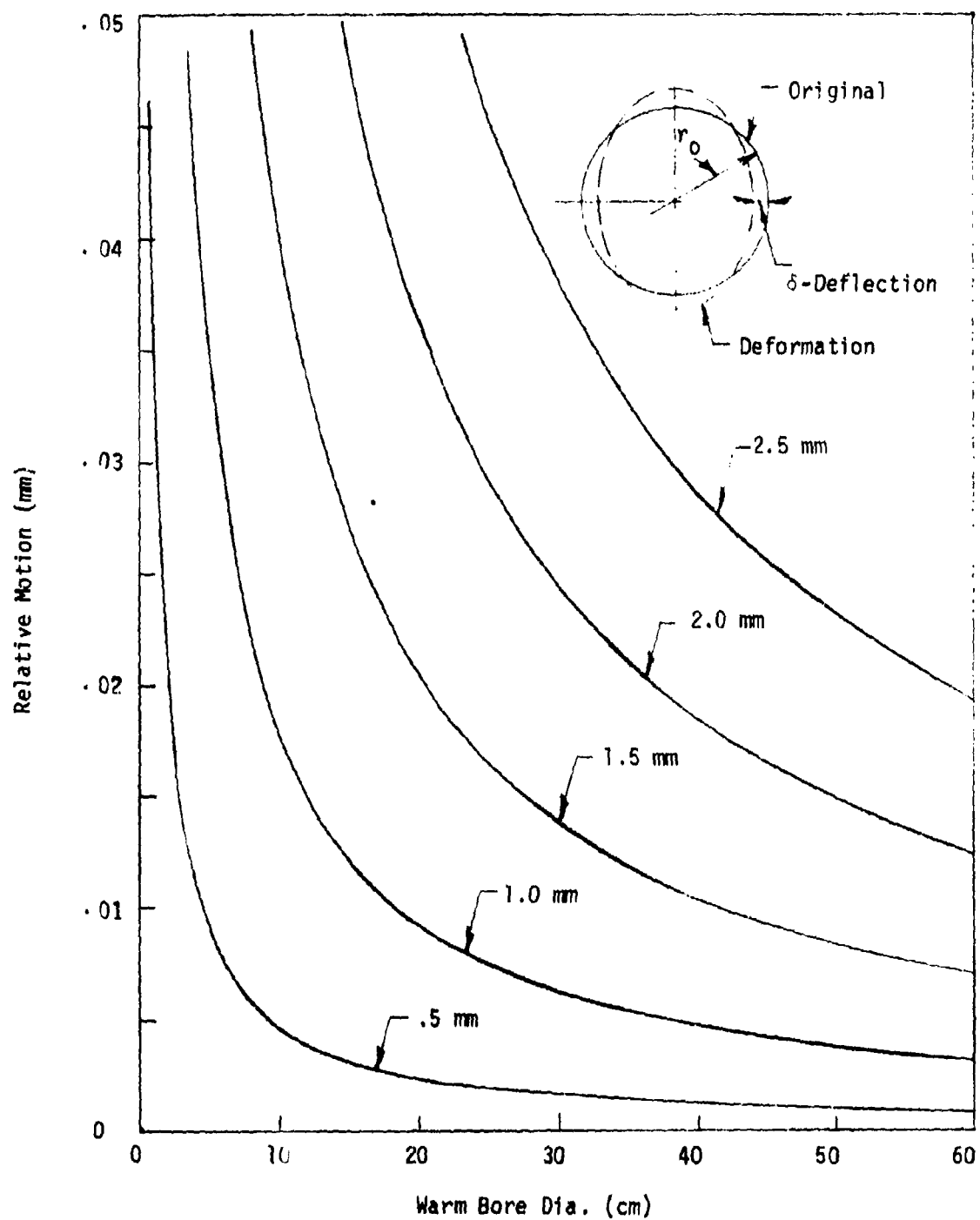


Figure 76 Relative Motion vs. Warm Bore Size for Various Values of Deflection  
FA 4698

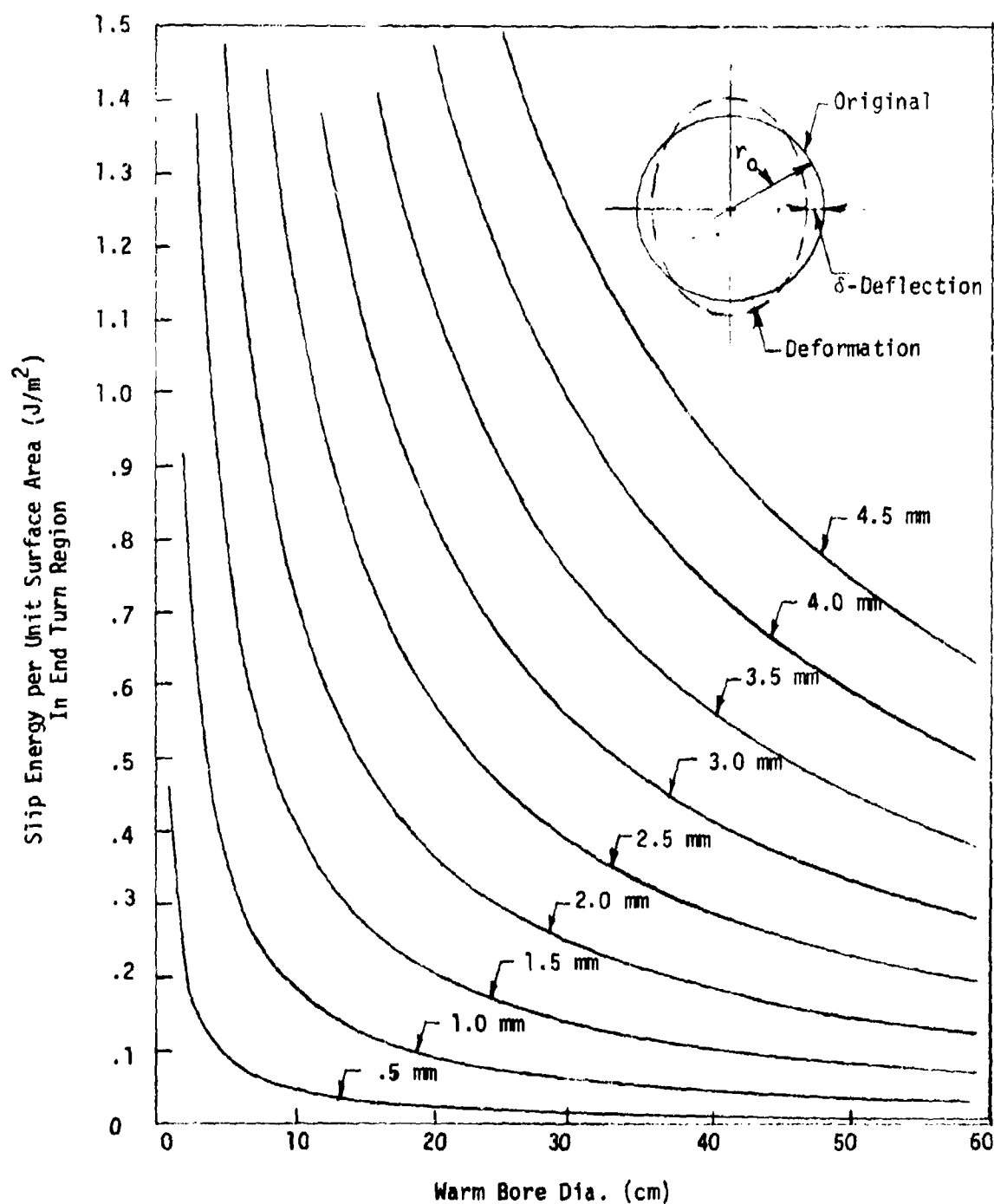
be the number of conductors times the operating current times the peak field magnitude. Once again, this is a conservative assumption. Figure 77 shows the slip energy per unit surface area in the end turn region versus magnet size for various values structural deflections.

Analyses of the radial deflection of the transverse structure in section 5.0 indicated that the deflection at the stress limit for aluminum was approximately .5 mm. Since the efficient use of structural material dictates operating at the stress limit, a deflection of .5 mm is assumed. Calculations of the peak temperature rise for this deflection show that 1 K is a maximum and occurs in the 29 cm, 30,000 A/cm<sup>2</sup> design.

The results of the three slip models and calculations are summarized in Tables 13 and 14. Table 13 shows the maximum slip, slip energy per unit surface area, slip time, peak temperature rise, and penetration depth for each magnet size for the 15,000 A/cm<sup>2</sup> conductor. Table 14 lists the same data for the 30,000 A/cm<sup>2</sup> design. It can be seen that the axial slip is the worst case situation for the 15,000 A/cm<sup>2</sup> design (for an allowable deflection of 1 mm). The peak temperatures occur for the 30,000 A/cm<sup>2</sup> due to the bundle compressive slip. It is quite easy to lower the temperature rise due to axial slip by increasing the axial structure and thereby, decreasing the deflection. However, it is not as easy to reduce the bundle compressive slip.

In summary, it appears that deflection limits discussed above produce acceptable local temperature rise and small penetration depths. However, during the detailed design phase, the analyses will be continued and refined.

Another aspect of the conductor stability investigated during Phase I was concerned with the diffusion of the current from a normal superconducting filament into the copper stabilizer. The non-uniform distribution of current can lead to high local resistive heating in the stabilizer.



FA 4697

Figure 77 Slip Energy per Unit Surface Area vs. Warm Bore Size for Various Values of Deflection

TABLE 13

SUMMARY OF SLIP CALCULATIONS15,000 A/cm<sup>2</sup> CONDUCTOR

	20 cm	29 cm	40 cm	50 cm
<u>BURDLE COMPRESSIVE SLIP</u>				
<u>HORIZONTAL</u>				
Maximum Slip (cm)	.025	.045	.049	.052
Maximum Slip Energy per Unit Surface Area (mJ/cm <sup>2</sup> )	16.6	29.5	31.7	34.0
Slip Time (μsec)	199	265	275	284
Maximum Temperature Rise (°K)	1.55	2.39	2.52	2.66
Penetration Depth (cm)	.013	.020	.021	.022
<u>VERTICAL</u>				
Maximum Slip (cm)	.0005	.0005	.0005	.0005
Maximum Slip Energy per Unit Surface Area (mJ/cm <sup>2</sup> )	1.28	1.71	1.77	1.83
Slip Time (μsec)	31.5	31.5	31.5	31.5
Maximum Temperature Rise (°K)	.30	.40	.42	.43
Penetration Depth (cm)	---	---	---	---
<u>AXIAL SLIP (Allowable Deflection 1.0 mm)</u>				
Maximum Slip (cm)	.05	.05	.05	.05
Maximum Slip Energy per Unit Surface Area (mJ/cm <sup>2</sup> )	14.3	15.3	18.1	18.4
Slip Time (μsec)	66.6	64.4	59.2	58.6
Maximum Temperature Rise (°K)	2.31	2.51	3.10	3.18
Penetration Depth (cm)	.083	.085	.089	.089
<u>TRANSVERSE RADIAL SLIP (Allowable Deflection .5 mm)</u>				
Maximum Slip (cm)	.0004	.0003	.0002	.0002
Maximum Slip Energy per Unit Surface Area (mJ/cm <sup>2</sup> )	2.27	2.42	2.12	1.87
Slip Time (μsec)	16.7	13.9	13.4	13.1
Maximum Temperature Rise (°K)	.73	.86	.77	.68
Penetration Depth (cm)	.024	.024	.013	.006

TABLE 14

SUMMARY OF SLIP CALCULATIONS30,000 A/cm<sup>2</sup> Conductor

	20 cm	29 cm	40 cm	50 cm
<u>Bundle Compressive Slip</u>				
<u>Horizontal</u>				
Maximum Slip (cm)	.033	.062	.066	.070
Maximum Slip Energy per Unit Surface Area (mJ/cm <sup>2</sup> )	32.2	60.9	64.8	68.8
Slip Time (μsec)	153	210	216	273
Maximum Temperature Rise (°K)	3.45	5.53	5.82	6.09
Penetration Depth (cm)	.182	.245	.246	.257
<u>Vertical</u>				
Maximum Slip (cm)	.0006	.0006	.0006	.0006
Maximum Slip Energy per Unit Surface Area (mJ/cm <sup>2</sup> )	2.4	3.3	3.4	3.5
Slip Time (μsec)	23.7	23.7	23.7	23.7
Maximum Temperature Rise (°K)	.65	.895	.922	.95
Penetration Depth (cm)	.017	.055	.057	.063
<u>Axial Slip (Allowable Deflection 1.0 mm)</u>				
Maximum Slip (cm)	.05	.05	.05	.05
Maximum Slip Energy per Unit Surface Area (mJ/cm <sup>2</sup> )	18.6	18.4	20.3	22.3
Slip Time (μsec)	217	209	208	193
Maximum Temperature Rise (°K)	1.67	1.64	1.86	1.59
Penetration Depth (cm)	.052	.050	.025	.055
<u>Transverse Radial Slip (Allowable Deflection .5 mm)</u>				
Maximum Slip (cm)	.0004	.0003	.0002	.0002
Maximum Slip Energy per Unit Surface Area (mJ/cm <sup>2</sup> )	2.72	2.70	2.29	1.94
Slip Time (μsec)	13.6	11.5	11.3	11.3
Maximum Temperature Rise (°K)	.97	1.05	.90	.76
Penetration Depth (cm)	.021	.018	.015	.011

The insert in Figure 78 illustrates the model used. When the current is carried by the superconductor, the distribution of field is linear (current constant) in the superconductor and constant in the stabilizer. If the superconductor is driven normal, the current is expelled from it, and it diffuses into the stabilizer. The steady state distribution of current in the stabilizer is constant (linear field variation). The analysis assumes that the current is expelled from the superconductor instantaneously (ie no current sharing). Figure 78 shows the profiles of field in the stabilizer at various times. Since the current density is proportional to the slope of field (ie  $j = \frac{1}{\mu_0} \frac{\partial B}{\partial x}$ ) there is a high instantaneous local heating ( $\rho j^2$ ) initially. It can be seen that the diffusion is completed after 1  $\mu$ sec.

Figure 79 illustrates the recovery process. In this figure, it was assumed that the diffusion had reached steady state (ie uniform current density in the stabilizer). At that time sufficient cooling took place to allow the superconductor to recover. The field profiles for various times are shown.

Figure 80 presents the average power dissipated by the resistive heating as a function of time for various recovery or reversal times. As expected, the initial power dissipation is infinite, and if no reversal occurs, it reaches a uniform value. If reversal occurs, the average power dissipation drops to zero.

The analyses indicate that the energy dissipated - the area under the power dissipation curve - is small compared to the slip energies discussed previously. Therefore, such analyses need not be repeated.

The final series of analyses to be discussed involves the solution of the ordinary differential equation governing the one-dimensional,



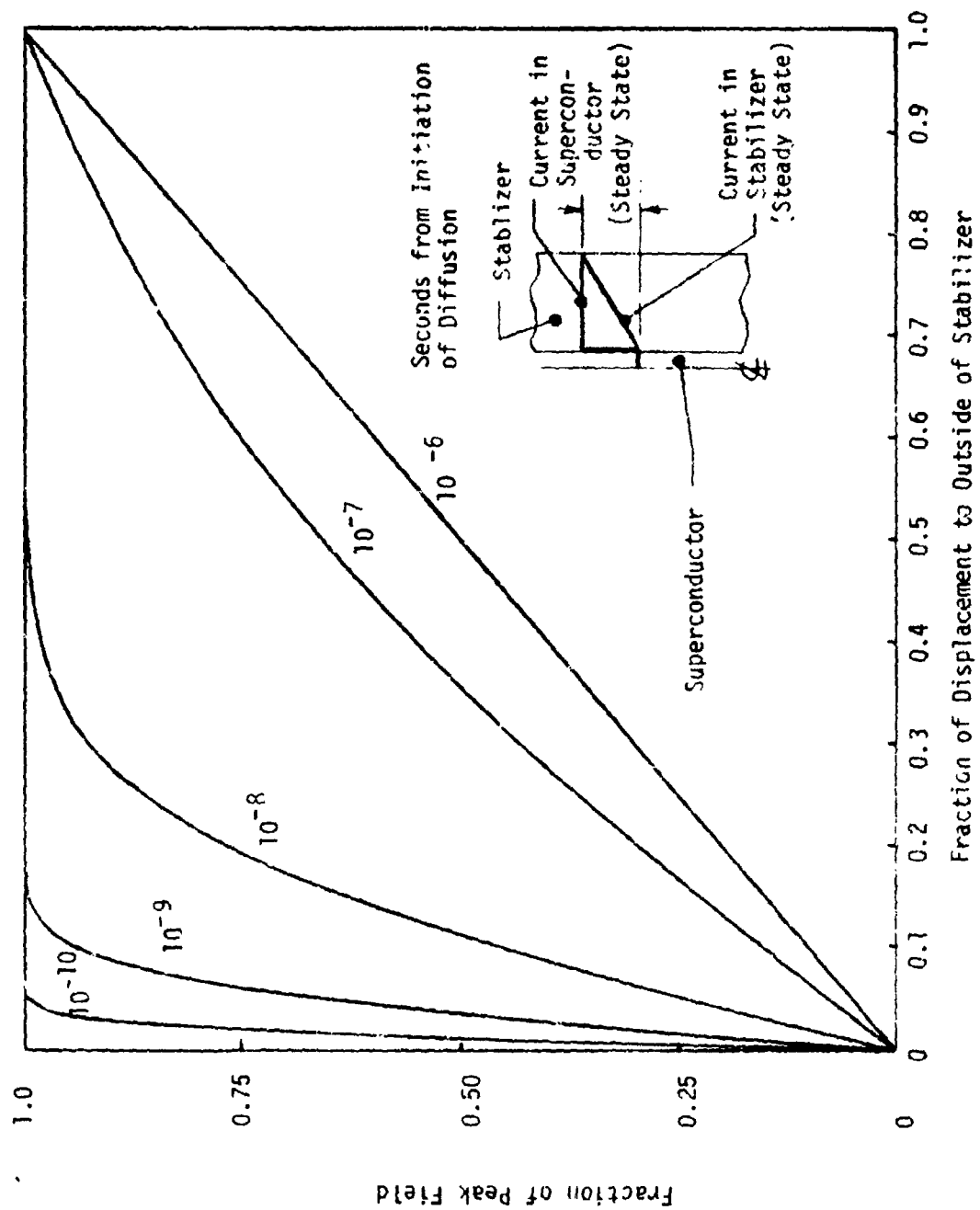


Figure 73 Diffusion of Magnetic Flux from Normal Superconducting Strand to Adjoining Stabilizer

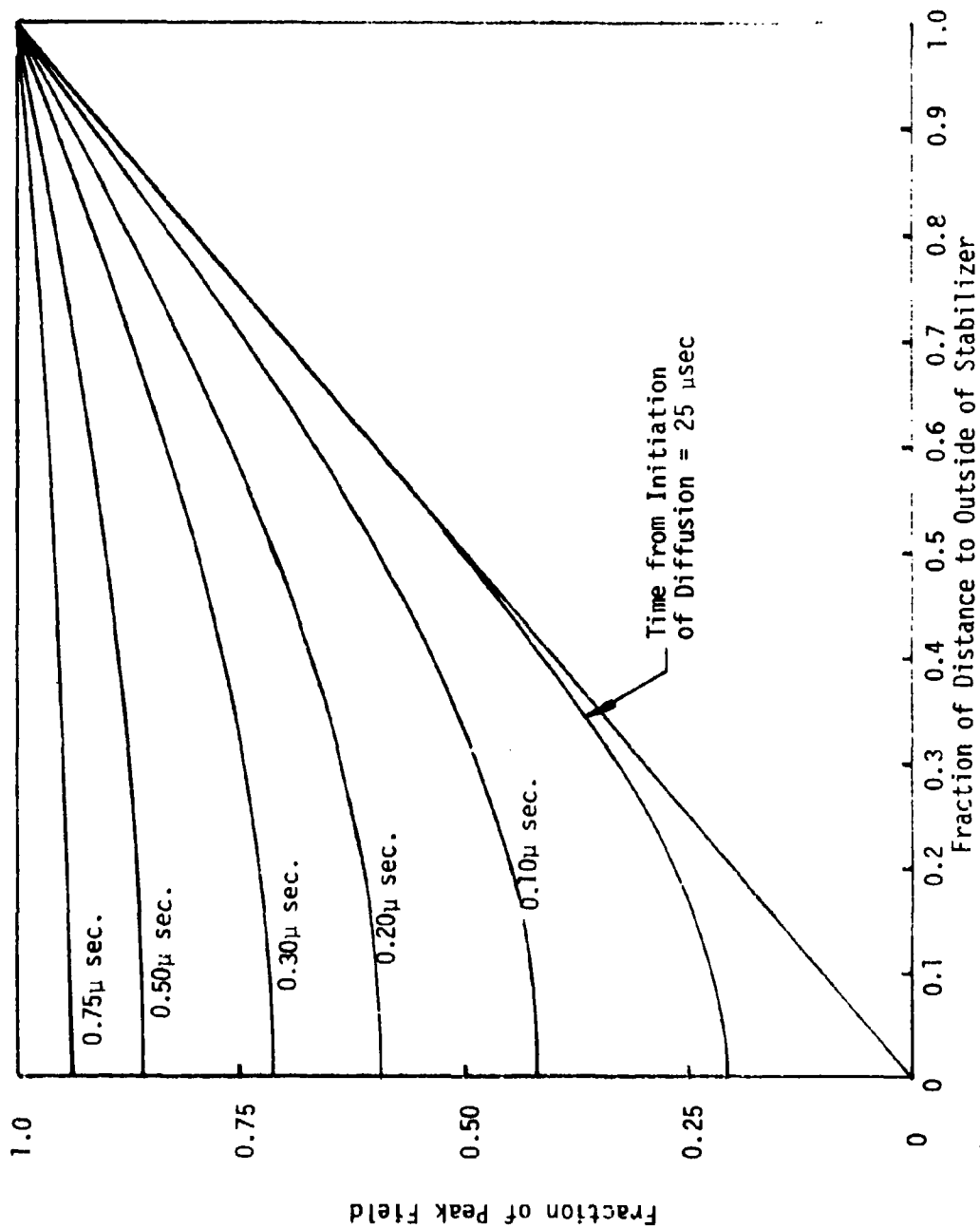


Figure 79 Diffusion of Magnetic Flux Through Stabilizer to Central Superconducting Strand from Steady State Distribution in Stabilizer

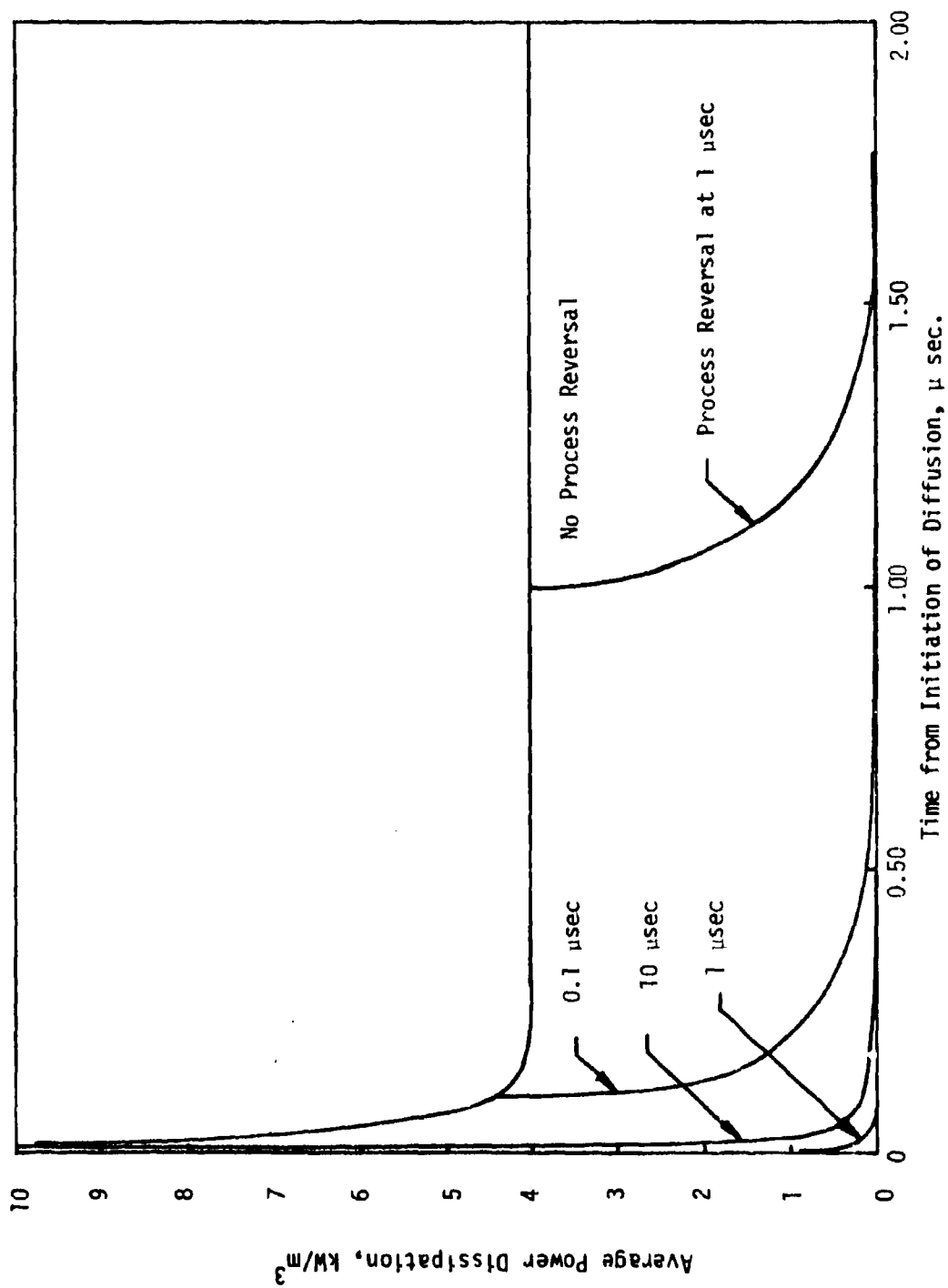


Figure 80 Average Power Density vs. Time Dissipated in Stabilizer During Current Diffusion with Process Reversal (i.e., Return to Superconducting State) Occurring at Several Intervals

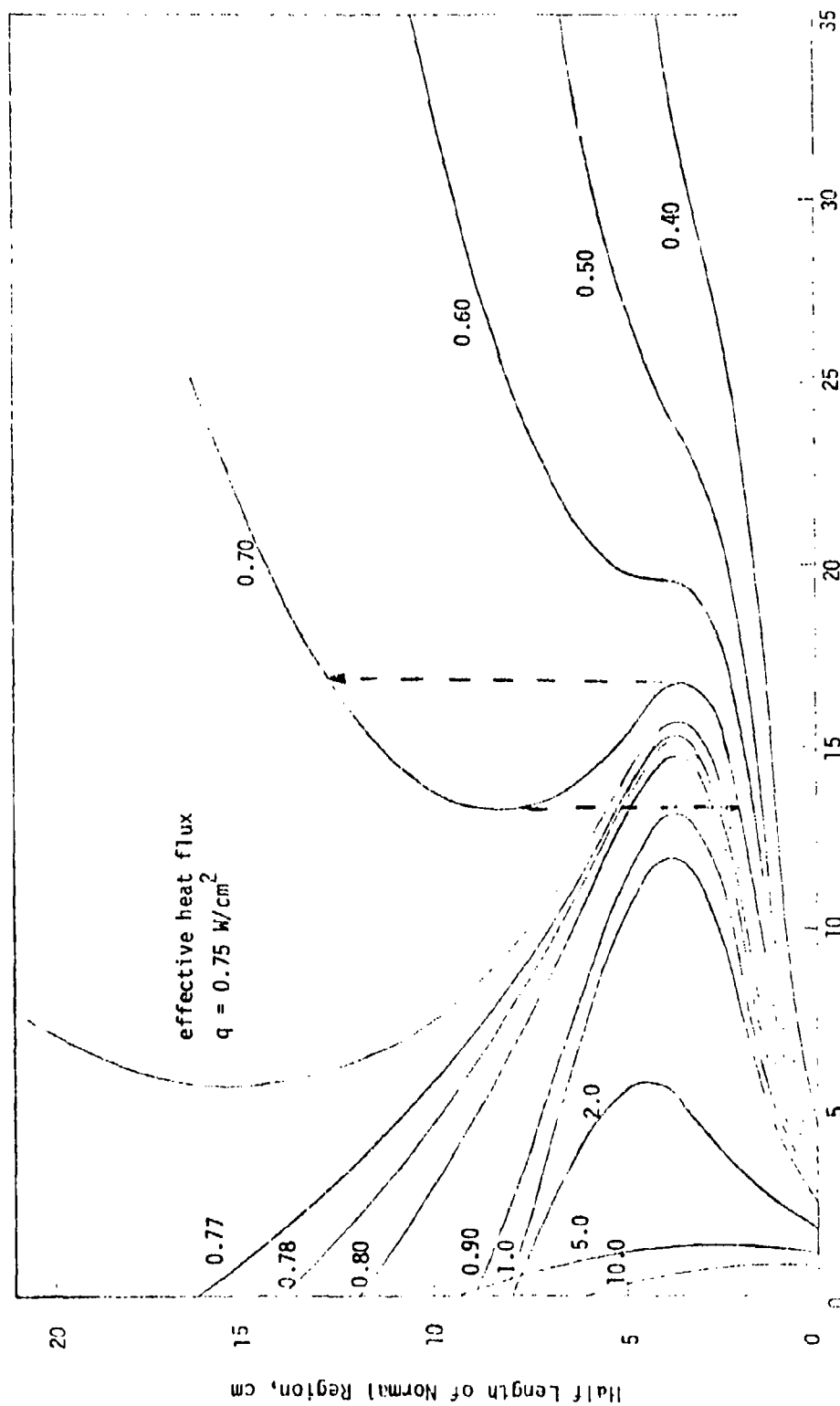
nonlinear, transient thermal behavior of the conductor. The equation is given by:

$$\gamma C_p(T) \frac{\partial T}{\partial t} - \frac{\partial}{\partial x} (k(T) \frac{\partial T}{\partial x}) = q_{\text{heat}}^{(T)} / \text{length} - q_{\text{cool}}^{(T)} / \text{length} \quad (6)$$

where  $\gamma$  is the conductor mass density and  $C_p(T)$  and  $k(T)$  are the temperature dependent conductor specific heat and thermal conductivity respectively. The right hand side of equation (6) consists of temperature dependent heating and cooling terms. The heating term is composed of external heating and resistive heating. The cooling term represents the convection of heat to the helium. Appendix B presents the details of the terms in the right hand side of equation (6).

Initially, Equation (6), without the transient term, was used to investigate the steady state behavior of the conductor in the neighborhood of a steady heat input. Figure 81 shows the normal region half-length versus net heating for a range of effective surface heat fluxes. The net heating is the external heat input plus the resistive heating minus the convective cooling. The half-length is the distance along the conductor from the point heat source to the location at which the temperature is low enough for the superconductor to retain the current. The temperature distribution is symmetric about the point at which the heat is applied.

The figure can be explained with the aid of the following example. For an effective surface heat flux of  $1.0 \text{ W/cm}^2$  and for net heating less than  $3 \text{ W/cm}^2$ , there is no normal region. For heating between 3 and  $13 \text{ W/cm}^2$  a normal region forms. The half-length of this region increases with increasing heating up to approximately 4 cm. If the heating is increased about the  $13 \text{ W/cm}^2$  level, the half-length goes to infinity, i.e., the entire conductor goes normal which implies a quench has taken place.



Net Heating per Unit Conductor Cross Section, 5. W/cm<sup>2</sup>  
Figure 81 Half Length of Normal Region Versus Heat Input

If the heating is set at  $13 \text{ W/cm}^2$  and a perturbation introduced, and the heating reduced in a quasi-steady manner, the normal region length will increase slightly with decreasing heating. Once the heating is reduced to zero a normal region remains. The half-length is approximately 8 cm. This situation corresponds to one in which the resistive heating equals the convective cooling with no external heat input.

If the effective surface heat flux is  $.70 \text{ W/cm}^2$  and the net heating is quasi-steadily increased to  $17 \text{ W/cm}^2$  and incremented, the normal region will increase rapidly with the last increment from approximately 4 cm to 13 cm., i.e., the upper portion of the curve. If the heating is then reduced slowly the half-length is slowly reduced until the heating reaches about  $13 \text{ W/cm}^2$  and the half-length decreases rapidly from 9 cm to 3 cm. This path is indicated by the dashed lines.

The lower effective heat fluxes do not exhibit the instability with respect to the length of the normal region. However, it should be noted that the assumption of infinite volume of available helium is inherent in the algorithm.

Figures 82 and 83 are cross plots of the information in Figure 81. Figure 82 shows the half-length of the normal region versus the effective heat flux for Zero heating. The lengths are determined as in the first example. That is, the heating is increased quasi-steadily until the "take-off" point is reached. The state is perturbed and the heating quasi-steadily decreased to Zero leaving a non-Zero normal region length. The curve shown in the figure effectively divides the region into a stable and unstable subregions. The curve itself represents a metastable point. For a given effective surface heat flux and Zero net heating normal region with half-lengths less than the value on the curve will shrink. For half-lengths greater than the value on the curve the region will propagate.

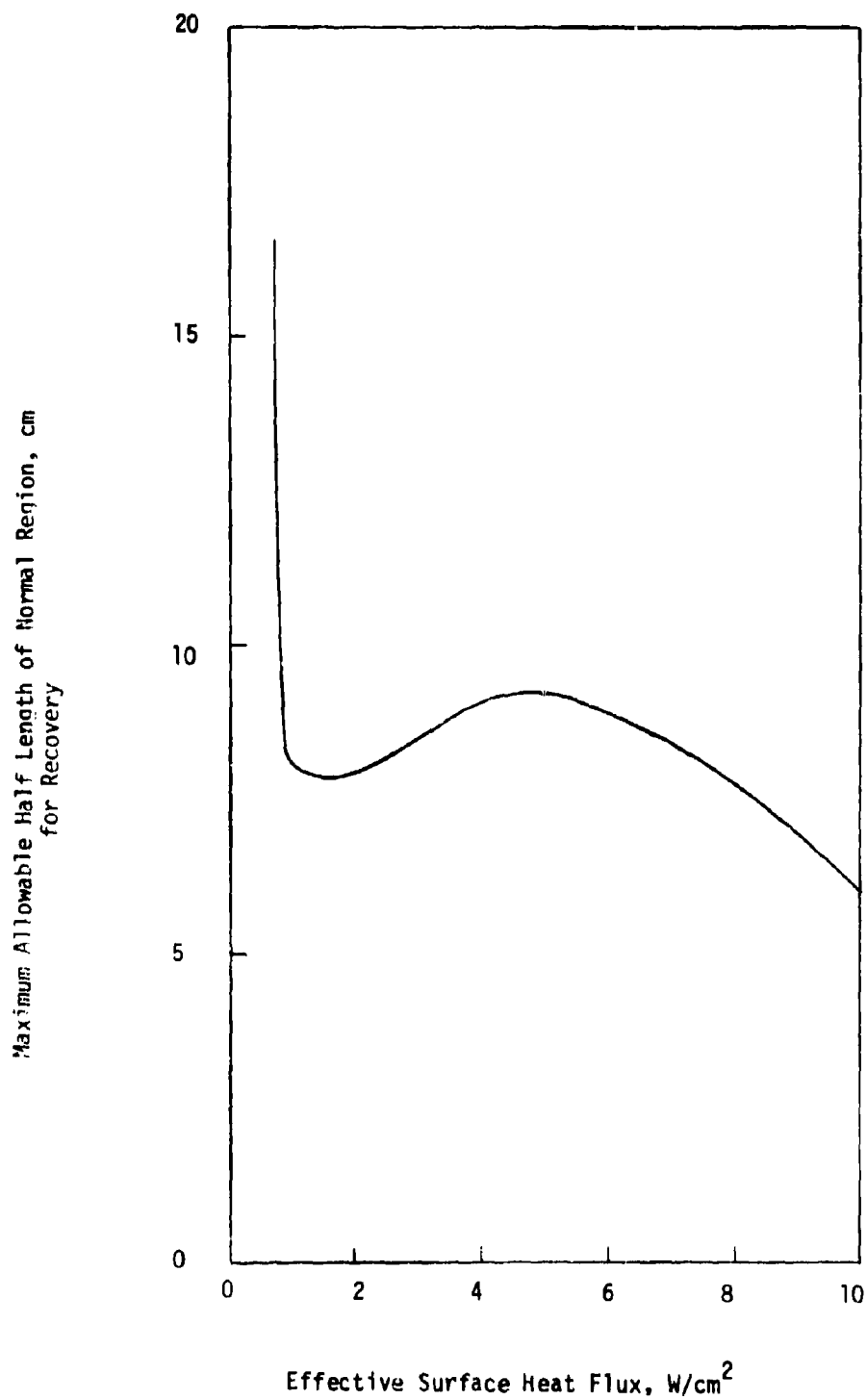


Figure 82 Half Length of Normal Region versus Effective heat Flux

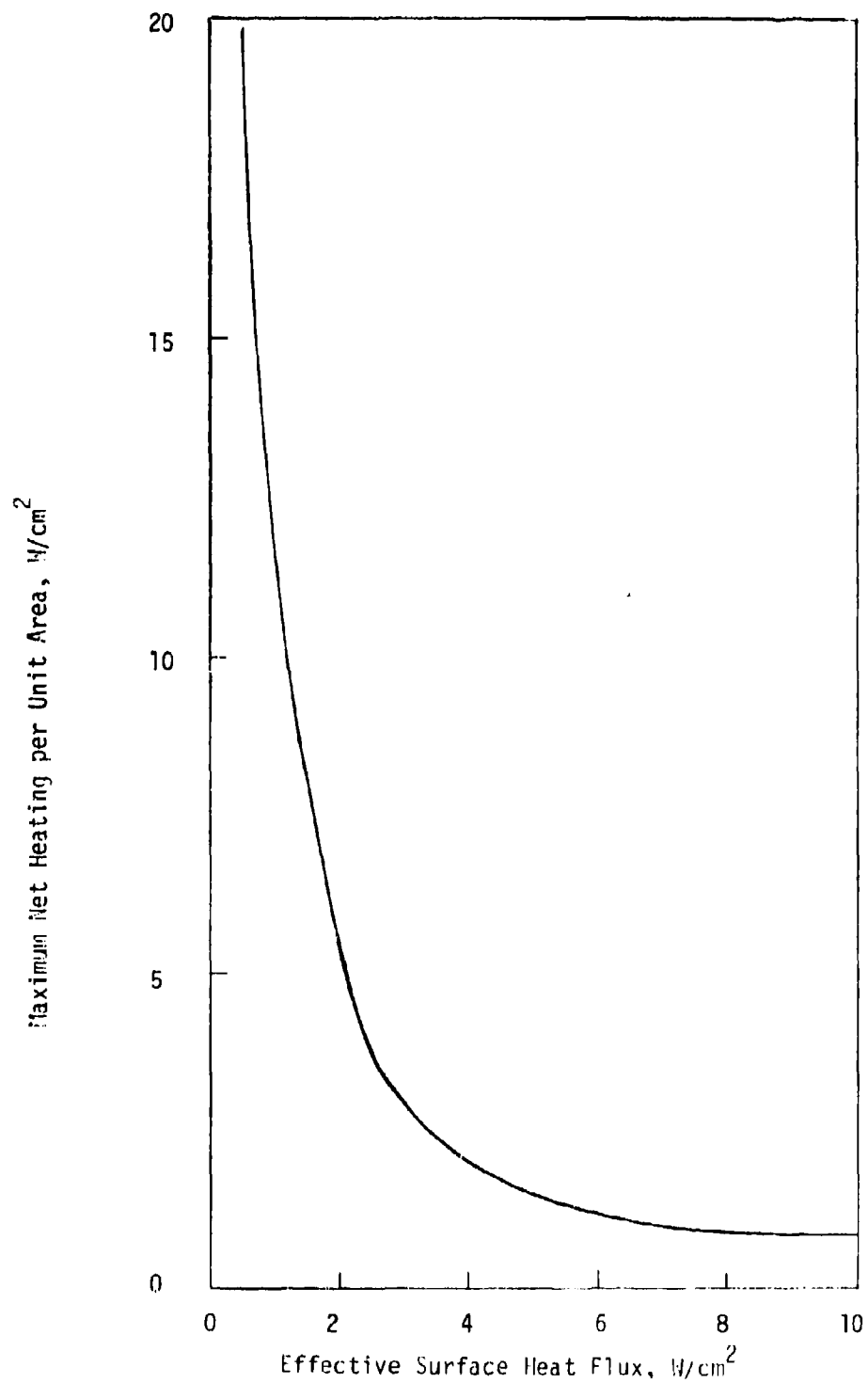


Figure 83 Maximum Net Heating versus Effective Heat Flux



Figure 83 shows the maximum net heating versus the effective surface heat flux. The curve corresponds to the point at which the normal region half-length will propagate if the heating is perturbed; e.g., for  $q''_{\text{eff}} = 1.0 \text{ W/cm}^2$ ;  $s = 13 \text{ W/cm}^2$ . This curve also divides the region into two sub-regions. For a net heating and at a surface heat flux that represents a point on or below the curve, the normal region is either stable or metastable. Points above the curve represent unstable normal regions.

The effective surface heat fluxes that were calculated for the two chosen conductors are  $.5 \text{ W/cm}^2$  for the  $15,000 \text{ A/cm}^2$  design and  $1.3 \text{ W/cm}^2$  for the  $30,000 \text{ A/cm}^2$  design. Using the preceding steady state criteria the  $15,000 \text{ A/cm}^2$  design remains stable for all values of steady state net heating. The  $30,000 \text{ A/cm}^2$  design, on the other hand, remains stable for net heating below approximately  $8 \text{ W/cm}^2$ .

Although the criteria established above is useful, the primary heating of conductor will most likely occur due to a frictional slip energy input. Since the slip is a nonsteady phenomena the transient thermal behavior of the conductor must be investigated. To this end, Equation (6) was solved with a forward time and spatial marching finite-difference algorithm. The heating term on the right-hand side of Equation (6) consisted of the resistive heating plus a heat pulse to simulate the frictional energy input. A current density of  $15,000 \text{ A/cm}^2$  was assumed.

Figure 84 shows a typical output from the algorithm. The figure shows the temperature versus position profiles along the conductor for various times. The heat pulse was assumed to be  $.14 \text{ J}$ . The pulse occurs at an axial position of 0 and over a  $.13 \mu \text{ sec}$  pulse time. It can be seen that for these inputs the conductor recovers to the superconducting state after  $17 \mu \text{ sec}$ . The peak temperature is  $9.5 \text{ K}$  and the maximum normal length is approximately  $2.5 \text{ cm}$ .

Figure 85 shows the normal region half-length as a function of time for various heat pulse inputs. The pulse time was .13  $\mu$  sec for each heat pulse. The heat pulses are up to and including .24 J. It can be seen that for pulses less than .24J the conductor recovers. The .24J appears to produce a metastable condition and pulses larger than .24J will cause the normal region to propagate.

The stability of the basic conductor configuration chosen for the model magnet has been demonstrated by the analyses presented. The advantages of a nonpotted design appear to far outweigh the disadvantages from the stability standpoint. Similarly, the partial solder-filling of the braid has a dramatic affect on the ability of the conductor to withstand local heat input. The structural deflection limits appear to be reasonable. During Phase II these stability analyses will be continued and extended to ensure a high level of confidence in the final conductor design.

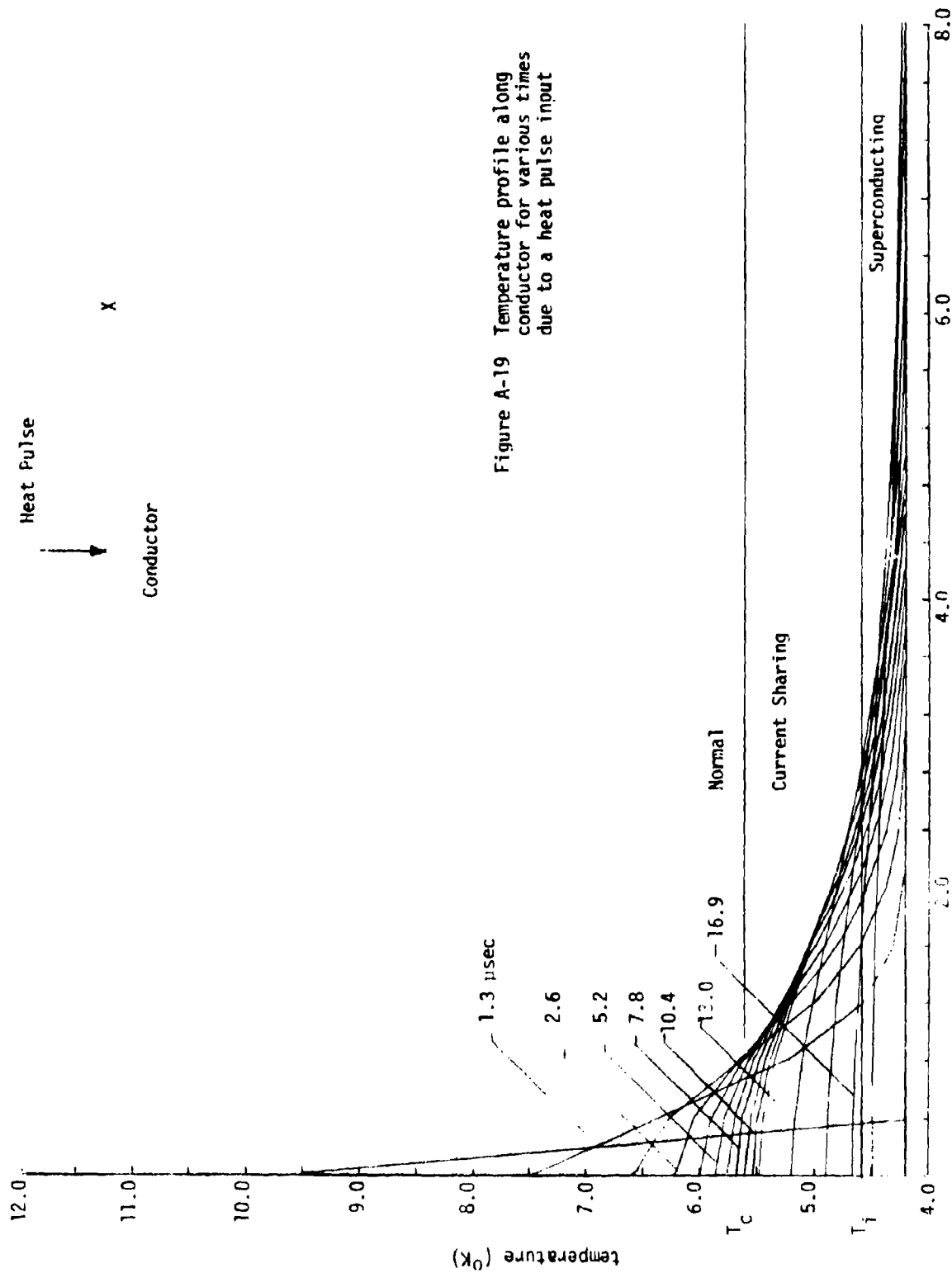


Figure A-19 Temperature profile along conductor for various times due to a heat pulse input

Figure 84 Distance Along Conductor (cm)

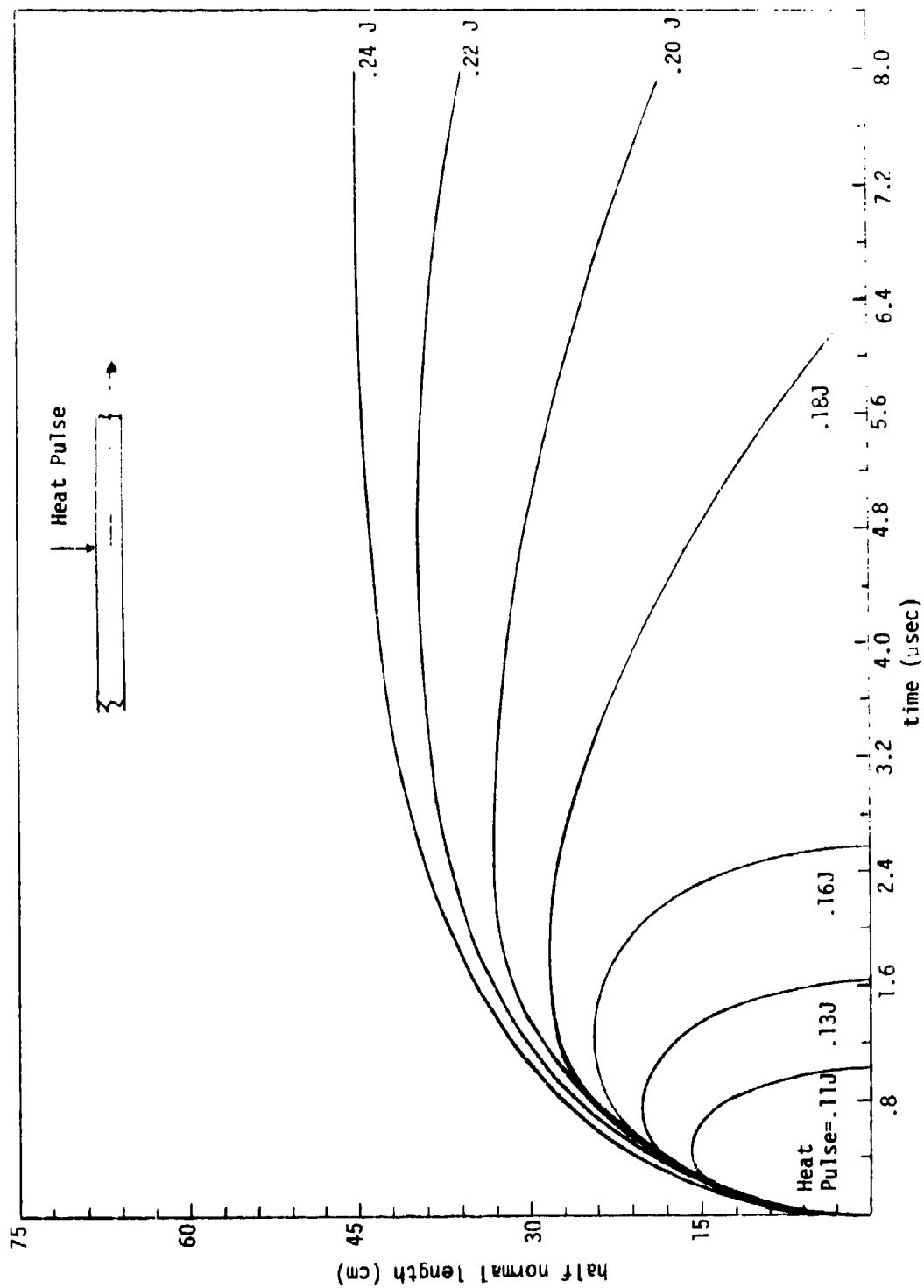


Figure 85 Conductor Half Normal Length Versus Time for Various Heat Pulse Inputs

## SECTION VII

### SYSTEM CHARGE, DISCHARGE, AND QUENCH

The MHD magnet operates in the DC mode. Transient electrical effects occur, however, during the magnet charge, discharge, and quench as well as during the MHD channel operation. Too rapid a charge or discharge can cause induced eddy current resistive heating high enough to boil off significant amounts of helium. Indeed, the rapidity of the process could potentially induce a quench. Preliminary analyses were performed to investigate the likelihood of such occurrences and to assess the risk to the system.

In order to characterize the performance of the magnet system during ordinary charge and discharge as well as quench a lumped parameter model of the magnet and its structure was developed.

Figure 86 shows the three circuits with  $L_1$  representing the main magnet,  $L_2$  the self-inductance of the conduction path in the system's metallic structure, and  $M$  is the mutual inductance between the magnet and the structure.  $R_2$  is the resistance of the current path through the structure, and  $R_1$ , when present, represents either the dump resistor (during ordinary discharge) or the propagating normal region (during a quench).

Each model is normalized to facilitate the comparison of scaling effects. The real time variables are represented by lower case symbols,  $i_1$ ,  $i_2$ ,  $p_1$ ,  $p_2$ ,  $e_1$ , and  $e_2$ , the current, power and energy dissipated in the magnet circuit (sub 1) or the structure (sub 2). The full operating current is  $i_{op}$ , and  $t$  is time.  $V_0$  is the charging voltage on the system.

Upper case symbols are used to represent the normalized variables as defined in Figure 87. The normalized differential equations have been solved for each of the three modes of system operation.

Using the 29 cm low current density design values, typical curves were generated showing normalized current, power and energy vs. normalized time for

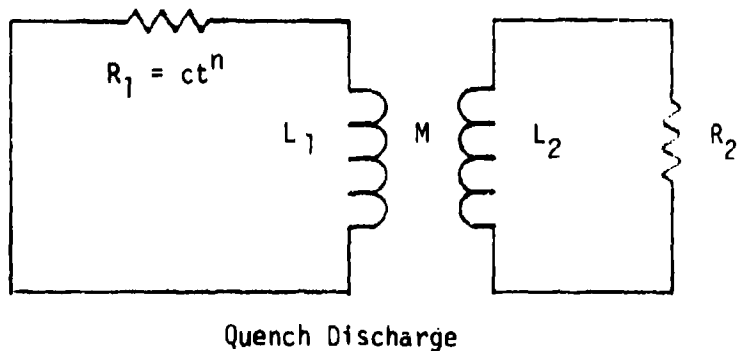
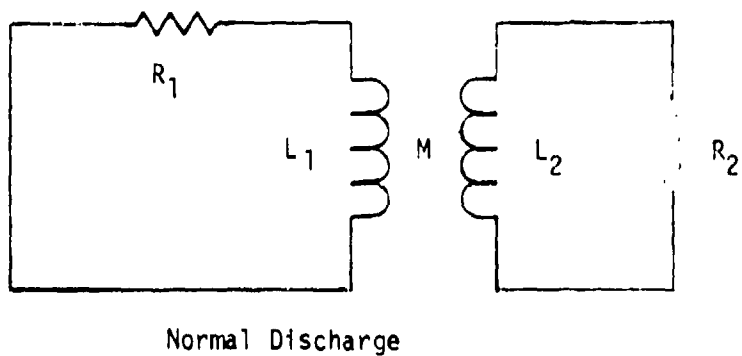
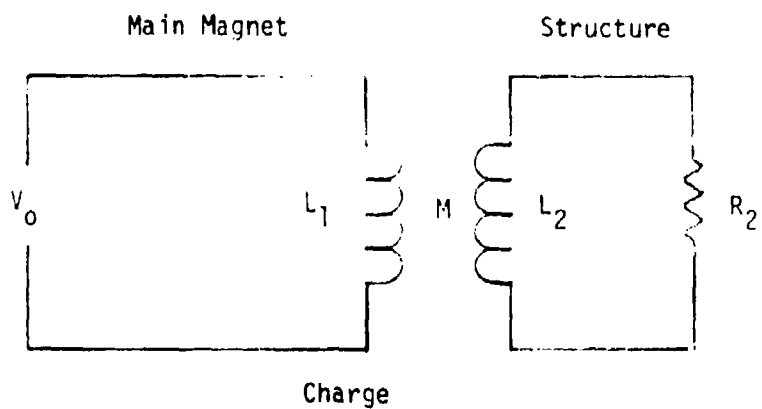


Figure 86 Circuit Models for Magnet Protection

### Ordinary Charge

$$\frac{dI_1}{d\tau} + k \frac{dI_2}{d\tau} - 1 = 0$$

$$\frac{dI_2}{d\tau} + AI_2 + k \frac{dI_1}{d\tau} = 0$$

where

$$I_1 = \frac{i_1}{i_{op}}$$

$$I_2 = \sqrt{\frac{L_2}{L_1}} \frac{i_2}{i_{op}}$$

$$\tau = \frac{t}{t_0}$$

$$k = \sqrt{\frac{M}{L_1 L_2}}$$

$$A = \frac{R_2}{L_2} t_0$$

and

$$t_0 = \frac{L_1 i_{op}}{V_0}$$

### Ordinary Discharge

$$\frac{dI_1}{d\tau} + BI_1 + k \frac{dI_2}{d\tau} = 0$$

$$\frac{dI_2}{d\tau} + AI_2 + k \frac{dI_1}{d\tau} = 0$$

with additionally

$$B = \frac{R_1}{L_1} t_0$$

and

$$t_0 = 1$$

Figure 87

# Quench discharge

$$\frac{dI_1}{d\tau} + \tau^n I_1 + k \frac{dI_2}{d\tau} = 0$$

$$\frac{dI_2}{d\tau} + AI_2 + k \frac{dI_1}{d\tau} = 0$$

where the normal region resistance is of the form

$$R_{NR}(t) = ct^n \text{ with } c \text{ and } n \text{ constants.}$$

In each case

$$E = \frac{\int_0^t i^2 R dt}{\frac{1}{2} L_1 i_{op}^2}$$

$$\text{and} \quad P = \frac{d}{d\tau} E(\tau)$$

Figure 87 (continued)



each mode. Figure 88, 89, 90, and 91 are illustrative of the results obtained in this analysis.

In order to gauge the helium lost during the magnet charge, the eddy current heating of a structure must be evaluated. For a range of charge times Figures 92 and 93 indicate the total energy dissipated in the structure during the charging sequence. If 4 liters of helium (10,000 Joules) is considered an acceptable loss due to structural eddy currents then Figure indicates the magnet may be charged in about 15 seconds. Figure shows the energy dissipated in the structure during an ordinary discharge (magnet is superconducting) for a range of discharge time constants. The corresponding dump resistor values are from  $0.022\Omega$  to  $15\Omega$ , and initial terminal-to-terminal potentials of 44 to 30,000 V. To keep the internal loss under 10,000 J, a time constant of 7 seconds is acceptable. This corresponds to a resistance of 0.52 and an initial voltage of 430 V end-to-end.

The quench is a slow enough process that the structure with a time constant of 0.025 seconds is not effective in absorbing energy. The analysis shows less than one percent of the system energy will be dissipated in the structure.

By limiting the rapid charges to be slower than 15 seconds and the discharges to have a time constant greater than 7 seconds, a reasonable design is possible. During a quench, the structural effects can be ignored.

The consequences of a quench in a large magnet system can be catastrophic. The effects of a quench in each of the systems has been studied to determine what level of protection is necessary to prevent permanent damage.

The resistive heating of a normal region is sufficient to generate high local temperatures at the point where the quench initiated. This peak temperature cannot exceed the melting point of solder, approximately 480 K. The voltage drop across the resistive region can also be great enough to endanger the insulation integrity; following standard practice, 50 volts per mil of insulation is a reasonable limit for long term endurance.

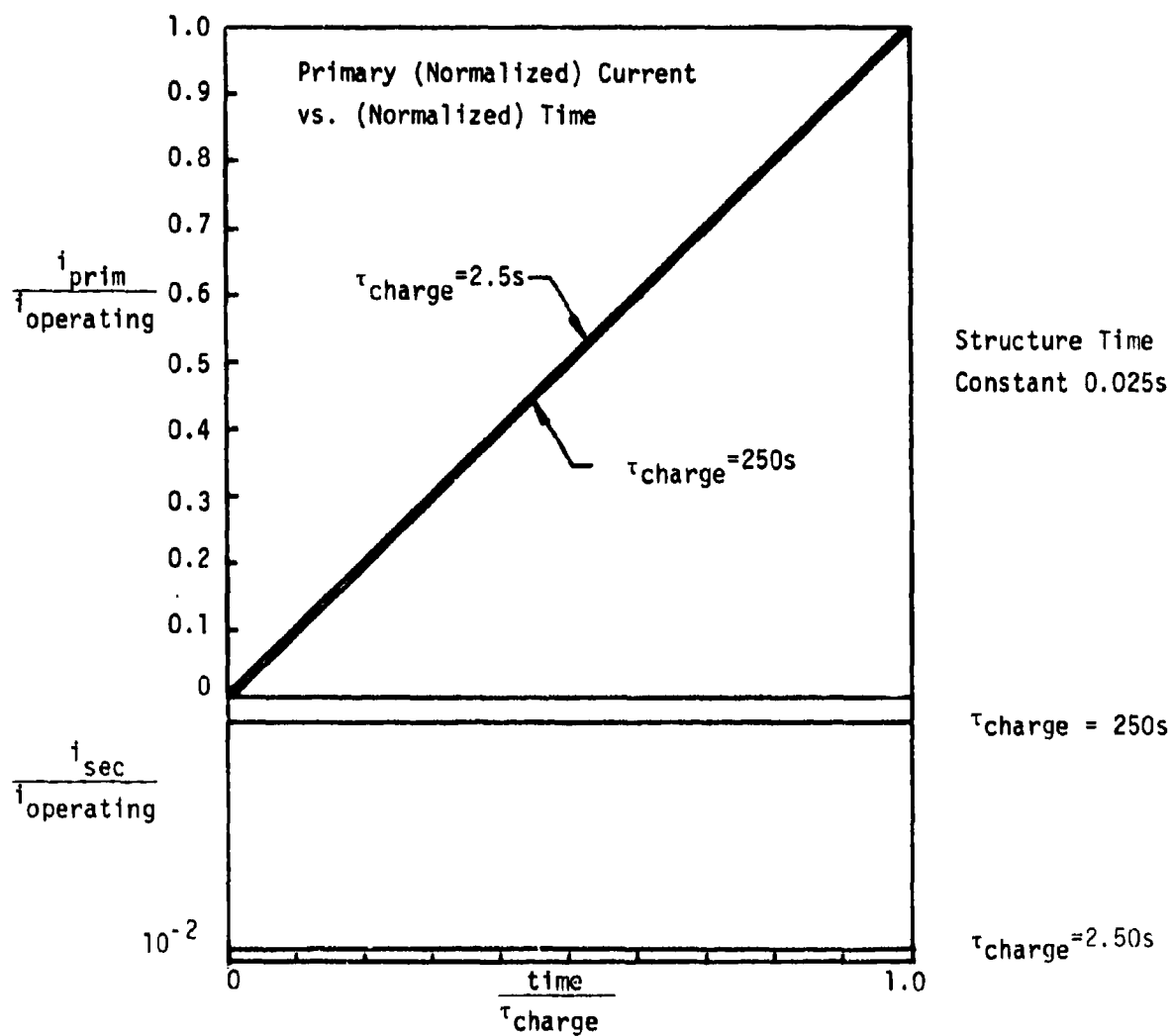


Figure 88 Secondary (Normalized) Current vs. (Normalized Time)

FA-4838

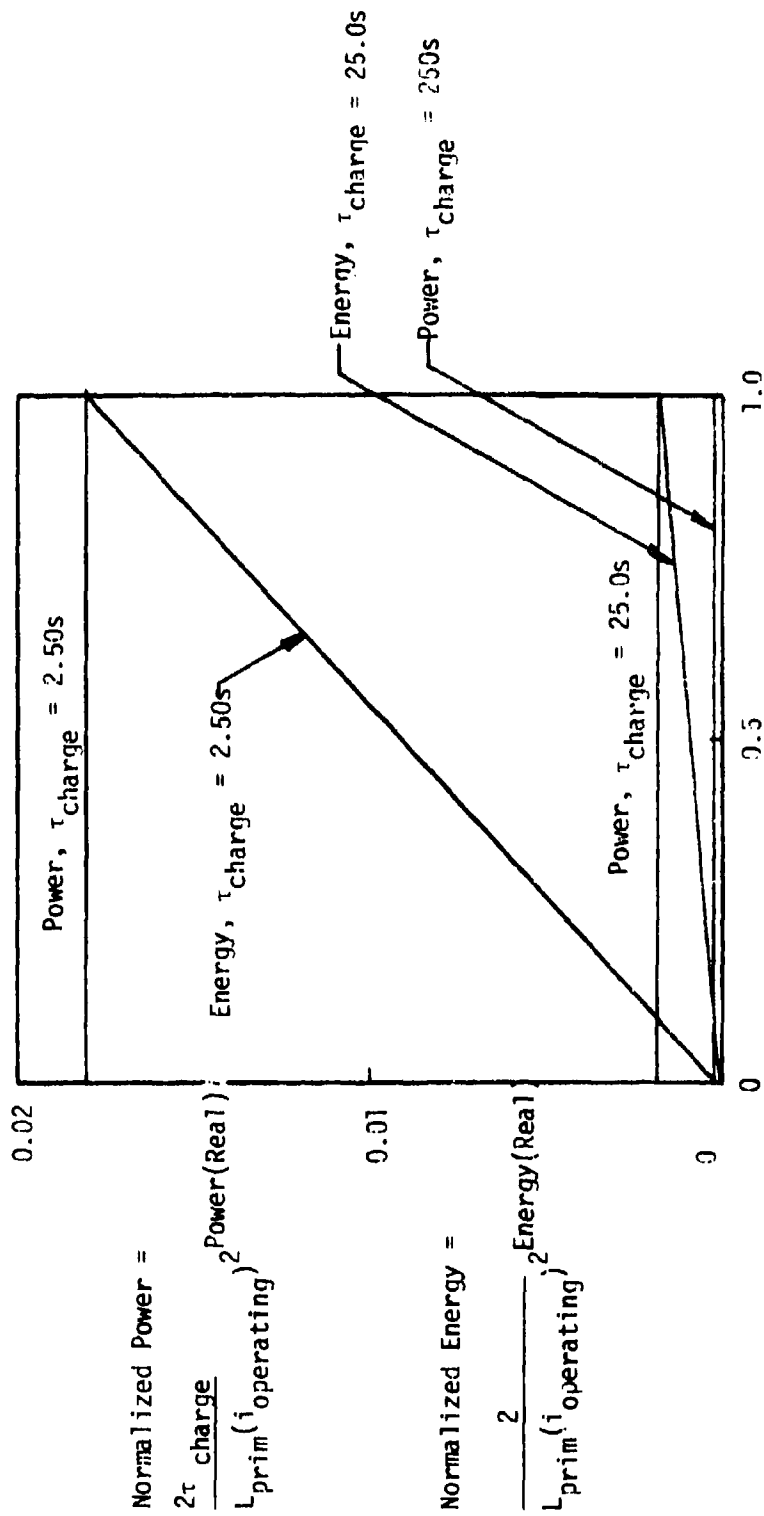


Figure 89 Power (Normalized) and Energy (Normalized) Dissipated in Structure ( $\tau_{\text{struct}} = 0.025\text{s}$ ) for Several Charge Rates Versus (Normalized) Time

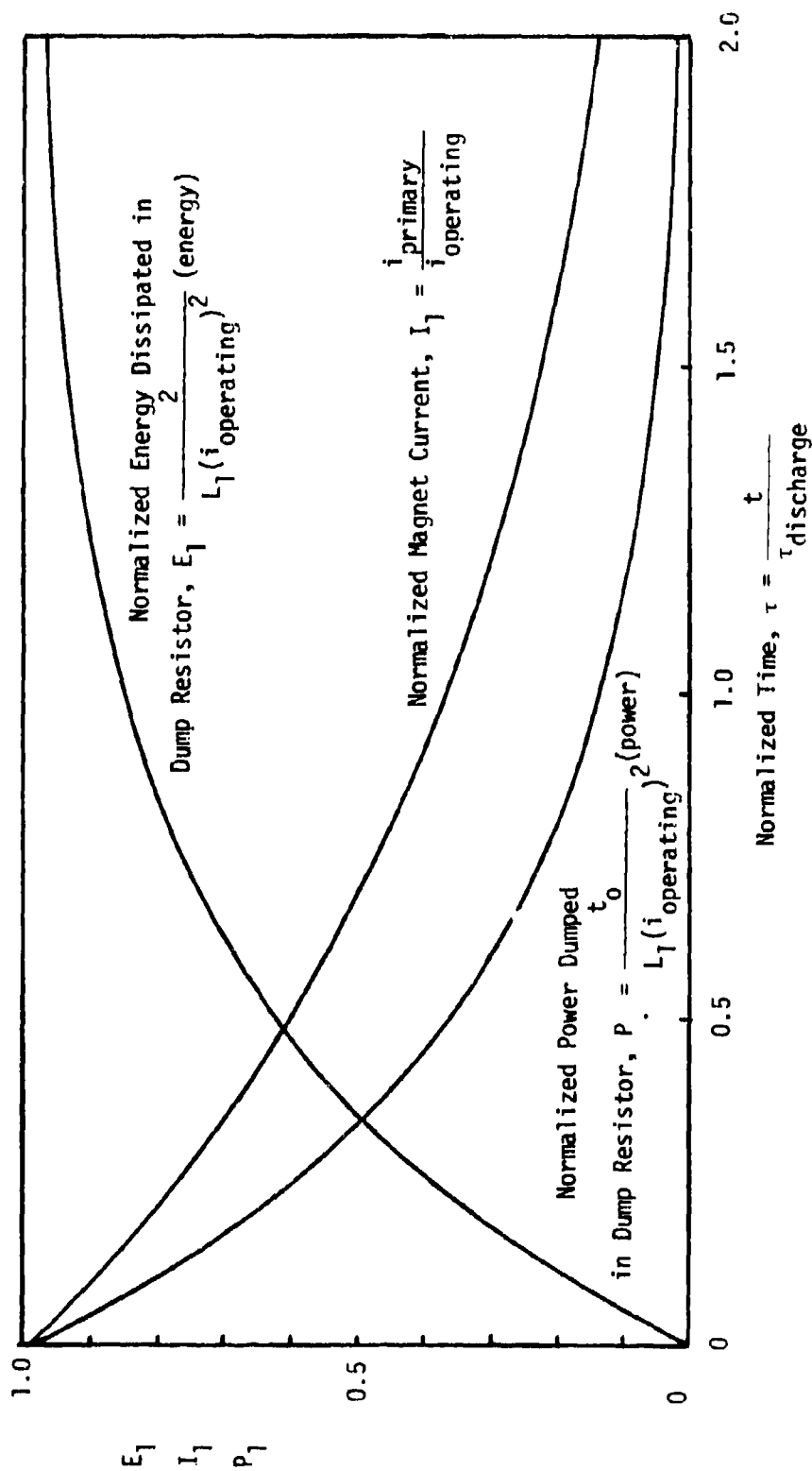


Figure 90 Normalized Magnet Current, Normalized Dumped Power and Normalized Dumped Energy versus Normalized Time for System Discharge ( $\tau = 2.0s$ ) with Structure Time Constant ( $\frac{L}{R} = 0.025s$ )

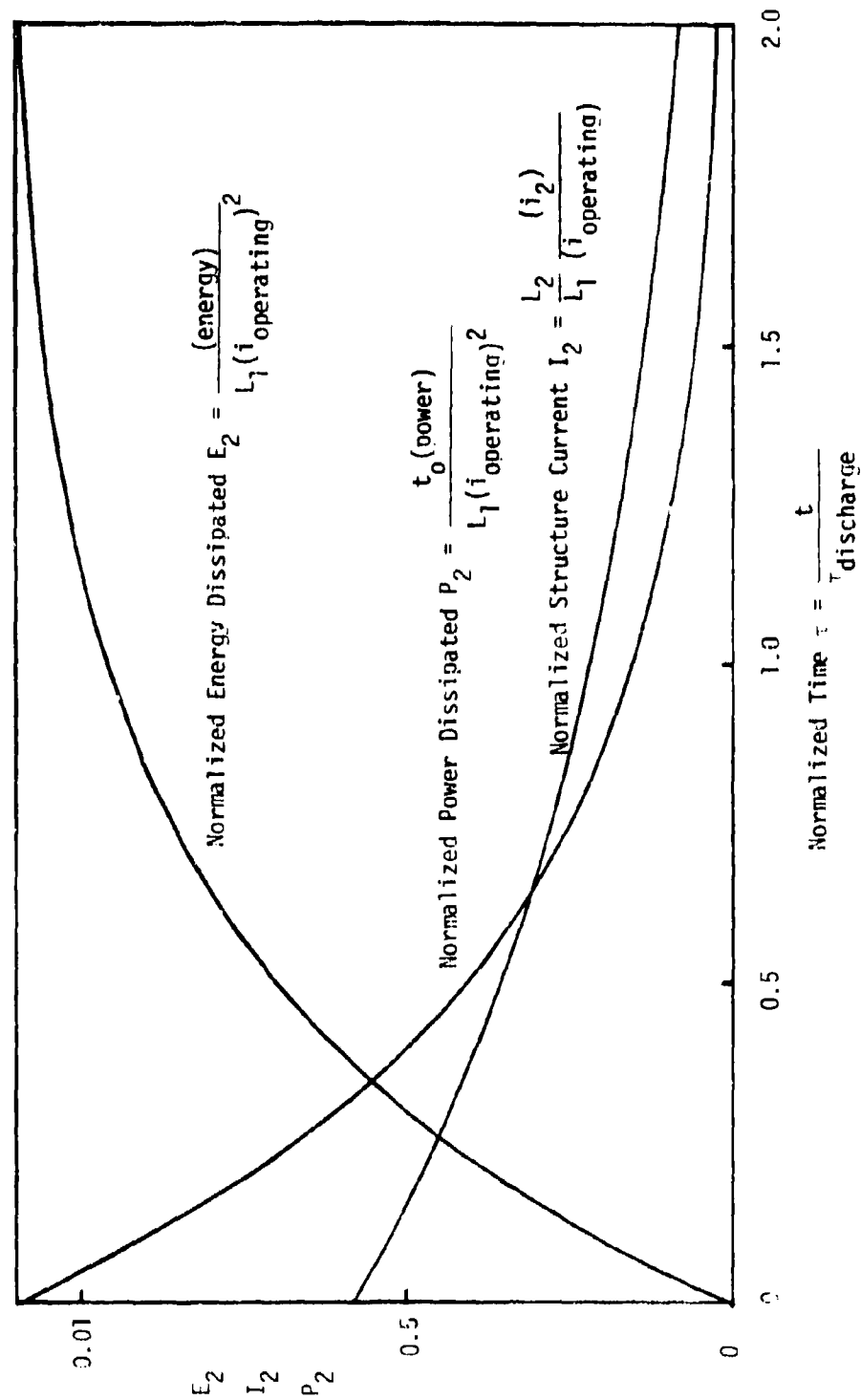


Figure 91 Normalized Structure Current, Normalized Dissipated Power and Normalized Dissipated Energy versus Normalized Time for System Discharge ( $\tau = 2.0\text{s}$ ) with Structure Time Constant ( $\frac{L}{R} = 0.0253$ )

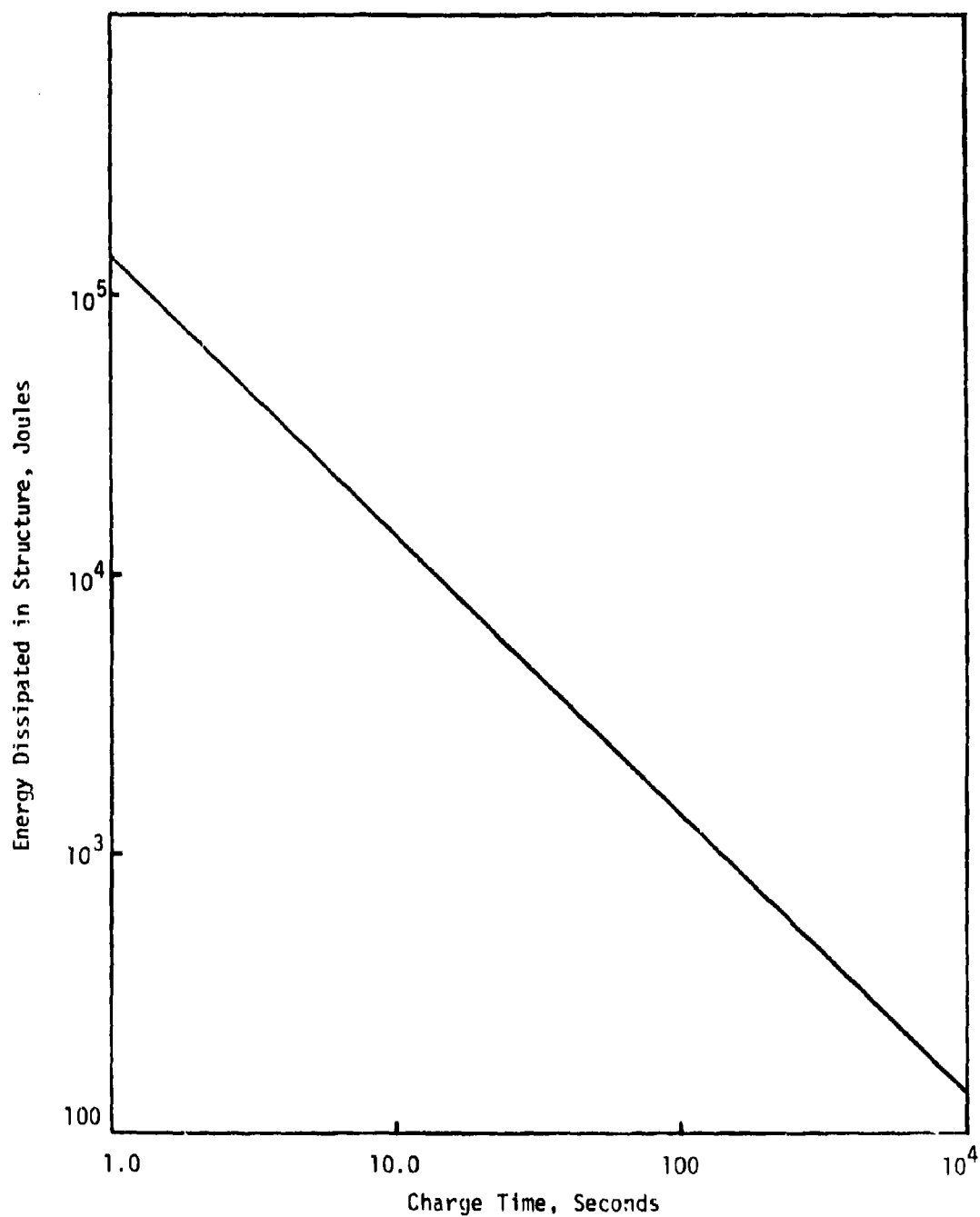


Figure 92 Energy Dissipated in Structure vs. Charge Time of Magnet System

FA-4836

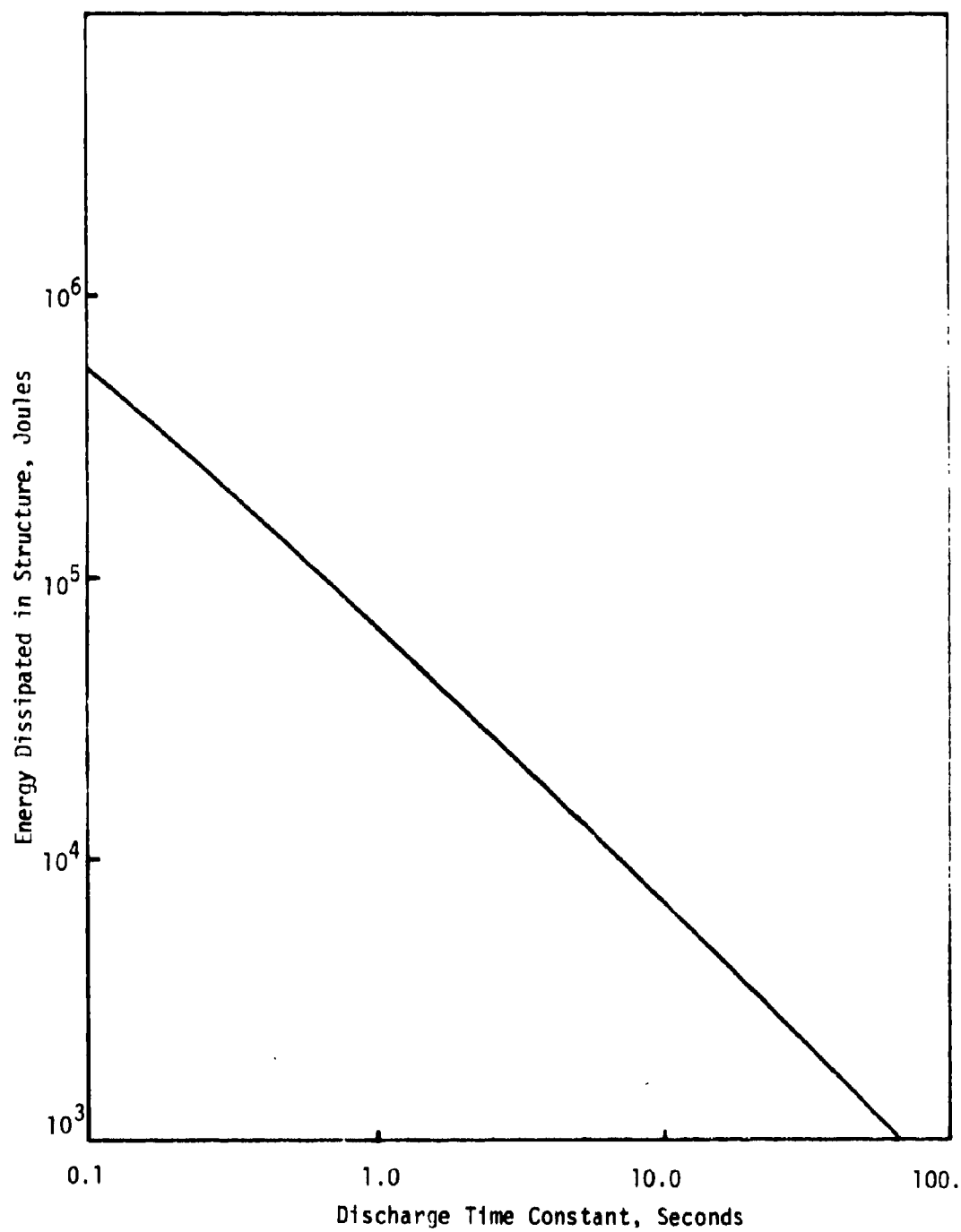


Figure 93 Energy Dissipated in Structure vs. Discharge Time Constant of Magnet System

It has been found in some previous designs that the inductive coupling between a coil and its associated structure can be great enough for the structure to dissipate via induced eddy current resistive heating a significant amount of the total magnet energy in the event of a rapid discharge. A model of a saddle winding undergoing a typical quench with structure similar to that proposed for this system indicates less than one percent of the total energy is dumped into the structure. Figures 94 and 95 show the expected current power and energy versus time profiles for this model. Since only a small fraction of the total energy was found to be dissipated in the structure, it was necessary to perform a more detailed analysis of the magnet quench.

The performance of a magnet system during a quench can be characterized if the conductor design specifications and the operation environment are known. The propagation of the normal region is determined by the properties of the conductor at its critical temperature exposed to an ambient magnetic field with the operating current extant. Tables 15 and 16 show the conductor specifications for the two conductors and the environment experienced in each of the four magnet sizes. Due to the difficulties involved in describing the critical current density versus temperature curve at an average field for a magnet, we have used a value of 6.6 K for each system. This represents the critical temperature for these conductors exposed to a 1.2 Tesla environment. A lower value for  $T_c$  would result in less damaging results during a quench due to the increase in velocity of propagation of the normal region.

The model of a magnet quench assumes adiabatic resistive heating of the conductor bundle (superconductor, stabilizer, and insulation). Calculations indicate that the heat conduction along the conductor is a negligible effect on the temperature at the point where the heat was generated, so the adiabatic assumption is reasonable. There is enough conduction for the normal region to propagate, but the energy involved in raising the temperature of the conductor a few degrees is small compared to that available. As the quench proceeds,



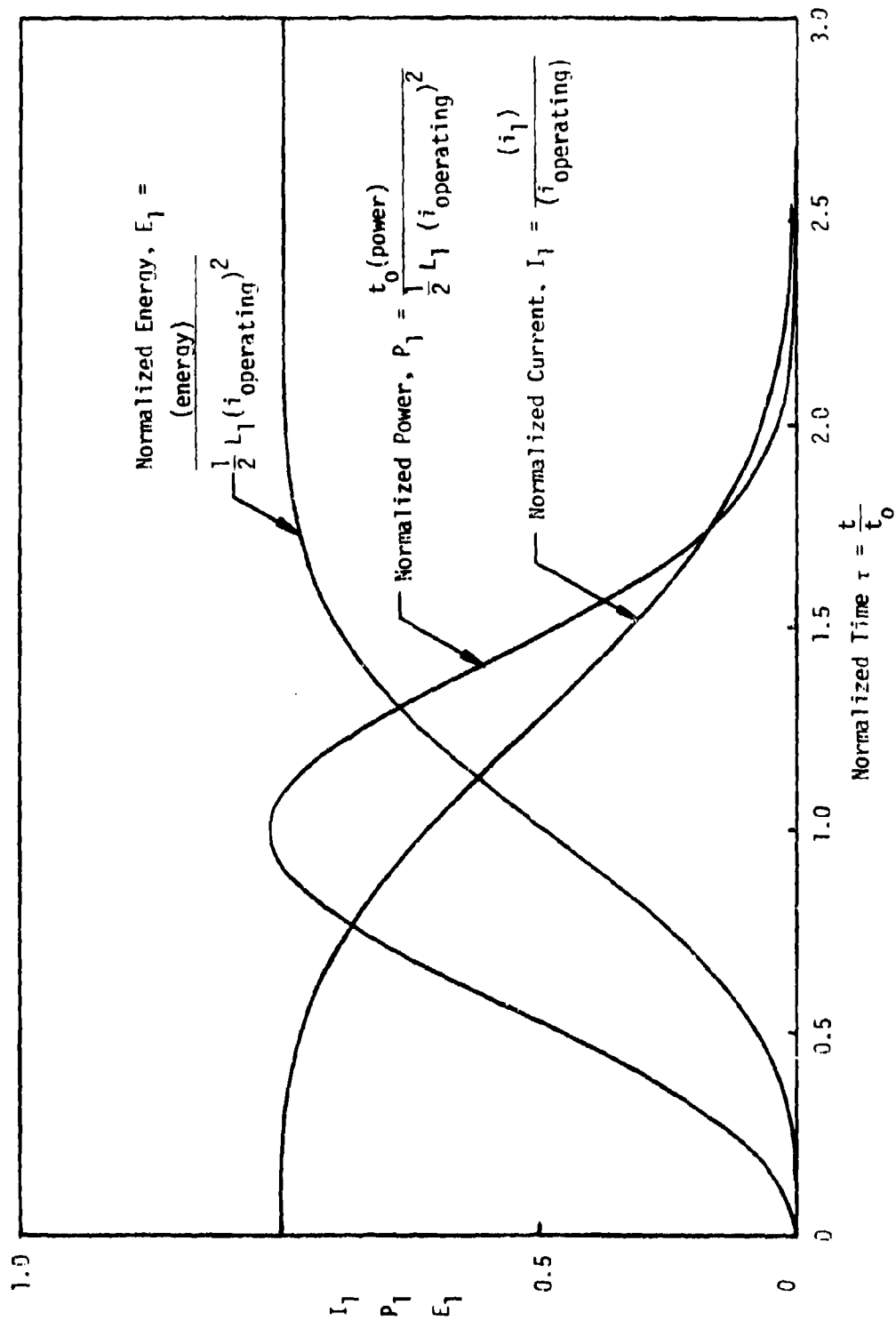


Figure 94 Normalized Magnet Current, Normalized Internally Absorbed Power and Normalized Internally Absorbed Energy in Quenching System versus Normalized Time with Structure Time Constant  $(\frac{L}{R}) = 0.025s$

$$R_N = 9.4 \times 10^{-4} \text{ } \Omega$$

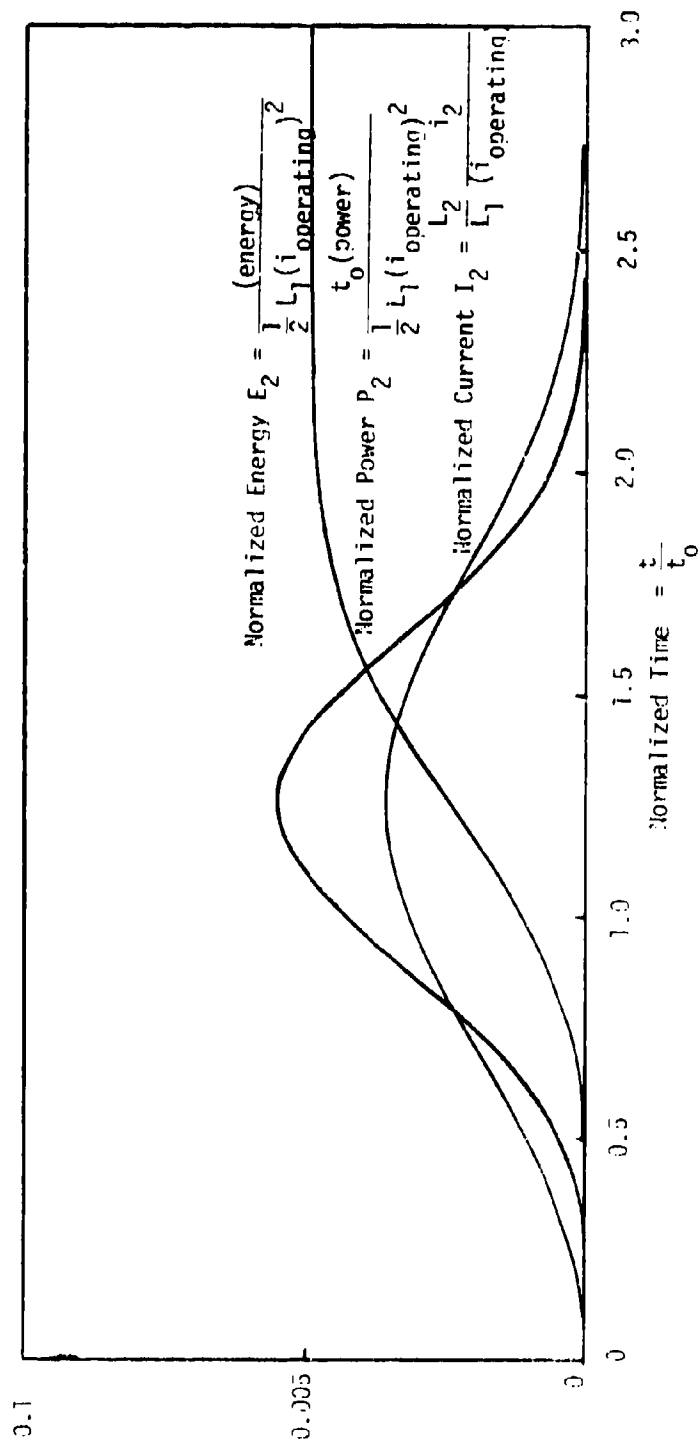


Figure 95 Normalized Structure Current, Normalized Structure Dissipated Power and Normalized Structure Dissipated Energy in Quenching System vs. Normalized Time with Structure Time Constant  $(\frac{L}{R}) = 0.025s$   
 $R_N = 9.4 \times 10^{-2} t^2$

TABLE 15  
CONDUCTOR SPECIFICATIONS FOR QUENCH ANALYSIS

Conductor Current Density, $\text{kA/cm}^2$	15	30
Conductor Cross-Sectional Area, $\text{cm}^2$	0.355	0.266
Copper-to-Superconductor Ratio	5.0:1	3.0:1
Packing Factor	0.52	0.48
Initial Resistivity of Stabilizer, $\Omega\text{-cm}$	$3.4 \times 10^{-8}$	$3.4 \times 10^{-8}$
Magnetoresistivity, $\Omega\text{-cm}$	$2.7 \times 10^{-8}$	$2.7 \times 10^{-8}$
Heat Capacity of Bundle, $\text{J/cm}^2\text{-K}$	0.205	0.21
Bath Temperature, K	4.2	4.2
Critical Temperature, K	6.6	6.6
Axial Thermal Conductivity, $\text{W/cm-K}$	18.2	16.4
Ratio of Normal Front Propagation Velocity in Transverse Direction to Velocity in Axial Direction	0.021	0.020
Ratio of Normal Front Propagation Velocity in Transverse Direction to Velocity in Axial Direction	0.093	0.086

TABLE 16  
WINDING SPECIFICATIONS FOR QUENCH ANALYSIS

<u>15 kA/cm<sup>2</sup> Conductor</u>				
Bore Inlet Diameter, cm	20	29	40	50
Coil Inductance, H	0.73	1.48	2.31	3.31
Operating Current, A	2000	2000	2000	2000
Dump Resistance (External), $\Omega$	0	0	0	0
Winding Volume, cm <sup>3</sup>	$9.63 \times 10^4$	$1.52 \times 10^5$	$2.04 \times 10^5$	$2.60 \times 10^5$

<u>30 kA/cm<sup>2</sup> Conductor</u>				
Bore Inlet Diameter, cm	20	29	40	50
Coil Inductance, H	0.65	1.38	2.15	2.98
Operating Current, A	2000	2000	2000	2000
Dump Resistance (External), $\Omega$	0	0	0	0
Winding Volume, cm <sup>3</sup>	$5.33 \times 10^4$	$8.72 \times 10^4$	$1.16 \times 10^5$	$1.44 \times 10^5$

additional resistive heating increases the temperature of the normal region, and also increases the normal region size. Changes in the material properties (resistivity and heat capacity) are accounted for with numerical curve fits of the variation with temperature. Iteration on this procedure gives a complete picture in time of the magnet's behavior during a quench. Figures 96 through 111 show the peak temperature and voltage versus time for the four magnet sizes at the two current densities.

The maximum voltage and the final temperature of the hotspot are then plotted versus the inlet warm bore diameter in Figures 112 and 113, for each current density. These figures indicate that the voltage levels are well within the range which can be handled by a standard (epoxy/glass) insulation system. The worst case, the 50 cm bore, 30 kA/cm<sup>2</sup> conductor develops close to 2 kV across the normal region, which involves 6.5% of the winding volume. There are 2690 turns in this magnet, so there are less than 12 V applied turn-to-turn. Two layers of 0.127 mm of insulation is 10 mils; 1.2 V/mil is well within the imposed limit of 50 V/mil.

The maximum local temperature of 880 K is observed in the same magnet system. This is well above the 480 K limit. In fact, only the two smallest systems at the low current density have peak temperatures below the solder melting point.

The best method of reducing the maximum temperatures in the magnet systems is to increase the spread of the normal region. The same energy (stored in the magnetic field) will be dissipated over a larger region, reducing the peak temperature at the expense of greater potential difference across the coil, and a higher average temperature.

Means of increasing the spread of the normal region can be completely passive. Design changes, for example, increasing the transverse propagation velocity by reducing the turn-to-turn insulation, or adding thermal conduction paths inside the windings, are possible solutions. One method used at MCA on previous

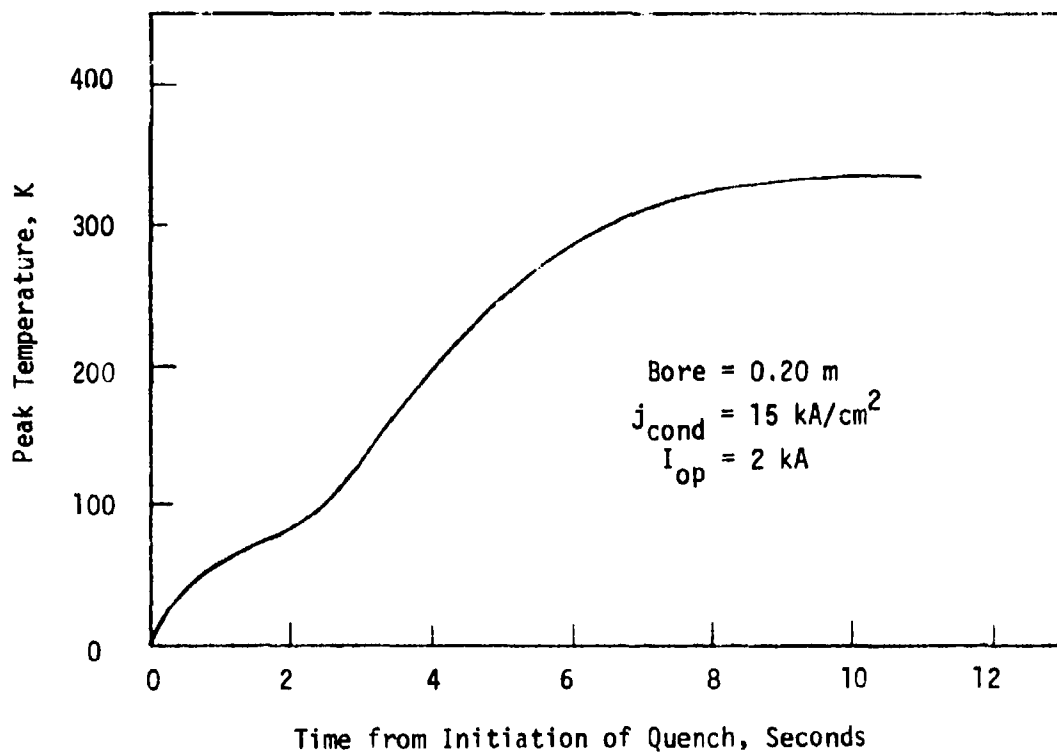


Figure 96 Peak Temperature vs. Time for an MHD Magnet Undergoing a Quench from Operating Current

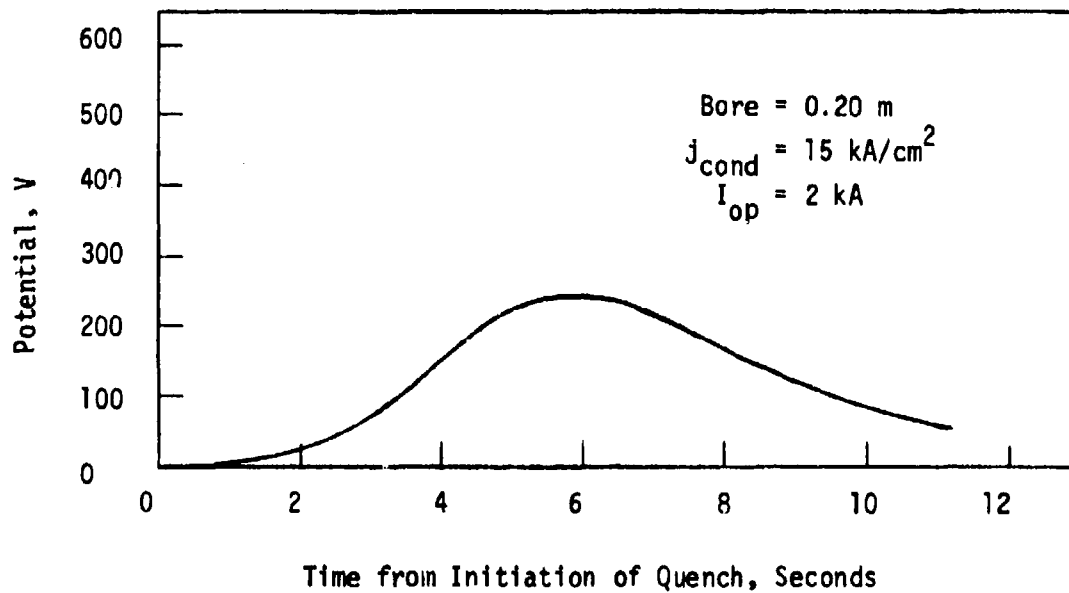


Figure 97 Potential Difference Across Normal Region vs. Time for an MHD Magnet Undergoing a Quench from Operating Current

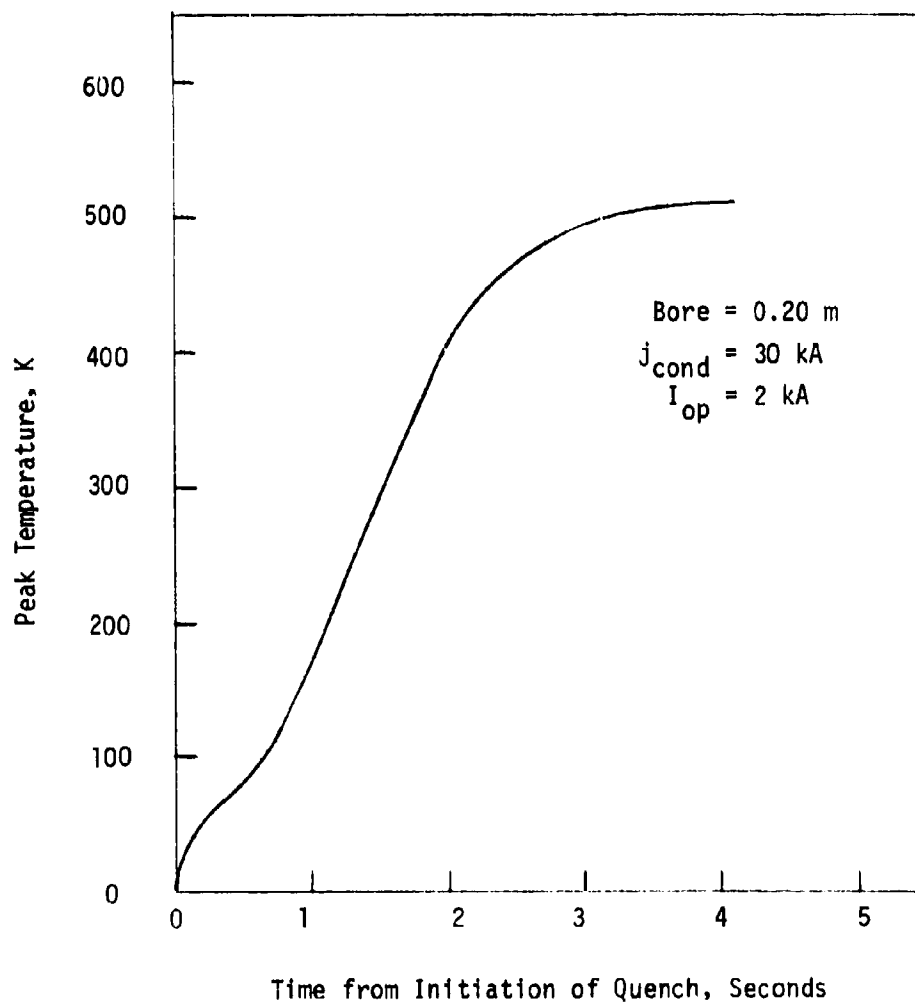


Figure 98 Peak Temperature vs. Time for an MHD Magnet Undergoing a Quench from Operating Current



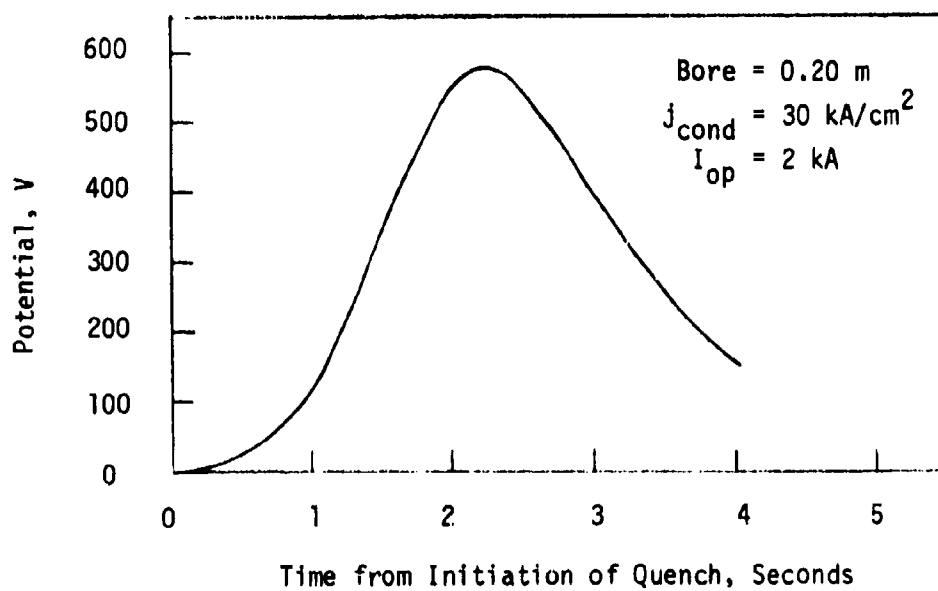


Figure 99 Potential Difference Across Normal Region vs. Time for an MHD Magnet Undergoing a Quench from Operating Current

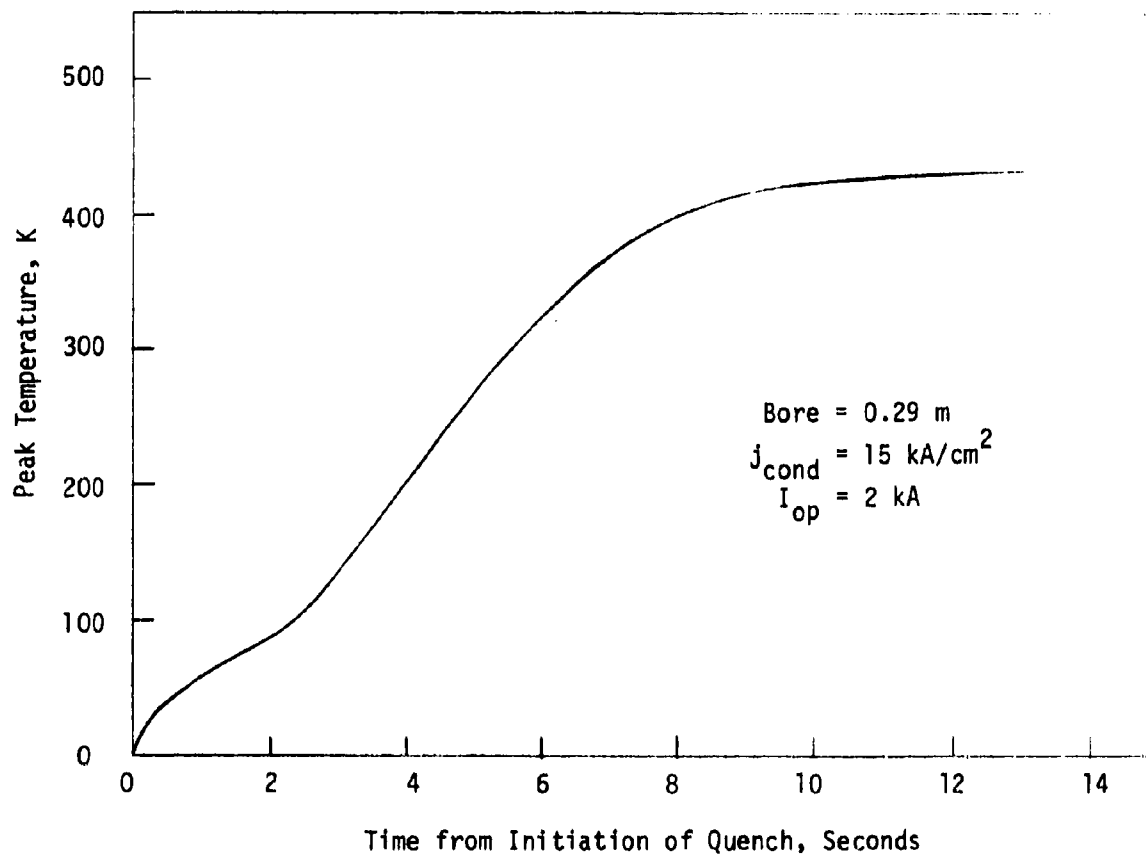


Figure 100 Peak Temperature vs. Time for an MHD Magnet Undergoing a Quench from Operating Current

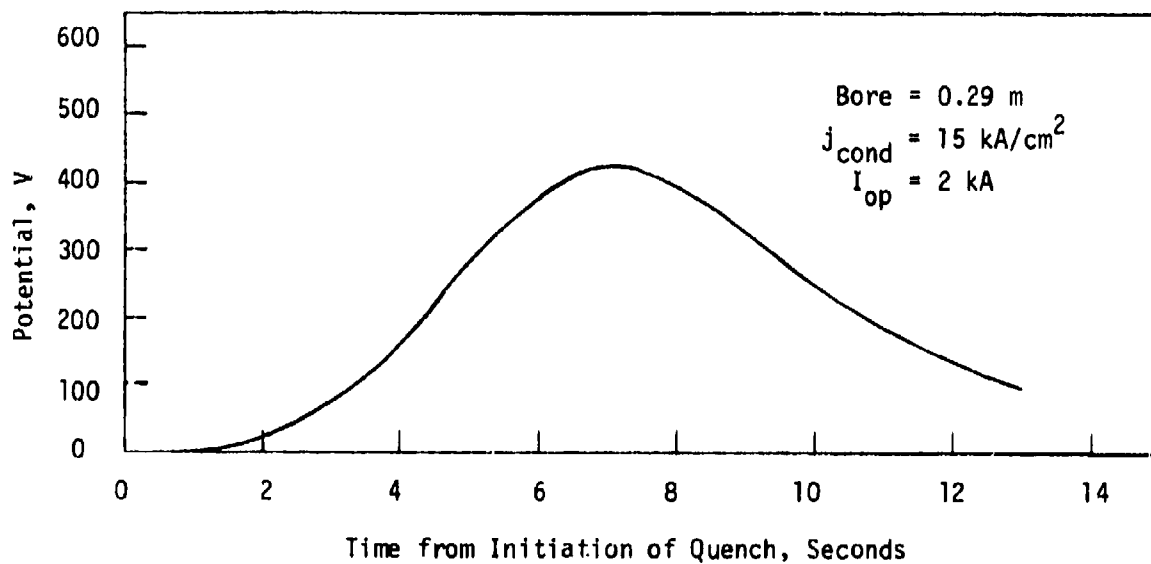


Figure 101 Potential Difference Across Normal Region vs. Time for an MHD Magnet Undergoing a Quench from Operating Current

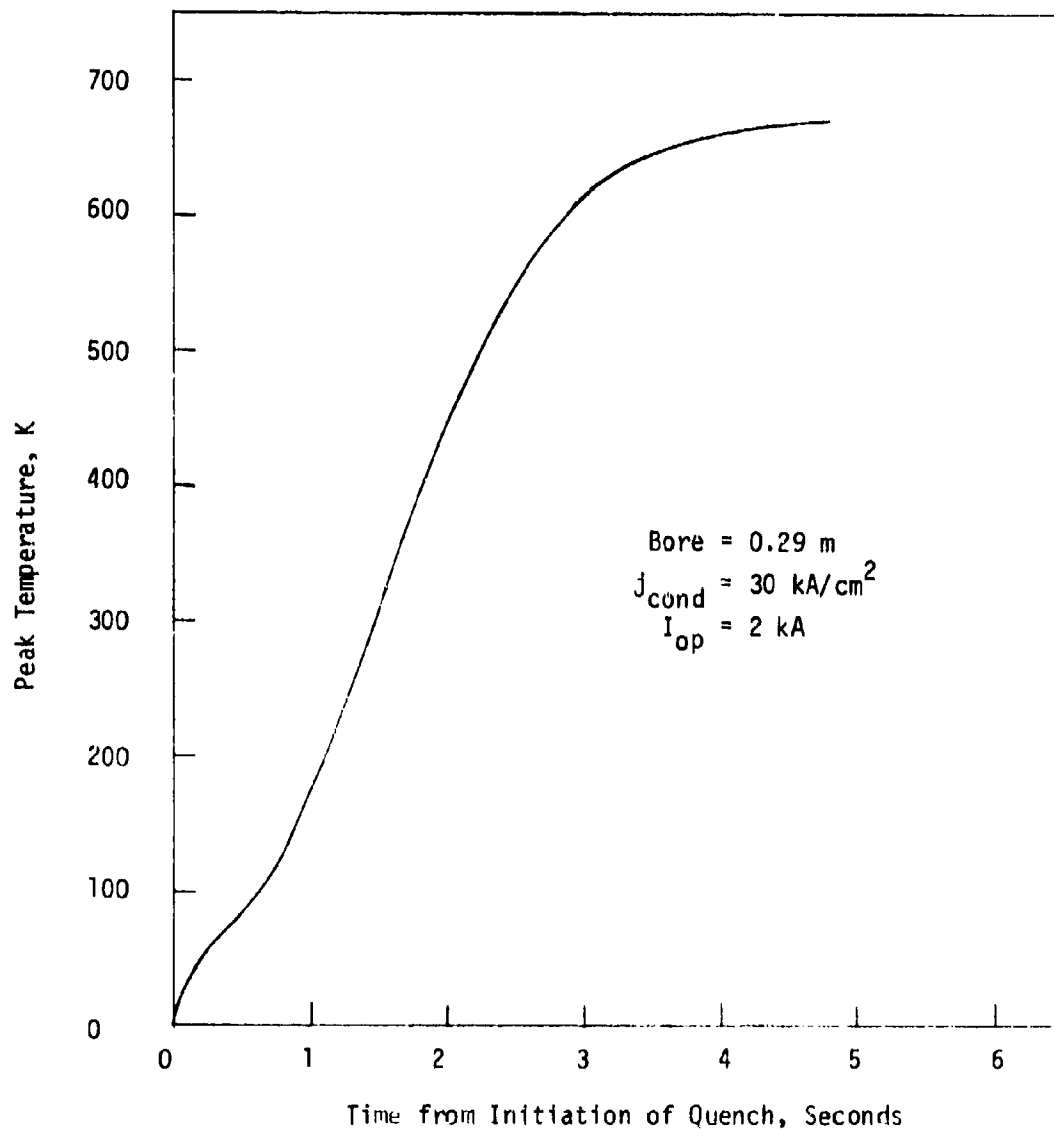


Figure 102 Peak Temperature vs. Time for an MHD Magnet Undergoing a Quench from Operating Current

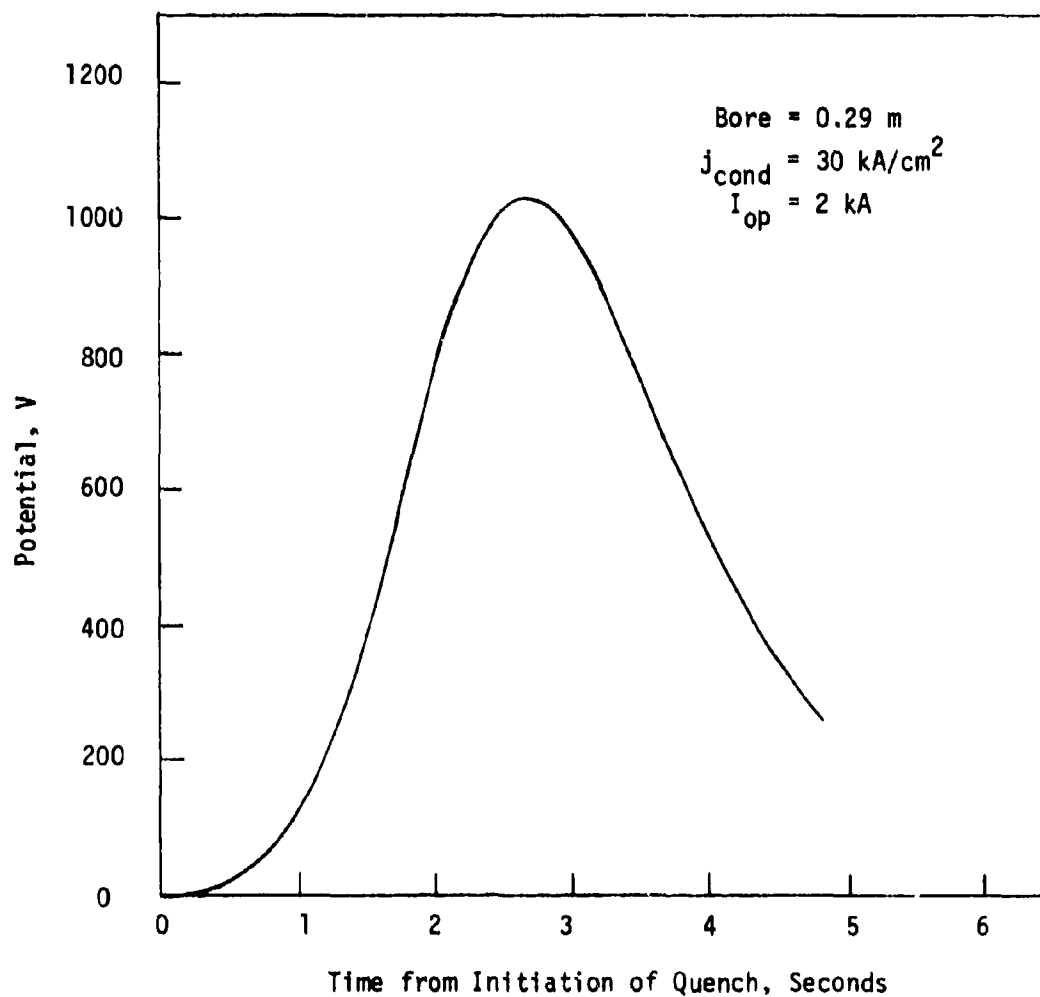


Figure 103 Potential Difference Across Normal Region vs. Time for an MHD Magnet Undergoing a Quench from Operating Current

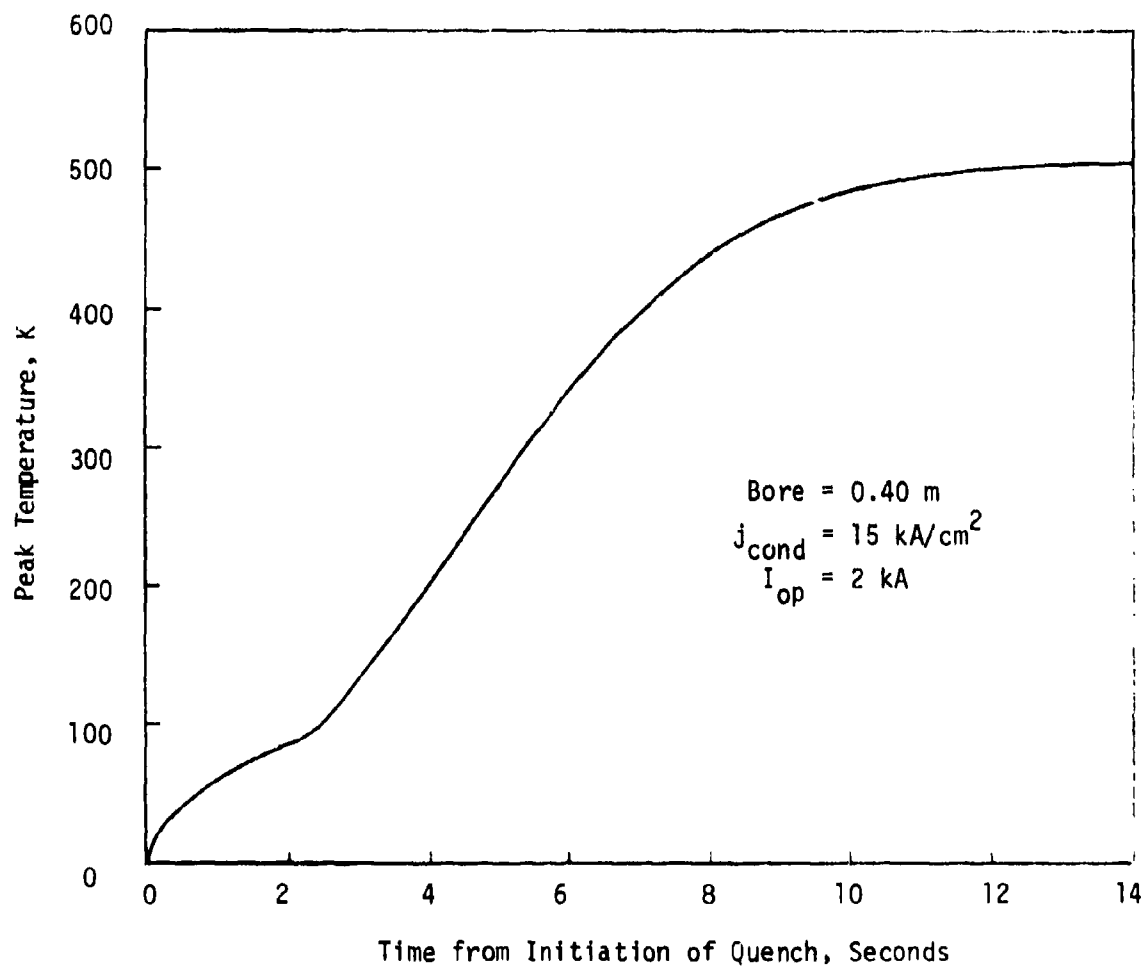


Figure 104 Peak Temperature vs. Time for an MHD Magnet Undergoing a Quench from Operating Current

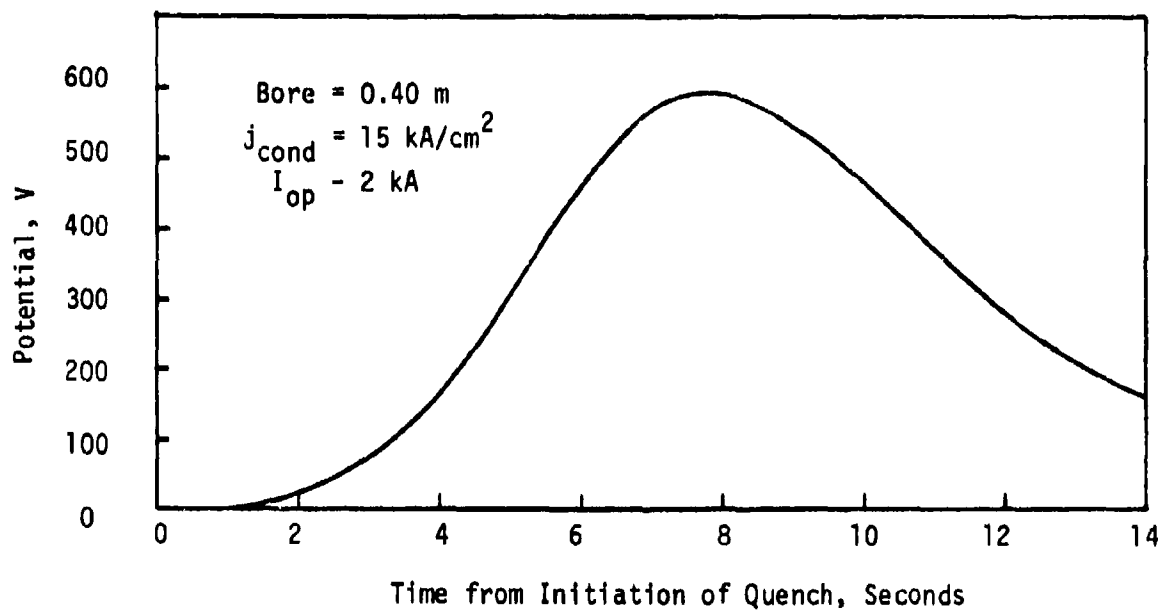


Figure 105 Potential Difference Across Normal Region vs. Time for an MHD Magnet Undergoing a Quench from Operating Current

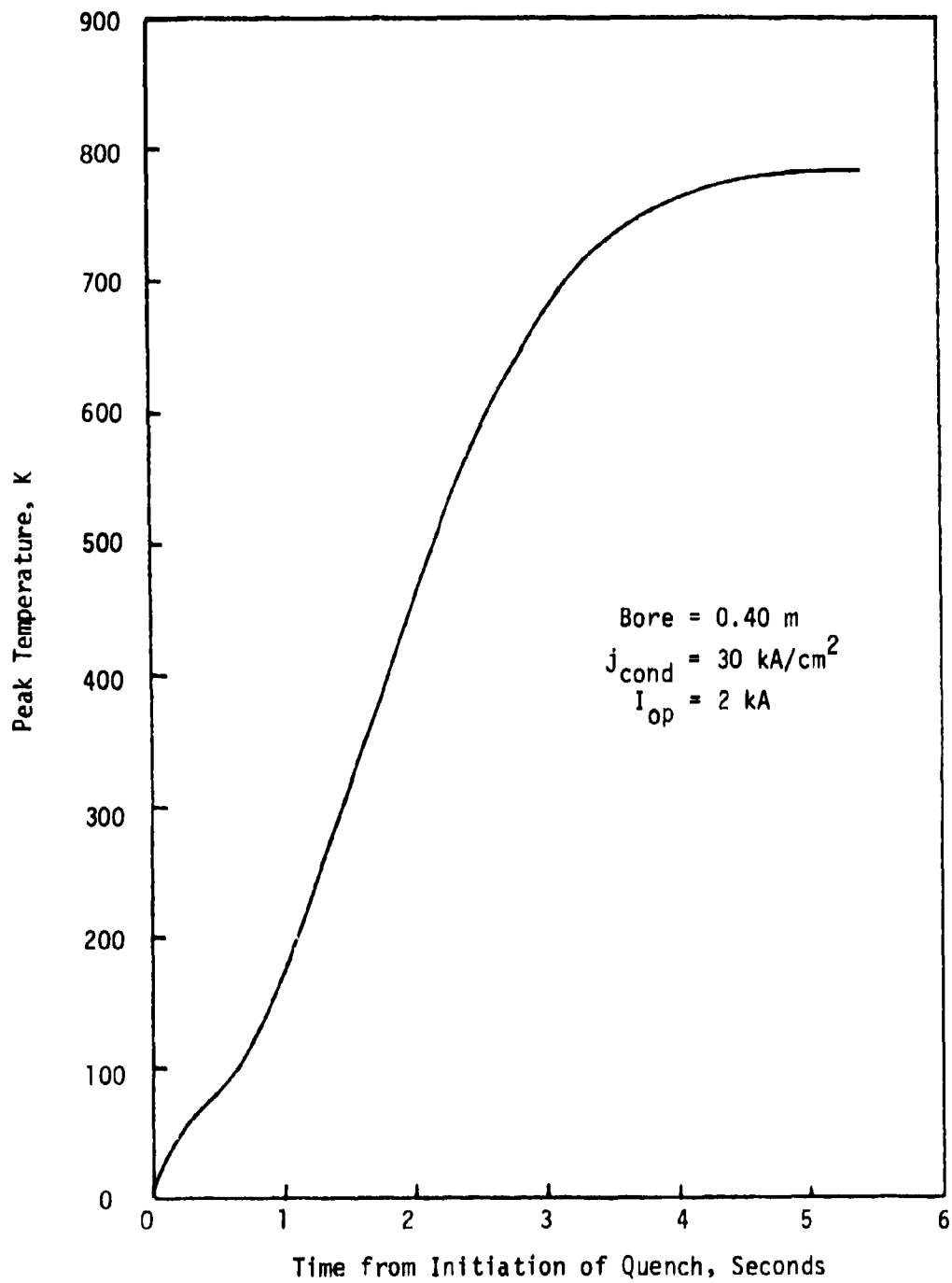


Figure 106 Peak Temperature vs. Time for an MHD Magnet Undergoing a Quench from Operating Current



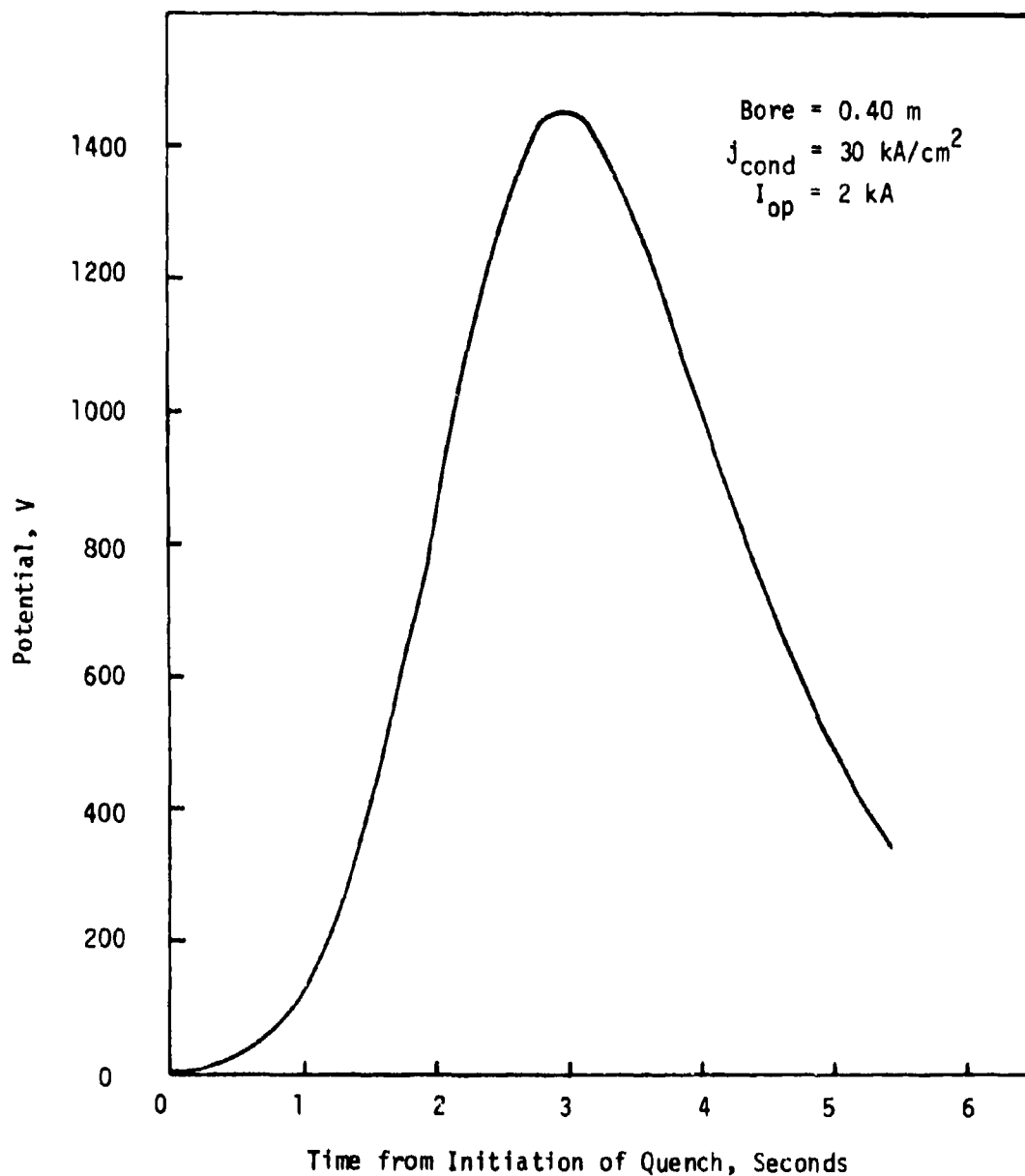


Figure 107 Potential Difference Across Normal Region vs. Time for an MHD Magnet Undergoing a Quench from Operating Current

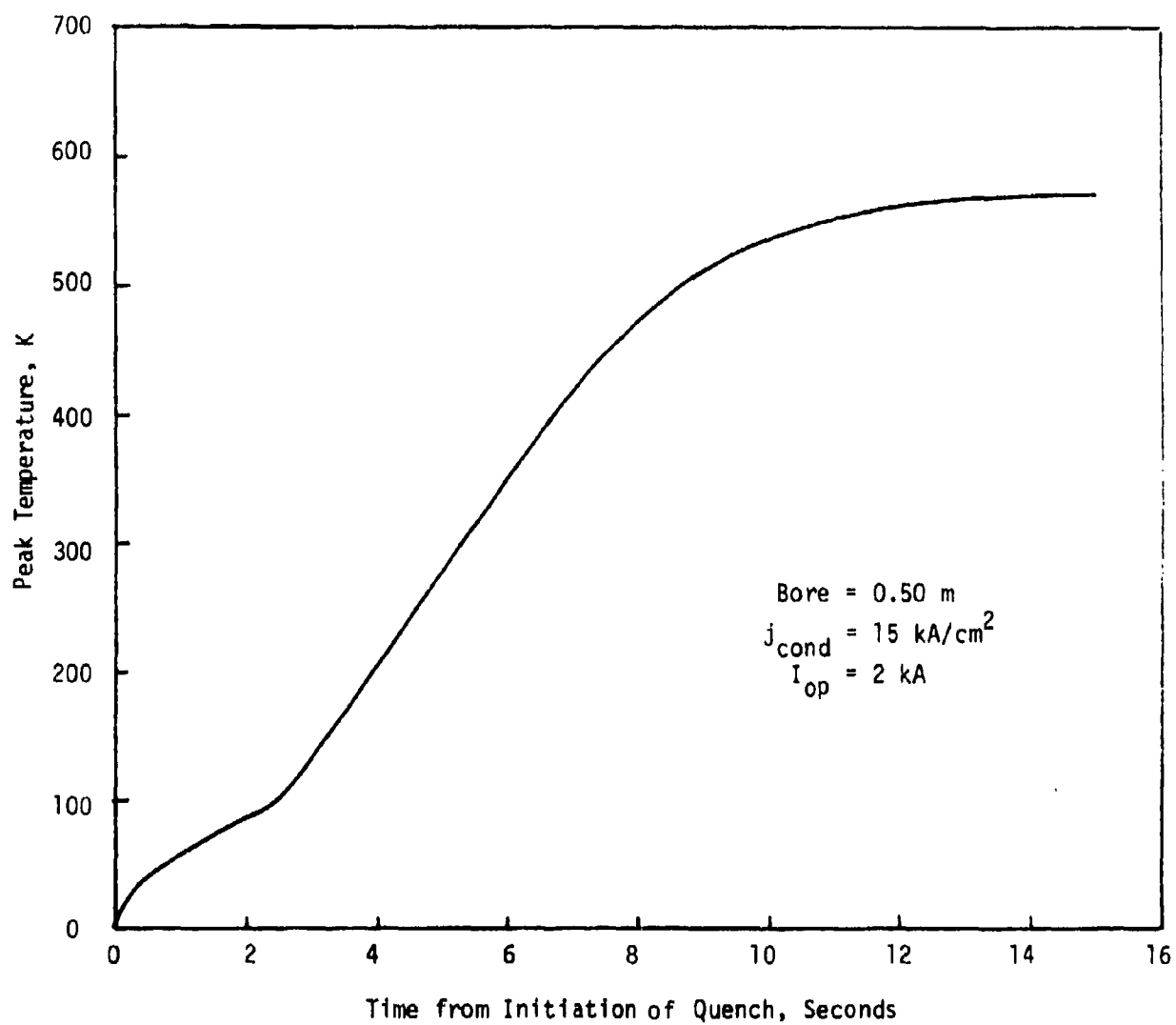


Figure 108 Peak Temperature vs. Time for an MHD Magnet Undergoing a Quench from Operating Current

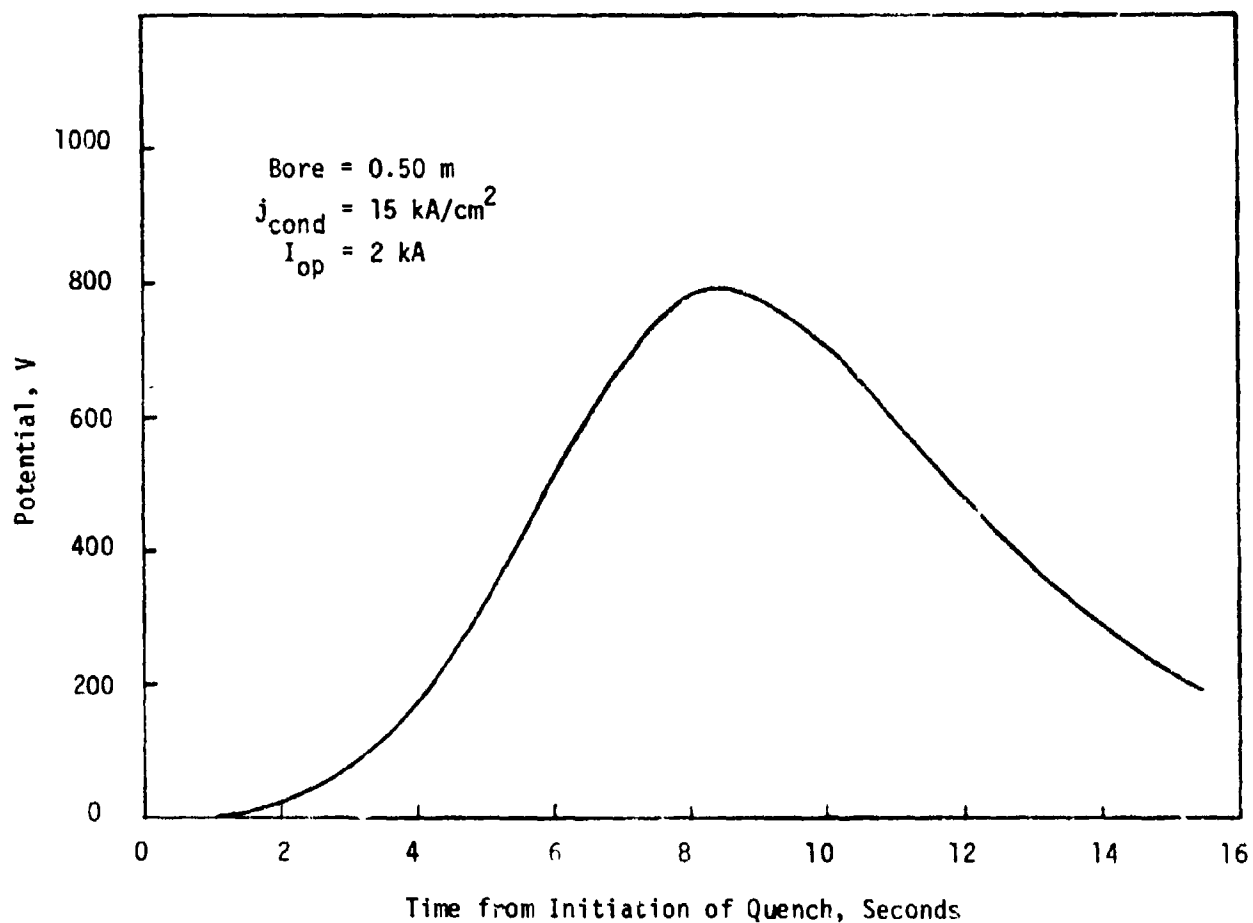


Figure 109 Potential Difference Across Normal Region vs. Time for an MHD Magnet Undergoing a Quench from Operating Current

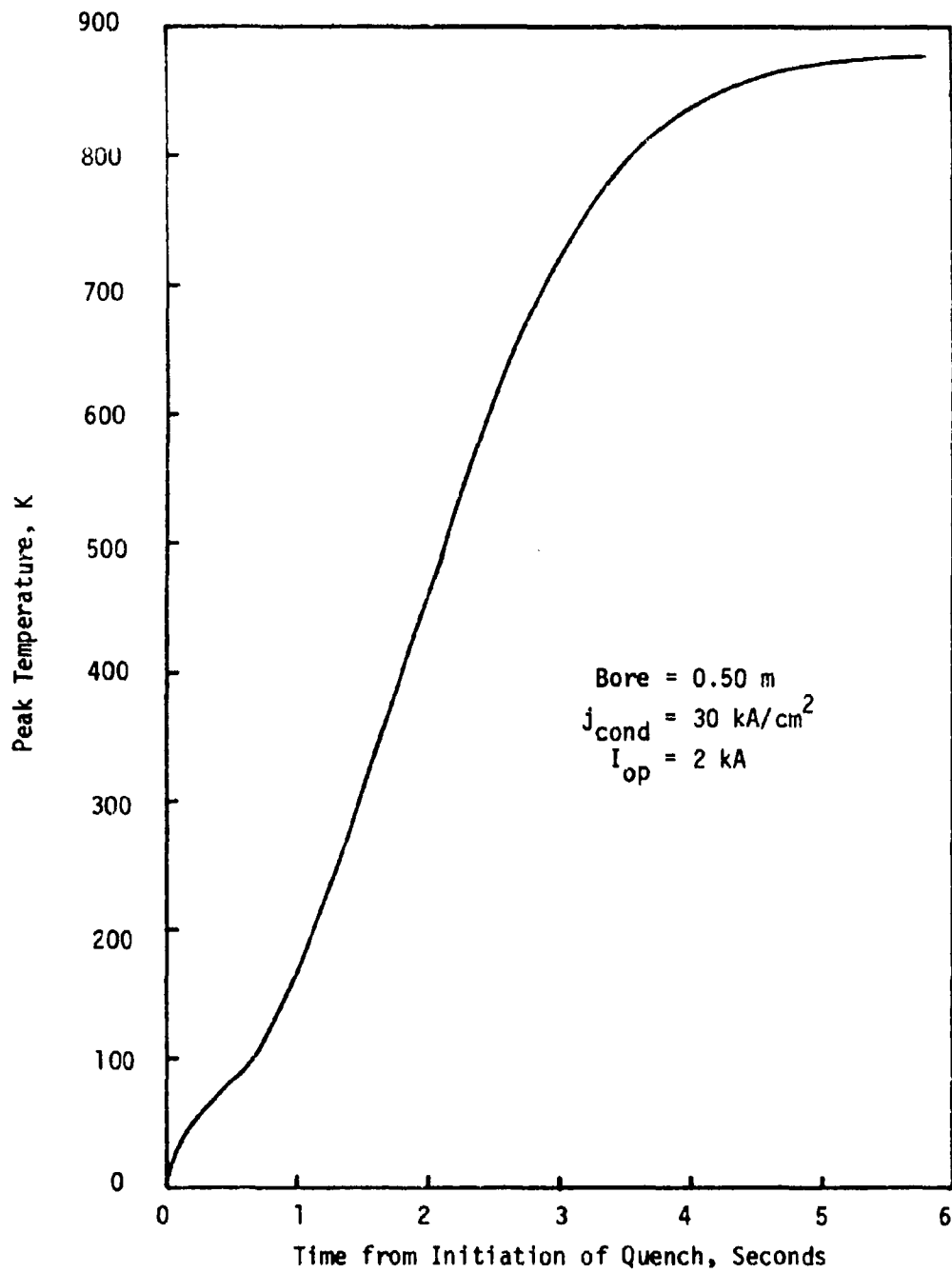


Figure 110 Peak Temperature vs. Time for an MHD Magnet Undergoing a Quench from Operating Current

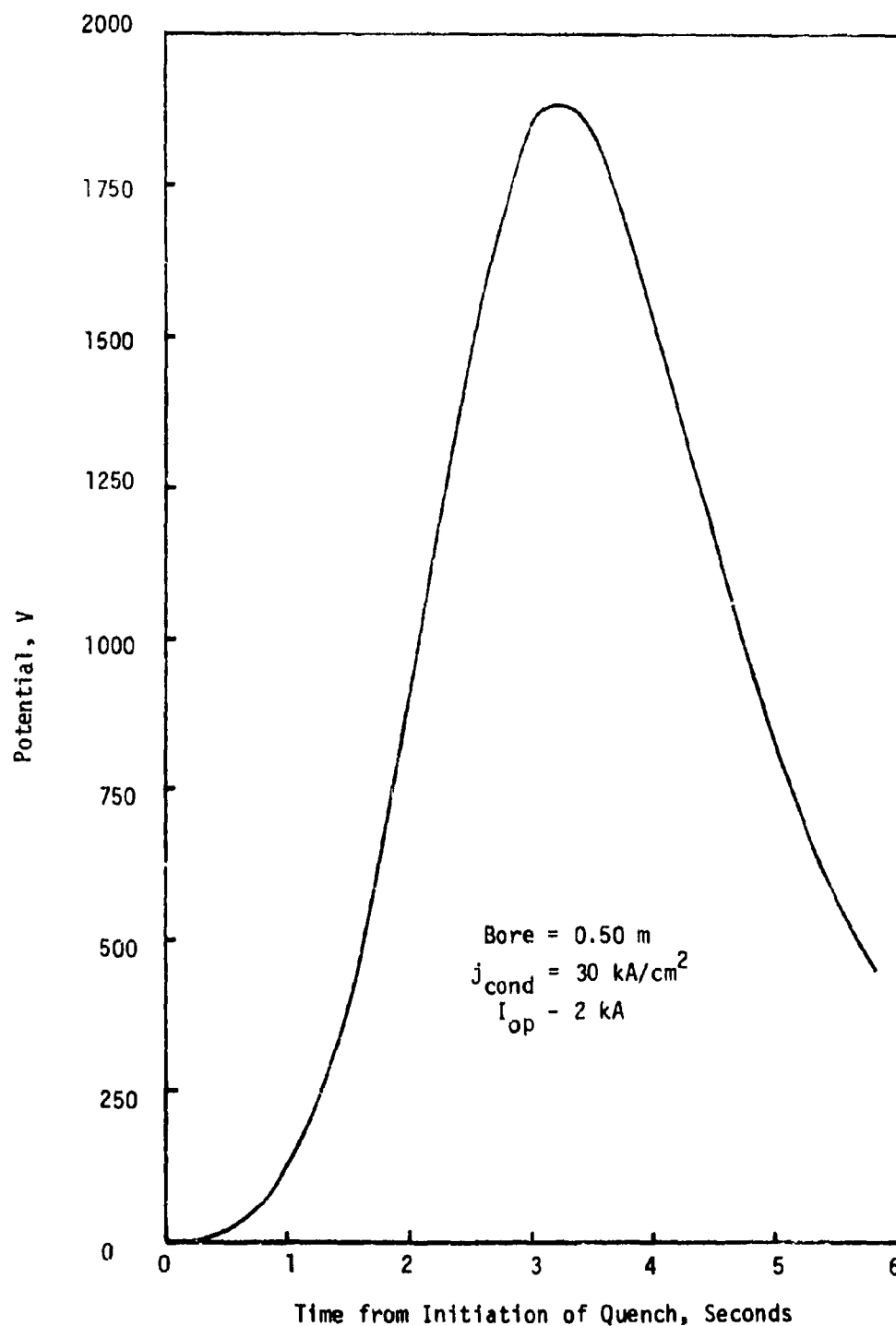


Figure 111 Potential Difference Across Normal Region vs. Time for an MID Magnet Undergoing a Quench from Operating Current

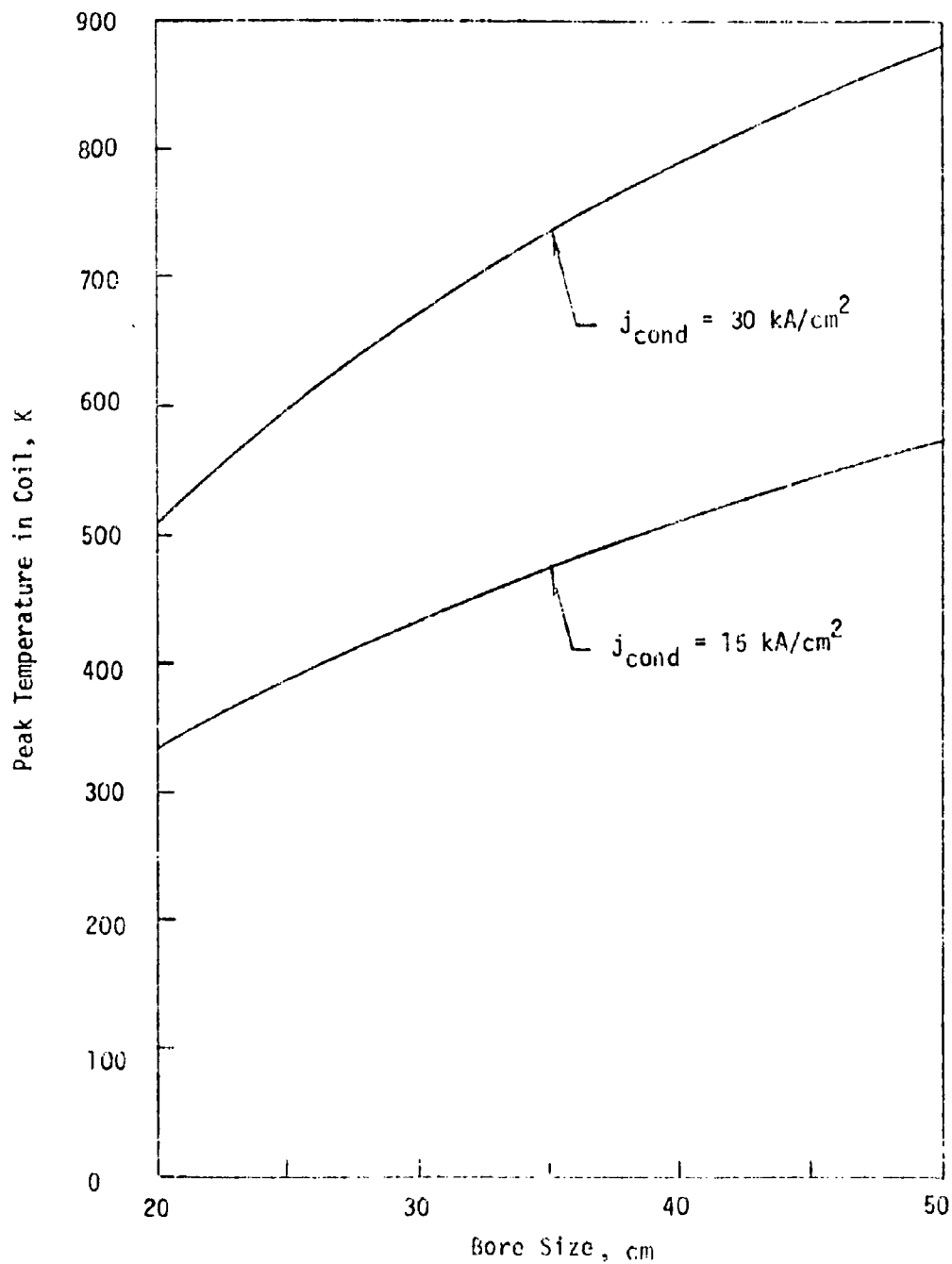


Figure 112 Peak Temperature in MHD Magnet Undergoing a Quench from Operating Current ( $I_{\text{op}} = 2000\text{A}$ ) vs. Bore Size.

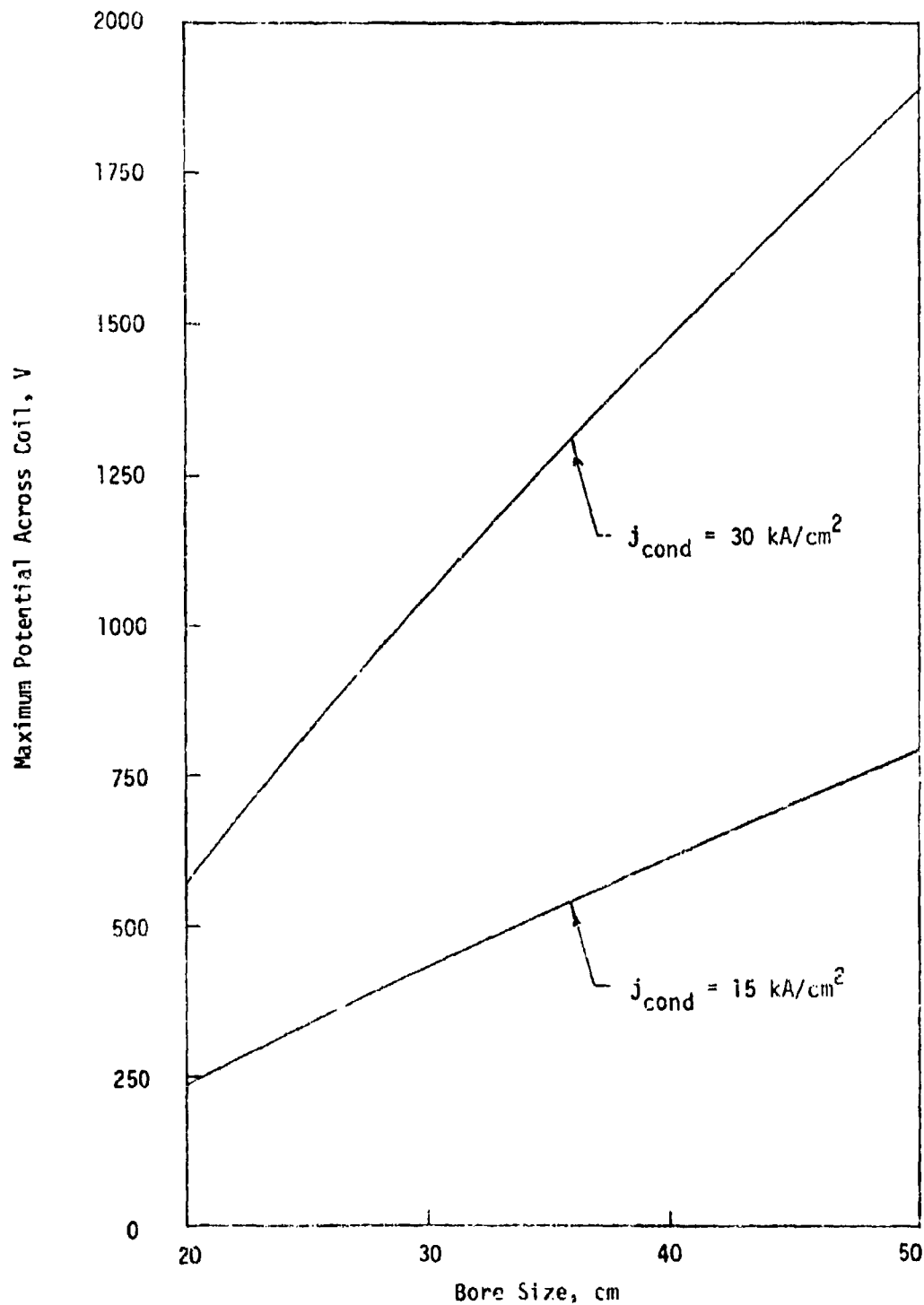


Figure 113 Maximum Potential in Normal Region in MHD Magnet Undergoing a Quench from Operating Current ( $I_{\text{op}} = 2000 \text{ A}$ ) vs. Bore Size.

FA 4723

magnets is to connect resistors across each winding bundle and insert the resistor, heating the adjacent bundle and initiating a normal region there. The process steps along the magnet until there are many normal regions, each expanding and dissipating energy.

A similar method involves putting externally-driven resistors inside the magnet. A sensor in the power supply can detect a voltage across the coil and switch on the heaters in the coil. This is an easier system to design than the completely passive bundle-to-bundle network, and can drive a large fraction of the magnet normal very rapidly. It does depend on an active response to a detected problem, and any component failure will impair the protection. Variations on this system are also possible; the heaters can be driven by the magnet current, or they can be external to the magnet (effectively, a dump resistor).

A dump resistor can dissipate a great deal of energy very rapidly by discharging the magnet. An active switch is still needed to disconnect the power supply and insert the resistor, and large potentials can be developed from terminal-to-terminal on the magnet. Careful design can alleviate these problems.

Several alternate protection schemes will be evaluated for the system during Phase II. Consideration of maximum local temperatures and potentials applied to the insulation along with confidence in any control circuitry will determine which protection method is to be employed.



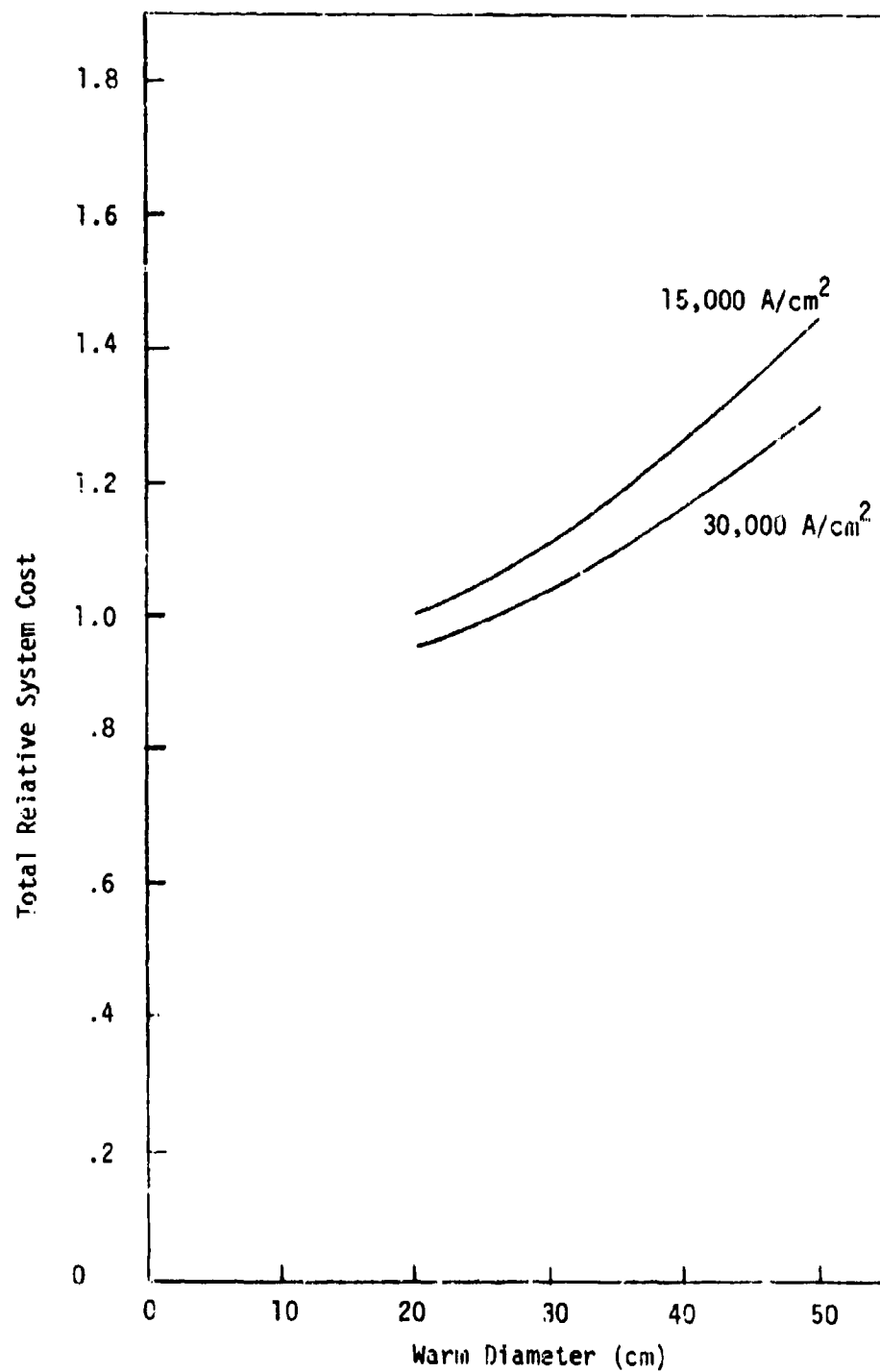


Figure 114 Total Relative System Cost Versus Warm Bore Diameter

Fa-4777

## SECTION VIII

### CONCLUSIONS AND RECOMMENDATIONS

The primary purpose of the Phase I effort was to determine a set of scaling criteria to be used to select the size of the MHD model magnet to be built in subsequent phases. The model must be sized so that it demonstrates the critical design features of the full scale system.

The active field length was set at 1.05 m for both the full scale and the model magnet systems. This requirement effectively set the magnet length. Therefore, the only major geometric parameter for a scale study became the winding diameter, and linear scaling of the geometry (in all dimensions) is not possible. Without a linear scaling of magnet dimensions many of the potential magnet dimensions many of the potential useful analytical techniques for deriving scaling criteria are lost. At best, only two-dimensional analyses can be used to yield closed form expressions for the effect of scale on the major magnet system parameters as discussed in Section 5.0 for the magnet structure.

The system scaling criteria are not unknown. Indeed, they were presented in the previous sections in both graphical and tabular form. However, due to the lack of linear geometric scaling of the magnet dimensions, these criteria are not expressible in equation form.

The major conclusions that can be made from the results of the Phase I analyses presented in this report are as follows:

- 1) A 97-strand partially solder filled braid with B-stage, glass-epoxy spiral wrap insulation is the preferred conductor configuration. It is chosen on the basis of the enhanced thermal stability accruing from the presence of interstitial and interturn helium. This particular braid has proven performance and has been manufactured in quantity by MCA.

2) A copper stabilizer and multifilamentary niobium titanium (NbTi) superconductor are chosen. The aluminum stabilizer and niobium tin ( $\text{Nb}_3\text{Sn}$ ) superconductor are judged unsuitable due to the lack of experience with their use. It is felt that developmental efforts would be required before these materials could be employed to their fullest potential and that this program could not and should not support such development.

3) A  $15,000 \text{ A/cm}^2$  conductor current density is chosen on the basis of conductor stability. The higher current density offers weight savings, but at the cost of increased risk of a magnet quench, and increased potential for damage in the event of a quench.

4) An annular saddle winding geometry is chosen on the basis of the efficient use of conductor weight. The winding is to be segmented with the segments separated by structural elements to pick up the circumferential magnetic loads.

5) Concentric structural elements and the intersegment structure will be used to contain the magnetic loads. The primary structural material will be aluminum.

6) Structural deflections of .5 mm are acceptable limits from a conductor slip/thermal stability standpoint. Detailed analyses, including the use of finite elements, are necessary and will be carried out in Phase II.

7) The chosen conductor design, current density, and winding design lead to quench induced peak temperatures close to the design limit. More detailed analyses are required. The effect of adding a protection system also needs investigation.

8) On the basis of risk and cost, the 20 cm warm bore diameter magnet is a proper model size to demonstrate the major parameters for the full scale system. However, it is felt that by choosing the 29 cm size, not only would the full scale system be modeled, but a more useful magnet system for MHD

research would become available. The increase in scale and concomitant increase in system weight, cost, and risk are felt to be reasonable in light of the ultimate usefulness of the larger system. Figure 114 shows the total relative system cost versus size for the two current densities. It can be seen that the increment in cost for the 29 cm size is approximately 10%.

APPENDIX

ADVANCED COMPOSITE MATERIAL (ACM)  
MAGNET STRUCTURE SCALING CRITERIA

## SECTION A-1

### INTRODUCTION

General Dynamics Convair Division (GDC) is under contract to Magnetic Corporation of America (MCA) in the development of a lightweight MHD superconducting magnet. The prime contractor (MCA) is conducting the overall program for the Aero Propulsion Lab of the Air Force Systems Command, Wright-Patterson AFB, Ohio. This interim report covers work performed by GDC during Phase 1 of the program.

The GDC role in this effort is in test support to MCA and the design and fabrication of the lightweight magnet support structure. The test support includes testing a heavy MHD magnet fabricated from conventional materials (designed and manufactured by MCA) and testing the lightweight MHD magnet fabricated using advanced composites.

The program is planned as a 48 months activity. The work phases in which GDC is involved are as follows:

- |         |   |
|---------|---|
| Phase 1 | Model Magnet Criteria Selection             |
| Phase 2 | Model Magnet Design (metal structure)       |
| Phase 3 | Model Magnet Fab and Test (metal structure) |
| Phase 5 | Lightweight Model Magnet Design             |
| Phase 6 | Lightweight Magnet Fab and Test             |

Phase 1 work activity officially began at GDC on 17 April 1978. It comprises the following elements.

- Establish Design Requirements
- Establish 3 Design Concepts
- Select Materials and Fabrication Methods
- Set up Analytical Methods
- Conduct Trade-off Studies
- Make Design Recommendations

Having established design requirements, three design concepts were derived and identified as Concepts A, B, and C. The three concepts are similar in the cold bore tube design and in the technique by which axial forces are reacted. To react the magnetic forces in the axial direction, a metal end ring is placed at each end of the magnet. Metal or composite tension rods join together the two end rings and react axial forces applied to the end rings.

Concept A employs continuous circumferential filament winding over the saddle magnets assembled on the cold bore tube. This shell structure is made lighter by using sandwich construction for separating the two filament wound facings. Graphite-epoxy is the primary building material for this concept.

Concepts B and C are quite similar to each other except in material and method of fabrication. Each concept employs two circumferential shell segments that are joined by a row of tension rods along the upper and lower edges of the shell segments. The primary building materials are boron/aluminum for Concept B and graphite/epoxy for Concept C.

Analytical methods were established to allow preliminary sizing of the structural elements for each concept. Trade studies then were performed on the basis of cost, weight, and risk. As a result of these studies, it was recommended that Concept A receive primary emphasis in subsequent studies.

This interim report reviews in some detail the various elements of Phase 1. Problem areas are highlighted and recommendations made for their solution.

SECTION A-2  
DESIGN CRITERIA

The design criteria established for the MHD model are taken from the contract SOW and as evolved during conduct of the program. In the design of the MHD structure, the criteria of major concern are related to applied loads, temperatures, design envelopes, and interface requirements.

The design envelopes and interface requirements are taken directly from the SOW and as further categorized in Table 2-1, supplied by MCA. Dimensional criteria are given in the table for three MHD sizes which represent scaling activities.

TABLE A-1  
CHARACTERISTICS

	<u>Design</u>		
	<u>29 cm</u>	<u>40 cm</u>	<u>50 cm</u>
<u>Inlet</u>			
Warm bore dia.* (m)	.29	.40	.50
Winding inner dia. (m)	.35	.46	.56
Winding outer dia. (m)	41.8	.54	.64
<u>Outlet</u>			
Warm bore dia.* (m)	.53	.64	.74
Winding inner dia. (m)	.59	.70	.97
Winding outer dia. (m)	.658	.78	1.05
<u>Lengths</u>			
Between end turn crossovers (m)	1.01	1.02	1.03
Overall (winding) (m)	1.65	1.80	1.88
Winding angle	68°	68°	68°
NI ( $10^6$ A-T)	2.60	3.40	4.21

\*At point of crossovers.



The design loads and design environment for the MHD may be considered as Operating and Nonoperating. The Operating conditions are based on the assumption that the model is operating as a superconducting magnet on board an aircraft. For nonoperating conditions, it is assumed that the unit is being handled, as in shipping, or is in storage.

#### OPERATING

- . Unit is energized at 4°K in liquid helium
- . Conduction forces as supplied by MCA
- . Consider 100 cycles from RT to 4°K and back to RT
- . Limit strains adjacent to conductor to  $< 0.2\%$
- . Aircraft load factors — TBD

#### NONOPERATING

- . Temperature range 219 to 344°K
- . Handling and shipping load factors — TBD

## SECTION A-3

### MATERIALS CONSIDERED

The use of advanced composites presents to the designer a wide choice of materials for consideration in the MHD structure design. The lack of high temperature requirements, however, rules out high temperature matrix materials such as polyimides. In addition, only those materials that are fully developed and readily available are afforded consideration for this program. This places under consideration the following categories of materials:

- . Boron/Aluminum
- . Kevlar/Epoxy
- . Graphite/Epoxy

A brief discussion is given for each of these categories. Mechanical and physical properties are tabulated in Section 5.

#### Boron/Aluminum

This advanced composite candidate is, without question, the most difficult material to process of the above categories. It requires not only very high temperature (above 1000°F), but pressures on the order of 8000 psi. A 6061 aluminum matrix is considered the most commonly used alloy for the matrix.

Though this material is difficult to process, it does have some advantages over the other advanced composites. First, its relatively high strength metal matrix allows the use of a unidirectional layup of this material. That is, all fibers can be placed in only one direction - circumferentially at 0° layup orientation. This can result in a structure with maximum strength in the fiber direction and sufficient strength in the axial direction.

Boron/aluminum is considerably more conductive than the epoxy matrix materials. This can result in greater heat dissipation and less likelihood of local heat spots in the conductor.

Little data is available on this material at cryogenic temperatures. It is expected that at the operating temperature, its static properties would be as great as at room temperature.

### Kevlar/Epoxy

Kevlar fiber is available as Kevlar-29 and as Kevlar-49. The latter is of higher strength and modulus and is considered the "Aerospace fiber" of the two. Hence, Kevlar-49 is the only Kevlar fiber considered for MHD.

Various epoxies are readily available as the Kevlar matrix material. The particular choice of resin should be made with respect to the method of fabrication and to the cryogenic operating temperature. The cryogenic operating temperature dictates the need for a low cure temperature resin that will lessen residual stresses in the material. This will lessen the possibility of microcracking as well as simplify processing - particularly for filament winding considerations.

Kevlar/epoxy is the lowest density material under consideration ( $\rho = .050$  pci) but its elastic modulus is considerably less than either of the other two material categories. Its negative coefficient of expansion (CTE) makes it an interesting candidate for a filament winding design, whereby the CTE feature may be used to create additional compressive forces on the superconductor at the operating temperature. Its lower modulus, however, makes it less attractive for building a stiff, low strain structure.

### Graphite/Epoxy

Graphite fiber is available in three distinct classes: high strength, high modulus, and ultra high modulus. The high strength fiber has the lowest modulus and highest strength of the three classes, and the ultra high modulus has the lowest strength of the three. The high modulus fiber falls between the other two in both strength and modulus.

The same epoxies available for Kevlar are also available for graphite. Similarly, the low cure temperature epoxies are a better choice for cryogenic operating temperature because of lower residual stresses and less likelihood of microcracking.

For the trade studies being conducted in this phase of the program, it is sufficient to consider each class of materials generically. That is, typical properties attainable in each class can be used to establish design concepts and approximate sizing. Properties within each class do not differ appreciably, and a particular fiber and matrix can be selected at a later date.

## SECTION A-4

### DESIGN CONCEPTS

In the design of ultra high efficiency, minimum weight structures, the two prime candidate materials are graphite composite and boron/aluminum composite.

Graphite/epoxy composite is the more commonly used due to its relative ease of fabrication, its greater design versatility, and its lower cost.

In order to drive out the optimum material selection for the MHD structural components, three candidate design concepts have been defined.

#### 4.1 CONCEPT A — FILAMENT WOUND GRAPHITE/EPOXY

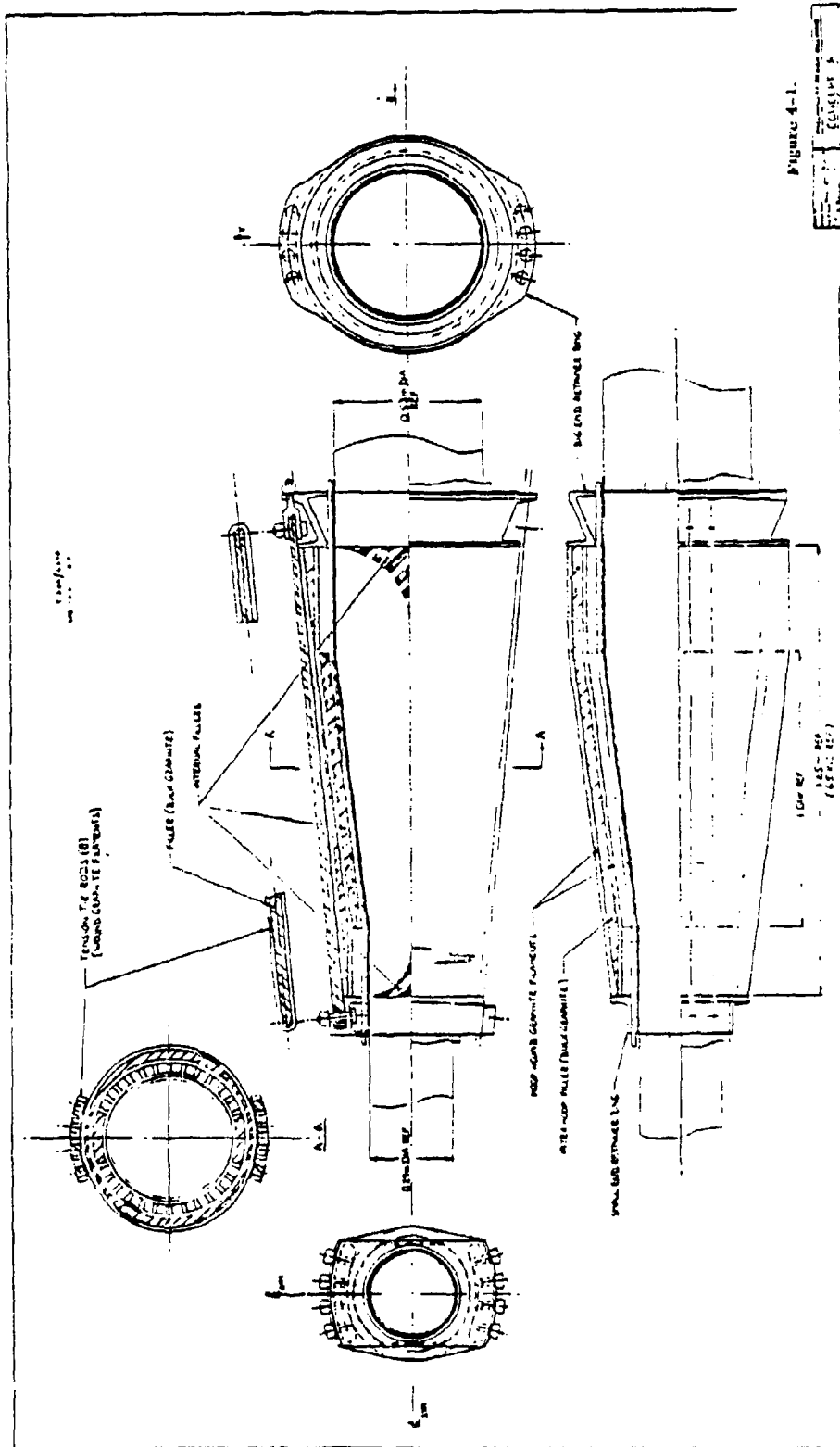
In the design of structures subject to high internal pressures and shaped as bodies of rotation such as tubes, cylinders and spheres, the concept of fabrication by winding filaments produces an optimum efficiency structure in which all filaments directly react the internal pressure by going into pure hoop tension.

Figure 4-1 illustrates a 29cm MHD magnet design in which the cylindrical/conical elements of the prime structure are produced by winding graphite filaments with an epoxy matrix. In order to compensate for the non-uniform magnetic "pressures," the cross section of the outer structure is of elliptical profile (reference Section A-A) with the major axis of the ellipse corresponding to the "Y" axis of the magnetic field, where the magnetic forces also peak. By thus matching the curvature of the external structure to the distribution of the radial magnetic forces, the concept of pure hoop tension is preserved and section bending effects are minimized.

Thus, as seen in Figure 4-1, the external structure consists of inner (circular) and outer (elliptical) filament wound shells with matching filler material providing, in effect, a sandwich construction outer structure.

Immediately inside the superconductor installation is the "cold bore" tube also filament wound but with filaments laid down in a more isotropic manner, possibly over a layer of Kevlar composite.

To prevent slippage of the conductors, due to the magnetic forces, it is necessary to restrain them in both the circumferential and axial (x) directions. This restraint is provided by bonding or mechanically keying the spacers (teeth), that fit between the conductors, to the cold bore tube, and/or to the inner shell of the outer structure. The conductors are thus securely confined. The accumulated axial loads (x) that result are considerable and are reacted by two end-retainer rings which transfer the load to eight



**Figure 4-1.**

[illegible]

**FIGURE A-1. CONCEPT A**

tension tie rods. These tie rods are also of filament wound graphite/epoxy construction. A non-structural filler material completes and stabilizes the cross section. Typically, the tie rods are installed by pinning both ends. One end mounts in a rod-end type fitting which allows preloading of the tie rod by applying torque to the rod-end nut.

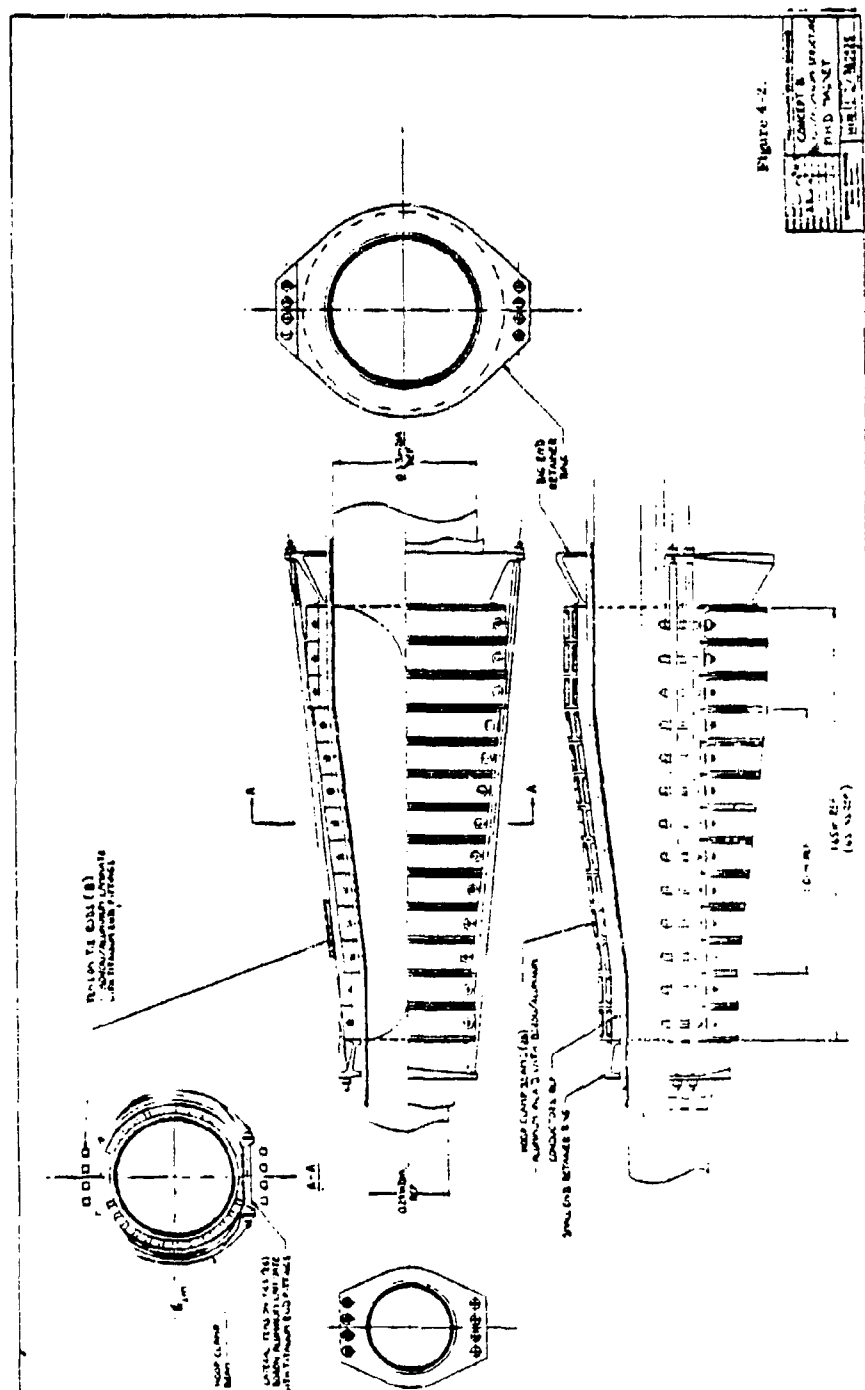
#### 4.2 CONCEPT B — BORON ALUMINUM

The basic structural principle is the same as for Concept A in that separate structural systems react radial and axial magnetic loads (see Figure 4-2). However, in place of continuous windings, the radial loads are contained by a multiplicity of semi-circular clamping beams on either side of the section plane of symmetry. Left and right hand beams are connected at their ends by tension bolts. Bending moments peak at the beam midspan point which corresponds to the location of the peak radial magnetic forces. The beams are aluminum, with an "H" section shape, built up to a solid rectangular section by the addition of unidirectional Boron/Aluminum inlaid between the upright flanges. As in all Boron/Aluminum applications, the effective continuation of the boron fibers into the more complex shape of the beam endings is a relatively inefficient feature and the transition to the tension bolt interface tends to be relatively massive and heavy.

Axial loads are reacted in similar fashion to Concept A except that the eight tie rods are Boron/Aluminum, of bar, rod or tubular section. Threaded titanium end fittings are fused to each end of the tie rods. The tie bolts that span between the ends of the half clamp beams could be similarly fabricated but since their length is relatively small it would be more cost effective to make them entirely of titanium.

#### 4.3 CONCEPT C

Concept C (Figure 4-3) reverts to graphite/epoxy except that the general configuration is similar to Concept B. The graphite/epoxy is in the form of a laminate, and clamping beams are laid up as curved channel sections. The eight longitudinal tie-straps are also laminated graphite/epoxy composite of bar, rod or tubular section shape. Their titanium end fittings are secondary bonded (room temperature bonding) in place.



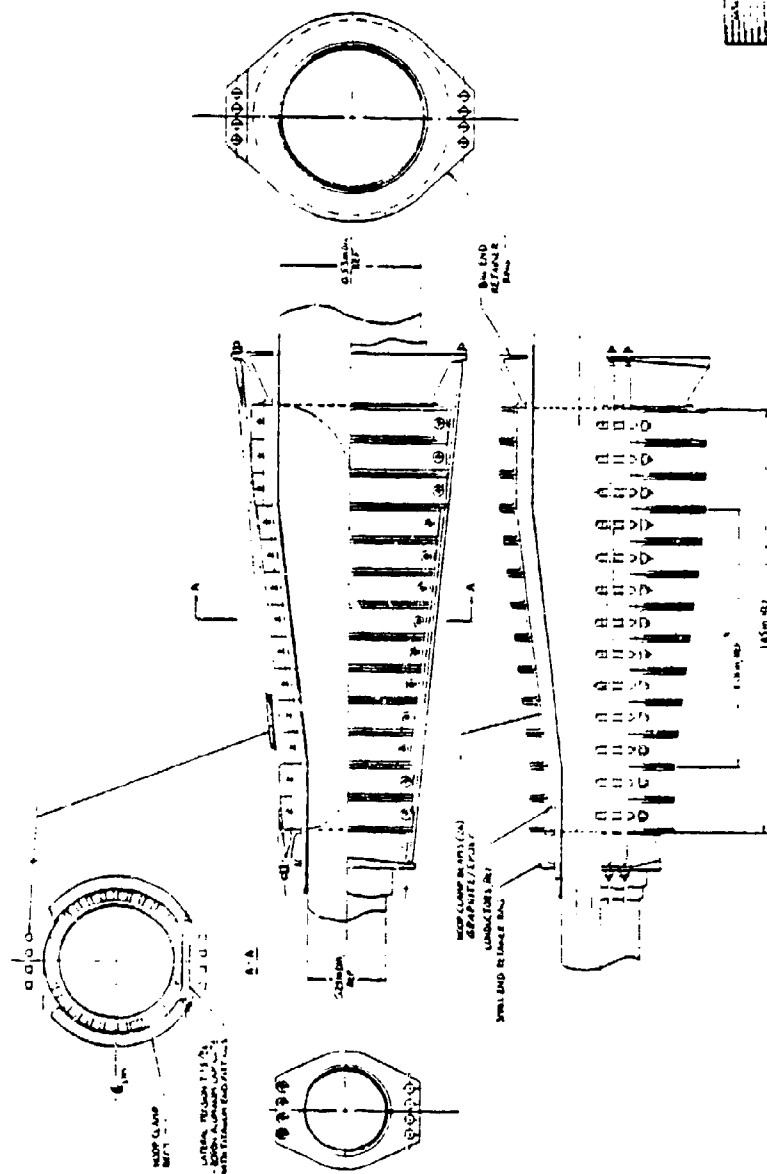


FIGURE A-3. CONCEPT C

4



## SECTION A-5

### ANALYTICAL CONSIDERATIONS

During the Phase I, analyses have been performed to establish the structural requirements of the three advanced composite design concepts. In particular, these analyses provided:

- 1) Preliminary structural element sizing.
- 2) Effect of changing design parameters on stress level and distribution.
- 3) Identification of potential structural problems.

#### 5.1 STRESS ANALYSIS PROCEDURE

The initial stress analysis procedure is shown in Figure A-4.

The loads were received from MCA and summed in the Y and Z directions for radial and circumferential loads, and in the X direction for axial loads. The axial loads were then used for sizing the axial tie rods.

The Y and Z loads were applied to a two dimensional plane strain finite element model in the transverse mid plane (Figure 5-2). By taking advantage of the available symmetry, only a single quadrant was modeled. At this point, design variables were selected and changed from their "baseline" value to determine their effect on stress levels and distribution.

The design variables included shell concept, material selection, layup angle (which will change the modulus, coefficient of thermal expansion, and strength), and geometry (i.e., model size, wall thickness and shell profile). For the Concept A 29cm model, the design variable inputs are shown in Table 5-1 and their resulting influence on stress in Figure 5-3. In addition to the maximum and minimum principal stresses, the material allowables are also plotted for the cold bore tube and external shell. It should be noted that the model stresses are limit, with no factor of safety included; and the material allowables are ultimate.

During the Phase I analysis, ultra-high modulus GY-70/X-30 was the primary material used for trade studies. Although this system offers high stiffness, it is significantly strength limited by low strains to failure.

Because the resulting stresses are in some cases higher than the allowables, Phase II design activity will therefore expand the materials selection to include graphite/epoxy systems in the medium and high strength category. While the high strength systems

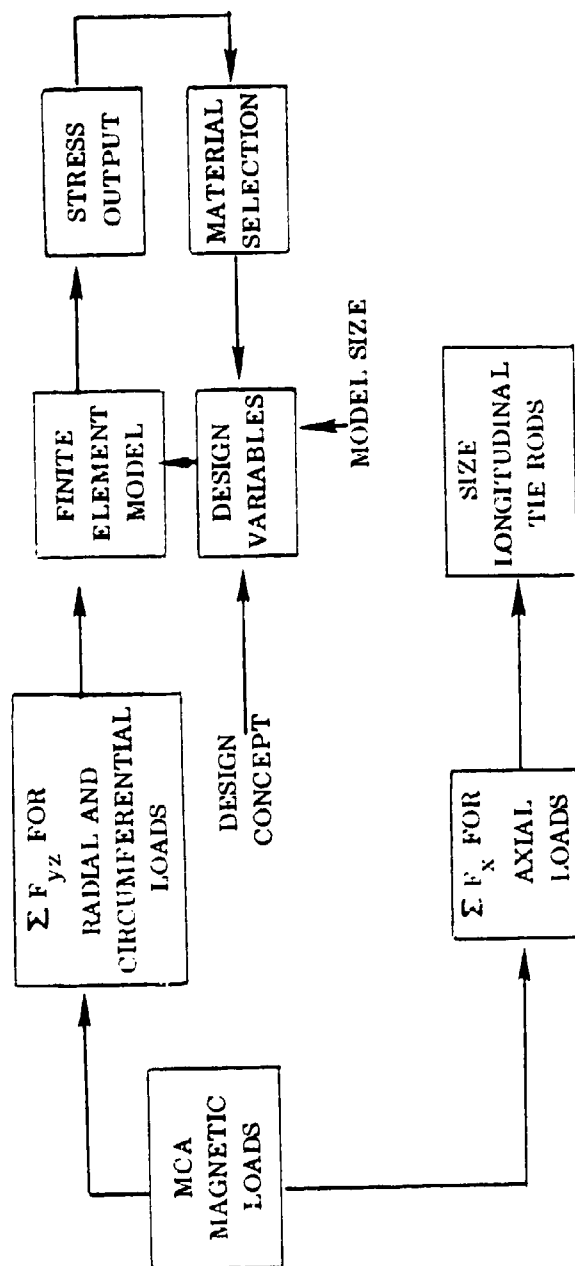


Figure A-4. Initial Stress Analysis Procedure

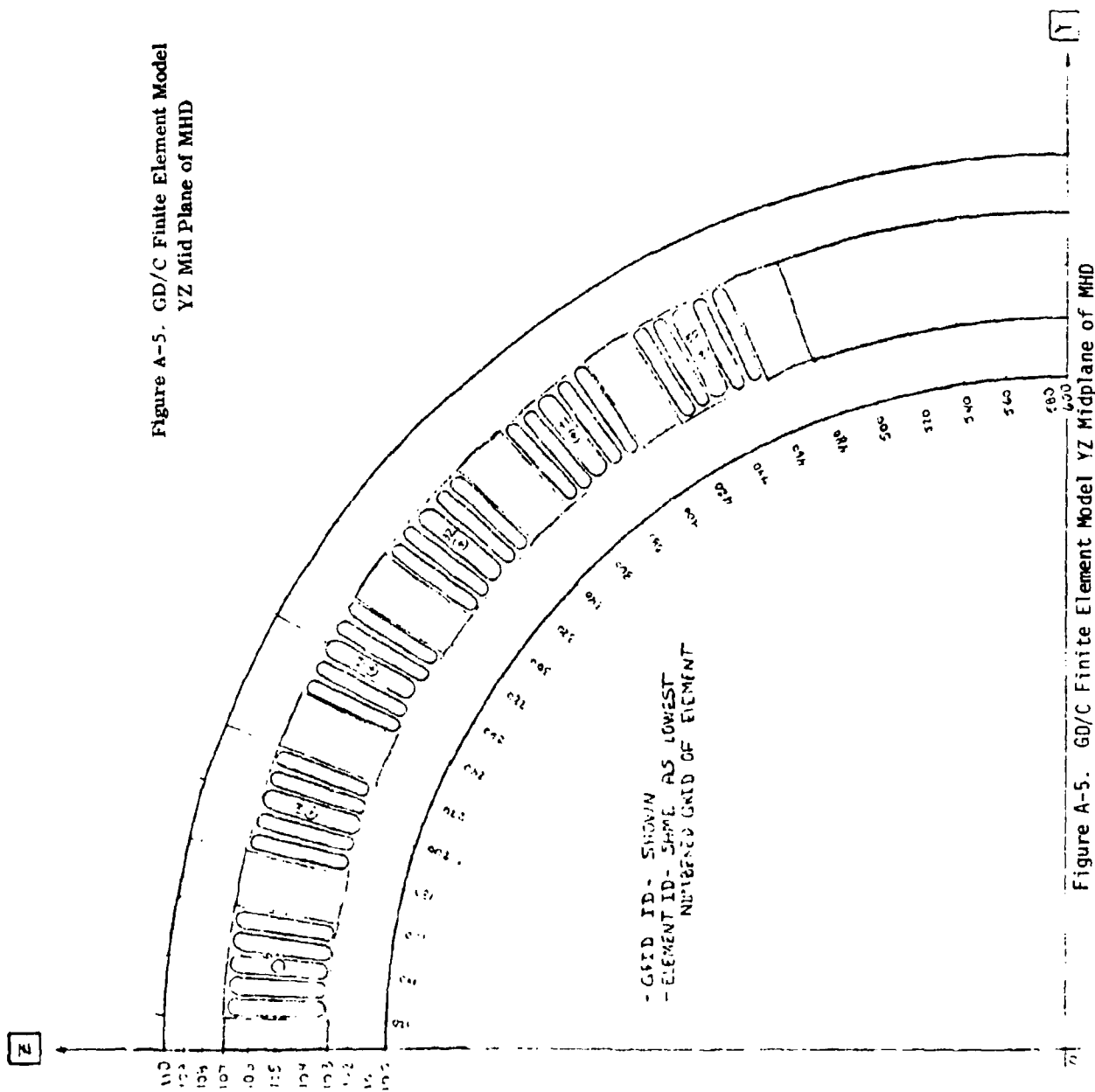


TABLE A-2

Design Variable Inputs for Concept A, 29 CM Model

	RUN 1	RUN 2	RUN 3	RUN 4 <sup>①</sup>	RUN 5	RUN 9	RUN 10	RUN 11	RUN 12
COLD BORE TUBE	LAYUP E11, MSI A11, in/in/°F t, IN	GY70 #7 36.1 -.181 .75	GY70 #3 20.7 .0594			GY70 #7B 30.0 -.561 .56			-.261
EXT. SHELL INNER	LAYUP E11, MSI A11, in/in/°F t, IN	GY70 #8 14.3 .614 .75			1.20	GY70 #7 35.1 -.481 .20	.40	.20	
EXT. SHELL OUTER	LAYUP E11, MSI A11, in/in/°F t, IN					GY70 #7A 38.6 -.409 .20	.40		

① CTE OF SPACERS CHANGED FROM 8.0 TO 1.8  $\times 10^6$  IN/IN/°F

LAYUPS: ZERO DEGREE ANGLE REFERENCED TO YZ PLANE

GY70 #3 (15, -15, 105, 105, 75, -15, 15)

GY70 #7 (15, -15, 15, 90, 15, -15, -15, 15)

GY70 #7A (10, -10, -10, 10, 90, 10, -10, -10, 10)

GY70 #7B (20, -20, -20, 20, 90, 20, -20, -20, 20)

GY70 #8 (90, 90, 15, -15, 90, 90)

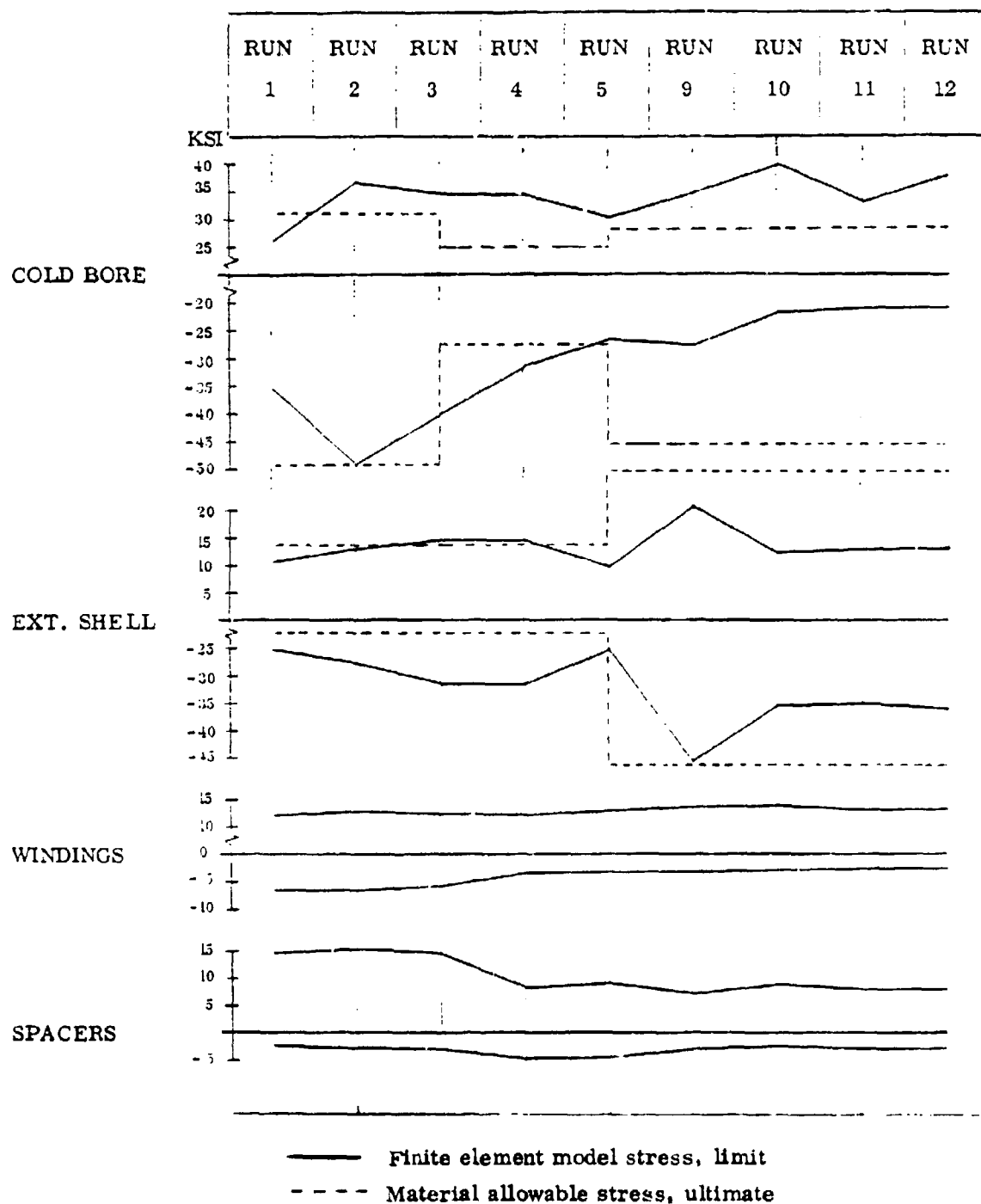


Figure A-6. Influence of Design Variables on Stress in  
Structural Components of MHD Concept "A"  
- 29 CM Model

are classified as being "low modulus," their composite modulus in the fiber direction is typically on the order of  $20-21 \times 10^6$  psi; or approximately twice that of aluminum.

## 5.2 CONCEPT "A", 29CM, 40CM AND 50CM MODELS

As part of the Phase I analysis activity, finite element models were run on the larger 40cm and 50cm sizes. For this preliminary analysis, a 29cm model was used with appropriate scale factors applied for size and load. The scale factors and the resulting principal stresses are shown in Table 5-2.

TABLE A-3  
MHD Concept "A" Summary for 29cm, 40cm  
and 50 cm Models

	29cm	40cm	50cm
Size Factor, $K_{size}^{(1)}$	1.00	1.26	1.58
Load Factor, $K_{load}$	1.00	1.41	1.68
$K_{load}/K_{size}$	1.00	1.12	1.06
<u>Cold Bore</u>			
$\sigma_{max}$ , ksi	30.6	34.3	32.6
$\sigma_{min}$ , ksi	-27.0	-30.2	-28.7
Shear, ksi	-10.6	-11.5	-11.1
<u>External Shell</u>			
$\sigma_{max}$ , ksi	9.8	11.0	10.4
$\sigma_{min}$ , ksi	-25.2	-26.4	-25.8
Shear, ksi	7.3	7.5	7.4

(1) Finite element model size based on average of Inlet, Outlet and winding dimensional change.

By applying a size scale factor to the model, all structural components are scaled the same amount. For the cold bore tube, the stresses are proportional to the load to size scale factor ratio, which suggests the loads are primarily axial. For the thicker external shell, the minimum principal stress and shear stress are roughly proportional to the square root of the load to size ratio and suggests that the loads are due to bending. Therefore, as the larger model sizes are considered, the weight of the external shell may be expected to increase at a rate less than the load to size ratio.

A second observation that may be made from Table 5-2 is the magnitude of the shear stresses. For the cold bore tube, the maximum shear stress is roughly proportional

to the load to size ratio, with a 29cm model value of 10.6 ksi. Based on the limited amount of data available (NBS Annual Report of Nov. 1977) shear strengths on the order of 5 ksi are typical for GY-70/934 at 4°K. This apparently weak load path in transferring the circumferential magnetic loads to the cold bore tube and external shell will require both innovative design approaches and further material testing of the selected composite system with the same layup angle that will be used. The layup angle will be a factor influencing the occurrence of microcracking that may not be present in a unidirectional laminate.

### 5.3 CONCEPT A, B AND C COMPARISON

A finite element model was also run for Concepts B and C. Table 5-3 is included as a partial stress summary and comparison. Because the models were run only once, no data is available on the influence of design variables on stress.

TABLE A-4  
Stress Comparison Between Concepts A, B and  
C for 29cm Model

	Concept "A" Filament Wound Graphite/Epoxy	Concept "B" Boron/Al	Concept "C" Gr/E Beam
<u>Cold Bore</u>			
Material	Gr/E	Gr/E	Kevlar/E
t, in	.50	.50	.50
$\sigma_{\max}$ , ksi	30.6	28.6	30.7
$\sigma_{\min}$ , ksi	-27.0	-53.0	-29.6
Shear, ksi	-10.6	17.5	7.8
<u>External Shell</u>			
Material	Gr/E	B/Al	Gr/E
t, in	1.20	1.20	.60
$\sigma_{\max}$ , ksi	9.8	15.7	18.6
$\sigma_{\min}$ , ksi	-25.2	-11.4	-35.2
Shear, ksi	7.3	-7.7	9.0

### 5.4 COMPUTER GRAPHICS

During the Phase I analysis task, the volume of stress data available was considerable. To reduce the stress data to a meaningful level, use was made of the GDC computer graphics system. Representative plots of the finite element model are shown in Figures 5-4 through 5-10. In this case, the stress contours are representative of Model Run Number 11. (Concept A, 29cm.)

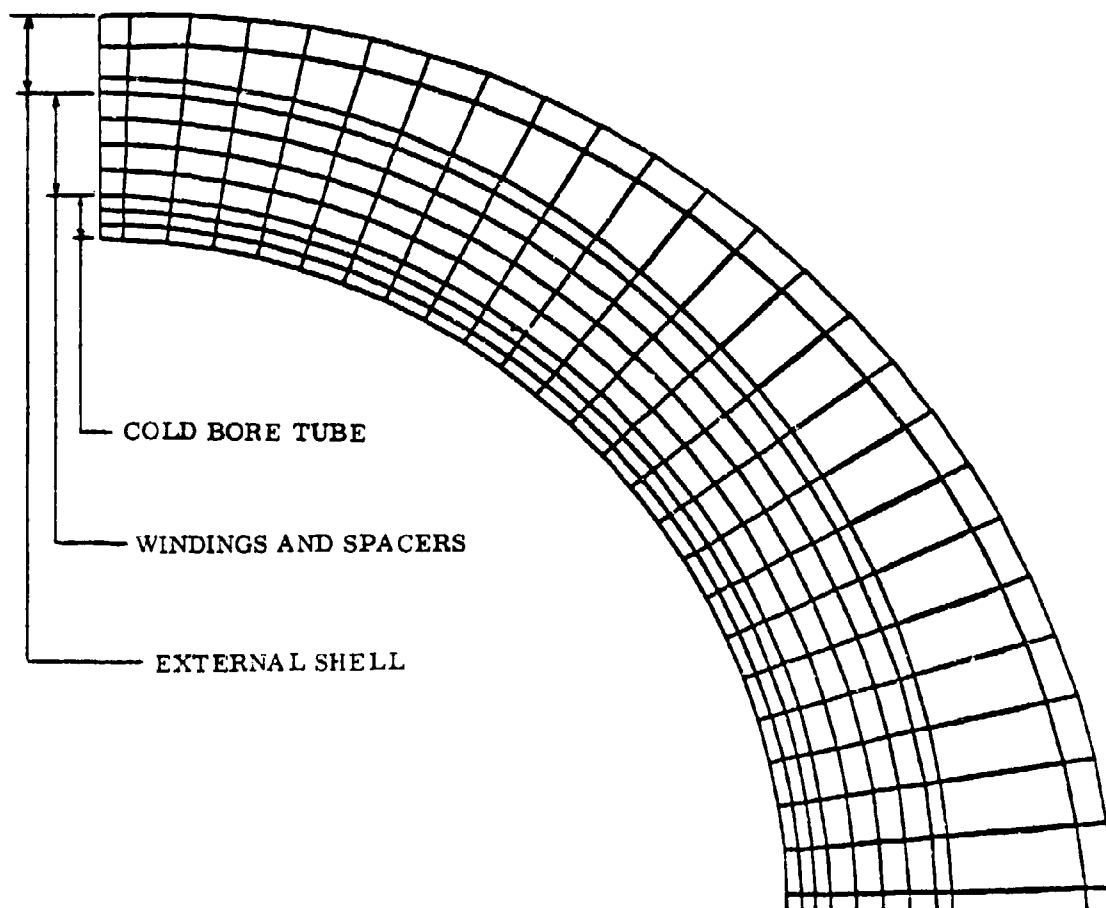


Figure A-7. Computer Graphics Plot of GDC Finite Element Model  
at MHD Transverse Mid-Plane



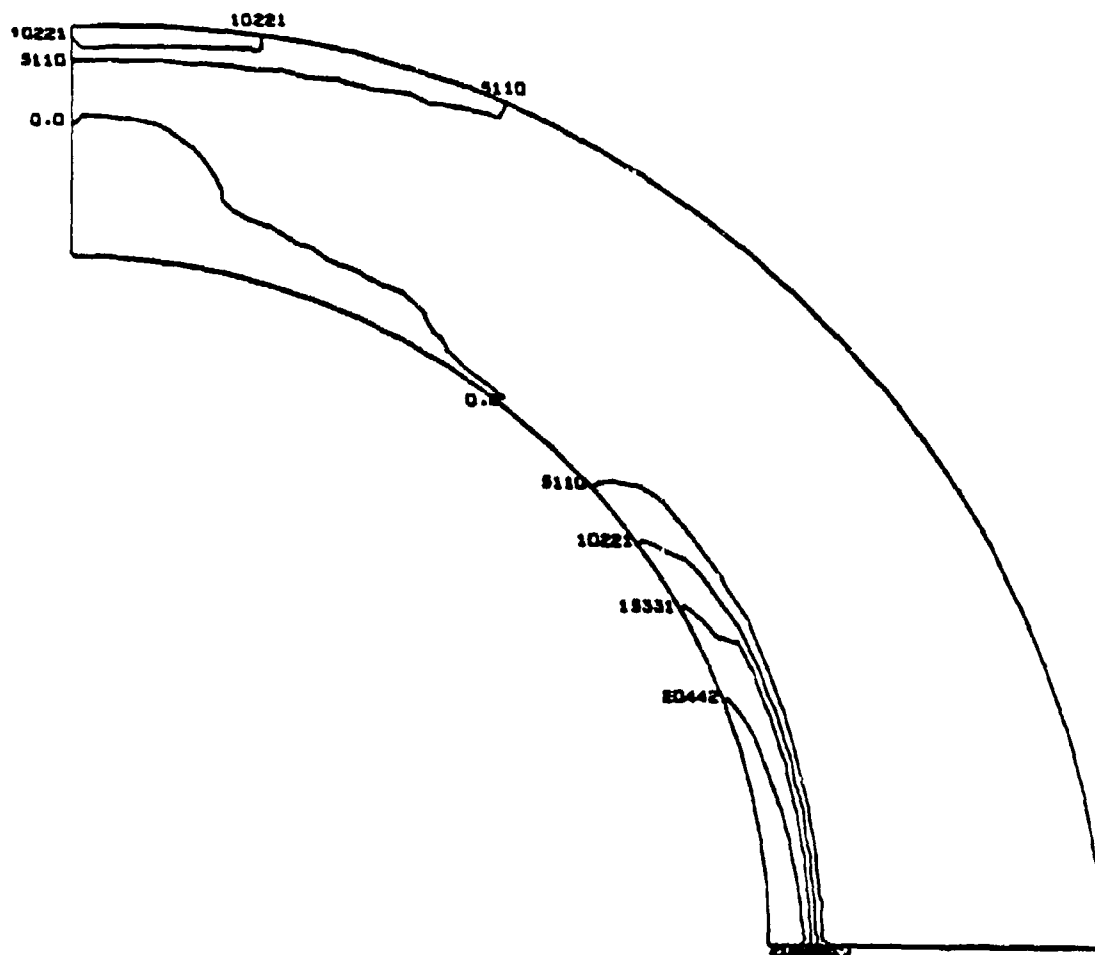


Figure A-8. Stress Contour Plot of Maximum Principal Stress  
due to Magnetic Loads

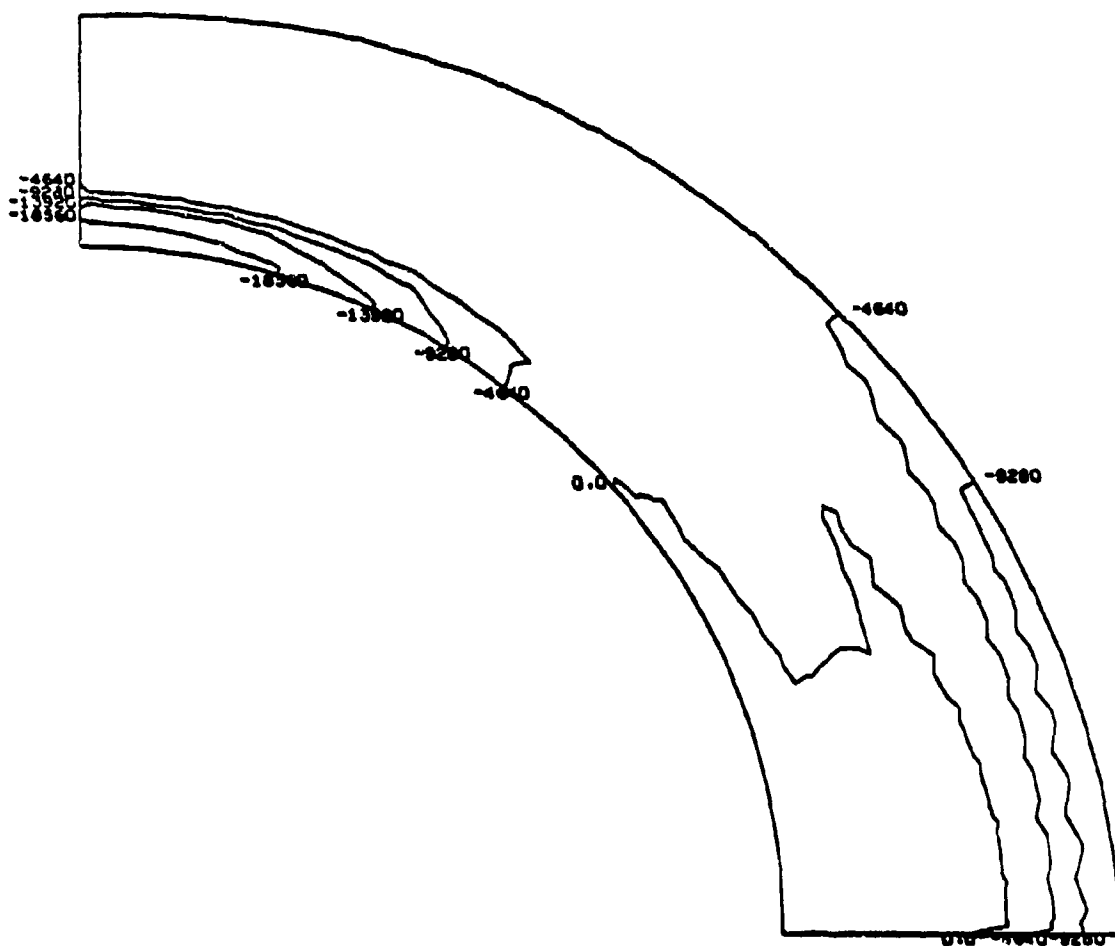


Figure A-9. Stress Contour Plot of Minimum Principal Stress  
due to Magnetic Loads

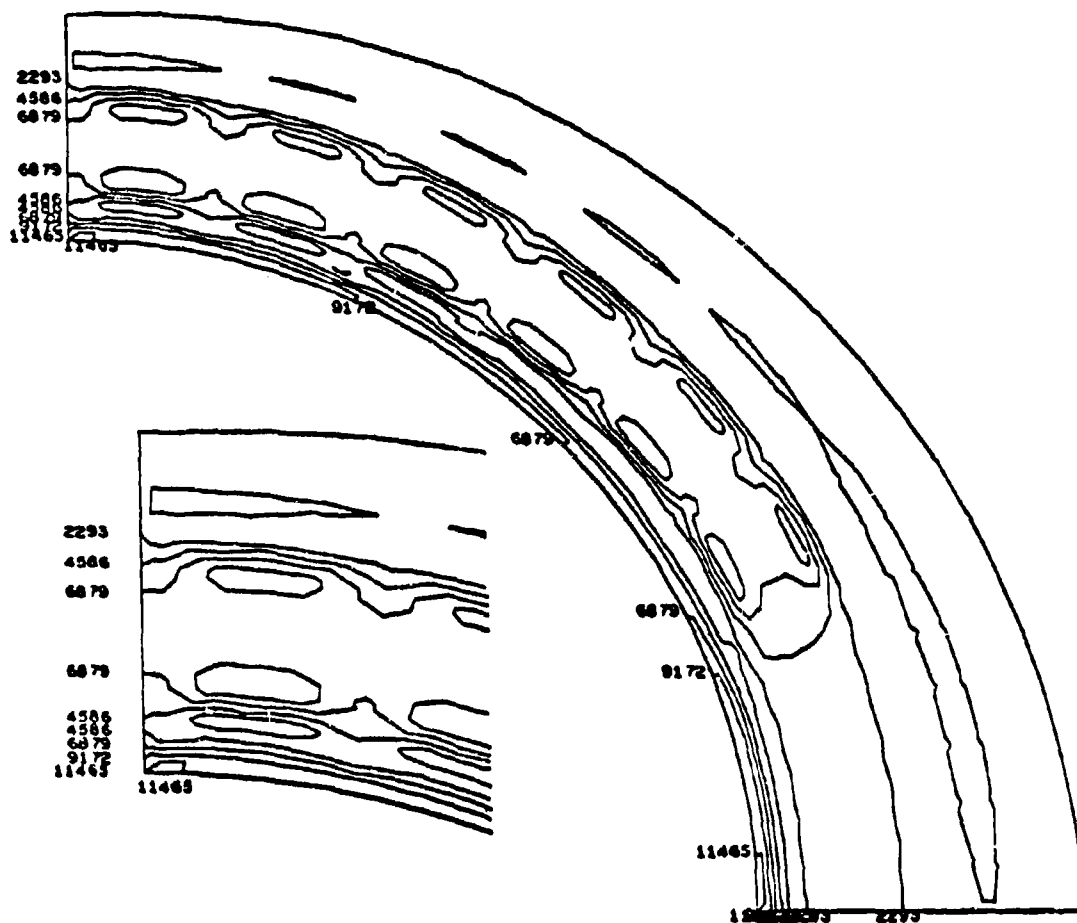


Figure A-10. Stress Contour Plot of Maximum Principal Stress  
due to Thermal Loads

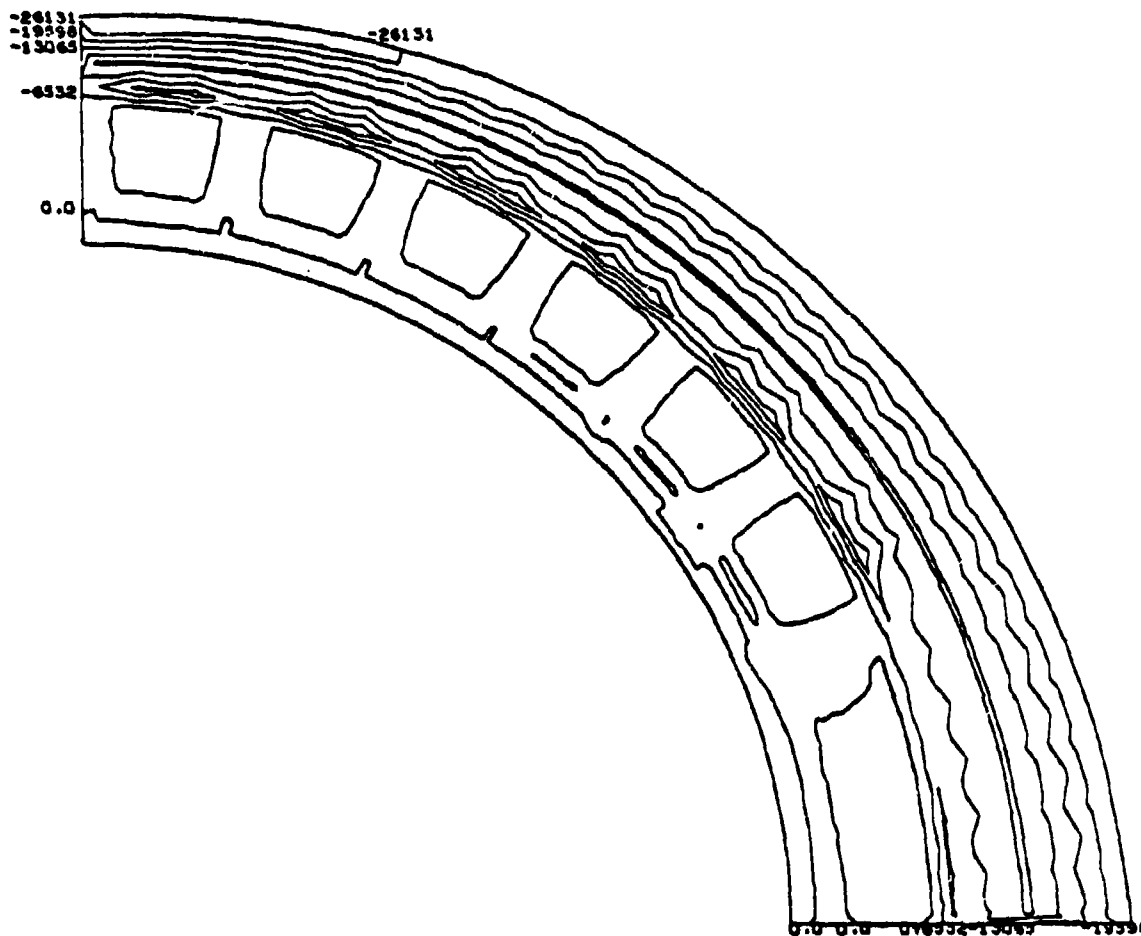


Figure A-11. Stress Contour Plot of Minimum Principal Stress  
due to Thermal Loads

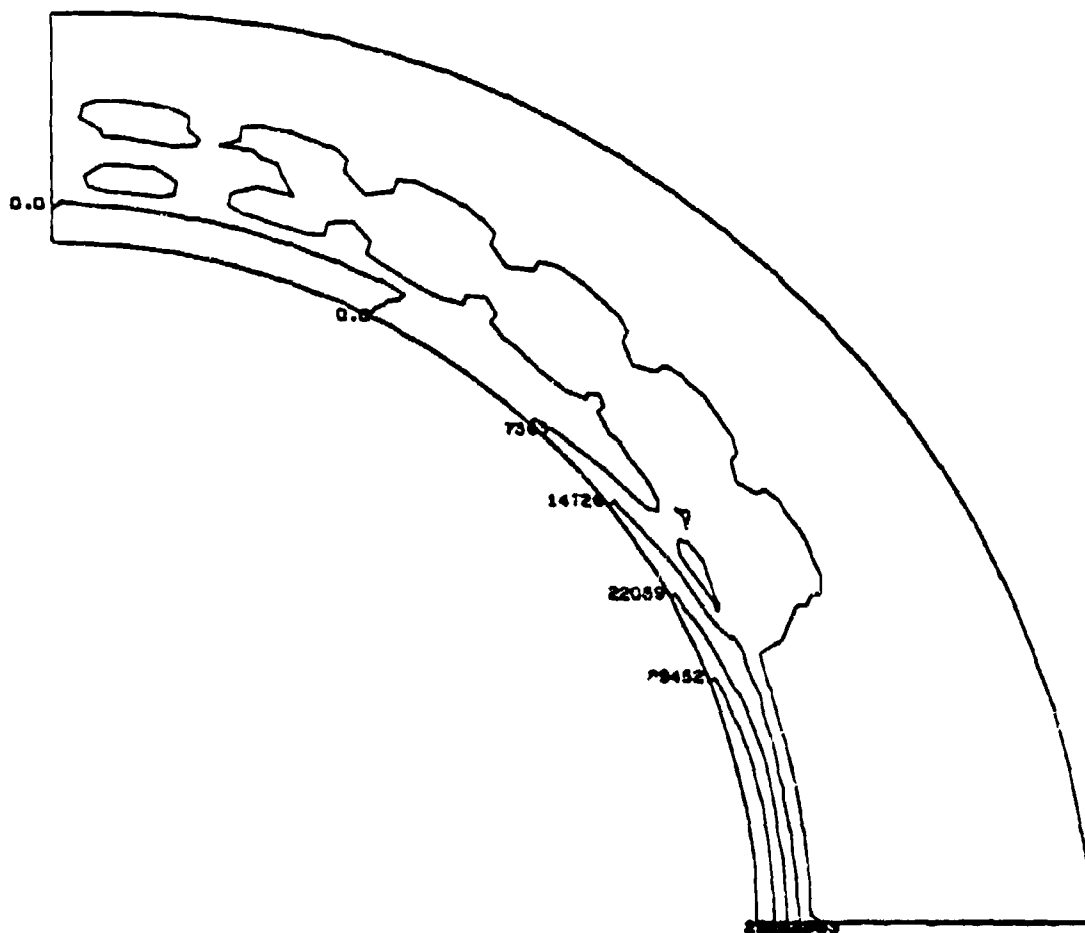


Figure A-12. Stress Contour Plot of Maximum Principal Stress  
for Combined Magnetic and Thermal Loading

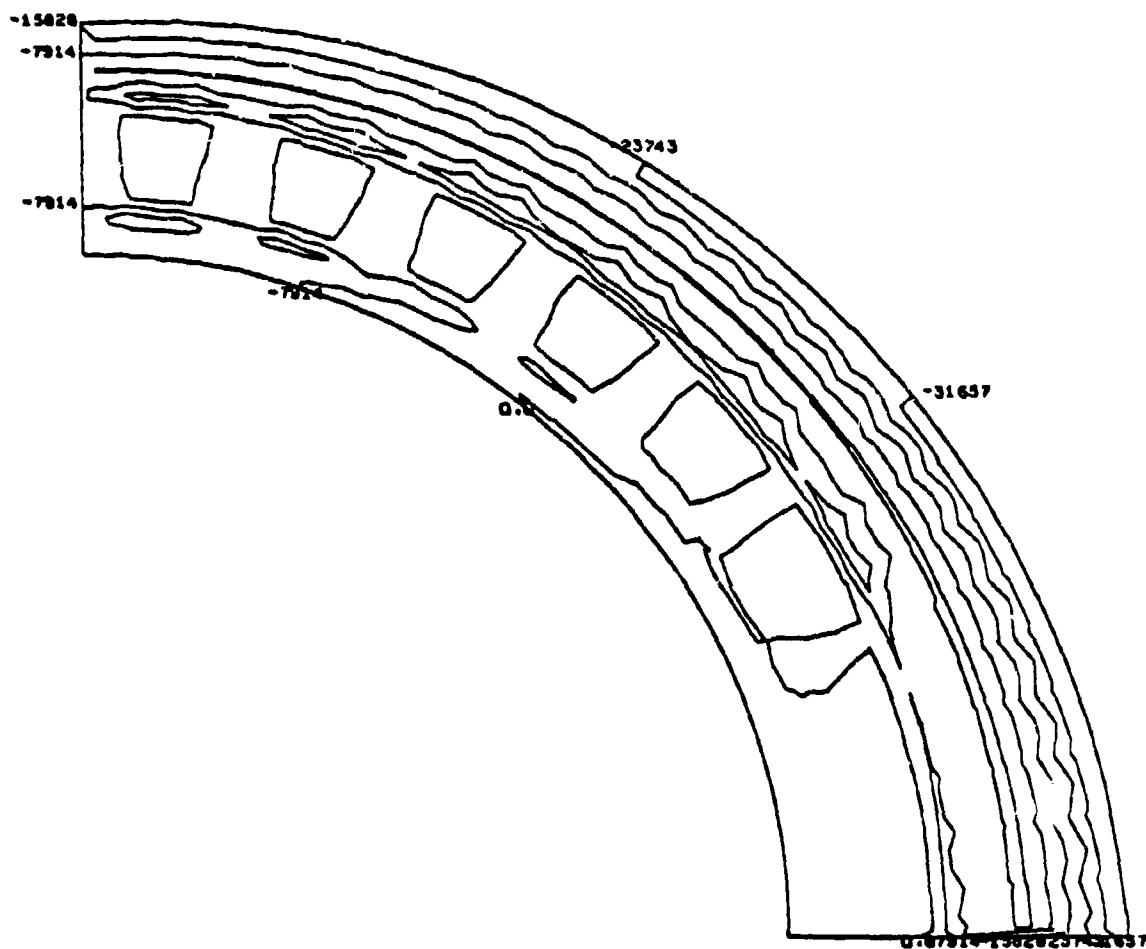


Figure A-13. Stress Contour Plot of Minimum Principal Stress  
for Combined Magnetic and Thermal Loading

## 5.5 GENERAL COMMENTS

Several aspects of the analysis will require more attention in subsequent phases. Some of these, such as the low interlaminar shear strength at cryogenic temperatures already have been discussed.

The recommended design concept is a filament wound structure. As the manufacturing methods become better defined, the filament winding pretension required will need to be included in the total state of strain in the graphite/epoxy. This may show that the winding tension can not be constant as a function of diameter.

The limited amount of material property data has also influenced the selection of composite systems. As more data becomes available, closer tolerances can be expected on the estimated wall thicknesses. In some instances, the lack of data led to the use of conservative values.

Another item that should be discussed early in Phase II is the selection of factors of safety. Normally a factor of safety of 1.50 would be applied, but due to the high forces and relatively foreign working environment, a factor of 2.00 may be desirable for the external shell. This decision should also be influenced by the importance given to safety during operation.

## SECTION A-6

### MANUFACTURING APPROACHES

The three design concepts described in this report differ only in the way in which the conductor winding is restrained. All manufacturing steps through bonding the honeycomb filler pieces around the conductor winding are common. These common steps are explained in the following paragraph. They are defined also in Figures 6-1, 6-2 and 6-3.

After the layup mandrel has been prepared with a release agent, the metal foil barrier will be fit trimmed and overlap bonded to itself on the mandrel. The bond will be autoclave cured under vacuum pressure. When the foil surface has been cleaned, the inner structural shell will be filament wound over it. The completed winding will be oven cured, and then profile machined to provide a controlled mating surface for the conductor winding. The wound assembly, including the mandrel, will be transported to M. C. A. for application of the conductor winding. When it is received back, hand trimmed pieces of honeycomb core will be positioned around the winding to fill all voids. These filler pieces will be bonded to the assembly in an oven under vacuum pressure. After a cleanup operation, one of the three concept option restraining structures will be applied.

#### 6.1 CONCEPT A

This concept utilizes a filament wound structure to restrain the conductor windings. A mid shell will be filament wound over the conductors and bonded filler pieces. This shell will be oven cured. A filler layer will then be wound onto the mid shell and subsequently oven cured. This filler will be profile machined so that clearance is provided for the tension tie rods. After the machining operation, the outer shell will be filament wound over the filler layer. It also will receive an oven cure. At this point, the wound structure, still on the tooling mandrel, will be end machined. The machined metal end retainer rings will be positioned and the tension tie rods installed. If the filament tension tie rod concept is chosen, they will be wound over a filler mandrel. It will be necessary to vary the winding tension to provide rods in which all filaments carry an equal load. Multiple cures may also be required. When the assembly tasks are completed, the mandrel will be removed.

#### 6.2 CONCEPT B

The individual aluminum hoop clamp beams will be machined in the curved configuration. Individual plies of boron/aluminum will be trimmed to fit into the beam recesses. These assemblies will be diffusion bonded and subsequently machined to mating contour. The lateral tension ties and the tension tie rods will be diffusion bonded also. They are fabricated as boron/aluminum tubes which have a titanium collar diffusion bonded at



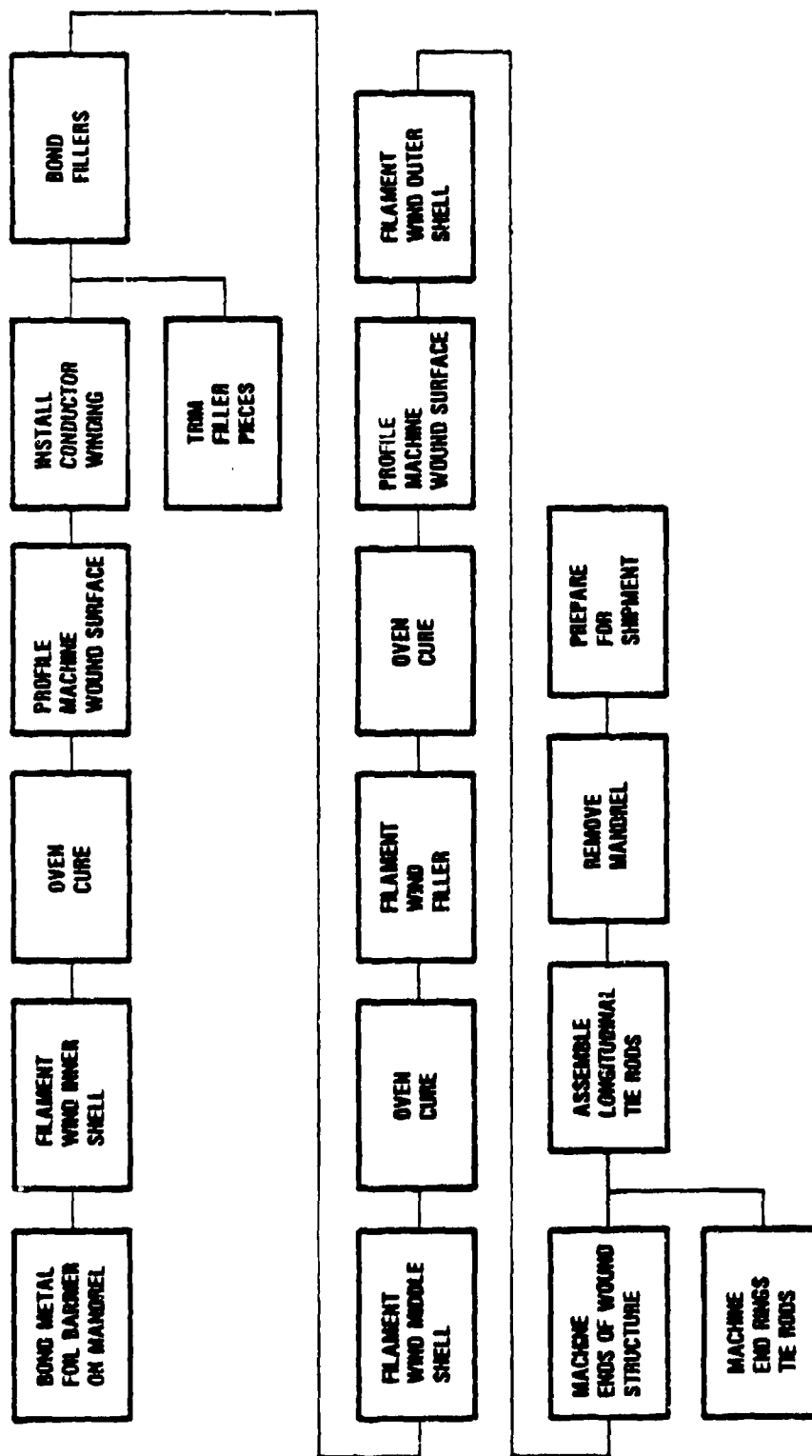


Figure A-14. MHD Magnet Modeling Manufacturing Sequence  
Concept A — Graphite/Epoxy, Filament Wound

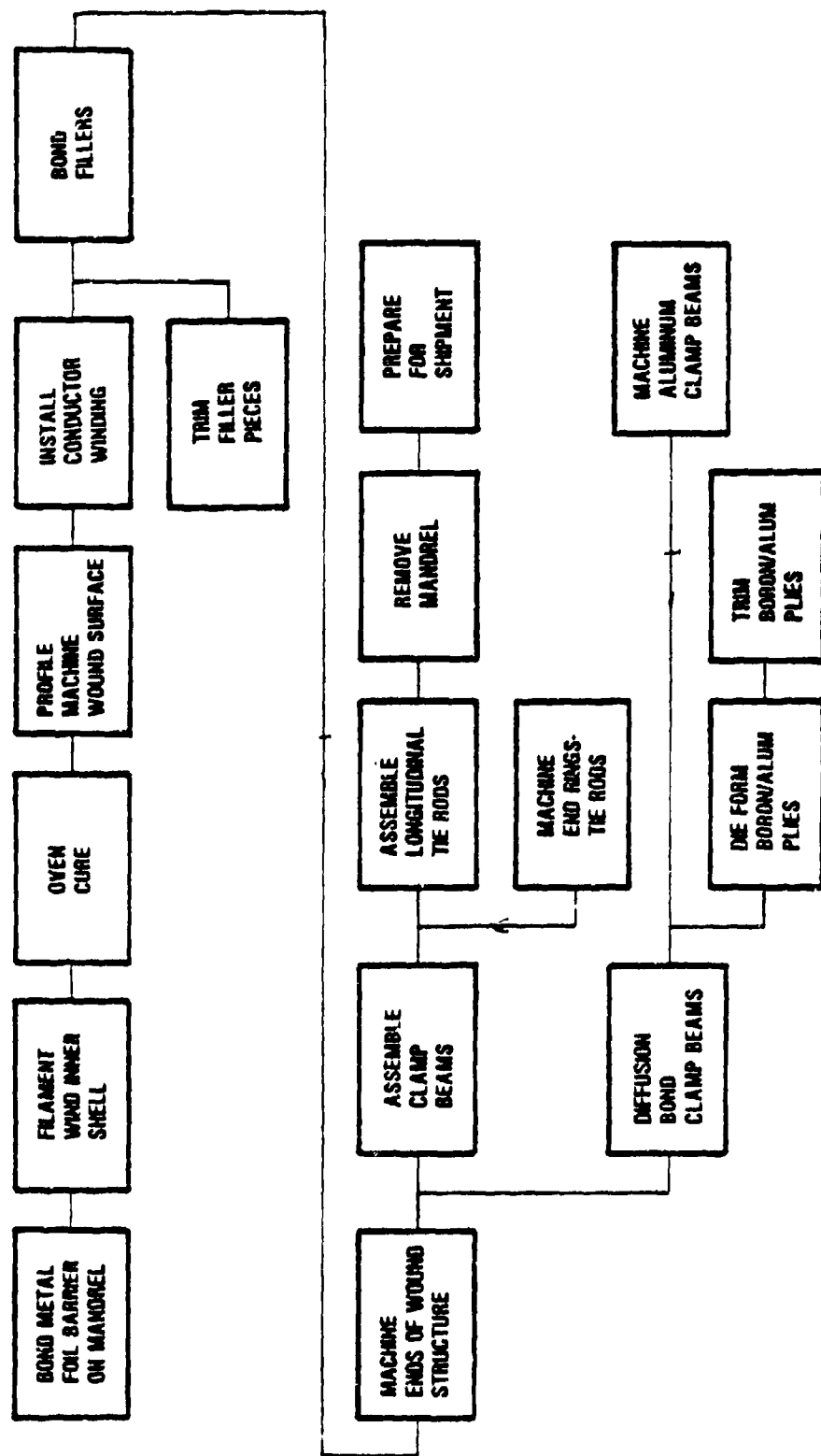


Figure A-15. MHD Magnet Modeling Manufacturing Sequence  
Concept B - Boron/Aluminum Structure

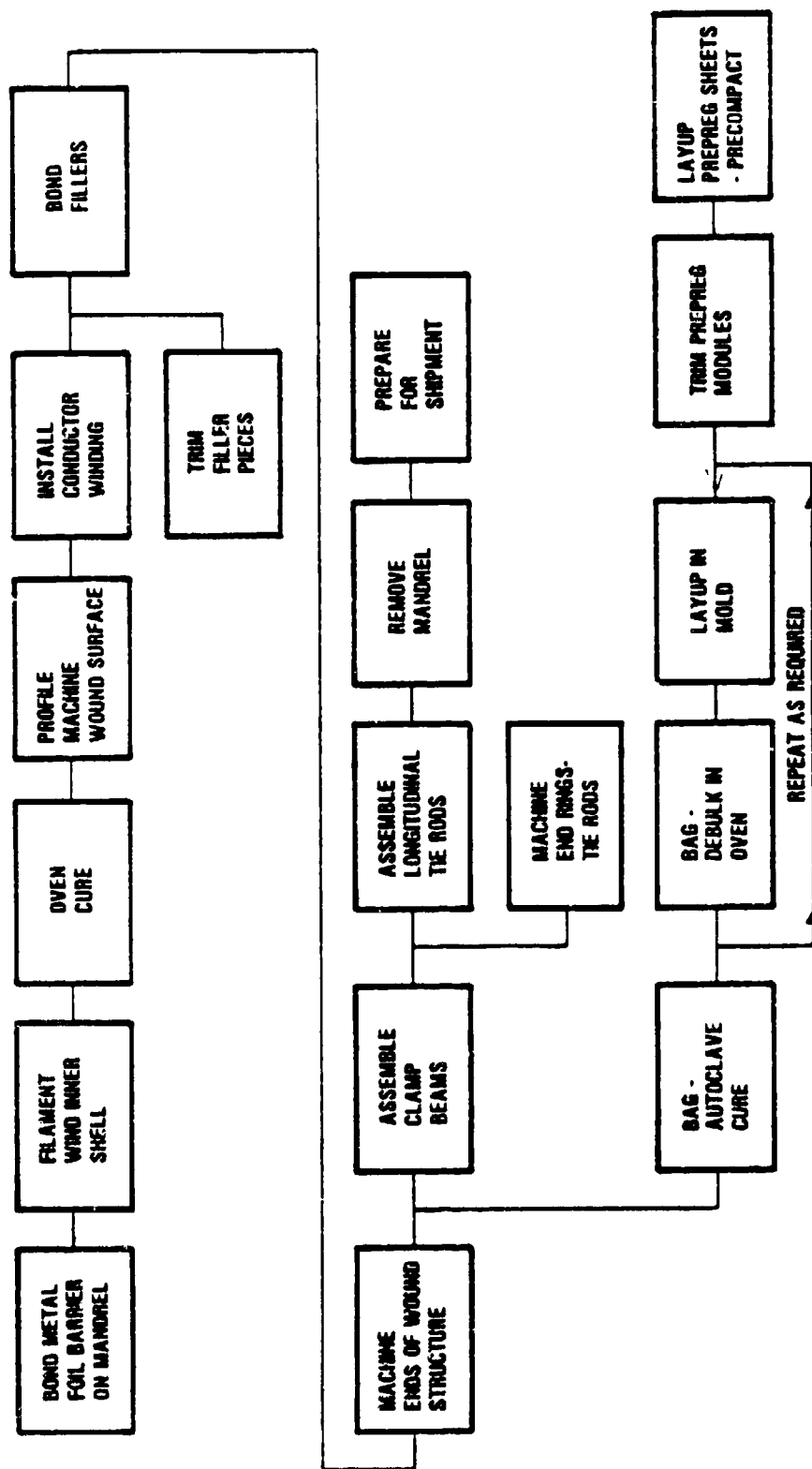


Figure A-16. MIID Magnet Modeling Manufacturing Sequence  
Concept C -- Graphite/Epoxy Structure

each end. Appropriate titanium end fittings will be electron beam welded to the titanium collars to complete the tension rod assemblies. The end retainer rings will be machined using conventional equipment and methods. After the restraining assembly is in place, the mandrel will be removed.

### 6.3 CONCEPT C

Each hoop clamp beam will be layed up in a cure mold. Individual plies of graphite-epoxy prepreg will be trimmed and fitted into the mold. The layup will be bagged and oven debulked approximately four times during the layup process. When the layup is complete, it will be bagged and autoclave cured. The end holes will then be machined. The boron/aluminum lateral tension ties and tension tie rods will be fabricated as described under Concept B. The end retainer rings will be machined by conventional methods. After the restraining assembly is in place, the mandrel will be removed.

## SECTION A-7

### TRADE STUDIES

The preceding sections have discussed materials, design concept, analytical considerations, and manufacturing approaches. All of these discussions have reviewed the various elements of our trade studies that were conducted. Hence, titling this present chapter Trade Studies is a bit misleading. What we actually wish to show here is a summary of our Phase I work in terms of the magnet structure weight, cost, and risk. To this end, Table 7-1 is presented as an overview of these studies when comparing the 29cm size model in the three design concepts. Details of the preparation of this table is given in the ensuing subsections.

#### 7.1 WEIGHT

Calculations were made for the expected structure weight of each design concept and for each size of model. The summary of weight totals is shown in Table 7-2. The weights shown are of the structure assembly only and do not include the dewar components nor the magnetic conductor windings.

To obtain the weights given in Table 7-2, individual weights of elements were first calculated for the 29cm model in each of the three design concepts. Appropriate scaling factors were then derived from the stress analysis results to project the expected weights for the 40cm and 50cm models. The initial weight breakdown for the 29cm models is given in Table 7-3.

#### 7.2 COST

The cost comparison was based on three factors: labor to fabricate a single unit, the use of low volume manufacturing methods, and tooling cost. The initial fabrication steps are common to all concepts and need not be considered in any comparison.

7.2.1 CONCEPT A. This concept ranks lowest in cost. The manhours required are significantly lower than those required for Concepts B or C. Within the field of composite fabrication, filament winding is not a labor intensive process. Filament winding on general purpose winding equipment requires only a mandrel support linked to the drive/leadscrew mechanism. Profile machining the winding to achieve an oval cross section will require a 180° trace pattern. The overall tooling cost, as well as the labor cost, is relatively low.

7.2.2 CONCEPT B. The boron/aluminum hoop clamp beam approach is the most expensive of the three concepts. Each beam segment must be machined before and after diffusion bonding. Individual plies of boron/aluminum must be hand trimmed

TABLE A-5  
MHD MAGNET MODELING CONCEPT COMPARISON

	CONCEPT		
	A	B	C
WEIGHT	1	2	3
COST	1	3	2
TECHNICAL AND SCHEDULE RISK	1	2	2

#### Notes

1. In the ranking above, 1 is the most advantageous, 3 is the least.
2. The approximate weights of the concepts are:  
 Concept A 1046 lb  
 Concept B 1113 lb  
 Concept C 1172 lb
3. The cost comparison is based primarily on the fabrication labor required to produce one article of each concept, and the tooling cost. Low volume manufacturing methods are assumed.
4. Technical risk includes required manufacturing development and tooling complexity.

TABLE A-6  
STRUCTURAL WEIGHTS (LBS)

Model Size	Concept		
	A	B	C
29cm	1046	1113	1172
40cm	2079	2159	2274
50cm	3159	3361	3539

TABLE A-7  
WEIGHT BREAKDOWN OF CONCEPTS A, B, AND C ~ 29cm SIZE

Item	Material	Density(pci)	Weight (lb)		
			A	B	C
Cold Bore Tube	G/E	0.063	141	141	141
Large End Ring	Ti	0.163	196	193	193
Small End Ring	Ti	0.163	82	54	54
Tension Tie Rods (8)	G/E	0.063	62	59	59
Tie Rod Fillers	HC 8 pcf	0.00465	5		
Hoop Clamps	Al <sup>(1)</sup> G/E <sup>(2)</sup>			358	215
Clamp Beams	B/Al	0.095		255	457
Structural Winding	G/E	0.063	528		
Conductor Filler	HC, 8 pcf	0.00465	3	3	3
Hardware	Ti	0.163	29	50	50
Totals			1046	1113	1172
Notes:					
(1) Concept B					
(2) Concept C					

and formed to contour. The individual beam segments must be welded into a metal bag prior to bonding, and this bag must then be removed by acid etching. All operations, whether layup or machining, contribute to the high labor input.

Since both Concept B and C utilize boron/aluminum tension rods, these rods are not a point of comparison between the two concepts.

7.2.3 CONCEPT C. The graphite/epoxy hoop clamp beam is judged to be slightly less expensive than Concept B. Though Concept C requires a higher labor input, the tooling required is less costly than the machining plus tooling required for Concept B.

### 7.3 RISK CONSIDERATIONS

An evaluation has been made of our design concepts with consideration to risk based on cost, schedule, and performance. To this end, we have assessed the probability that the MHD model structure will succeed in (1) achieving the specified performance, (2) meeting time constraints, and (3) meeting cost constraints. The means for risk elimination in a program of this type normally may be categorized within work phases of:

- . Design
- . Element/Subcomponent Development
- . Full-Scale Fabrication and Test

It is recognized at the outset that funding constraints of the MHD model program have precluded element and subcomponent development. Similarly full-scale fabrication and test will be of the actual model itself, i.e., a major part of the full-scale unit will not be built and tested as a step toward the end item. Hence, it is essential that attempts be made to eliminate risk through conservative design approaches using tried and proven design concepts, materials, and fabrication methods.

We have given due consideration to the above and qualitatively assessed risk for each of the three design concepts (A, B and C). This assessment (see Table 7-1) has aided in the selection of Concept A as the recommended design for further study.



## SECTION A-8

### RECOMMENDED DESIGN

The design concept recommended for further studies is the filament wound approach -- Concept A. This concept was shown in Figure 1. Our studies have shown that this concept will result in the least weight, least cost, and least risk of the concepts studied. It is further recommended that existing contractual funds of Phase 2 be allocated solely to the development and improvement of this design approach. It is not felt that Concepts B or C show sufficient promise to justify further consideration.